

NONLINEAR INTEGRATED PHOTONICS FOR QUANTUM  
STATE ENGINEERING

by

Chaohan Cui

---

Copyright © Chaohan Cui 2023

A Dissertation Submitted to the Faculty of the  
JAMES C. WYANT COLLEGE OF OPTICAL SCIENCES

In Partial Fulfillment of the Requirements  
For the Degree of

DOCTOR OF PHILOSOPHY

In the Graduate College


THE UNIVERSITY OF ARIZONA

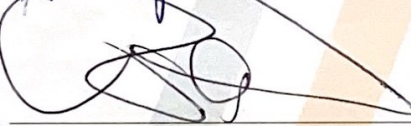
2023

THE UNIVERSITY OF ARIZONA  
GRADUATE COLLEGE

As members of the Dissertation Committee, we certify that we have read the dissertation prepared by **Chaohan Cui**, titled ***Nonlinear Integrated Photonics for Quantum State Engineering*** and recommend that it be accepted as fulfilling the dissertation requirement for the Degree of Doctor of Philosophy.

  
\_\_\_\_\_  
Professor Linran Fan Date: 4/4/23

  
\_\_\_\_\_  
Professor Salkat Guha Date: 4/4/2023

  
\_\_\_\_\_  
Professor Robert A. Norwood Date: 4/4/23

Final approval and acceptance of this dissertation is contingent upon the candidate's submission of the final copies of the dissertation to the Graduate College.

I hereby certify that I have read this dissertation prepared under my direction and recommend that it be accepted as fulfilling the dissertation requirement.

  
\_\_\_\_\_  
Professor Linran Fan  
Dissertation Committee Chair  
Wyant College of Optical Sciences Date: 4/28



## ACKNOWLEDGEMENTS

*Time is an illusion:  
our naive perception of its flow doesn't correspond to physical reality.*

—Carlo Rovelli

*People like us, who believe in physics, know that the distinction  
between past, present, and future is only a stubbornly persistent illusion.*

—Albert Einstein

Time is an illusion. The far I dive into the infinite dimension and possibility that time offers us, the more belief I give to those quotes, especially when science is too specific but the reality is too general. Time seems to get accelerated when people get old and get used to their surroundings. The reason, either philosophical, psychological, or even caused by the pandemic of coronavirus would not stop the clock from endlessly ticking toward the end of my Ph.D. life. Despite the irreversible arrow, I appreciate each piece of time my mind is oscillating between enjoying the research and hating the race and gambling for publication.

First and foremost, I would like to wholeheartedly thank my first academic advisor, professor Linran Fan, for the support and guidance he has provided me throughout my dissertation. As one of his first batch of students, he and I have been building the lab together and observing the development of the group. Despite his busy schedule at times, he is always willing to discuss any detail, from theoretical modeling to experimental realizations, with me. His broad view has also been enlightening me to break the boundary of my knowledge. I always appreciate his calm, patience, and insightful intuitions when listening to my fancy or even naive ideas.

On the other side, I would also like to thank my second academic advisor, professor Zheshen Zhang, for his support and earnest teachings over the four years. He introduces many opportunities for me to connect with a lot of wise minds all around the nation. In addition to his rigorous attitude toward science and technology, he has also helped me carefully plan and manage research projects in the early days. I really appreciate his mentoring on experimental design and scientific writing, which must significantly benefit my career.

Thanks to the two advisors, I have truly learned a lot from you during this voyage, which, I believe, has reached beyond science itself.

The College of Optical Sciences at the University of Arizona is a magical place where I am deeply addicted to the casual and warm atmosphere here, paired with

the unique experience of exploring mysterious aspects of light. It was my pleasure to have discussions with so many great researchers, in particular, Prof. Linran Fan, Prof. Zheshen Zhang, Prof. Dalziel Wilson, Prof. Quntao Zhuang, Prof. Saikat Guha, and others. Over the years, I have enjoyed interacting with students and post-docs around similar research themes, Dr. Kaushik P. Seshadreesa, Dr. Christos N. Gagatsos, Dr. Shuai Liu, Dr. Yongzhou Xue, Dr. Bo-Han Wu, Dr. Songyan Hou, Dr. Shuhong Hao, Dr. Yi Xia, Dr. Wei Li, Pao-Kang Chen, Ian Briggs, Manav Shah, Dalton Anderson, William Horrocks, William Roberts, Jack Postlewaite, Abdulkarim Hariri, Zhihan Hong, and Haowei Shi. In particular, I have most enjoyed working with Dr. Liang Zhang, who helped me a lot with nanofabrications. We are a team, and our strengths are complementary. We have shared the successes and the failures equally, and I really appreciate Liang for discussions, brainstorming, and inspiration throughout these days. Outside the research, I would like to thank all of my friends in Tuscon for the parties and activities that enhanced my life.

Last but not least, I wish to thank a special group of people. It's my fortune to have met Yisha Tang, who has enriched my life in every aspect. I thank her for all the love, support, and encouragement that she brought to me. I also want to thank Boyuan Lu, who has been playing games with me since young. In addition, I wish to thank my parents, my mother, Yujie Zheng, and my father Fuhong Cui. Their support and love, far from my homeland across the ocean, have always turned into my motivation and inspiration. They encourage me to confront the challenge and break through the bottleneck. It is to them, I wish to dedicate this thesis.

*Chaohan Cui*

Chaohan Cui  
Tucson, AZ, 2023

## DEDICATION

*This dissertation is dedicated to my parents.  
Thanks for always encouraging and supporting me in overcoming unending  
challenges throughout my youth.*

## TABLE OF CONTENTS

LIST OF FIGURES . . . . .	9
LIST OF TABLES . . . . .	11
ABSTRACT . . . . .	12
CHAPTER 1 Introduction . . . . .	13
CHAPTER 2 Fundamental Theory . . . . .	19
2.1 Linearly Quantized Electromagnetic Field . . . . .	19
2.1.1 Transverse Mode . . . . .	20
2.1.2 Spectral Mode . . . . .	25
2.1.3 Resonator . . . . .	26
2.1.4 Field Quantization and the Concept of Photon . . . . .	28
2.1.5 Quantized Field in an Infinite Space . . . . .	34
2.1.6 Quantized Field in a Resonator . . . . .	37
2.1.7 Nonlinear Optical Effects . . . . .	41
2.2 Second-Order Nonlinearity . . . . .	43
2.2.1 Second-Harmonic Generation . . . . .	44
2.2.2 Phase-Matching Techniques . . . . .	47
2.2.3 Cavity Enhancement . . . . .	49
2.2.4 Sum-Frequency Generation . . . . .	51
2.2.5 Parametric Down-Conversion . . . . .	51
2.3 Third-Order Nonlinearity . . . . .	53
2.3.1 Self-Phase Modulation . . . . .	54
2.3.2 Cross-Phase Modulation . . . . .	55
2.3.3 Four-Wave Mixing . . . . .	56
2.4 Cascaded Second-Order Nonlinearities . . . . .	57
CHAPTER 3 On-Chip Photon-Pair Generation in Dressed Modes: the Pho- tonic Mollow Triplet . . . . .	61
3.1 Abstract . . . . .	61
3.2 Main Article . . . . .	61
3.2.1 Introduction . . . . .	61
3.2.2 Theoretical Model . . . . .	63
3.2.3 Experimental Results and Discussion . . . . .	66



TABLE OF CONTENTS – *Continued*

3.2.4	Conclusion . . . . .	69
3.3	Supplementary Materials . . . . .	69
3.3.1	Theoretical Description of Quantum Photonic Mollow Triplet . . . . .	69
3.3.2	Effect of Pump Frequency Detuning . . . . .	73
3.3.3	Data for All Signal-Idler Pairs . . . . .	74
CHAPTER 4 Reconfigurable Kerr Nonlinearity Enabled by Cascaded Second-Order Nonlinear Processes . . . . . 77		
4.1	Abstract . . . . .	77
4.2	Main Article . . . . .	77
4.2.1	Introduction . . . . .	77
4.2.2	Conceptual Model . . . . .	79
4.2.3	Experiments . . . . .	83
4.2.4	Discussion . . . . .	85
4.2.5	Methods . . . . .	85
4.3	Supplementary Materials . . . . .	86
4.3.1	Theoretical Model of the Effective Kerr Nonlinearity with Cascaded Pockels Processes . . . . .	86
4.3.2	Device Characterization . . . . .	90
4.3.3	Single-Photon Measurement . . . . .	93
CHAPTER 5 Reconfigurable Kerr Nonlinearity: Controlling the Spontaneous Symmetry Breaking of Photonic Chirality . . . . . 96		
5.1	Abstract . . . . .	96
5.2	Main Article . . . . .	97
5.2.1	Introduction . . . . .	97
5.2.2	Reconfigurable Kerr Nonlinearity . . . . .	99
5.2.3	Spontaneous Chiral Symmetry Breaking . . . . .	105
5.2.4	Conclusion . . . . .	107
5.3	Supplementary Materials . . . . .	107
5.3.1	Theoretical Model for Reconfigurable Kerr Nonlinearity . . . . .	107
5.3.2	Theoretical Model for Spontaneous Chiral Symmetry Breaking . . . . .	110
5.3.3	Experimental Setups . . . . .	113
5.3.4	Basic Device Parameters . . . . .	116
5.3.5	Additional Data for Spontaneous Chiral Symmetry Breaking . . . . .	117
CHAPTER 6 High-Purity Pulsed Squeezing Generation in Integrated Photonics . . . . . 118		
6.1	Abstract . . . . .	118
6.2	Main Article . . . . .	118

TABLE OF CONTENTS – *Continued*

6.2.1	Introduction . . . . .	118
6.2.2	Theoretical Model . . . . .	120
6.2.3	Numerical Simulation . . . . .	124
6.2.4	Discussion . . . . .	128
6.2.5	Conclusion . . . . .	130
CHAPTER 7 Customized Poling for High-Purity Indistinguishable Photon-		
	Pair Generation . . . . .	132
7.1	Abstract . . . . .	132
7.2	Main Article . . . . .	132
7.2.1	Introduction . . . . .	132
7.2.2	Bi-Photon JSA and Phase Matching . . . . .	135
7.2.3	The GVM Condition and Gaussian Phase-Matching Profile . . . . .	138
7.2.4	General Phase Matching without the GVM Condition . . . . .	139
7.2.5	The Machine-Learning Framework . . . . .	140
7.2.6	Poling-Design Recipe . . . . .	145
7.2.7	Simulation Results . . . . .	146
7.2.8	Discussion . . . . .	148
7.2.9	Conclusions . . . . .	150
7.3	Supplementary Materials . . . . .	150
7.3.1	Definition of the Purity of a Bi-Photon State . . . . .	150
7.3.2	Definition of the Indistinguishability of a Bi-Photon State . . . . .	151

## LIST OF FIGURES

2.1	Transverse modes in waveguides. . . . .	22
2.2	Micro-ring resonator . . . . .	26
2.3	Quantum harmonic oscillator and squeezed field. . . . .	31
2.4	Second-order nonlinearity. . . . .	44
2.5	Illustrations of phase-matching techniques. . . . .	48
2.6	Third-order nonlinearity. . . . .	54
3.1	Photonic analogue of Mollow triplet. . . . .	62
3.2	Entangled photon pair generation. . . . .	64
3.3	Observation of Mollow triplet with quantum temporal correlations . .	65
3.4	Mollow phenomena with single sideband . . . . .	68
3.5	Intepretation to the detuned photonic Mollow triplet . . . . .	74
3.6	Additional data . . . . .	75
4.1	Effective Kerr nonlinearity with cascaded Pockels process . . . . .	79
4.2	Enhancement of Kerr nonlinearity . . . . .	80
4.3	Quantum interference between nonlinear processes . . . . .	82
4.4	Continuous tuning of Kerr nonlinear strength in the quantum regime	83
4.5	Linear measurement setup and device design . . . . .	89
4.6	Resonances for stimulated FWM measurement . . . . .	90
4.7	Second-harmonic generation with different phase-matching wavelengths	91
4.8	Thermal tuning calibrations of frequency detune for two pairs of phase-matching modes . . . . .	92
4.9	Single photon measurement . . . . .	94
5.1	Schematics for reconfigurable Kerr nonlinearity . . . . .	98
5.2	Anomalous Kerr nonlinearity . . . . .	100
5.3	In-situ control of spontaneous symmetry breaking of photonic chirality	103
5.4	Control of spontaneous symmetry breaking condition . . . . .	104
5.5	Simulation of complex effective Kerr nonlinearity . . . . .	110
5.6	Spontaneous symmetry breaking of photonic chirality . . . . .	113
5.7	Experimental setups . . . . .	115
5.8	Linear and nonlinear properties of the target cavities. . . . .	116
5.9	Additional data . . . . .	117
6.1	Proposed configuration for high-purity pulsed squeezing generation .	120

LIST OF FIGURES – *Continued*

6.2	Equivalent photonic circuit of parametric down-conversion in a photonic cavity with pulsed pump. . . . .	124
6.3	The intra-cavity pump threshold power with dependence on the pump bandwidth. . . . .	125
6.4	The spectral amplitude and phase of the first three characteristic modes near the pump threshold. . . . .	126
6.5	Squeezing levels . . . . .	127
6.6	Effective mode numbers . . . . .	128
6.7	Proposed setup for local oscillator shaping. . . . .	129
6.8	Simulations with different pulsed pumps . . . . .	130
7.1	Poling profiles for a nonlinear crystal . . . . .	137
7.2	KTP's Type-II SPDC phase mismatch. . . . .	138
7.3	A general machine-learning model. . . . .	141
7.4	The evolution of the cost during poling optimization . . . . .	142
7.5	Poling profiles for the generation of spectrally-uncorrelated bi-photons in the 1550-nm band. . . . .	143
7.6	Simulated purities at different wavelengths . . . . .	144
7.7	Bi-photon joint-power spectrum after each design step . . . . .	144



## LIST OF TABLES

3.1	Additional parameters . . . . .	75
4.1	Coupling rates and total loss rates . . . . .	90
7.1	Comparison of the performance metrics between prior works and the present work . . . . .	148

## ABSTRACT

Nonlinear photonics has provided a scientific cornerstone for a majority of modern technology during the past half-century, such as diversifying laser wavelengths, manufacturing nanostructures, and guiding the design of telecommunication systems. Moreover, it keeps supporting the emergence of novel applications, including high-resolution spectroscopy, atomic clocks, and especially quantum technology. However, in photonic quantum state engineering, current recipes for design and modeling are impotent in specific quantum applications, for which advanced techniques are urgently needed. In this dissertation, the quantum-level interplay between the linear response of integrated photonic devices and multiple nonlinearities within the system has been investigated in detail. We utilize these interactions to manage the generation of limit-breaking quantum photonic states, including customized temporal-spectral entanglement, high-brightness quantum sources, and high-purity quantum states.

## CHAPTER 1

### Introduction

In nature, most systems are inherently nonlinear, such as the biosphere we live in and the intelligence we have. Unlike linear systems, whose solutions can be clearly determined by a linear transformation, the states and dynamics of nonlinear systems can not be described as a linear combination of any characteristics. A simple modification of the input may influence the system and lead to a counterintuitive output. Therefore, a plethora of phenomena, either beautiful or chimerical, harmonic or chaotic, can be tailored from nonlinear systems. This built-in enigma makes the physical world unpredictable with partial knowledge but offers surprises at any time.

Fortunately, nonlinear systems are not always too complex to be solved by humankind. Scientists have examined some simple nonlinear systems in laboratories and learned their possible behaviors. During the past half century, the rapid development of mathematical modeling and computing technologies has provided various tools for efficiently solving and simulating simple nonlinear systems, which accumulates more insights towards real complex systems. With these techniques, we understand the world and its dynamics better than ever. Now, we benefit from the short-term forecast for weather, astronomy, and even some parts of the global economy.

Nonlinearity does not only produce puzzles. However, it could be a key to solving the puzzles. There are many practical nonlinear systems embedded into the apparatus that keep rolling our world into new eras, including engines and aerodynamics for transportation, semiconductors for computers and smartphones, as well as laser systems and optical amplifiers for the Internet. In recent years, scientists also find that the nonlinearity in the computation models is essential for achieving artificial intelligence, which, if possible, will bring a huge wave of revolutions to

our lives. Therefore, it could be confidently predicted that, in the future, more newly-designed nonlinear systems will be applied to technologies around us.

Among known nonlinear systems, nonlinear photonics contain fruitful research topics tightly bonded with the information technologies and beyond, such as laser, imaging, communication, sensing, and computation. They enjoy incomparable advantages of the highest traveling speed and high bandwidth. Moreover, applications based on nonlinear photonics have the potential to be miniaturized and integrated into chip-scale devices. They benefit from less energy consumption since a smaller volume of optical fields will provide higher energy density and nonlinearity.

To date, nonlinear photonic phenomena keep drawing interest from scientists and engineers as there are challenges toward profitable upgrades over the current technology. On the other side, nonlinear photonics has already been shining for decades in quantum information processing. Quantum photonic platforms can be operated at room temperature by choosing high-frequency photons as the information carrier. They are also the only solution to efficiently convey quantum information through long distances, such as quantum communication and quantum remote sensing. Photonic nonlinearities are needed to generate designated quantum states, such as squeezed state, and operate them universally. Despite the importance, the current recipes in quantum state engineering are less effective than the requirements of most promising applications. New techniques for exceeding the current limits are necessary.

Fortunately, since photonic nonlinearity fundamentally derives from the light-matter interactions at the sub-wavelength scale, it is possible to overcome the limits based on recent developments of nonlinear integrated photonics. They enable the fabrication of nano-scale artificial geometries that can enhance and modify the nonlinear effects by their fruitful linear responses. This dissertation primarily concentrates on our recent discoveries and developments in integrated nonlinear photonics as they can provide insights and solutions to some challenges in quantum state engineering.

To understand the novel effects enabled by integrated nonlinear photonics and



their impact on applications, it is necessary to prepare the necessary mathematical tools and physical models beforehand. In Chapter 2, we are going to introduce a simplified interpretation of the quantized electromagnetic fields, the concept of photons, and the squeezed bosonic fields. Hence, the leading nonlinear photonic effects can be clearly mapped onto photon-photon interactions. We then discuss the linear and nonlinear dynamics in a photonic cavity. In the end, the cascaded nonlinearities are introduced.

In Chapter 3, we show that a single photonic cavity can show linear properties of dressed modes [1]. Combined with the nonlinear effect, we can experimentally generate the photonic Mollow triplet by the four-wave mixing. This unveils the symbiosis between the linear and nonlinear properties of a single photonic cavity.

In Chapter 4, we demonstrate that the interplay among the linear responses and multiple nonlinear effects of a single photonic cavity can significantly alter the effective Kerr nonlinear coefficient without redesigning the device [2]. It enables the first *in-situ* control of the third-order nonlinearity of a fixed structure. The manipulated coefficient is reflected from the photon-pair-generation rate by the four-wave mixing.

Moreover, in Chapter 5, we directly see the change in the effective Kerr nonlinear coefficient by monitoring the self-phase modulation strength [3]. It is also the first proof of the reconfigurable phase relation between third-order and cascaded second-order nonlinearities. In the experiment, the anomalous Kerr coefficient, i.e. the negative Kerr effect, is achieved. By applying this technique, we successfully demonstrate the tunability between facilitating and suspending the spontaneous chiral symmetry breaking in a nanophotonic platform, which was widely regarded as impossible.

In Chapter 6, we proposed a route to generate high-purity pulsed squeezing in an integrated photonic cavity [4]. The numerical simulation promises the possibility of achieving the required squeezed level with current technology.

In Chapter 7, we proposed a machine-learning-assisted architecture to customize the poling design [5]. This architecture helps us automatically optimize the poling

profile toward the target time-energy correlation between generated photon pairs. Typically, it can generate two identical pure single photons instead of a pair of entangled photons, which is useful in Boson sampling and other applications requiring high single-photon purity. Although in this work, the technique is applied to the KTP crystals, the architecture indeed fits the integrated photonics by a slight modification.

Besides those works, we have also investigated time-energy entanglement and the arbitrary linear operation over the set of frequencies by time-resolved detection [6]. Furthermore, the nonlinear behavior of a system can emerge from the hybrid action of single-photon measurement and feed-forward control, which can boost the capability of quantum information processing. We develop a reinforcement-learning architecture to generate a better strategy for the target task. The experiment confirms the quantum advantage of this type of quantum receiver in decoding quantum information [7].

## Published Contents and Contributions

- **Chaohan Cui**, Liang Zhang, and Linran Fan. In situ control of effective Kerr nonlinearity with Pockels integrated photonics. *Nature Physics*, **18**(5), 497–501 (2022). C.C. conceived the idea, derived the theoretical model, devised the experiment, and wrote the paper supervised by L.F.
- **Chaohan Cui**, Liang Zhang, and Linran Fan. Control spontaneous symmetry breaking of photonic chirality with reconfigurable anomalous nonlinearity. Preprint at <https://arxiv.org/abs/2208.04866> (2022). C.C. participated in conceiving the idea, derived the theoretical model, developed the experiment, and wrote the paper supervised by L.F.
- **Chaohan Cui**, Liang Zhang, and Linran Fan. Photonic analog of Mollow triplet with on-chip photon-pair generation in dressed modes. *Optics Letters*, **46**(19), 4753–4756 (2021). C.C. participated in conceiving the idea, derived

the theoretical model, finished the experiment, and wrote the paper supervised by L.F.

- **Chaohan Cui**, Christos N Gagatsos, Saikat Guha, and Linran Fan. High-purity pulsed squeezing generation with integrated photonics. *Physical Review Research*, **3**(1), 013199 (2021). C.C. derived the theoretical model, realized the simulation, and wrote the paper supervised by L.F.
- **Chaohan Cui**, Kaushik P Seshadreesan, Saikat Guha, and Linran Fan. High-dimensional frequency-encoded quantum information processing with passive photonics and time-resolving detection. *Physical Review Letters*, **124**(19), 190502 (2020). C.C. conceived the idea, derived the theoretical model, and wrote the paper supervised by L.F.
- **Chaohan Cui**, William Horrocks, Shuhong Hao, Saikat Guha, Nasser Peyghambarian, Quntao Zhuang, and Zheshen Zhang. Quantum receiver enhanced by adaptive learning. *Light: Science & Applications*, **11**(1), 344 (2022). C.C. conceived the idea, developed the code, finished the experiment, and wrote the paper supervised by Z.Z.
- **Chaohan Cui**, Reeshad Arian, Saikat Guha, N Peyghambarian, Quntao Zhuang, and Zheshen Zhang. Wave-function engineering for spectrally uncorrelated biphotons in the telecommunication band based on a machine-learning framework. *Physical Review Applied*, **12**(3), 034059 (2019). C.C. conceived the idea, derived the theoretical model, and wrote the paper supervised by Z.Z.
- Jing Wu, **Chaohan Cui**, Linran Fan, and Quntao Zhuang. Deterministic microwave-optical transduction based on quantum teleportation. *Physical Review Applied*, **16**(6), 064044 (2021). C.C. participated in deriving the theoretical model and contributed to the appendix of the paper.
- Liang Zhang, **Chaohan Cui**, Jianchang Yan, Yanan Guo, Junxi Wang,

and Linran Fan. On-chip parallel processing of quantum frequency combs for high-dimensional hyper-entanglement generation. Preprint at <https://arxiv.org/abs/2111.12784> (2021). C.C. participated in conceiving the idea, deriving the theoretical model, and contributing to the supplementary materials of the paper.

- Ian Briggs, Songyan Hou, **Chaohan Cui**, and Linran Fan. Simultaneous type-I and type-II phase matching for second-order nonlinearity in integrated lithium niobate waveguide. *Optics Express*, **29**(16), 26183-26190 (2021). C.C. participated in handling the superconducting single-photon detectors.
- **Chaohan Cui** and Linran Fan. Zero-assumption determination of individual optical resonance coupling conditions with binary phase modulation. In preparation. C.C. devised the idea, developed the model, and finished the experiment under L.F.'s supervision.



## CHAPTER 2

### Fundamental Theory

In this chapter, we are going to introduce a uniform mathematical framework with quantized electromagnetic fields to describe the material-property-determined nonlinear photonic processes in waveguides and resonators. Most of the contents are derived or summarized from famed textbooks [8, 9, 10, 11, 12, 13].

This methodical framework is provided to ease understanding of the theoretical model of the following chapters. We will cover multiple aspects of the second and third-order nonlinearities under the picture of photon-photon interaction. We will also introduce the concept of phase matching and cavity enhancement, which have been recognized as common techniques for boosting nonlinear effects. In the end, we will glance at the cascaded second-order nonlinearities.

#### **2.1 Linearly Quantized Electromagnetic Field**

Nonlinear photonics focuses on the interactions among electromagnetic fields across the infrared, visible light, and ultraviolet spectra, with their wavelengths ranging from sub-millimeter to one hundred nanometers. This spectrum span has dynamic physical properties where materials behaviors are distinctive, and it has historical connections with visual optics, which studies the light spectrum detectable by human eyes.

The interaction between light and matter is direct within this spectral range. For a longer wavelength towards the radio frequency region, the collective movement of electrons in electrical conductors or the vibration of dipoles will cause severe absorption, scattering, or re-emission. On the other hand, shorter wavelengths, such as X-rays or gamma rays, are ionizing radiation that can damage or penetrate most of the materials. Hence, weak but meaningful parametric interactions between

light fields can emerge. To determine the nonlinear interaction, especially including the quantum behavior, we need a quantized description of the linear electromagnetic fields.

As a type of electromagnetic field, the dynamics of light fields follow the group of Maxwell equations in Cartesian coordinates.

$$\nabla \cdot \mathbf{D} = \rho, \quad \nabla \times \mathbf{E} = -\frac{\partial \mathbf{B}}{\partial t} \quad (2.1)$$

$$\nabla \cdot \mathbf{B} = 0, \quad \nabla \times \mathbf{H} = \mathbf{J} + \frac{\partial \mathbf{D}}{\partial t} \quad (2.2)$$

$$\mathbf{D} = \varepsilon_0 \mathbf{E} + \mathbf{P}, \quad \mathbf{H} = \frac{\mathbf{B}}{\mu_0} - \mathbf{M} \quad (2.3)$$

In current nonlinear photonics, researchers are mostly focusing on the interaction between light fields in transparent dielectric materials, where no free charge, current, or magnetization exists.  $\rho = 0$ ,  $\mathbf{J} = 0$ , and  $\mathbf{M} = 0$ . Since the nonlinear effects are generally weak, they are usually considered as a perturbation upon the linear solutions for the electromagnetic field.

The linear basis are solutions to Maxwell's equations. They constitute a linearly-independent complete set, which means any solution of the Maxwell equations can be decomposed into a linear superposition of these basis functions with suitable weights. Conventionally, each basis function is presented as a product of a spatial mode and a spectral mode. The spatial mode contains the distribution of the light field in space, while the spectral mode indicates how the light field varies in time.

We begin with a discussion on monochromatic spatial modes. As a convention, the light wave is propagating in the  $\hat{z}$  direction of a Cartesian coordinate system in most situations considered in this dissertation.

### 2.1.1 Transverse Mode

In an infinite large isotropic transparent dielectric medium, the linear part of the polarization in the homogeneous medium can be written as  $\mathbf{P} = \varepsilon_0 \chi^{(1)} \mathbf{E}$ . The Maxwell equations can now be reduced to two homogeneous wave equations that

are valid at any point within space-time.

$$\left(\nabla^2 - \frac{1}{c^2} \frac{\partial^2}{\partial t^2}\right) \mathbf{E} = 0 \quad (2.4)$$

$$\left(\nabla^2 - \frac{1}{c^2} \frac{\partial^2}{\partial t^2}\right) \mathbf{B} = 0, \quad (2.5)$$

where  $c = c_0/n$  and  $n = \sqrt{\mu\varepsilon_0(1 + \chi^{(1)})}$ . In vacuum, we have  $c_0 = 1/\sqrt{\mu_0\varepsilon_0} = 299792458 \text{ nm} \cdot \text{GHz}$ . The electromagnetic field can be expressed as plane waves

$$\mathbf{E}(\mathbf{r}, t; \mathbf{k}, \omega) = \mathbf{E}_0(\mathbf{k}, \omega)e^{-i(\omega t - \mathbf{k} \cdot \mathbf{r})} + \mathbf{E}_0^*(\mathbf{k}, \omega)e^{i(\omega t - \mathbf{k} \cdot \mathbf{r})} \quad (2.6)$$

$$\mathbf{B}(\mathbf{r}, t; \mathbf{k}, \omega) = \frac{1}{\omega} [\mathbf{k} \times \mathbf{E}_0(\mathbf{k}, \omega)e^{-i(\omega t - \mathbf{k} \cdot \mathbf{r})} - \mathbf{k} \times \mathbf{E}_0^*(\mathbf{k}, \omega)e^{i(\omega t - \mathbf{k} \cdot \mathbf{r})}] \quad (2.7)$$

Each solution of the wave equations indicates an electromagnetic wave propagating at the speed of light  $c$  along the direction defined by wave vector  $|\mathbf{k}| = \omega/c$ . In this case, the electric field  $\mathbf{E}$ , the magnetic field  $\mathbf{B}$ , and the wave vector  $\mathbf{k}$  are mutually perpendicular so that these solutions are transverse electromagnetic modes.

Any monochromatic light field at frequency  $\omega$  can be decomposed into a series of plane waves with different amplitudes associated with wave vectors.

$$\mathbf{E}_{\text{tot}}(\mathbf{r}, t) = \int d^3\mathbf{k} \mathbf{E}(\mathbf{r}, t; \mathbf{k}, \omega) \quad (2.8)$$

$$\mathbf{B}_{\text{tot}}(\mathbf{r}, t) = \int d^3\mathbf{k} \mathbf{B}(\mathbf{r}, t; \mathbf{k}, \omega) \quad (2.9)$$

Despite its convenience in theoretical modeling, the plane wave is always an ideal solution that can not be fully realized in practice since there is always a finite aperture in the optical setup. In bulk-optical experiments, researchers usually apply lenses to put the waist of a Gaussian beam at the center of the nonlinear material and ensure the effective thickness to be shorter than the Rayleigh range. Therefore, plane waves are reasonable approximations when considering nonlinear photonics in bulk materials, unless the nonlinear effect incurs a severe distortion of the wavefront.

However, in integrated photonics, the electromagnetic field is confined in the structure composed of several types of materials with distinct refractive indices. The waveguide is a typical design for guiding the light, which usually has a nontrivial profile of the dielectric constant  $\chi^{(1)}(x, y)$  in the  $x$ - $y$  plane but uniform behavior

along the  $z$  axis. As the electromagnetic wave is guided through, additional boundary conditions make the electric and magnetic fields no longer both perpendicular to the direction of propagation.

To solve the Maxwell equations, we intentionally choose either the electric or magnetic field to be perpendicular to the direction of propagation, separating spatial modes into either transverse electric or transverse magnetic modes, respectively. As a result, an effective wave vector  $\beta$  and a field distribution can be found to satisfy the boundary conditions accordingly. The complete solution typically shows a profile where a fixed transverse vector field is propagating along the  $z$  axis with a periodicity of  $1/\beta$ .

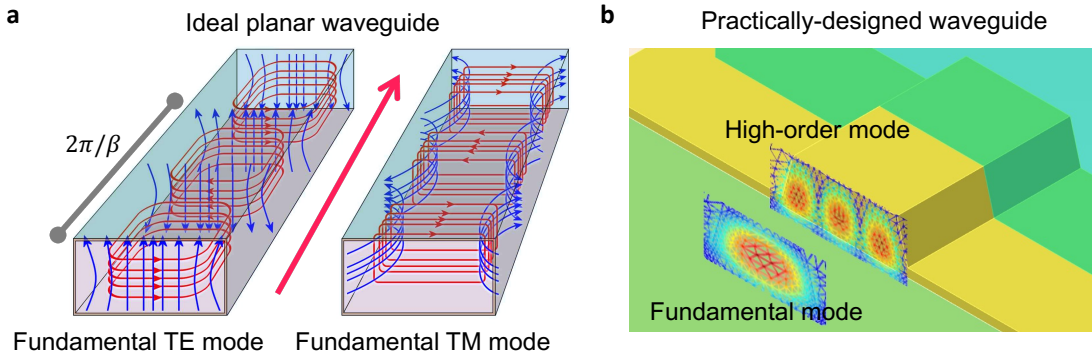


Figure 2.1: **Transverse modes in waveguides.** **a.** Electromagnetic field distribution in slab waveguide. **b.** The simulation of a practical LiNbO<sub>3</sub> waveguide by Lumerical, Ansys Optics.

Depending on the geometry, the refractive indices, and the frequency of the light field, a waveguide may hold none or multiple orders of transverse modes. We use  $m \geq 0$  to indicate the effective wave vector for the  $m$ th mode. For example, we designate the transverse magnetic zeroth mode as the TM<sub>0</sub> mode or the fundamental TM mode without ambiguity.

$$\text{TE}_m : \mathbf{E}_m(\mathbf{r}, t; \omega) = \mathbf{E}_m(x, y; \omega)e^{-i(\omega t - \beta_m z)} + \mathbf{E}_m^*(x, y; \omega)e^{i(\omega t - \beta_m z)}, \quad E_{m,z} = 0 \quad (2.10)$$

$$\text{TM}_m : \mathbf{B}_m(\mathbf{r}, t; \omega) = \mathbf{B}_m(x, y; \omega)e^{-i(\omega t - \beta_m z)} + \mathbf{B}_m^*(x, y; \omega)e^{i(\omega t - \beta_m z)}, \quad B_{m,z} = 0 \quad (2.11)$$

Based on the decomposition in solving the Maxwell equations, The orthogonality

holds between any two different orders of the same type of transverse field [13].

$$\int dx dy \mathbf{E}_m^*(x, y; \omega) \mathbf{E}_n(x, y; \omega) \propto \delta_{mn} \quad (2.12)$$

$$\int dx dy \mathbf{B}_m^*(x, y; \omega) \mathbf{B}_n(x, y; \omega) \propto \delta_{mn} \quad (2.13)$$

Therefore, the guided light field profile can now be described by a linear combination in the mode basis.

$$\text{TE field : } \mathbf{E}_{\text{tot}}(\mathbf{r}, t) = \sum_m \zeta_m \mathbf{E}_m(\mathbf{r}, t; \omega) \quad (2.14)$$

$$\text{TM field : } \mathbf{B}_{\text{tot}}(\mathbf{r}, t) = \sum_m \zeta_m \mathbf{B}_m(\mathbf{r}, t; \omega) \quad (2.15)$$

Then, the determined transverse mode can be easily chosen as a basic dynamical variable for mechanics guided by the Lagrangian and the Hamiltonian, which is compatible to the field quantization as introduced below.

For the TE<sub>m</sub> mode, we can define the vector potential  $\mathbf{A}_m = \{A_{m,0}, \mathbf{A}_m\}$  by,

$$\mathbf{E}_m = -\nabla A_{m,0} - \frac{\partial \mathbf{A}_m}{\partial t}, \quad \mathbf{B}_m = \nabla \times \mathbf{A}_m. \quad (2.16)$$

Thus, by inserting  $A_{m,0} = 0$ , a transverse vector potential field can be derived,

$$\mathbf{A}_m(\mathbf{r}, t; \omega) = \frac{1}{i\omega} [\mathbf{E}_m(x, y; \omega) e^{-i(\omega t - \beta_m z)} - \mathbf{E}_m^*(x, y; \omega) e^{i(\omega t - \beta_m z)}], \quad (2.17)$$

which obeys the Coulomb gauge  $\nabla \cdot \mathbf{A}_m = 0$ . The Lagrangian density with the same unit as energy density becomes

$$\mathcal{L}_{\text{TE}_m}(\mathbf{A}_m, \dot{\mathbf{A}}_m; \omega) = \frac{1}{2} \left[ \varepsilon_0 (1 + \chi^{(1)}) |\dot{\mathbf{A}}_m|^2 - \frac{|\nabla \times \mathbf{A}_m|^2}{\mu_0} \right] \quad (2.18)$$

$$= \frac{1}{2} \left[ \varepsilon_0 (1 + \chi^{(1)}(x, y)) |\mathbf{E}_m(x, y; \omega)|^2 - \frac{|\mathbf{B}_m(x, y; \omega)|^2}{\mu_0} \right]. \quad (2.19)$$

For the TM<sub>m</sub> mode, we can use the technique of the dual potential  $\mathbf{\Lambda}_m = \{\Lambda_{m,0}, \mathbf{\Lambda}_m\}$  defined by,

$$\mathbf{B}_m = \mu_0 \left( \nabla \Lambda_{m,0} + \frac{\partial \mathbf{\Lambda}_m}{\partial t} \right), \quad \mathbf{D}_m = \nabla \times \mathbf{\Lambda}_m. \quad (2.20)$$

Similarly, by setting  $\Lambda_{m,0} = 0$ , a transverse dual potential field can be derived,

$$\mathbf{\Lambda}_m(\mathbf{r}, t; \omega) = \frac{i}{\mu_0 \omega} [\mathbf{B}_m(x, y; \omega) e^{-i(\omega t - \beta_m z)} - \mathbf{B}_m^*(x, y; \omega) e^{i(\omega t - \beta_m z)}]. \quad (2.21)$$

The Lagrangian density becomes

$$\mathcal{L}_{\text{TM}_m}(\mathbf{\Lambda}_m, \dot{\mathbf{\Lambda}}_m; \omega) = \frac{1}{2} \left[ \mu_0 |\dot{\mathbf{\Lambda}}_m|^2 - \frac{|\nabla \times \mathbf{\Lambda}_m|^2}{\varepsilon_0(1 + \chi^{(1)})} \right] \quad (2.22)$$

$$= \frac{1}{2} \left[ \frac{|\mathbf{B}_m(x, y; \omega)|^2}{\mu_0} - \frac{|\mathbf{D}_m(x, y; \omega)|^2}{\varepsilon_0(1 + \chi^{(1)}(x, y))} \right], \quad (2.23)$$

which is essentially the negative version of the Lagrangian density for the vector potential. Therefore, the two sets of transverse modes are mathematically equal in the following derivations.

In this framework, we will no longer distinguish the choice of the dynamical variables since they are dual representations. Then, the normalized primary field profile,  $\mathbf{E}_m(\mathbf{r}; \omega)$  or  $\mathbf{B}_m(\mathbf{r}; \omega)$  for either transverse mode profile can be replaced by  $\mathbf{u}_m(\mathbf{r}; \omega) = \mathbf{u}_{\perp m}(x, y; \omega) e^{i\beta_m(\omega)z}$  with spatial-mode orthogonality  $\int d\mathbf{r}^3 \mathbf{u}_m^* \mathbf{u}_n = V_m \delta_{mn}$ , where  $V_m$  stands for the mode volume of the  $m$ th mode. The unit and mode index associated with the fields will be omitted if there is no ambiguity. For any normalized monochromatic single-transverse-mode field, the potential  $\mathbf{U}$  and the primary field functional variable  $\mathbf{\Gamma}$  are

$$\mathbf{U}(\mathbf{r}, t; \omega) \propto \sqrt{\frac{1}{\omega^2 V}} [\mathbf{u}(\mathbf{r}; \omega) e^{-i\omega t} - \mathbf{u}^*(\mathbf{r}; \omega) e^{i\omega t}] \quad (2.24)$$

$$\mathbf{\Gamma}(\mathbf{r}, t; \omega) \propto \sqrt{\frac{1}{V}} [\mathbf{u}(\mathbf{r}; \omega) e^{-i\omega t} + \mathbf{u}^*(\mathbf{r}; \omega) e^{i\omega t}] \quad (2.25)$$

The other field  $\mathbf{X}$  is

$$\mathbf{X}(\mathbf{r}, t; \omega) \propto \sqrt{\frac{1}{V}} [\nabla \times \mathbf{u}(\mathbf{r}; \omega) e^{-i\omega t} + \nabla \times \mathbf{u}^*(\mathbf{r}; \omega) e^{i\omega t}] \quad (2.26)$$

The Lagrangian density with suitable coefficient for units reads

$$\mathcal{L}(\mathbf{U}, \dot{\mathbf{U}}; \omega) = \frac{1}{2} (\sigma |\dot{\mathbf{U}}|^2 - \nu |\nabla \times \mathbf{U}|^2) = \frac{1}{2} (\sigma |\mathbf{\Gamma}(\mathbf{r}; \omega)|^2 - \nu |\mathbf{X}(\mathbf{r}; \omega)|^2) \quad (2.27)$$

By definition, the canonical momentum field is

$$\Pi_0 = \frac{\partial \mathcal{L}}{\partial(\partial_t U_0)} = 0, \quad \Pi_i = \frac{\partial \mathcal{L}}{\partial(\partial_t U_i)} = \sigma \dot{U}_i. \quad (2.28)$$

After Legendre transformation, the Hamiltonian density reads

$$\mathcal{H}(\mathbf{U}, \mathbf{\Pi}; \omega) = \frac{1}{2} (\sigma |\mathbf{\Gamma}(\mathbf{r}; \omega)|^2 + \nu |\mathbf{X}(\mathbf{r}; \omega)|^2) \quad (2.29)$$

Thus, for a monochromatic single-mode propagating field in dielectric materials, the same time-invariant Hamiltonian density is obtained no matter which transverse mode is chosen to be the primary variable.

$$\tilde{\mathcal{H}}(\mathbf{r}; \omega) = \frac{1}{2} \left[ \varepsilon(\mathbf{r}) |\mathbf{E}(\mathbf{r}; \omega)|^2 + \frac{|\mathbf{B}(\mathbf{r}; \omega)|^2}{\mu_0} \right], \varepsilon = \varepsilon_0 (1 + \chi^{(1)}) \quad (2.30)$$

Based on orthogonality, the total Hamiltonian would be a sum of the Hamiltonian of each mode. So far, we have figured out the characteristics of transverse modes at a specific frequency. For other frequencies, the derivation is the same, but the transverse mode profiles and effective wave vectors will change depending on the material and geometrical dispersion.

### 2.1.2 Spectral Mode

After obtaining the monochromatic transverse modes of the system, the last step in representing an arbitrary light field is the link to a complete set of spectral basis functions. The spectral mode determines the propagation characteristics of the light field. Each frequency components can be a spectral basis function of the system and the linear combination of them can form a spectral mode.

When space is finite with the periodic boundary condition, monochromatic fields at some frequencies can no longer be kept in the system. Even though they can be generated, they will destructively interfere with each other and fade away in time. Particularly, when the finite system has a span  $L$  along the  $z$  axis, only the monochromatic fields with effective wave vector obeying an integer  $j = L\beta_{m,j}/2\pi$  can survive. The remaining spectral modes for each transverse mode now become a set of discrete-frequency basis functions  $a_{m,j}(t) = \frac{1}{\sqrt{2\pi}} e^{-i\omega_{m,j}t}$ . They have wave-vector gap  $\delta\beta = 2\pi/L$  and frequency gap  $\delta\omega = 2\pi c/L$  in between. Furthermore, they naturally hold the round-trip orthogonality  $\int_0^T dt a_{m,j}^* a_{n,k} = \delta_{mn} \delta_{jk}$ . Therefore,

any normalized total field profile in a finite system can be expressed in this basis by a set of normalized spectrum mode coefficients  $\sum_{m,j} |\zeta_{m,j}|^2 = 1$ .

$$\mathbf{u}_{\text{tot}}(\mathbf{r}, t) = \sum_{m,j} \zeta_{m,j} \mathbf{u}_{m,j}(\mathbf{r}) a_{m,j}(t) + \zeta_j^* \mathbf{u}_{m,j}^*(\mathbf{r}) a_{m,j}^*(t) \quad (2.31)$$

If the linear system is infinite in  $z$  direction, the spectrum can be continuous by  $L \rightarrow +\infty$ ,  $\delta\beta \rightarrow 0$ , and  $\delta\omega \rightarrow 0$ . Hence, each transverse mode is bonded to a set of continuous monochromatic basis  $a_{m,j}(t) \rightarrow a_m(t; \omega) = \frac{1}{\sqrt{2\pi}} e^{-i\omega t}$ . These spectral basis also have orthogonality  $\int dt a_m^*(t; \omega') a_m(t; \omega) = \delta(\omega' - \omega)$ . Therefore, any normalized total field profile can be described by the spectrum density  $\zeta_m(\omega)$  with normalization  $\sum_m \int d\omega |\zeta_m(\omega)|^2 = 1$ .

$$\mathbf{u}_{\text{tot}}(\mathbf{r}, t) = \sum_m \int d\omega \zeta_m(\omega) \mathbf{u}_m(\mathbf{r}; \omega) a_m(t; \omega) + \zeta_m^*(\omega) \mathbf{u}_m^*(\mathbf{r}; \omega) a_m^*(t; \omega) \quad (2.32)$$

The decomposition now gives a full description of the linear electromagnetic system.

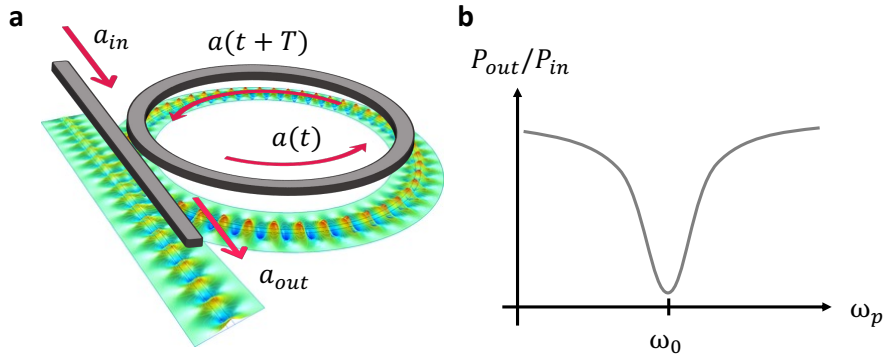


Figure 2.2: **Micro-ring resonator.** **a.** Sketch of a typical micro-ring resonator with an intra-cavity mode and an input-output field. **b.** The transmitted power response lineshape to the detuned input monochromatic pump field.

### 2.1.3 Resonator

The optical resonator, also known as the photonic cavity, is an artificial structure that has the periodic boundary condition since it has a closed loop to trap light. There are many geometries for resonators. In this thesis, we focus on the micro-ring



resonator, which is the most common structure compatible with the demands of integrated photonics.

By bending waveguides into a ring, a micro-ring resonator is constructed. For the light field traveling in circles, both the transverse and spectral modes (azimuthal modes from the top view) are defined accordingly by solving the bending waveguide problem. Therefore, the intra-cavity field is a linear combination of orthogonal modes. Without loss of generality, we pick one discrete mode  $a(t)$  and focus its intra-cavity dynamics around the resonating frequency  $\omega_0$ .

If the resonator is lossless, the energy within this discrete mode will last forever. Otherwise, the field will decay in time without an energy supply. Hence, these discrete modes are no longer spectral eigenstates of this open system, and a continuous-spectral description is needed. Similar to in the infinite space case, we use  $a(t; \omega)$  to describe the slowly-varying field with frequency at  $\omega$ . Moreover, we may have an external source  $a_{\text{in}}(t; \omega)$  to replenish the intra-cavity field  $a(t; \omega)$  at the same frequency. The coupling between the input field and the intra-cavity field can be modeled as a beamsplitter with a power transmittance rate  $\eta$ .

At the beginning of each round-trip, the intra-cavity field is  $a(t)$ . The amplitude after round-trip time  $T$  is labeled as  $a_f(t+T) = a(t)e^{-i\omega T - \gamma_i T/2}$  with intrinsic power loss rate  $\gamma_i$ . At the input and output ports of the beamsplitter, the state evolution must obey

$$a(t+T) = \sqrt{1-\eta}a_f(t+T) + \sqrt{\eta}a_{\text{in}}(t+T) \quad (2.33)$$

$$a_{\text{out}}(t) = \sqrt{1-\eta}a_{\text{in}}(t) - \sqrt{\eta}a_f(t) \quad (2.34)$$

For a high-quality cavity, the coupling rate  $\eta$ , round-trip loss  $\gamma_i T$ , and the round-trip phase shift  $(\omega - \omega_0)T$  are much smaller than 1. We will check to see if this assumption is self-consistent later. After switching to the rotation frame at  $\omega_p$ , the above evolution equations are reduced to the first order relationship.

$$a(t+T) - a(t) = i(\omega - \omega_0)T a(t) - \frac{\gamma_i T + \eta}{2} a(t) + \sqrt{\eta} a_{\text{in}} \quad (2.35)$$

The intra-cavity total energy is  $\mathcal{E}_{\text{cav}} = V_{\text{eff}}|a(t)|^2 \propto cT|a(t)|^2$  and the pump power is  $P_{\text{in}} = V_{\text{eff}}|a_{\text{in}}|^2/T \propto c|a_{\text{in}}|^2$ . Then, we can define a normalized intra-cavity

amplitude  $\tilde{a}(t) = \sqrt{T}a(t)$  and the coupling loss rate  $\eta/T = \gamma_c$ . Then, the dynamics of normalized intra-cavity amplitude now reads as

$$\frac{\tilde{a}(t+T) - \tilde{a}(t)}{T} = i(\omega - \omega_0)\tilde{a}(t) - \frac{\gamma_i + \gamma_c}{2}\tilde{a}(t) + \sqrt{\gamma_c}a_{\text{in}} \quad (2.36)$$

For cases only involving slowly-varying fields, the round-trip time is negligible, thus

$$\dot{\tilde{a}} = i\Delta\tilde{a} - \frac{\gamma}{2}\tilde{a} + \sqrt{\gamma_c}a_{\text{in}} \quad (2.37)$$

$$a_{\text{out}} = a_{\text{in}} - \sqrt{\gamma_c}\tilde{a} \quad (2.38)$$

where  $\Delta = \omega - \omega_0$  is the detuning relative to resonance and  $\gamma = \gamma_i + \gamma_c$  stands for the total loss rate. The equation of motion for the intra-cavity dynamics and the boundary condition for input-output relation will be the starting point for almost all cavity-based applications.

After solving the steady-state solution at  $d\tilde{a}/dt = 0$ , the spectral response to a continuous-wave pump has a Lorentzian lineshape.

$$\tilde{a}(\Delta) = \frac{\sqrt{\gamma_c}a_{\text{in}}}{-i\Delta + \frac{\gamma}{2}}, \quad \mathcal{E}_{\text{cav}}(\Delta) = \frac{\gamma_c P_{\text{in}}}{\Delta^2 + \frac{\gamma^2}{4}} \quad (2.39)$$

$$a_{\text{out}}(\Delta) = \left[ 1 - \frac{\gamma_c}{-i\Delta + \frac{\gamma}{2}} \right] a_{\text{in}}, \quad \frac{P_{\text{out}}(\Delta)}{P_{\text{in}}} = \frac{4\Delta^2 + (\gamma_i - \gamma_c)^2}{4\Delta^2 + \gamma^2} \quad (2.40)$$

#### 2.1.4 Field Quantization and the Concept of Photon

The electromagnetic modes provide all the classical knowledge of electrodynamics, which is sufficient for describing many nonlinear photonic processes. However, classic electro-dynamics are sometimes insufficient in situations where the light field shows a particle-like behavior, especially when being detected. In this case, the quantum description of light and its interaction with matter is necessary, which expresses the particle-wave duality of the light.

Photons, the particle manifestation of light, are massless basic particles carrying definite energy  $\hbar\omega$ , momentum  $\hbar\lambda$ , and spin 1 at the speed of light. The origin of photon concept is the subject of a long-lasting historical debate, but it provides

a clear picture for describing interactions with other systems, such as electrons in atoms and solid states.

Technically, the second quantization of electromagnetic fields within a finite space can lead to a somewhat restricted formalism of a photon<sup>1</sup>. To date, the conventional quantum description of a monochromatic single-mode photon can be directly modified from the orthogonal basis we obtained before. The bridge to the quantum world begins at the Poisson bracket over canonical field variables  $q_i(\mathbf{r})$  and their generalized momenta  $p_j(\mathbf{r})$  in classic field theory.

$$\{q_i(\mathbf{r}), p_j(\mathbf{r}')\} = \delta_{ij}\delta(\mathbf{r} - \mathbf{r}'), \quad \int dV \{q_i(\mathbf{r}), p_j(\mathbf{r}')\} = \delta_{ij} \quad (2.41)$$

The second orthogonality after integration over the space holds when  $q_i$  and  $p_j$  are associated with orthogonal mode profiles.

To go across the bridge and enter the quantum world, we impose the equal-time canonical commutation relations between the primary field variables and generalized momenta in Eq.(2.29). The mode-dependent equal-time canonical commutation relations are

$$\int dV \varepsilon [\hat{\mathbf{A}}_{m,j}(\mathbf{r}, t), \dot{\hat{\mathbf{A}}}_{n,k}(\mathbf{r}', t)] = \mu_0 [\dot{\hat{\mathbf{A}}}_{m,j}(\mathbf{r}, t), \hat{\mathbf{A}}_{n,k}(\mathbf{r}', t)] = i\hbar\delta_{mn}\delta_{jk} \quad (2.42)$$

Then, we can introduce pairs of operators  $\hat{a}_{m,j}$  and  $\hat{a}_{n,k}^\dagger$ , following the commutation relation  $[\hat{a}_{m,j}, \hat{a}_{n,k}^\dagger] = \delta_{mn}\delta_{jk}$  to establish the formalism. In the following discussion, we concentrate on the single-mode field with the mode order subscripts  $m, j$  omitted. After applying adjustment to units and convention to signs, the monochromatic single-mode potential field operators can have the following forms to maintain the above equal-time commutation relations.

$$\hat{\mathbf{A}}(\mathbf{r}, t; \omega) = \sqrt{\frac{\hbar}{2\varepsilon V\omega}} [\mathbf{u}(\mathbf{r}; \omega)\hat{a}e^{-i\omega t} + \mathbf{u}^*(\mathbf{r}; \omega)\hat{a}^\dagger e^{i\omega t}], \quad (2.43)$$

$$\text{or } \hat{\mathbf{A}}(\mathbf{r}, t; \omega) = i\sqrt{\frac{\hbar}{2\mu_0 V\omega}} [\mathbf{u}'(\mathbf{r}; \omega)\hat{a}e^{-i\omega t} - \mathbf{u}'^*(\mathbf{r}; \omega)\hat{a}^\dagger e^{i\omega t}]. \quad (2.44)$$

---

<sup>1</sup>Please refer to textbook [8] for a formally restricted quantization of the light field.

Now, we can substitute the classic fields  $\mathbf{E}$  and  $\mathbf{B}$  by observable operators  $\hat{\mathbf{E}}$  and  $\hat{\mathbf{B}}$ . The TE mode has the primary field of vector potential  $\hat{\mathbf{A}}$  so that the fields are

$$\hat{\mathbf{E}}(\mathbf{r}, t) = i\sqrt{\frac{\hbar\omega}{2\varepsilon V}} [\mathbf{u}(\mathbf{r}; \omega)\hat{a}e^{-i\omega t} - \mathbf{u}^*(\mathbf{r}; \omega)\hat{a}^\dagger e^{i\omega t}] \quad (2.45)$$

$$\hat{\mathbf{B}}(\mathbf{r}, t) = \sqrt{\frac{\hbar}{2\varepsilon V\omega}} [\nabla \times \mathbf{u}(\mathbf{r}; \omega)\hat{a}e^{-i\omega t} + \nabla \times \mathbf{u}^*(\mathbf{r}; \omega)\hat{a}^\dagger e^{i\omega t}]. \quad (2.46)$$

The TM mode with the primary field of dual potential  $\hat{\mathbf{A}}$  are

$$\hat{\mathbf{B}}(\mathbf{r}, t) = \sqrt{\frac{\hbar\omega\mu_0}{2V}} [\mathbf{u}'(\mathbf{r}, \omega)\hat{a}e^{-i\omega t} + \mathbf{u}'^*(\mathbf{r}, \omega)\hat{a}^\dagger e^{i\omega t}] \quad (2.47)$$

$$\hat{\mathbf{D}}(\mathbf{r}, t) = i\sqrt{\frac{\hbar}{2\mu_0 V\omega}} [\nabla \times \mathbf{u}'(\mathbf{r}; \omega)\hat{a}e^{-i\omega t} - \nabla \times \mathbf{u}'^*(\mathbf{r}; \omega)\hat{a}^\dagger e^{i\omega t}]. \quad (2.48)$$

Since the nonlinear effects are mostly described by  $\hat{\mathbf{E}}$  and  $\hat{\mathbf{D}}$ , we need to transform the TM mode profile for better illustration of nonlinearities later. By the identities of  $\mathbf{u}' \cdot (\nabla \times \mathbf{u}') = 0$  and  $\nabla \times \hat{\mathbf{D}} = -\frac{\partial}{\partial t}\hat{\mathbf{B}}$ , we can re-define a normalized spatial mode profile and phase by  $\nabla \times \mathbf{u}' \rightarrow |\mathbf{k}|\mathbf{u}$  in Eq.(2.48) and  $\mathbf{u}' \rightarrow \frac{1}{|\mathbf{k}|}\nabla \times \mathbf{u}$  in Eq.(2.47) for the TM mode. Therefore, the definitions of quantized field operators are identical for both types of transverse modes. Later on, we will use two unit-free quadratures  $\hat{Q}$  and  $\hat{P}$  to describe two observables of the light field.

$$\hat{Q} = \frac{1}{\sqrt{2}}(\hat{a} + \hat{a}^\dagger), \quad \hat{P} = \frac{i}{\sqrt{2}}(\hat{a}^\dagger - \hat{a}) \quad (2.49)$$

Furthermore, the Hamiltonian operator  $\hat{\mathcal{H}}$  and photon number operator  $\hat{N}$  of the enclosed quantized single-mode field is defined in

$$\hat{\mathcal{H}} = \int dV \hat{\mathcal{H}} = \frac{1}{2}\hbar\omega(\hat{a}^\dagger\hat{a} + \hat{a}\hat{a}^\dagger) = \hbar\omega(\hat{a}^\dagger\hat{a} + \frac{1}{2}) = \hbar\omega(\hat{N} + \frac{1}{2}), \quad (2.50)$$

where the fast oscillation terms are negligible after spatial integration. The zero-point energy is usually ignored, and the Hamiltonian becomes  $\hbar\omega\hat{a}^\dagger\hat{a}$ .

This quantized Hamiltonian follows a similar formalism as the quantum harmonic oscillator, where  $\hat{a}$  and  $\hat{a}^\dagger$  are annihilation and creation ladder operators. Indeed, photon fields can intuitively be interpreted as operators for consuming or generating a photon at the target mode. Specifically, if we apply  $\hat{a}^\dagger$  to the vacuum

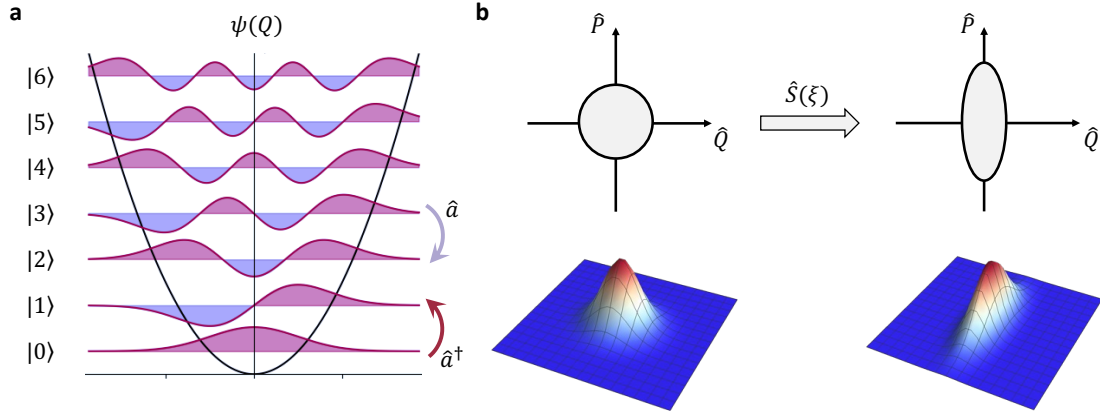


Figure 2.3: **Quantum harmonic oscillator and squeezed field.** **a.** The energy diagram and wave functions of quantum harmonic oscillator expanded in  $Q$  basis. **b.** illustration of a single-mode squeezed field in a phase diagram.

state, the state will become a single-photon state. Due to the quantum nature of a monochromatic field, there is no meaning of where or when this photon should be. To indicate more photons at the same mode, we have Fock states  $|n\rangle$ ,  $n \geq 0$  to represent a field containing  $n$  identical photons.

$$\hat{N}|n\rangle = n|n\rangle, \hat{a}|n\rangle = \sqrt{n}|n-1\rangle, \hat{a}^\dagger|n\rangle = \sqrt{n+1}|n+1\rangle \quad (2.51)$$

The evolution of operators is guided by the Heisenberg equation.

$$i\hbar \frac{d}{dt} \hat{O} = [\hat{O}, \hat{\mathcal{H}}] \quad (2.52)$$

Equivalently, the operator, after the evolution of time  $T$ , can be written in a direct unitary transformation from the initial operator.

$$\hat{O}(T) = \hat{U}^\dagger(T) \hat{O}(0) \hat{U}(T), \quad \hat{U}(T) = \exp\left(\frac{1}{i\hbar} \int_0^T dt \hat{\mathcal{H}}\right) \quad (2.53)$$

Then we have  $\hat{a}(t) = e^{-i\omega t} \hat{a}(0)$  which is self-consistent with the definition. Furthermore, based on ladder operators and similar concepts from quantum harmonic oscillators, we can construct a coherent state of light which is the eigenstate of the operator  $\hat{a}$ .

$$\hat{a}|\alpha\rangle = \alpha|\alpha\rangle, \quad |\alpha\rangle = e^{-\frac{|\alpha|^2}{2}} \sum_{n=0}^{\infty} \frac{\alpha^n}{\sqrt{n!}} |n\rangle = e^{-\frac{|\alpha|^2}{2}} \sum_{n=0}^{\infty} \frac{\alpha^n}{n!} (\hat{a}^\dagger)^n |0\rangle \quad (2.54)$$

The effective energy of a coherent state is  $\hbar\omega|\alpha|^2$ .

Beyond that, we can construct a single-mode squeezed state of light by the squeezing operator with a complex parameter  $\xi = re^{i\phi}$  describing the intensity of the squeezing operation.

$$\hat{S}(\xi) = \exp \left[ \xi \frac{(\hat{a}^\dagger)^2}{2} - \xi^* \frac{\hat{a}^2}{2} \right], \quad (2.55)$$

When we apply this to the vacuum field, a single-mode squeezed vacuum will be generated.

$$|\xi\rangle = \hat{S}(\xi)|0\rangle = \frac{1}{\sqrt{\cosh r}} \sum_{n=0}^{\infty} \frac{[(2n)!]^{\frac{1}{2}}}{2^n n!} [e^{i\phi} \tanh r]^n |2n\rangle \quad (2.56)$$

This mode is an eigenstate of another operator  $\hat{b}|\xi\rangle = 0$ . The squeezing operator leads to the Bogoliubov transformation between  $\hat{b}$  and  $\hat{a}$ .

$$\hat{b} = \hat{S}(\xi)\hat{a}\hat{S}^\dagger(\xi) = \cosh r \hat{a} - \sinh r e^{i\phi} \hat{a}^\dagger \quad (2.57)$$

The coherent and squeezed state of light both feature the minimum uncertainty of conjugate observables.

$$(\Delta\hat{Q})^2(\Delta\hat{P})^2 = \frac{1}{4} \quad (2.58)$$

The coherent state has an equal variance for any quadrature direction,  $(\Delta\hat{Q})^2 = (\Delta\hat{P})^2 = \frac{1}{2}$ . Nevertheless, the squeezed state enjoys less variance in one quadrature but a larger variance in another. For example, if the quadrature  $\hat{Q}$  is getting squeezed to  $r$ ,

$$(\Delta\hat{Q})^2 = \frac{e^{-2r}}{2}, \quad (\Delta\hat{P})^2 = \frac{e^{2r}}{2}. \quad (2.59)$$

Now, considering the mode decomposition in previous subsections, any multi-mode state can be written as a linear combination of a series of single-mode states. For example, in a finite space decomposed by transverse modes  $\{\mathbf{u}_{m,j}\}$  and spectral modes  $\{\omega_{m,j}\}$ , we can expand the generated single-photon state with amplitudes  $\sum_{m,j} |\zeta_{m,j}|^2 = 1$  to a superposition state  $|\tilde{a}_{\text{ph}}\rangle = \sum_{m,j} \zeta_{m,j} a_{m,j}^\dagger |0, 0, \dots, 0\rangle$ . This

single-photon state has the normalization  $|\langle \tilde{a}_{\text{ph}} | \tilde{a}_{\text{ph}} \rangle|^2 = 1$ . For a multi-mode system, one of the total field operators reads

$$\hat{\mathbf{E}}_{\text{tot}} = \sum_{m,j} i \sqrt{\frac{\hbar \omega_{m,j}}{2\epsilon V_{m,j}}} \left[ \mathbf{u}_{m,j} \hat{a}_{m,j} e^{-i\omega_{m,j}t} - \mathbf{u}_{m,j}^* \hat{a}_{m,j}^\dagger e^{i\omega_{m,j}t} \right]. \quad (2.60)$$

The Hamiltonian reads

$$\hat{\mathcal{H}} = \sum_{m,j} \hbar \omega_{m,j} \hat{a}_{m,j}^\dagger \hat{a}_{m,j}. \quad (2.61)$$

This indicates that a single photon will have total energy as

$$\hat{\mathcal{E}}_{\text{ph}} = \sum_{m,j} \hbar \omega_{m,j} |\zeta_{m,j}|^2 \hat{a}_{m,j}^\dagger \hat{a}_{m,j}. \quad (2.62)$$

Multi-mode coherent light can be defined as either a superposition of spectral modes,

$$|\tilde{\alpha}\rangle = e^{-\frac{|\alpha|^2}{2}} \sum_{n=0}^{\infty} \frac{\alpha^n}{n!} \left( \sum_{m,j} \zeta_{m,j}^* \hat{a}_{m,j}^\dagger e^{i\omega_{m,j}t} \right)^n |0, 0, \dots, 0\rangle, \quad (2.63)$$

or as a product state of multiple coherent single-mode fields,

$$|\tilde{\alpha}\rangle = \otimes_{m,j} |\alpha_{m,j}\rangle = |\alpha_{0,1}, \alpha_{0,2}, \dots, \alpha_{m,j}, \dots\rangle, \quad (2.64)$$

If we focus only on two modes, there is a two-mode squeezed vacuum generated by the transform

$$|\xi\rangle_{12} = \hat{S}_{12}(\xi)|0, 0\rangle, \quad \hat{S}_{12}(\xi) = \exp \left[ \xi \hat{a}_1^\dagger \hat{a}_2^\dagger - \xi^* \hat{a}_1 \hat{a}_2 \right]. \quad (2.65)$$

In the Fock basis, the two-mode squeezed vacuum reads

$$|\xi\rangle_{12} = \frac{1}{\sqrt{\cosh r}} \sum_{n_1, n_2=0}^{\infty} [e^{i\phi} \tanh r]^n |n_1, n_2\rangle. \quad (2.66)$$

The covariance between the two modes will show quantum correlation or anti-correlation. We will not go any deeper into the squeezed state here.

Energy exchange can occur between two modes  $\hat{a}$  and  $\hat{b}$ . Depending on the mechanics, the two modes could be different modes in one space or modes from two

interacting spaces. The energy exchange obeys an arbitrary unitary transformation. In the interaction picture, this transformation has the form as  $\hat{U}_{\text{BS}}(t; \gamma) = \exp \left[ i\gamma t \left( \hat{a}^\dagger \hat{b} + \hat{b}^\dagger \hat{a} \right) \right]$ . This is commonly called a coupler or a beamsplitter, which is a basic component in quantum photonics.

$$\hat{U}_{\text{BS}}^\dagger \hat{a} \hat{U}_{\text{BS}} = \cos(\gamma t) \hat{a} + i \sin(\gamma t) \hat{b} \quad (2.67)$$

$$\hat{U}_{\text{BS}}^\dagger \hat{b} \hat{U}_{\text{BS}} = \cos(\gamma t) \hat{b} + i \sin(\gamma t) \hat{a} \quad (2.68)$$

The energy oscillates between the two modes in time.

### 2.1.5 Quantized Field in an Infinite Space

The photon field in a finite space is successfully quantized via discrete operators. When the volume approaches infinite, the spectral basis become continuous. This means that the discrete operators  $\hat{a}_{m,j}$  must be generalized to incorporate the continuous spectrum and hold the equal-time commutation relation under limitations [14, 15]  $L \rightarrow +\infty$ ,  $\delta\beta \rightarrow 0$ , and  $\delta\omega \rightarrow 0$ . Infinite space is always an approximation since the light field is confined between the generation and the detection apparatus. Such an approximation reduces the distracting details that the detector would never resolve. It also gives us a way to describe the quantized traveling fields and their interactions through propagation.

We impose the transformation  $\hat{a}_{m,j} \rightarrow \delta\omega^{1/2} \hat{a}_m(\omega)$ , with the spectral commutation relation,  $[\hat{a}_m(\omega), \hat{a}_n^\dagger(\omega')] = \delta_{mn} \delta(\omega - \omega')$ . The Kronecker delta function becomes the Dirac delta function,  $\delta_{jk} \rightarrow \delta\omega \delta(\omega - \omega')$ . Unlike the discrete modes,  $\hat{a}_m(\omega)$  has units of  $1/\sqrt{\text{Hz}}$ . It can be understood as eliminating or generating a continuous piece of the photon in transverse mode  $m$  with an infinitely small range of frequency around  $\omega$ .

Then, the sum over discrete modes is converted by  $\sum_j \rightarrow \int \frac{d\omega}{\delta\omega}$ . A single-photon state represented by a normalized continuous spectral profile,  $\int d\omega |\zeta(\omega)|^2 = 1$ , can be written in

$$|\tilde{a}_{\text{ph}}\rangle = \sum_m \int d\omega \zeta_m(\omega) a_m^\dagger(\omega) |0, 0, \dots, 0\rangle, \quad |\langle \tilde{a}_{\text{ph}} | \tilde{a}_{\text{ph}} \rangle|^2 = 1. \quad (2.69)$$



Similarly, the other states of the light fields can be generalized to the continuous-spectral basis.

For each transverse mode, the Hamiltonian has the form of

$$\hat{\mathcal{H}}_m = \hbar \int d\omega \omega \hat{a}_m^\dagger(\omega) \hat{a}_m(\omega). \quad (2.70)$$

Recalling the frequency gap  $\delta\omega = 2\pi c/L$ , the corresponding total field operator is converted to the limit

$$\hat{\mathbf{E}}_m = \int \frac{d\omega}{\sqrt{2\pi}} i \sqrt{\frac{\hbar\omega}{2\varepsilon_0 c S_m}} [\mathbf{u}_m(\mathbf{r}; \omega) \hat{a}_m(\omega) e^{-i\omega t} - \mathbf{u}_m^*(\mathbf{r}; \omega) \hat{a}_m^\dagger(\omega) e^{i\omega t}], \quad (2.71)$$

with  $S_m = \frac{\beta_m}{2\pi} \int_0^{2\pi/\beta_m} dz \int dx dy |\mathbf{u}_m|^2$ .

In practice, the frequency dependence of the transverse modes is usually negligible due to a small bandwidth or a weak dispersion. Hence, we can neglect the transverse modes behavior initially. If we are not interested in the details within a few cycles of wavelength, the propagation terms can also be isolated from spatial mode by re-normalizing the transverse mode to an averaged value along the propagation direction,  $S_m = \int dx dy |\mathbf{u}_{\perp m}|^2$  and  $\mathbf{u}_m = \mathbf{u}_{\perp m} e^{i\beta_m z}$ .

By doing so, the free-propagating field operator can also be described on temporal basis. The creation or annihilation of a monochromatic photon at a specific time  $t$  within a given transverse mode is defined by Fourier transforming the spectral operators

$$\hat{a}_m(t) = \frac{1}{\sqrt{2\pi}} \int d\omega \hat{a}_m(\omega) e^{-i\omega t}. \quad (2.72)$$

The commutation relation on temporal basis has the form as

$$[\hat{a}_m(t), \hat{a}_n^\dagger(t')] = \frac{1}{2\pi} \int d\omega' d\omega \delta_{mn} \delta(\omega - \omega') e^{-i\omega(t-t')} = \delta_{mn} \delta(t - t') \quad (2.73)$$

The last equation is held by identity  $\int d\omega e^{-i\omega(t-t')} = 2\pi \delta(t - t')$ .

For each single-spatial-mode field, the field operator in continuous-temporal basis becomes

$$\hat{\mathbf{E}}_m(t) = i \sqrt{\frac{\hbar\omega}{2\varepsilon_0 c S_m}} [\mathbf{u}_{\perp m} \hat{a}_m(t) e^{i\beta_m z} - \mathbf{u}_{\perp m}^* \hat{a}_m^\dagger(t) e^{-i\beta_m z}]. \quad (2.74)$$

The instant total power operator going through the entire  $x-y$  plane can be written approximately as

$$\hat{P}_m(t) = \int dx dy \varepsilon_0 c |\hat{\mathbf{E}}_m(t)|^2 = \hbar \omega \hat{a}_m^\dagger(t) \hat{a}_m(t). \quad (2.75)$$

Recalling the Hamiltonian definition in Eq.(2.70) around  $\omega_0$ , we can check  $\hat{\mathcal{H}}_m = \int dt \hat{P}_m(t)$ . This means that the slowly-varying traveling fields, which are usually valid approximations in most experiments, can be effectively modeled by continuous-temporal mode and corresponding power operators. Hence, the other states of light can also be defined on temporal basis. For example, a free-propagating single-mode coherent state  $|\alpha(t)\rangle$  at carrier frequency  $\omega_0$  with slowly-varying amplitude will have time-dependent average power  $\langle P(t) \rangle = \hbar \omega_0 |\alpha(t)|^2$ .

With a similar treatment of approaching infinity, we can model the beamsplitter for the quantized fields. The unitary transformation between two modes  $\hat{a}(\omega)$  and  $\hat{b}(\omega)$  in infinite space becomes

$$\hat{U}_{\text{BS}}(\theta) = \exp \left\{ i\theta \int d\omega [\hbar a^\dagger(\omega) \hbar b(\omega) + \hbar b^\dagger(\omega) \hbar a(\omega)] \right\}, \quad (2.76)$$

which models a beamsplitter with conversion rate  $\eta = \sin^2(\theta)$ .  $\theta$  is the parameter of the coaxial interaction strength between the two modes.

$$\hat{U}_{\text{BS}}^\dagger(\theta) \hat{a}(\omega) \hat{U}_{\text{BS}}(\theta) = \cos(\theta) \hat{a}(\omega) + i \sin(\theta) \hat{b}(\omega) \quad (2.77)$$

$$\hat{U}_{\text{BS}}^\dagger(\theta) \hat{b}(\omega) \hat{U}_{\text{BS}}(\theta) = \cos(\theta) \hat{b}(\omega) + i \sin(\theta) \hat{a}(\omega) \quad (2.78)$$

When  $\theta$  is small,  $\theta \approx \sin \theta = \sqrt{\eta}$ . We can define a Hamiltonian to describe this process by  $\hat{U}_{\text{BS}} = \exp\{\frac{1}{i\hbar} \int dt \hat{H}_{\text{BS}}\}$ , where

$$\hat{H}_{\text{BS}} = \hbar \sqrt{\eta} \int \frac{d\omega}{\sqrt{2\pi}} \frac{d\omega'}{\sqrt{2\pi}} \left[ \hat{a}^\dagger(\omega) \hat{b}(\omega') e^{i(\omega-\omega')t} + \hat{b}^\dagger(\omega') \hat{a}(\omega) e^{i(\omega'-\omega)t} \right] \quad (2.79)$$

$$= \hbar \sqrt{\eta} \left[ \hat{a}^\dagger(t) \hat{b}(t) + \hat{b}^\dagger(t) \hat{a}(t) \right]. \quad (2.80)$$

By mapping back to the classic electric field, this is identical to the boundary condition of the beamsplitter.

### 2.1.6 Quantized Field in a Resonator

The quantized formalism introduced above is suitable to describe the interactions either among intra-cavity fields or among free-propagating fields. Despite this, we still need a few more steps to draw the dynamics of a leaky resonator where the discrete cavity modes are excited by the input light with a continuous spectrum.

Considering a micro-ring resonator as the standard case, the bus waveguide holds the input and output fields with continuous spectral mode. The resonator holds the discrete spectral modes  $\hat{a}_{m,j}$  at  $\omega_{m,j}$ . The total Hamiltonian is separated into three parts.

$$\hat{\mathcal{H}}_{\text{tot}} = \hat{\mathcal{H}}_{\text{in}} + \hat{\mathcal{H}}_{\text{cav}} + \hat{\mathcal{H}}_c \quad (2.81)$$

First, the free-propagation Hamiltonian of input fields is apparently shown as

$$\hat{\mathcal{H}}_{\text{in}} = \hbar \sum_m \int d\omega \omega \hat{a}_{m,\text{in}}^\dagger(\omega) \hat{a}_{m,\text{in}}(\omega). \quad (2.82)$$

Then, if there is no coupling between intra-cavity and the input fields, the intra-cavity Hamiltonian would stay in the form of  $\hat{\mathcal{H}}_{\text{cav}} = \sum_{m,j} \hbar \omega_{m,j} \hat{a}_{m,j}^\dagger \hat{a}_{m,j}$  since other spectral modes are diminished by destructive interference with themselves. However, within a single round-trip of the cavity, the continuous spectral modes are still alive. The Hamiltonian for intra-cavity fields is also a free-propagation Hamiltonian with continuous spectral modes around the resonance frequency  $\omega_{m,j}$ .

$$\hat{\mathcal{H}}_{\text{cav}} = \hbar \sum_{m,j} \int_{\delta\omega} d\omega \omega \hat{a}_{m,j}(\omega)^\dagger \hat{a}_{m,j}(\omega) \quad (2.83)$$

The coupling between intra-cavity and input fields happens at  $t > 0$  and can be described by a beamsplitter Hamiltonian with a small conversion rate  $\eta$  between each pair of intra-cavity mode and input mode on the same basis.

$$\hat{\mathcal{H}}_c(t) = i\hbar \sum_m \left[ \sqrt{\eta} \hat{a}_{m,j}^\dagger(t) \hat{a}_{m,\text{in}}(t) - \sqrt{\eta} \hat{a}_{m,j}(t) \hat{a}_{m,\text{in}}^\dagger(t) \right] \quad (2.84)$$

We recover a unit-less intra-cavity mode operator at frequency  $\omega_{m,j}$  by

$$\hat{a}_m(t) = \int_{\delta\omega} \frac{d\omega}{\sqrt{2\pi}} \hat{a}_m(\omega) e^{-i\omega t} \rightarrow \sum_j \delta\omega^{1/2} \hat{a}_{m,j}(t) e^{-i\omega_{m,j} t}, \quad (2.85)$$

while the input fields stays as  $\hat{a}_{m,\text{in}}(t) = \int \frac{d\omega}{\sqrt{2\pi}} \hat{a}_{m,\text{in}}(\omega) e^{-i\omega t}$ . Hence the Hamiltonian at  $t = 0$  becomes

$$\hat{\mathcal{H}}_c(0) = i\hbar \sum_{m,j} \int \frac{d\omega}{\sqrt{2\pi}} \left[ \sqrt{\gamma_{m,j}^{(c)}} \hat{a}_{m,j}^\dagger \hat{a}_{m,\text{in}}(\omega) - \sqrt{\gamma_{m,j}^{(c)}} \hat{a}_{m,j} \hat{a}_{m,\text{in}}^\dagger(\omega) \right], \quad (2.86)$$

where coefficients  $\gamma_{m,j}^{(c)} = \frac{\delta\omega}{2\pi} \cdot \eta = \frac{c}{L} \eta$ .

Without loss of generality, we neglect the subscriptions and focus on only a single-mode field  $\hat{a}_{m,j} \rightarrow \hat{a}$  with the input field presented by  $\hat{a}_{\text{in}}$ . In the interaction picture at on-resonance frequency, the input field is labeled in detuning  $\Delta = \omega - \omega_{m,j}$ . The round-trip unitary transformation of the system can be written as

$$\hat{U}_T = \exp\left(\frac{1}{i\hbar} \int_0^T dt \hat{\mathcal{H}}_c\right) = 1 + \left(\frac{1}{i\hbar} \int_0^T dt \hat{\mathcal{H}}_c\right) + \frac{1}{2} \left(\frac{1}{i\hbar} \int_0^T dt \hat{\mathcal{H}}_c\right)^2 + \dots, \quad (2.87)$$

with the coupling Hamiltonian at a specific time  $0 < t < T$ .

$$\hat{\mathcal{H}}_c(t) = i\hbar \int \frac{d\Delta}{\sqrt{2\pi}} \left[ \sqrt{\gamma^{(c)}} \hat{a}^\dagger \hat{a}_{\text{in}}(\Delta) e^{-i\Delta t} - \sqrt{\gamma^{(c)}} \hat{a} \hat{a}_{\text{in}}^\dagger(\Delta) e^{i\Delta t} \right] \quad (2.88)$$

Here, we first assume the finite-space commutation relation is valid for initial states,  $[\hat{a}, \hat{a}^\dagger] = 1$ . After a short round-trip time  $T$ , the final intra-cavity field becomes

$$\begin{aligned} \hat{a}_f &= \hat{U}_T^\dagger \hat{a} \hat{U}_T = \hat{a} + \left[ \hat{a}, \int_0^T dt \frac{\hat{\mathcal{H}}_c}{i\hbar} \right] + \frac{1}{2} \left[ \left[ \hat{a}, \int_0^T dt \frac{\hat{\mathcal{H}}_c}{i\hbar} \right], \int_0^T dt \frac{\hat{\mathcal{H}}_c}{i\hbar} \right] + \dots \\ &= \hat{a} + \sqrt{\gamma^{(c)}} \int_0^T dt \int \frac{d\Delta}{\sqrt{2\pi}} \hat{a}_{\text{in}}(\Delta) e^{-i\Delta t} - \frac{\gamma^{(c)} T}{2} \hat{a} + O(T^2). \end{aligned} \quad (2.89)$$

With the same unitary transformation, The field remaining in the bus waveguide will immediately pass to the output port at time  $0 < t < T$ .

$$\hat{a}_{\text{out}}(t) = \lim_{T \rightarrow 0} \hat{U}_T^\dagger \hat{a}_{\text{in}}(t) \hat{U}_T = \hat{a}_{\text{in}}(t) - \sqrt{\gamma^{(c)}} \hat{a} + O(T^2) \quad (2.90)$$

The above transformations can link the arbitrary input field to the excited intra-cavity field. Technically, it is more convenient to Fourier transform the time-dependent operators to slowly-varying spectral operators at each detune,  $\hat{a}(t) = \int \frac{d\Delta}{\sqrt{2\pi}} \hat{a}(\Delta) e^{-i\Delta t}$ , which is a continuous-spectral mode in the unit of 1/Hz.

Then, each monochromatic component follows the dynamics after applying the first-order approximation at small  $T$ .

$$\frac{d}{dt}\hat{a}(\Delta) = \lim_{T \rightarrow 0^+} \frac{\hat{a}_f(\omega) - \hat{a}(\omega)}{T} = \left(i\Delta - \frac{\gamma^{(c)}}{2}\right)\hat{a}(\Delta) + \sqrt{\gamma^{(c)}}\hat{a}_{\text{in}}(\Delta) \quad (2.91)$$

For the boundary condition of each frequency component,

$$\hat{a}_{\text{out}}(\Delta) = \hat{a}_{\text{in}}(\Delta) - \sqrt{\gamma^{(c)}}\hat{a}(\Delta). \quad (2.92)$$

It is almost identical to the dynamics of classic fields but misses the description of intrinsic loss. Fortunately, the energy loss to a Markovian environment can also be modeled as energy exchange to an entire undetectable continuous mode in a similar manner. With the intaking field from environment  $\hat{a}^{(i)}$  and the emitting field  $\hat{a}^{(e)}$ , we can apparently obtain the single-mode master equation and the equal-time input-output relation as below.

$$\frac{d\hat{a}}{dt} = \left(i\Delta - \frac{\gamma}{2}\right)\hat{a} + \sqrt{\gamma^{(c)}}\hat{a}_{\text{in}} + \sqrt{\gamma^{(i)}}\hat{a}^{(i)} \quad (2.93)$$

$$\hat{a}_{\text{out}} = \hat{a}_{\text{in}} - \sqrt{\gamma^{(c)}}\hat{a}, \quad \hat{a}^{(e)} = \hat{a}^{(i)} - \sqrt{\gamma^{(i)}}\hat{a} \quad (2.94)$$

The above equation of motion and the input-output relations are identical to the derivation in references [9, 16].

The steady-state solution is

$$\hat{a}(\Delta) = \frac{\sqrt{\gamma^{(c)}}\hat{a}_{\text{in}}(\Delta) + \sqrt{\gamma^{(i)}}\hat{a}^{(i)}(\Delta)}{-i\Delta + \frac{\gamma}{2}} \quad (2.95)$$

An interesting fact is that the steady-state intra-cavity field operator,  $\hat{a}(\Delta)$ , has a different spectral commutation relation than free-propagating fields.

$$[\hat{a}(\Delta), \hat{a}^\dagger(\Delta')] = \frac{\gamma}{\Delta^2 + \frac{\gamma^2}{4}}\delta(\Delta - \Delta') \quad (2.96)$$

This relation means the system can be somehow expanded by monochromatic field operators  $\hat{a}(\Delta)$  since they are orthogonal spectral basis. However, the non-unity means none of them can solely serve as a full description of an intra-cavity photon. The conceptual explanation for this is that any photon excitation in the cavity must

have an exponentially decaying amplitude in time so that it's never a monochromatic field. The entity of any current intra-cavity photon should be described in a superposition of operators  $\hat{a} = \int \frac{d\Delta}{\sqrt{2\pi}} \hat{a}(\Delta)$ , which holds the commutation relation. Actually, this complete operator for the intra-cavity photon is exactly the initial state at the beginning of each round, which confirms the validity of the assumption beforehand.

$$[\hat{a}, \hat{a}^\dagger] = \int \frac{d\Delta}{\sqrt{2\pi}} \int \frac{d\Delta'}{\sqrt{2\pi}} \frac{\gamma}{\Delta^2 + \frac{\gamma^2}{4}} \delta(\Delta - \Delta') = 1 \quad (2.97)$$

We can also check that the commutation relations of the output field are identical to what the free-propagating quantized field should have.

$$[\hat{a}_{\text{out}}(\Delta), \hat{a}_{\text{out}}^\dagger(\Delta')] = \delta(\Delta - \Delta'), \quad [\hat{a}_{\text{out}}(t), \hat{a}_{\text{out}}^\dagger(t')] = \delta(t - t') \quad (2.98)$$

In addition, the linear motion of each mode is independent across multiple resonances. If all the light fields are coherent light, these equations and boundary conditions are reduced to the classic cases.

Back to the lab coordinate, we have

$$\frac{d}{dt} \hat{a}_{m,j} = \left( -i\omega_{m,j} - \frac{\gamma_{m,j}}{2} \right) \hat{a}_{m,j} + \sqrt{\gamma_{m,j}^{(c)}} \hat{a}_{m,\text{in}} + \sqrt{\gamma_{m,j}^{(i)}} \hat{a}_m^{(i)}, \quad (2.99)$$

$$\hat{a}_{m,\text{out}} = \hat{a}_{m,\text{in}} - \sqrt{\gamma_{m,j}^{(c)}} \hat{a}_{m,j}. \quad (2.100)$$

These equations of motion are equivalent to a set of master equations in the Heisenberg picture over the lab time-space coordinates.

$$i\hbar \dot{\hat{a}}_{m,j} = [\hat{a}_{m,j}, \hat{\mathcal{H}}_0] + \sqrt{\gamma_{m,j}^{(c)}} \hat{a}_{m,\text{in}} + \sqrt{\gamma_{m,j}^{(i)}} \hat{a}_m^{(i)}, \quad \hat{\mathcal{H}}_0 = \sum_{m,j} \omega_{m,j} \hat{a}_{m,j}^\dagger \hat{a}_{m,j} \quad (2.101)$$

It can be interpreted that the cavity is an environment for discrete field operators to evolve at the resonance frequency. If a discrete field operator carries multiple spectral components, the portion not on the resonance will suffer a phase change in time.

We will use this type of master equation in later sections. It is worthwhile to mention that they are only valid for the macroscopic time scale. For some dramatic intra-cavity dynamics within a few rounds, it may not be a good approximation.

### 2.1.7 Nonlinear Optical Effects

Optical nonlinearity is defined by the nonlinear response of a system to the external light field. Generally, the total polarization density of a system can be expanded into order series of the total electric field with tensor-like coefficients  $\chi^{(n)}$  for inhomogeneous materials.

$$\mathbf{P}_{\text{tot}} = \varepsilon_0 \left( \chi^{(1)} \cdot \mathbf{E}_{\text{tot}} + \chi^{(2)} : \mathbf{E}_{\text{tot}}^2 + \chi^{(3)} : \mathbf{E}_{\text{tot}}^3 + \dots \right) \quad (2.102)$$

The second term of the right-hand side stands for the second-order nonlinearity, while the third term describes the third-order nonlinearity. The dots indicate the tensor product.

$$\chi^{(1)} \cdot \mathbf{E}_{\text{tot}} \equiv \sum_j \chi_{ij}^{(1)} E_{\text{tot},j} \quad (2.103)$$

$$\chi^{(2)} : \mathbf{E}_{\text{tot}}^2 \equiv \sum_{j,k} \chi_{ijk}^{(2)} E_{\text{tot},j} E_{\text{tot},k} \quad (2.104)$$

$$\chi^{(3)} : \mathbf{E}_{\text{tot}}^3 \equiv \sum_{j,k,l} \chi_{ijkl}^{(3)} E_{\text{tot},j} E_{\text{tot},k} E_{\text{tot},l} \quad (2.105)$$

When using vector potential as the primary field, the Lagrangian density becomes

$$\mathcal{L}(\mathbf{A}, \dot{\mathbf{A}}) = \varepsilon_0 \left[ \frac{1}{2} (\mathbf{E}_{\text{tot}}^2 - c^2 \mathbf{B}_{\text{tot}}^2) + \frac{1}{2} \chi^{(1)} \mathbf{E}_{\text{tot}}^2 + \frac{1}{3} \chi^{(2)} \mathbf{E}_{\text{tot}}^3 + \frac{1}{4} \chi^{(3)} \mathbf{E}_{\text{tot}}^4 + \dots \right] \quad (2.106)$$

The corresponding Hamiltonian density reads<sup>2</sup>

$$\tilde{\mathcal{H}} = \varepsilon_0 \left[ \frac{1}{2} (\mathbf{E}_{\text{tot}}^2 + c^2 \mathbf{B}_{\text{tot}}^2) + \chi^{(1)} \mathbf{E}_{\text{tot}}^2 + \frac{2}{3} \chi^{(2)} \mathbf{E}_{\text{tot}}^3 + \frac{3}{4} \chi^{(3)} \mathbf{E}_{\text{tot}}^4 + \dots \right] \quad (2.108)$$

---

<sup>2</sup>The Hamiltonian has usually been expanded in orders of  $\mathbf{D}_{\text{tot}}$  and  $\tilde{\chi}^{(i)}$  due to quantization over the primary field  $\mathbf{A}$  and conjugate field  $\mathbf{\Pi} = -\mathbf{D}$ . The relations between tensor-like coefficients are clearly discussed in Ref. [9, 17].

$$\tilde{\mathcal{H}} = \frac{\mu_0}{2} \mathbf{B}_{\text{tot}}^2 + \frac{1}{2} \tilde{\chi}^{(1)} \mathbf{D}_{\text{tot}}^2 + \frac{1}{3} \tilde{\chi}^{(2)} \mathbf{D}_{\text{tot}}^3 + \frac{1}{4} \tilde{\chi}^{(3)} \mathbf{D}_{\text{tot}}^4 + \dots \quad (2.107)$$

. As far as we know, both conventions only result in different definitions of coefficients. They will not infect the relative behaviors of nonlinear phenomena discussed later.

In experiment, it is more common to use the convention to reduce the rotating symmetries of indices, which results in ordered nonlinear coefficients by defining  $\chi_{i\bar{j}\bar{k}}^{(2)} = 2\chi_{ijk}^{(2)}$ ,  $\chi_{i\bar{j}\bar{k}\bar{l}}^{(3)} = 3\chi_{ijkl}^{(3)}$ , and so on [10]. Then without further mention, the ordered Hamiltonian density becomes

$$\tilde{\mathcal{H}} = \varepsilon_0 \left[ \frac{1}{2}(\mathbf{E}_{\text{tot}}^2 + c^2\mathbf{B}_{\text{tot}}^2 + \chi^{(1)}\mathbf{E}_{\text{tot}}^2) + \frac{1}{3}\chi^{(2)}\mathbf{E}_{\text{tot}}^3 + \frac{1}{4}\chi^{(3)}\mathbf{E}_{\text{tot}}^4 + \dots \right]. \quad (2.109)$$

It is possible to simulate the system directly from the full Lagrangian or the derived Hamiltonian. Practically, in common materials,  $\chi^{(n)}$  fades quickly when  $n$  becomes larger. Hence, if the pump light field does not have extremely high power, only the lower-order nonlinear effects will perturb the system.

One conventional way to model the classic nonlinear system is to set up nonlinear-coupled mode equations as a perturbation from the linear system. These nonlinear mode equations are usually derived by decomposing the Hamiltonian into linearly-defined modes. To better illustrate the mode decomposition, we begin with a discrete spectrum.

$$\mathbf{E}_{\text{tot}}(t) = \sum_{m,j} \zeta_{m,j}(t) \mathbf{E}_{m,j} e^{-i(\omega_{m,j}t - \beta_{m,j}z)} \quad (2.110)$$

The Hamiltonian is separated into a linear Hamiltonian density and a nonlinear interaction Hamiltonian density.

$$\tilde{\mathcal{H}} = \tilde{\mathcal{H}}_0 + \tilde{\mathcal{H}}_I \quad (2.111)$$

$$\tilde{\mathcal{H}}_0 = \frac{\varepsilon_0}{2}(\mathbf{E}_{\text{tot}}^2 + c^2\mathbf{B}_{\text{tot}}^2 + \chi^{(1)}\mathbf{E}_{\text{tot}}^2) \quad (2.112)$$

$$\tilde{\mathcal{H}}_{\text{int}} = \varepsilon_0 \left( \frac{1}{3}\chi^{(2)}\mathbf{E}_{\text{tot}}^3 + \frac{1}{4}\chi^{(3)}\mathbf{E}_{\text{tot}}^4 + \dots \right) \quad (2.113)$$

The linear Hamiltonian density describes the linear time evolution of each mode, keeping the phase relation and the dispersion among modes. The interaction Hamiltonian works in a perturbation manner. For a finite space, the Hamiltonian needs integral over the whole interaction space.

$$\mathcal{H} = \int dV \tilde{\mathcal{H}}, \quad \mathcal{H}_0 = \int dV \tilde{\mathcal{H}}_0, \quad \mathcal{H}_{\text{int}} = \int dV \tilde{\mathcal{H}}_{\text{int}}. \quad (2.114)$$



By substitution to decomposed modes, the interaction Hamiltonian is time-dependent since multiple frequency components are involved in higher-order nonlinearities. However, in experiments, rapid oscillation may not get recorded by devices under bandwidth limits. We can assume the interaction happens gradually for enough long time so that the interaction terms with disparate frequencies are averaged down to negligible. Therefore, only the fields whose frequencies hold conservation laws can have significant interaction rates with each other. For example, second-order nonlinearity requires the sum frequencies of two fields to equal another field. Otherwise, the interaction rate will be averaged to zero. Thus, we can just retain those high-rate interaction terms in the Hamiltonian to simplify the derivation.

For dealing with quantized fields, this technique also shows great effectiveness in formalism and agreement to experiments. By replacing linearly-defined modes with quantized operators accordingly, the nonlinear dynamics of quantized fields can be directly established.

$$\mathbf{E}_{\text{tot}} \rightarrow \hat{\mathbf{E}}_{\text{tot}} , \quad \mathcal{H} \rightarrow \hat{\mathcal{H}} , \quad \mathcal{H}_0 \rightarrow \hat{\mathcal{H}}_0 , \quad \mathcal{H}_{\text{int}} \rightarrow \hat{\mathcal{H}}_{\text{int}} . \quad (2.115)$$

Moreover, the conceptual picture of photons and the interactions in between are pedagogically more clear and clean. We can explain the microscopic interaction as converting some photons into other photons. Hence, the relation rules in frequencies and wave vectors become the conservation laws of energy and momentum, respectively. In the following sections, we will introduce the model of optical nonlinear effects case by case.

## 2.2 Second-Order Nonlinearity

The second-order nonlinearity is also known as the  $\chi^{(2)}$  effect or Pockels effect. This type of interaction requires the material to have a  $\chi^{(2)}$  coefficient, which is usually found in non-centrosymmetric crystals. Among non-centrosymmetric crystals, some crystals can show ferroelectric properties, which has a clear understanding of how second-order nonlinearity is evoked. Ferroelectric material has a hysteresis

loop when excited by a varying external field. It also owns spontaneous electric polarization density when the external field is absent. We can Taylor expand the relation between polarization density within orders of the electric field. Since each branch of the hysteresis loop is not odd, there must be a non-zero second-order term, which leads to the  $\chi^{(2)}$  coefficient. Other non-centrosymmetric materials also show less symmetry in their response curve to the external field. Thus, they also have non-zero  $\chi^{(2)}$  coefficients. If the crystal is transparent, then it could be used as an optical medium for second-order nonlinearity.

For state-of-the-art platforms, doped phosphates and barium borate crystals, such as KTP and BBO, are commercialized for manufacturing laser systems and quantum experiments. For nano-fabrication purpose, widely-used high- $\chi^{(2)}$  materials are gallium nitride (GaN), aluminum nitride (AlN), lithium niobate (LiNbO<sub>3</sub>), and silicon carbide (SiC). Their  $\chi^{(2)}$  ranges from 1-40 pm/V.

Depending on the setup of input and output fields, the second-order nonlinearity has multiple manifestations. When only one input field is involved in the nonlinear interaction, the second-order nonlinear effect generates new fields with either double or half the input frequency of the pump. For the case where the frequency is doubled, we call it the second-harmonic generation (SHG). For the case of generating a half-frequency field, we call it the parametric down-conversion (PDC).

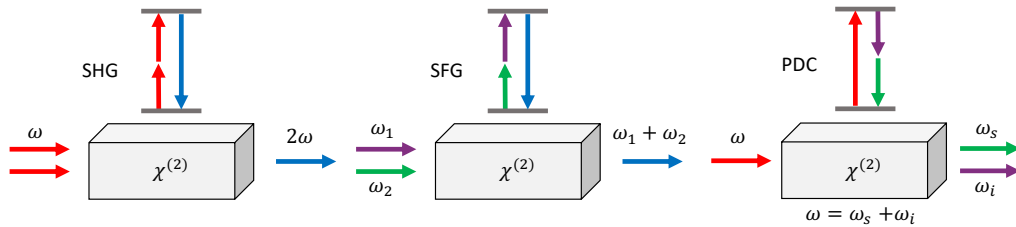


Figure 2.4: **Second-order nonlinearity.**

### 2.2.1 Second-Harmonic Generation

The SHG merges two photons from the pump field into one photon with doubled frequency. From now on, the linear permittivity of the material is absorbed into the

effective volumes and cross-sections for better illustrations. Based on the quantized linear fields in a box,

$$\hat{\mathbf{E}}_{\text{tot}}(t) = i\sqrt{\frac{\hbar\omega_p}{2\varepsilon_0}} \left[ \frac{\mathbf{u}_{\text{SHG}}}{\sqrt{V_{\text{SHG}}}} \hat{a}_{\text{SHG}} e^{-i2\omega_p t} + \frac{\mathbf{u}_p}{\sqrt{V_p}} \hat{a}_p e^{-i\omega_p t} \right] + c.c., \quad (2.116)$$

the total interaction Hamiltonian within the box has the form of <sup>3</sup>

$$\hat{\mathcal{H}}_{\text{SHG}} = \frac{i\hbar}{2} (g_{\text{SHG}} \hat{a}_{\text{SHG}}^\dagger \hat{a}_p^2 - g_{\text{SHG}}^* \hat{a}_p^{\dagger 2} \hat{a}_{\text{SHG}}), \quad (2.117)$$

where  $\hat{a}_{\text{SHG}}$  and  $\hat{a}_p$  are annihilation operators for the second-harmonic field and the pump field with effective mode volumes  $V_{\text{SHG}}$  and  $V_p$ , respectively.

$$g_{\text{SHG}} = \sqrt{\frac{\hbar\omega_p^3}{\varepsilon_0 V_{\text{SHG}} V_p^2}} \int d\mathbf{r}^3 \mathbf{u}_{\text{SHG}}^* \cdot \chi^{(2)} : \mathbf{u}_p^2 \quad (2.118)$$

is the normalized photon-photon interaction rate (Hz) proportional to the spatial overlapping between  $\mathbf{u}_{\text{SHG}}$  and  $\mathbf{u}_p$ . The unitary transformation generated by this time-invariant Hamiltonian is

$$\hat{U}_{\text{SHG}}(t) = e^{-\frac{i}{\hbar} \hat{\mathcal{H}}_{\text{SHG}} t} \quad (2.119)$$

Accordingly, the equations of motion are

$$\frac{d}{dt} \hat{a}_{\text{SHG}} = \frac{i}{2} g_{\text{SHG}} \hat{a}_p^2, \quad \frac{d}{dt} \hat{a}_p = -i g_{\text{SHG}}^* \hat{a}_p^\dagger \hat{a}_{\text{SHG}}. \quad (2.120)$$

It indicates that high conversion efficiency requires small effective volumes. If the mode is confined to half of their original effective volumes, the power conversion efficiency will be double higher.

In addition, the SHG is usually seen between traveling waves in experiments. For this case, the evolution can be derived by following a reference wavefront. Therefore, decomposed over  $z$  basis, the photon temporal profile is described as a spatial wave package  $\hat{a}_m(z) = \hat{a}_m(-t)/\sqrt{c_m}$  in the unit of  $1/\sqrt{m}$  with  $z = -c_m t$ . The equal-time commutation relation is held by

$$[\hat{a}_m(z), \hat{a}_n^\dagger(z')] = \frac{1}{c_m} [\hat{a}_m(t), \hat{a}_n^\dagger(t')] = \delta_{mn} \delta(z - z') \quad (2.121)$$

---

<sup>3</sup>By setting a different phase reference, the Hamiltonian can have the form of  $\hat{\mathcal{H}}_{\text{SHG}} = \frac{\hbar}{2} (g_{\text{SHG}} \hat{a}_{\text{SHG}}^\dagger \hat{a}_p^2 + g_{\text{SHG}}^* \hat{a}_p^{\dagger 2} \hat{a}_{\text{SHG}})$ . This does not influence the dynamics in most cases.

The power operator of each mode passing the plane at  $z$  becomes

$$\hat{P}_m(z) = \hbar\omega_m c_m \hat{a}_m^\dagger(z) \hat{a}_m(z). \quad (2.122)$$

Hence, the power of the fields are

$$P_{\text{SHG}}(z) = \langle \hbar\omega_{\text{SHG}} c_{\text{SHG}} \hat{a}_{\text{SHG}}^\dagger(z) \hat{a}_{\text{SHG}}(z) \rangle, \quad P_p(z) = \langle \hbar\omega_p c_p \hat{a}_p^\dagger(z) \hat{a}_p(z) \rangle \quad (2.123)$$

The total field with slowly-varying operators along  $z$ -direction becomes

$$\hat{\mathbf{E}}_{\text{tot}}(z) = i \left[ \sqrt{\frac{\hbar\omega_{\text{SHG}}}{2\varepsilon_0 S_{\text{SHG}}}} \mathbf{u}_{\text{SHG}} \hat{a}_{\text{SHG}}(z) e^{i\omega_{\text{SHG}}z} + \sqrt{\frac{\hbar\omega_p}{2\varepsilon_0 S_p}} \mathbf{u}_p \hat{a}_p(z) e^{i\beta_p z} \right] + c.c. \quad (2.124)$$

The interaction ends after the reference wavefront of the pump field passes through a distance of  $L$ . As such, the unitary transformation is

$$\hat{U}_{\text{SHG}}(z) = e^{-\frac{i}{\hbar} \int_0^z dz' \hat{P}_{\text{SHG}}(z')} \quad (2.125)$$

$$\hat{P}_{\text{SHG}}(z) = \frac{\varepsilon_0}{3c_p} \int dxdy \chi^{(2)} \mathbf{E}_{\perp\text{tot}}^3(z) \quad (2.126)$$

$$= \frac{i\hbar}{2} \left[ g_{\perp\text{SHG}} \hat{a}_{\text{SHG}}^\dagger(z) \hat{a}_p^2(z) e^{-i\Delta\beta z} - g_{\perp\text{SHG}}^* \hat{a}_p^{\dagger 2}(z) \hat{a}_{\text{SHG}}(z) e^{i\Delta\beta z} \right] \quad (2.127)$$

The normalized interaction rate is defined in the unit of  $1/\sqrt{m}$ .

$$g_{\perp\text{SHG}} = \frac{1}{c_p} \sqrt{\frac{\hbar\omega_p^3}{\varepsilon_0 S_p^2 S_{\text{SHG}}}} \left( \int dxdy \mathbf{u}_{\perp\text{SHG}}^* \cdot \chi^{(2)} : \mathbf{u}_{\perp p}^2 \right). \quad (2.128)$$

Similar to the case with a finite volume, the cross-section determines the efficiency of interactions between free-propagating fields. If the mode is confined to half the effective area, it will double the power efficiency.

The evolution in the interaction picture is formed as

$$\frac{d}{dz} \hat{a}_{\text{SHG}} = \frac{i}{2} g_{\perp\text{SHG}} \hat{a}_p^2 e^{-i\Delta\beta z}, \quad (2.129)$$

$$\frac{d}{dz} \hat{a}_p = -i g_{\perp\text{SHG}}^* \hat{a}_p^\dagger \hat{a}_{\text{SHG}} e^{i\Delta\beta z}. \quad (2.130)$$

Here,  $\Delta\beta = \beta_{\text{SHG}} - 2\beta_p$  is the wave-vector mismatch, a.k.a. phase mismatch between the interacting fields along the propagation direction. It describes the dislocation

between traveling waves. When  $\Delta\beta = 0$ , the fields are walking at the same pace from an oscillation perspective. For this case, the interaction is phase-matched and will obtain the highest possible interaction rate.

Considering the non-depleted CW pump, which means it keeps a constant power throughout the process, the SHG power conversion efficiency is

$$\eta_{\text{SHG}} = \frac{P_{\text{SHG}}(L)}{P_p^2} = \frac{|g_{\perp\text{SHG}}|^2 L^2}{2\hbar\omega_p c_p} \text{sinc}^2\left(\frac{\Delta\beta L}{2}\right) \quad (2.131)$$

When the phase mismatch becomes larger, the overall nonlinear efficiency will diminish quickly.

### 2.2.2 Phase-Matching Techniques

The phase mismatch forbids the nonlinear interactions that involve distinct frequencies due to both the unavoidable chromatic dispersion in materials and geometric dispersion led by structures such as waveguides. However, given a target process, we can engineer the materials or structures to match the phase of traveling waves to some extent. Here, we are going to introduce two widely-used techniques for phase-matching.

The first technique is engineering the geometric dispersion to cancel out the chromatic dispersion. This approach is usually applied when designing straight or bending waveguides for high second-order nonlinearity. In the example of SHG, we have the pump and second-harmonic fields traveling in the same waveguide. We would like to optimize the width or height of the waveguide to let one mode of each field have the same wave vectors, i.e.,  $\beta_{\text{SHG},m} = \beta_{p,n}$ . Generally, the mode of a shorter wavelength field will have a larger effective refractive index, whereas the higher order mode will have a smaller effective refractive index. Then, there would be a sweet point where a higher-order second-harmonic mode will have the same refractive index as a lower-order pump mode. By designing the waveguide at this sweet point, phase-matching is guaranteed.

The second technique is called quasi-phase-matching. It introduces a periodic change in the material along the propagation direction to compensate for the phase

mismatch. In each period, the positive and negative phase mismatch will cancel with each other so that the overall efficiency will not diminish after a long propagation. Pedagogically, this periodic change will incur a pseudo wave vector to the system, which keeps a subtle balance with the phase mismatch.

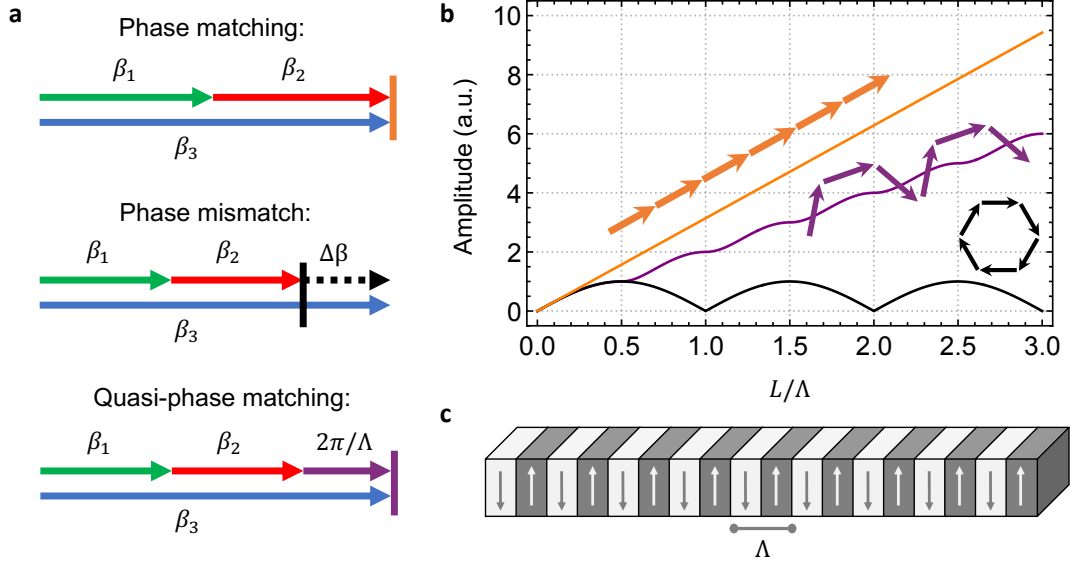


Figure 2.5: **Illustrations of phase-matching techniques.** **a.** Wave-vector relations of phase-matching, phase mismatch, and quasi-phase matching. **b.** The generated amplitude corresponding to the propagation distance and coherent length  $\Lambda$ . **c.** Domains of periodic-poled crystal.

It is possible to inverse the phase mismatch by flipping the sign of  $\chi^{(2)}$  in some ferroelectric materials such as KTP and LiNbO<sub>3</sub>. To do so, we can apply an extreme external static-electric field to pole a region of the ferroelectric material from one hysteresis branch to the other. The material initial polarization density will be forced to align with the external electric field and be fixed after tuning the external field off. Hence, the value of  $\chi^{(2)}$  coefficient from Taylor expansion will flip the sign. We can design the period based on the second-order nonlinear process we want.

Back to the example of non-depleted SHG, the quasi-phase matching is to have

poling period  $\Lambda = 2\pi/\Delta\beta$ . The equation of motions along the propagation become

$$\frac{d}{dz}\hat{a}_{\text{SHG}} = \frac{i}{2}G(z)g_{\perp\text{SHG}}\hat{a}_p^2e^{-i\Delta\beta z}, \quad (2.132)$$

$$\frac{d}{dz}\hat{a}_p = -iG(z)g_{\perp\text{SHG}}^*\hat{a}_p^\dagger\hat{a}_{\text{SHG}}e^{i\Delta\beta z}, \quad (2.133)$$

where

$$G(z) = \begin{cases} 1 & \text{if } n\Lambda \leq z < (n + \frac{1}{2})\Lambda, \\ -1 & \text{if } (n + \frac{1}{2})\Lambda \leq z < (n + 1)\Lambda. \end{cases} \quad (2.134)$$

The output second-harmonic field amplitude is

$$\hat{a}_{\text{SHG}} = \frac{i}{2}g_{\perp\text{SHG}}\hat{a}_p^2 \int_0^L G(z)e^{-i\Delta\beta z} \approx \frac{i}{2}g_{\perp\text{SHG}}\hat{a}_p^2 \times \frac{2}{\pi} \text{sinc}\left(\frac{\Delta\beta L}{2}\right) \quad (2.135)$$

Despite the fact that the overall power efficiency decreases by a factor of  $4/\pi^2$ , the quasi-phase matching enables engineering high nonlinear efficiency across a large bandwidth with limited choices of materials.

### 2.2.3 Cavity Enhancement

In practice, the confined nonlinear interactions between discrete modes are usually established inside a leaky cavity. Hence, the system will reach a steady state where the input and output fields are balanced. Nevertheless, the leaky cavity can accumulate much higher amplitudes of interacting fields by letting them cycle inside, which enhances the overall nonlinear efficiency.

Based on the linear Hamiltonians in Eq.(2.81)-(2.86) and the Hamiltonian  $\mathcal{H}_{\text{int}}$  of the target nonlinear process, such as (2.117), we can derive the general master equation for an arbitrary intra-cavity field mode  $\hat{a}$  as

$$\dot{\hat{a}} = \frac{i}{\hbar}[\hat{\mathcal{H}}_0 + \hat{\mathcal{H}}_{\text{int}}, \hat{a}] - \frac{\gamma}{2}\hat{a} + \sqrt{\gamma_c}\hat{a}_{\text{in}}. \quad (2.136)$$

This will reduce to the equation of motion of a single-mode field in Eq.(2.93). The boundary condition for the output field is

$$\hat{a}_{\text{out}} = \hat{a}_{\text{in}} - \sqrt{\gamma_c}\hat{a}. \quad (2.137)$$

Here, we use the SHG process as an example to show how to solve the intra-cavity dynamics. In this case, the discrete intra-cavity pump field  $\hat{b}$  is excited by the input pump field  $\hat{b}_{\text{in}}$ . When cycling inside the cavity, the pump field is converted to the discrete intra-cavity second-harmonic field  $\hat{a}$  at a rate of  $g$ . The master equation reads

$$\dot{\hat{b}} = \left(-i\omega_0 - \frac{\gamma}{2}\right)\hat{b} - ig^*\hat{a} + \sqrt{\gamma_c}\hat{b}_{\text{in}}, \quad (2.138)$$

$$\dot{\hat{a}} = \left(-i\omega_{\text{SHG}} - \frac{\kappa}{2}\right)\hat{a} + \frac{ig}{2}\hat{b}^2. \quad (2.139)$$

The intra-cavity second-harmonic field has no external source but a total loss rate of  $\kappa$ . After Fourier transforming to the spectral basis at  $\omega$  for mode  $\hat{b}$  ( $2\omega$  for mode  $\hat{a}$ ) and seeking for steady-state solutions, we obtain

$$0 = \left(i\Delta_p - \frac{\gamma}{2}\right)\hat{b} - ig^*\hat{a} + \sqrt{\gamma_c}\hat{b}_{\text{in}}(\omega), \quad (2.140)$$

$$0 = \left(i\Delta_{\text{SHG}} - \frac{\kappa}{2}\right)\hat{a} + \frac{ig}{2}\hat{b}^2, \quad (2.141)$$

where  $\Delta_p = \omega - \omega_0$  and  $\Delta_{\text{SHG}} = 2\omega - \omega_{\text{SHG}0}$  are cavity detunes. We can solve the second equation first, which gives the steady relation between intra-cavity fields.

$$\hat{a}(2\omega) = -\frac{ig\hat{b}^2}{i\Delta_{\text{SHG}} - \kappa/2} \quad (2.142)$$

Inserting it back to the first equation, the pump depletion is shown as an additional power-dependent loss rate.

$$\hat{b}(\omega) = \frac{-\sqrt{\gamma_c}\hat{b}_{\text{in}}(\omega)}{\left(i\Delta_p - \frac{\gamma}{2}\right) + \frac{|g|^2\hat{b}(\omega)^2}{i\Delta_{\text{SHG}} - \kappa/2}} \quad (2.143)$$

One intriguing fact is if the second-harmonic mode has non-zero detune, the back-action of the living second-harmonic field will alter both the phase shift and the internal loss rate of the pump mode. The motion of field  $\hat{b}$  shows the power dependency, which has a similar behavior as a type of third-order nonlinearity. We will discuss it later. Now, before going into the next order of nonlinearity, let's discuss other manifestations of second-order nonlinearity.



### 2.2.4 Sum-Frequency Generation

If the  $\chi^{(2)}$  system has a pair of input fields, the second-order nonlinearity can generate a third field whose frequency is equal to the sum of two pump fields. This process is called sum-frequency generation (SFG). In this way, SHG is a special case of SFG, where the two input fields degenerate into one pump field.

Following a similar derivation as the SHG, the Hamiltonian of sum-frequency generation in a box reads

$$\hat{\mathcal{H}}_{\text{SFG}} = i\hbar \left[ g_{\text{SFG}} \hat{a}_{\text{SFG}}^\dagger \hat{a}_{p1} \hat{a}_{p2} - g_{\text{SFG}}^* \hat{a}_{p1}^\dagger \hat{a}_{p2}^\dagger \hat{a}_{\text{SFG}} \right], \quad (2.144)$$

with interaction rate

$$g_{\text{SFG}} = \sqrt{\frac{\hbar\omega_{p1}\omega_{p2}(\omega_{p1} + \omega_{p2})}{2\varepsilon_0 V_{\text{SFG}} V_{p1} V_{p2}}} \int dV \mathbf{u}_{\text{SFG}}^* \cdot \chi^{(2)} : \mathbf{u}_{p1} \mathbf{u}_{p2} \quad (2.145)$$

### 2.2.5 Parametric Down-Conversion

The parametric down-conversion (PDC) is the inverse process of the SFG, where a single pump photon is split into a pair of single photons. Hence the Hamiltonian is the same one.

$$\hat{\mathcal{H}}_{\text{PDC}} = i\hbar \left[ g_{\text{PDC}} \hat{a}_p^\dagger \hat{a}_s \hat{a}_i - g_{\text{PDC}}^* \hat{a}_s^\dagger \hat{a}_i^\dagger \hat{a}_p \right], \quad (2.146)$$

with  $\omega_p = \omega_s + \omega_i$  and

$$g_{\text{PDC}} = \sqrt{\frac{\hbar\omega_s\omega_i\omega_p}{2\varepsilon_0 V_p V_s V_i}} \int dV \mathbf{u}_p^* \cdot \chi^{(2)} : \mathbf{u}_s \mathbf{u}_i. \quad (2.147)$$

Otherwise, if the output fields are degenerate, PDC can be treated as the inverse process of SHG.

$$\hat{\mathcal{H}}_{\text{PDC}} = \frac{i\hbar}{2} \left[ g_{\text{PDC}} \hat{a}_p^\dagger \hat{a}_s^2 - g_{\text{PDC}}^* \hat{a}_s^{\dagger 2} \hat{a}_p \right]. \quad (2.148)$$

Besides, if there is no seeded field to stimulate the process, PDC is also called the spontaneous parametric down-conversion (SPDC).

The generalizations of the above-confined interactions to traveling waves are apparent after imposing the correct phase mismatch, such as  $\Delta\beta = \beta_s + \beta_i - \beta_p$  in PDC.

Another interesting phenomenon is that the SPDC processes are able to generate entangled photon pairs and even squeeze the light field. The unitary operator of the SPDC process for traveling waves is generated by  $\hat{\mathcal{P}}_{\text{SPDC}}$ . If the pump field is a coherent state with amplitude  $\alpha_p$ , the unitary transform of length  $L$  with perfect phase-matching becomes

$$\hat{U}_{\text{SPDC}} = \exp [Lg_{\perp\text{PDC}}\alpha_p^*\hat{a}_s^2 - Lg_{\perp\text{PDC}}^*\alpha_p\hat{a}_s^{\dagger 2}] = \hat{S}(-2Lg_{\perp\text{PDC}}\alpha_p^*). \quad (2.149)$$

It has a similar form as the squeezing operator in Eq. (2.55). Similarly, the SPDC process will lead to the two-mode squeezed fields as Eq. (2.65).

With the cavity enhancement, the dynamics of SPDC between input pump field  $\hat{a}_p$  and generated signal field  $\hat{a}_s$  in a rate of  $g$  becomes

$$\dot{\hat{a}}_p = (-i\omega_p - \frac{\gamma}{2})\hat{a}_p + \frac{g}{2}\hat{a}_s^2 + \sqrt{\gamma_c}\hat{a}_{p,\text{in}} + \sqrt{\gamma_i}\hat{a}_p^{(i)} \quad (2.150)$$

$$\dot{\hat{a}}_s = (-i\omega_s - \frac{\kappa}{2})\hat{a}_s - g\hat{a}_p\hat{a}_s^\dagger + \sqrt{\kappa_c}\hat{a}_{s,\text{in}} + \sqrt{\kappa_i}\hat{a}_s^{(i)} \quad (2.151)$$

With on-resonance CW pump  $\alpha(\omega_p)$ , the back-actions from the signal field and environment are ignored. The first equation gives intra-cavity pump amplitude at  $\hat{a}_p \rightarrow \epsilon = \frac{2\sqrt{\gamma_c}\alpha}{\gamma}$ . After expansion in continuous spectral basis, we obtain the relation between frequency components and their conjugations

$$0 = (i\Delta - \frac{\kappa}{2})\hat{a}_s(\Delta) - g\epsilon\hat{a}_s^\dagger(-\Delta) + \sqrt{\kappa_c}\hat{a}_{s,\text{in}}(\Delta) + \sqrt{\kappa_i}\hat{a}_s^{(i)}(\Delta) \quad (2.152)$$

$$0 = (-i\Delta - \frac{\kappa}{2})\hat{a}_s^\dagger(-\Delta) - g^*\epsilon^*\hat{a}_s(\Delta) + \sqrt{\kappa_c}\hat{a}_{s,\text{in}}^\dagger(-\Delta) + \sqrt{\kappa_i}\hat{a}_s^{(i)\dagger}(-\Delta) \quad (2.153)$$

The solution of the conjugate signal field with omitted subscript is

$$\hat{a}_s^\dagger(-\Delta) = \frac{-g^*\epsilon^*\hat{a}_s(\Delta) + \sqrt{\kappa_c}\hat{a}_{s,\text{in}}(-\Delta) + \sqrt{\kappa_i}\hat{a}_s^{(i)}(-\Delta)}{i\Delta + \frac{\kappa}{2}} \quad (2.154)$$

Then, the on-resonance signal at around  $\Delta = 0$  obeys

$$\left(\frac{\kappa^2}{4} - |g\epsilon|^2\right)\hat{a} = \frac{\kappa}{2}\sqrt{\kappa_c}\hat{a}_{\text{in}} + \frac{\kappa}{2}\sqrt{\kappa_i}\hat{a}^{(i)} + g\epsilon\sqrt{\kappa_c}\hat{a}_{\text{in}}^\dagger + g\epsilon\sqrt{\kappa_i}\hat{a}^{(i)\dagger} \quad (2.155)$$

With a suitable pump phase to make  $g\epsilon$  a positive real number, the output signal is

$$\hat{a}_{\text{out}} = \hat{a}_{\text{in}} - \sqrt{\kappa_c} \hat{a} \quad (2.156)$$

$$= \left(1 - \frac{\kappa_c \frac{\kappa}{2}}{\frac{\kappa^2}{4} - |g\epsilon|^2}\right) \hat{a}_{\text{in}} - \frac{\kappa_c g \epsilon \hat{a}_{\text{in}}^\dagger}{\frac{\kappa^2}{4} - |g\epsilon|^2} - \frac{\sqrt{\kappa_c \kappa_i} \left(\frac{\kappa}{2} \hat{a}^{(i)} + g \epsilon \hat{a}^{(i)\dagger}\right)}{\frac{\kappa^2}{4} - |g\epsilon|^2} \quad (2.157)$$

The quadrature  $\hat{P}_{\text{out}}$  is

$$\hat{P}_{\text{out}} = \frac{i}{\sqrt{2}} (\hat{a}_{\text{out}}^\dagger - \hat{a}_{\text{out}}) = \frac{\frac{\kappa}{2} + g\epsilon - \kappa_c}{\frac{\kappa}{2} + g\epsilon} \hat{P}_{\text{in}} + \frac{\sqrt{\kappa_c \kappa_i}}{\frac{\kappa}{2} + g\epsilon} \hat{P}^{(i)} \quad (2.158)$$

The variance is

$$\langle (\Delta \hat{P}_{\text{out}})^2 \rangle = \left(\frac{\frac{\kappa}{2} + g\epsilon - \kappa_c}{\frac{\kappa}{2} + g\epsilon}\right)^2 \langle (\Delta \hat{P}_{\text{in}})^2 \rangle + \left(\frac{\sqrt{\kappa_c \kappa_i}}{\frac{\kappa}{2} + g\epsilon}\right)^2 \langle (\Delta \hat{P}^{(i)})^2 \rangle \quad (2.159)$$

The input field and environment are all vacuum so that  $\langle (\Delta \hat{P}_{\text{in}})^2 \rangle = \langle (\Delta \hat{P}^{(i)})^2 \rangle = \frac{1}{2}$ . Then, the output field from the cavity is squeezed since the variance is less than the vacuum field. Considering  $g\epsilon = \kappa/2$  and  $\kappa_c = \kappa$ , the variance of the output field can even be infinitely squeezed to zero.

When the squeezing is weak, i.e.,  $g\epsilon \ll \kappa/2$ , the generated field will decay fast in a few cycles. Hence, it is better to approximate the generated field at the single-photon level in Schrödinger picture.

$$|\phi\rangle = \exp\left(\frac{1}{i\hbar} \int_0^T dt \hat{\mathcal{H}}_{\text{SPDC}}\right) |0\rangle \approx -gT\epsilon \frac{\hat{a}^{\dagger 2}}{2} |0\rangle \quad (2.160)$$

Similarly, in the continuous spectral limit, we have

$$|\phi\rangle = \exp\left(\frac{1}{i\hbar} \int_0^T dt \hat{\mathcal{H}}_{\text{PDC}}\right) |00\rangle \approx -g\epsilon \int d\Delta \hat{a}^\dagger(\Delta) \hat{a}^\dagger(-\Delta) |00\rangle \quad (2.161)$$

Further discussion on second-order nonlinearities will be embedded in later sections when necessary. Now, we are diving into the next order of nonlinearity.

### 2.3 Third-Order Nonlinearity

All dielectric materials can show third-order nonlinearity under extremely-intense pump fields. From a microscopic view, the polarization density will reach the boundary of the cell so that it can not be proportional to the external field. At this point,

the electronic response of the material requires the approximation up to the third-order nonlinear coefficient,  $\chi^{(3)}$ , which is usually negative.

In nanophotonics, Si, SiN, SiO<sub>2</sub>, and other silicon-based materials are widely used in fabrications. Their third-order nonlinear coefficient leads to several unique manifestations.

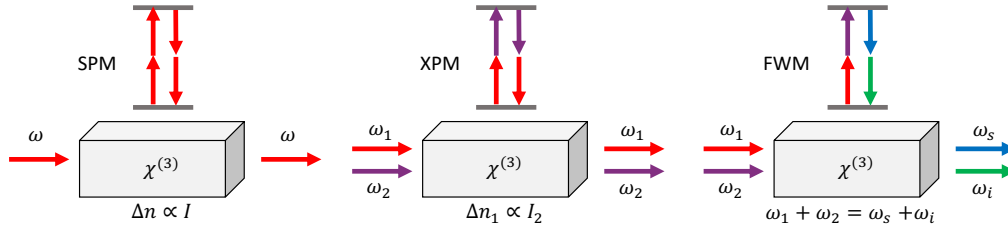


Figure 2.6: **Third-order nonlinearity.**

### 2.3.1 Self-Phase Modulation

The self-phase modulation is what causes the power-dependent change in the refractive index. A general relation is

$$n = n_0 + n_2 I, \quad (2.162)$$

where  $I = P/S$  is the flux of the light field. For common crystals,  $n_2$  is usually positive at the level of  $10^{-20} - 10^{-17} \text{ m}^2/\text{W}$  [18]. In this process, only one pump field  $\hat{a}$  at  $\omega$  is involved. Hence, the total field operator of this finite space is

$$\hat{\mathbf{E}}_{\text{tot}}(t) = i\sqrt{\frac{\hbar\omega}{2\epsilon_0 V}} \mathbf{u} \hat{a} e^{-i\omega t} + c.c., \quad (2.163)$$

and the Hamiltonian reads

$$\hat{\mathcal{H}}_{\text{SPM}} = -\frac{\hbar}{4} g_{\text{SPM}} \hat{a}^{\dagger 2} \hat{a}^2, \quad (2.164)$$

with a positive photon-photon interaction rate

$$g_{\text{SPM}} = -\frac{3}{2} \frac{\hbar\omega^2}{\epsilon_0 V} \chi^{(3)}. \quad (2.165)$$

Inside the cavity with cavity mode  $\hat{a}$  at resonance frequency  $\omega_0$ , the SPM is described in the equation of motion as

$$\dot{\hat{a}} = \left(-i\omega_0 - \frac{\gamma}{2}\right) \hat{a} + \frac{ig_{\text{SPM}}}{2} \hat{a}^\dagger \hat{a}^2 + \sqrt{\gamma_c} \hat{a}_{\text{in}}(\omega). \quad (2.166)$$

The steady-state solution for the pump at  $\omega$  follows the equation

$$\hat{a}(\omega) = \frac{\sqrt{\gamma_c} \hat{a}_{\text{in}}(\omega)}{\left(-i\Delta + \frac{\gamma}{2}\right) + \frac{ig_{\text{SPM}}}{2} \hat{a}^\dagger(\omega) \hat{a}}. \quad (2.167)$$

If the SPM happens in a traveling wave,  $g_{\perp\text{SPM}} = -\frac{3}{2} \frac{\hbar\omega^2}{\epsilon_0 S} \chi^{(3)}$ . Then we have  $n_2 = -\frac{3}{4\epsilon_0 n_0 c} \chi^{(3)}$ , which goes back to the positive nonlinear refractive index.

### 2.3.2 Cross-Phase Modulation

More third-order nonlinear interaction will emerge if we are interested in two or more fields. The cross-phase modulation happens when the power of another field determines the additional phase of the target field. This effect is inevitable when any of the pump fields has notable power. Due to the homogeneity of coefficient  $\chi^{(3)}$  in forward and backward directions, the XPM does not depend on whether the fields are co-propagating or counter-propagating. Hence, for a system with two fields  $\hat{a}_1$  and  $\hat{a}_2$ , we have

$$\hat{\mathbf{E}}_{\text{tot}}(t) = i \left[ \sqrt{\frac{\hbar\omega_1}{2\epsilon_0 V_1}} \mathbf{u}_1 \hat{a}_1 e^{-i\omega_1 t} + \sqrt{\frac{\hbar\omega_2}{2\epsilon_0 V_2}} \mathbf{u}_2 \hat{a}_2 e^{-i\omega_2 t} \right] + c.c.. \quad (2.168)$$

The Hamiltonian becomes

$$\hat{\mathcal{H}}_{\text{SPM}} = -\hbar g_{\text{XPM}} \hat{a}_1^\dagger \hat{a}_2^\dagger \hat{a}_1 \hat{a}_2, \quad (2.169)$$

with a positive photon-photon XPM interaction rate

$$g_{\text{XPM}} = -\frac{3}{2} \frac{\hbar\omega_1\omega_2}{\epsilon_0 V_1 V_2} \int dV \mathbf{u}_1^* \mathbf{u}_2^* : \chi^{(3)} : \mathbf{u}_1 \mathbf{u}_2. \quad (2.170)$$

. This XPM interaction rate is defined to match the scale of the SPM rate. Taking both SPM and XPM into account, the intra-cavity dynamics follow

$$\dot{\hat{a}}_1 = \left(-i\omega_1 - \frac{\gamma_1}{2}\right) \hat{a}_1 + i \left(g_{\text{XPM}} \hat{a}_2^\dagger \hat{a}_2 + \frac{g_{\text{SPM}}}{2} \hat{a}_1^\dagger \hat{a}_1\right) \hat{a}_1 + \sqrt{\gamma_{c1}} \hat{a}_{1,\text{in}}(\omega_1), \quad (2.171)$$

$$\dot{\hat{a}}_2 = \left(-i\omega_2 - \frac{\gamma_2}{2}\right) \hat{a}_2 + i \left(g_{\text{XPM}} \hat{a}_1^\dagger \hat{a}_1 + \frac{g_{\text{SPM}}}{2} \hat{a}_2^\dagger \hat{a}_2\right) \hat{a}_2 + \sqrt{\gamma_{c2}} \hat{a}_{2,\text{in}}(\omega_2). \quad (2.172)$$

It is noteworthy that if the overlapping ratio between modes is unity, i.e.,  $g_{\text{XPM}} = g_{\text{SPM}}$ , the phase shift by XPM is twice as much as SPM under the same amount of power.

In addition, XPM can be easily generated for the interactions between more fields since phase-matching is not involved in this process.

### 2.3.3 Four-Wave Mixing

If we focus on more fields involved in a  $\chi^{(3)}$  system, the four-wave mixing will inevitably affect their dynamics, especially when their powers are high enough. In the degenerate-pump FWM, the system has three modes labeled by  $\hat{a}_p$  for the pump,  $\hat{a}_s$  for the signal, and  $\hat{a}_i$  for the idler. The total field is

$$\hat{\mathbf{E}}_{\text{tot}}(t) = i \left[ \sqrt{\frac{\hbar\omega_s}{2\varepsilon_0 V_s}} \mathbf{u}_s \hat{a}_s e^{-i\omega_s t} + \sqrt{\frac{\hbar\omega_i}{2\varepsilon_0 V_i}} \mathbf{u}_i \hat{a}_i e^{-i\omega_i t} + \sqrt{\frac{\hbar\omega_p}{2\varepsilon_0 V_p}} \mathbf{u}_p \hat{a}_p e^{-i\omega_p t} \right] + c.c. \quad (2.173)$$

FWM converts two pump photons into a pair of signal and idler photons or vice versa. The total frequency of the generated photons is equal to the photon annihilated. The Hamiltonian for degenerate pump FWM is

$$\hat{\mathcal{H}}_{\text{FWM}} = -\frac{\hbar}{2} \left( g_{\text{FWM}} \hat{a}_p^{\dagger 2} \hat{a}_s \hat{a}_i + g_{\text{FWM}}^* \hat{a}_s^{\dagger} \hat{a}_i^{\dagger} \hat{a}_p^2 \right), \quad (2.174)$$

with photon conversion rate

$$g_{\text{FWM}} = -\frac{3}{2} \sqrt{\frac{\hbar\omega_s\omega_i\omega_p^2}{\varepsilon_0 V_s V_i V_p^2}} \int dV \mathbf{u}_p^{*2} : \chi^{(3)} : \mathbf{u}_s \mathbf{u}_i. \quad (2.175)$$

The phase-matching is embedded inside the integral of spatial modes. This conversion rate can also be reduced to the rate of SPM and XPM if the system has perfect phase-matching, unity overlapping ratio, and the same mode volumes.

Under suitable conditions of the pump field, spontaneous FWM (SFWM) can also generate the squeezed states of light since the dynamics can be reduced to a form similar to the SPDC process. The discussion of this is embedded in the chapter later.

Moreover, the general form of FWM has four modes, which describe the photon conversion from a pair of  $\hat{a}_{p1}$  and  $\hat{a}_{p2}$  to a pair of signal and idler photons. The Hamiltonian is written in

$$\hat{\mathcal{H}}_{\text{FWM}} = -\hbar \left( g_{\text{FWM}} \hat{a}_{p1}^\dagger \hat{a}_{p2}^\dagger \hat{a}_s \hat{a}_i + g_{\text{FWM}}^* \hat{a}_s^\dagger \hat{a}_i^\dagger \hat{a}_{p1} \hat{a}_{p2} \right), \quad (2.176)$$

with photon-pair conversion rate

$$g_{\text{FWM}} = -\frac{3}{2} \sqrt{\frac{\hbar \omega_s \omega_i \omega_{p1} \omega_{p2}}{\epsilon_0 V_s V_i V_{p1} V_{p2}}} \int dV \mathbf{u}_{p1}^* \mathbf{u}_{p2}^* : \chi^{(3)} : \mathbf{u}_s \mathbf{u}_i. \quad (2.177)$$

## 2.4 Cascaded Second-Order Nonlinearities

Nonlinearities are coherent processes that can happen simultaneously. Therefore, the new fields generated by one nonlinearity may stimulate another type of nonlinearity. In the SHG process, we have seen that the back action from the second-harmonic field can act equivalently as the SPM, which changes the phase and loss of the pump field with power dependence. In the model of cascaded nonlinearities, this back action is caused by PDC from the second-harmonic field cycling inside the cavity.

$$\text{SHG} + \text{PDC} \rightarrow \text{SPM or XPM} \quad (2.178)$$

Similarly, the second-harmonic field can trigger the SPDC process to generate photon pairs that are equivalent to SFWM.

$$\text{SHG} + \text{SPDC} \rightarrow \text{SFWM} \quad (2.179)$$

The Hamiltonian describing the nonlinear photonic cavity with the cascaded-second-order nonlinear processes can be written as

$$H_{\text{sys}} = H_0 + H_1 + H_2, \quad (2.180)$$

$$H_0 = \hbar \omega_p \hat{b}^\dagger \hat{b} + \hbar \omega_0 \hat{a}^\dagger \hat{a} + \hbar \omega_+ \hat{b}_+^\dagger \hat{b}_+ + \hbar \omega_- \hat{b}_-^\dagger \hat{b}_-, \quad (2.181)$$

$$H_1 = \frac{i\hbar}{2} (g_2 \hat{a}^\dagger \hat{b}^2 - g_2^* \hat{a} \hat{b}^{\dagger 2}), \quad (2.182)$$

$$H_2 = i\hbar (g_2 \hat{a}^\dagger \hat{b}_+ \hat{b}_- - g_2^* \hat{a} \hat{b}_+^\dagger \hat{b}_-^\dagger), \quad (2.183)$$

with  $a$ ,  $b$ ,  $b_+$ , and  $b_-$  representing the second-harmonic field, the pump field, the signal field, and the idler field, respectively.  $H_0$  describes the free evolution of the cavity.  $H_1$  describes the SHG process.  $H_2$  describes the PDC interaction among the second-harmonic, signal, and idler modes. The nonlinear strength  $g_2$  for them can be written as

$$g_2 = \sqrt{\frac{\hbar\omega_0\omega_p^2}{2\epsilon_0 V_a V_b^2}} \int_V dr^3 \mathbf{u}_a^* \cdot \chi^{(2)} : \mathbf{u}_b^2 \quad (2.184)$$

with  $\mathbf{u}_a$  and  $\mathbf{u}_b$  the transverse mode profile of the second-harmonic and pump fields, respectively. The mode volumes are defined as  $V_a = 2\pi R n_a \iint_\sigma dr^2 |\mathbf{u}_a|^2$  and  $V_b = 2\pi R n_b \iint_\sigma dr^2 |\mathbf{u}_b|^2$ , with  $R$  the ring radius,  $n_a$  and  $n_b$  the refractive index for the second-harmonic and pump modes, and  $\sigma$  the cross-section. Here we assume that the signal and idler modes share the same transverse mode profile with the pump mode. While we do not include the interaction Hamiltonian for self-phase and cross-phase modulation, the corresponding frequency shift can be taken into account by re-defining the cavity resonance frequencies. Then the equations of motion can be written as

$$\dot{\hat{a}} = (-i\omega_0 - \frac{\gamma}{2})\hat{a} + g_2(\frac{1}{2}\hat{b}^2 + \hat{b}_+\hat{b}_-) + \sqrt{\gamma_c}\hat{a}_{\text{in}} + \sqrt{\gamma_i}\hat{a}^{(i)} \quad (2.185)$$

$$\dot{\hat{b}} = (-i\omega_p - \frac{\kappa}{2})\hat{b} - g_2\hat{a}\hat{b}^\dagger + \sqrt{\kappa_c}\hat{b}_{\text{in}} + \sqrt{\kappa_i}\hat{b}^{(i)} \quad (2.186)$$

$$\dot{\hat{b}}_+ = (-i\omega_+ - \frac{\kappa_+}{2})\hat{b}_+ - g_2^*\hat{a}\hat{b}_+^\dagger + \sqrt{\kappa_{c,+}}\hat{b}_{+, \text{in}} + \sqrt{\kappa_{i,+}}\hat{b}_+^{(i)} \quad (2.187)$$

$$\dot{\hat{b}}_- = (-i\omega_- - \frac{\kappa_-}{2})\hat{b}_- - g_2^*\hat{a}\hat{b}_-^\dagger + \sqrt{\kappa_{c,-}}\hat{b}_{-, \text{in}} + \sqrt{\kappa_{i,-}}\hat{b}_-^{(i)}. \quad (2.188)$$

with  $\gamma_c$ ,  $\gamma_i$ ,  $\gamma = \gamma_c + \gamma_i$  ( $\kappa_c$ ,  $\kappa_i$ ,  $\kappa = \kappa_c + \kappa_i$ ;  $\kappa_{c,\pm}$ ,  $\kappa_{i,\pm}$ ,  $\kappa_{\pm} = \kappa_{c,\pm} + \kappa_{i,\pm}$ ) the coupling, intrinsic, and total loss rate of the second-harmonic (pump; signal; idler) mode respectively. The input operators of the second-harmonic, pump, signal, and idler modes due to coupling loss (intrinsic loss) are labeled as  $\hat{a}_{\text{in}}$ ,  $\hat{b}_{\text{in}}$ ,  $\hat{b}_{+, \text{in}}$ ,  $\hat{b}_{-, \text{in}}$  ( $\hat{a}^{(i)}$ ,  $\hat{b}^{(i)}$ ,  $\hat{b}_+^{(i)}$ ,  $\hat{b}_-^{(i)}$ ) respectively.

With coherent input power  $P$  into the pump mode  $\hat{b}_{\text{in}} = \sqrt{\frac{P}{\hbar\omega_p}} e^{-i\omega t}$ , Eq. (2.185) and Eq. (2.186) can be treated classically using the mean fields  $\langle \hat{a} \rangle = \alpha$ ,  $\langle \hat{b} \rangle = \beta$ . Then



the static solutions of Eq. (2.185) and Eq. (2.186) are

$$\beta = \frac{\sqrt{\kappa_c}\beta_{\text{in}}}{-i(\omega - \omega_p) + \frac{\kappa}{2} + \frac{g_2^2|\beta|^2}{-2i(2\omega - \omega_0) + \frac{\gamma}{2}}}, \quad \alpha = \frac{\frac{1}{2}g_2\beta^2}{-i(2\omega - \omega_0) + \frac{\gamma}{2}} \quad (2.189)$$

In the non-depletion regime, the solution is further simplified to

$$\beta = \frac{\sqrt{\kappa_c}\beta_{\text{in}}}{-i(\omega - \omega_p) + \frac{\kappa}{2}}, \quad \alpha = \frac{\frac{1}{2}g_2\beta^2}{-i(2\omega - \omega_0) + \frac{\gamma}{2}}. \quad (2.190)$$

The effective interaction Hamiltonian for the signal and idler modes is

$$H_2 = i\hbar(g_2\alpha^*\hat{b}_+\hat{b}_- - g_2^*\alpha\hat{b}_+\hat{b}_-) \quad (2.191)$$

$$= \frac{\hbar}{2} \left[ \frac{i|g_2|^2}{i(2\omega - \omega_0) + \frac{\gamma}{2}} \beta^{*2}\hat{b}_+\hat{b}_- + \frac{-i|g_2|^2}{-i(2\omega - \omega_0) + \frac{\gamma}{2}} \beta^2\hat{b}_+\hat{b}_- \right]. \quad (2.192)$$

Therefore, the overall process is equivalent to Kerr interaction Hamiltonian

$$H_I = -\frac{\hbar}{2}(g_{c2}\hat{b}^{\dagger 2}\hat{b}_+\hat{b}_- + g_{c2}^*\hat{b}^2\hat{b}_+\hat{b}_-) \quad (2.193)$$

under coherent pump  $P$  with effective third-order nonlinearity

$$g_{c2} = -\frac{i|g_2|^2}{i(2\omega - \omega_0) + \frac{\gamma}{2}} \quad (2.194)$$

The equations of motion for the signal and idler modes are

$$\dot{\hat{b}}_+ = (-i\omega_+ - \frac{\kappa_+}{2})\hat{b}_+ + i\frac{1}{2}g_{c2}^*\beta^2\hat{b}_-^\dagger + \sqrt{\kappa_{c,+}}\hat{b}_{+, \text{in}} + \sqrt{\kappa_{i,+}}\hat{b}_+^{(i)} \quad (2.195)$$

$$\dot{\hat{b}}_- = (-i\omega_- - \frac{\kappa_-}{2})\hat{b}_- + i\frac{1}{2}g_{c2}^*\beta^2\hat{b}_+^\dagger + \sqrt{\kappa_{c,-}}\hat{b}_{-, \text{in}} + \sqrt{\kappa_{i,-}}\hat{b}_-^{(i)}, \quad (2.196)$$

with output boundary conditions:

$$\hat{b}_{+, \text{out}} = \hat{b}_{+, \text{in}} - \sqrt{\kappa_{c,+}}\hat{b}_+, \quad \hat{b}_{-, \text{out}} = \hat{b}_{-, \text{in}} - \sqrt{\kappa_{c,-}}\hat{b}_-. \quad (2.197)$$

For the classical stimulate four-wave mixing with idler input  $\beta_i e^{-i\omega_i t}$ , the static solution of Eq. (2.195) and Eq. (2.196) under the mean field approximation  $\langle \hat{b}_+ \rangle = \beta_+$ ,  $\langle \hat{b}_- \rangle = \beta_-$  can be obtained

$$\beta_- = \frac{i\frac{1}{2}g_{c2}^*\beta^2\beta_+^*}{i(\omega_- - \omega_i) + \frac{\kappa_-}{2}}, \quad \beta_+ = \frac{\sqrt{\kappa_{c,+}}\beta_i}{i(\omega_+ - \omega_i) + \frac{\kappa_+}{2} - \frac{1}{4} \frac{|g_{c2}|^2|\beta|^4}{-i(\omega_- - \omega_i) + \frac{\kappa_-}{2}}}. \quad (2.198)$$

With on-resonance pump and idler input, the photon number conversion efficiency under perfect phase-matching  $\omega_+ + \omega_- = 2\omega_p$  is

$$\eta = \frac{|\beta_{+,out}|^2}{|\beta_i|^2} = \frac{16\kappa_{c,+}\kappa_{c,-}|g_{c2}|^2|\beta|^4}{(\kappa_+\kappa_- - |g_{c2}|^2|\beta|^4)^2} \approx \frac{16\kappa_{c,+}\kappa_{c,-}|g_{c2}|^2|\beta|^4}{\kappa_+^2\kappa_-^2} \quad (2.199)$$

For the photon-pair generation, the output state can be written as

$$|\psi\rangle = \left[ 1 - \frac{ig_{c2}^*\beta^2}{2} \iint \frac{d\omega'}{\sqrt{2\pi}} \frac{d\omega''}{\sqrt{2\pi}} \frac{\sqrt{\kappa_{c,+}}\hat{b}_{+,out}^\dagger(\omega'')}{i(\omega_+ - \omega'') + \frac{\kappa_+}{2}} \frac{\sqrt{\kappa_{c,-}}\hat{b}_{-,out}^\dagger(\omega')}{i(\omega_- - \omega') + \frac{\kappa_-}{2}} \delta(\omega' + \omega'' - 2\omega_p) \right] |00\rangle + O\left(\frac{\kappa_{c,+}\kappa_{c,-}|g_{c2}|^2|\beta|^4}{\kappa_+^2\kappa_-^2} |22\rangle\right) \quad (2.200)$$

Therefore, the photon-pair generation rate under a weak pump can be calculated as

$$R = \langle \psi | \hat{b}_{+,out}^\dagger \hat{b}_{+,out} \hat{b}_{-,out}^\dagger \hat{b}_{-,out} | \psi \rangle \propto |g_{c2}|^2 P_{in}^2 Q_b^3, \quad (2.201)$$

with  $Q_b \approx \frac{\omega_p}{\kappa} \approx \frac{\omega_+}{\kappa_+} \approx \frac{\omega_-}{\kappa_-}$ . This dynamics is identical to the third-order nonlinear effect.

Hence, cascaded second-order nonlinearity can mimic third-order nonlinearity if the condition allows it. In the later chapters, we will show that the cascaded second-order nonlinearity can interplay with the third-order nonlinearity to modify the effective strength to the range beyond the material constraints.

## CHAPTER 3

On-Chip Photon-Pair Generation in Dressed Modes: the Photonic Mollow Triplet<sup>†</sup>**3.1 Abstract**

Making an analogy with atomic physics is a powerful tool for photonic technology, witnessed by the recent development in topological photonics and non-Hermitian photonics based on parity–time symmetry. The Mollow triplet is a prominent atomic effect with both fundamental and technological importance. Here we demonstrate the analogue of the Mollow triplet with quantum photonic systems. Photonic entanglement is generated with spontaneous nonlinear processes in dressed photonic modes, which are introduced through coherent multimode coupling. We further demonstrate the possibility of the photonic system to realize different configurations of dressed states, leading to the modification of the Mollow triplet. Our work would enable the investigation of complex atomic processes and the realization of unique quantum functionalities based on photonic systems.

**3.2 Main Article****3.2.1 Introduction**

The modification of internal energy levels can lead to a dramatic change in the optical response in atoms and molecules. As an example, one central peak with two symmetric sidebands can be observed in the fluorescence spectrum of atomic systems driven by a resonant optical field due to the energy splitting between dressed states, which is known as Mollow triplet [19]. Along with Rabi oscillation, it is regarded as an important confirmation of the light-atom interaction model in quantum optics [20, 21]. Recently, the study of Mollow triplet has attracted a renewed interest due to

---

<sup>†</sup>This chapter has been published previously as [1]

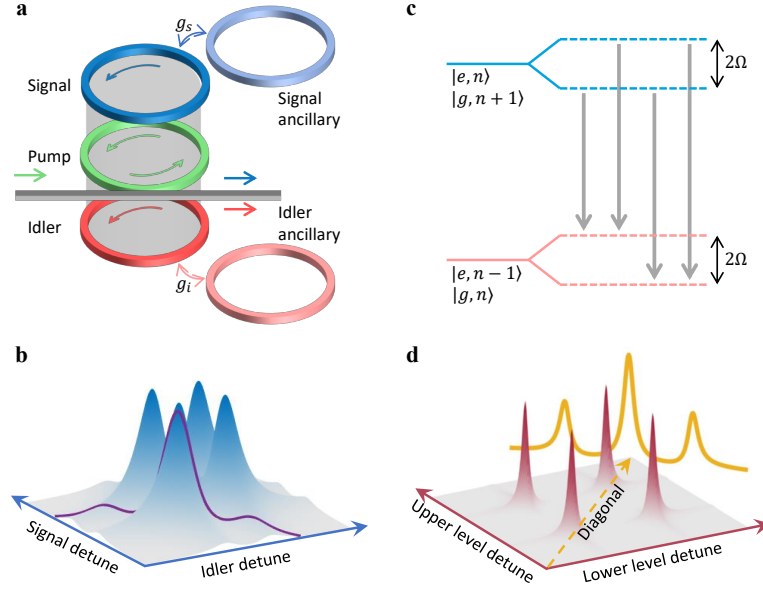


Figure 3.1: **Photonic analogue of Mollow triplet.** **a.** Schematic to realize Mollow triplet with quantum photonic systems. In a photonic ring cavity with one coherent drive (green), a pair of signal (blue) and idler (red) photons are created from spontaneous nonlinear processes. The signal and idler modes are further coupled to two ancillary modes, respectively (light blue and pink). **b.** Joint spectral density of signal-idler generation. The purple line shows the case with a continuous-wave pump and non-zero dispersion. **c.** Energy-level diagram for the atomic system under the resonant optical drive. The degeneracy is lifted between  $|e, n\rangle$  and  $|g, n + 1\rangle$  with  $|e\rangle$  ( $|g\rangle$ ) the atomic excited (ground) state and  $|n\rangle$  the photon number state. Rabi frequency is  $\Omega$ . Four transition paths are labeled with grey arrows. **d.** The probability density for atomic transitions. The integral along the diagonal direction (orange) is proportional to the fluorescence spectrum.

its potential applications in quantum information science [22, 23, 24, 25, 26, 27, 28, 29]. Highlighted by the capability of tailoring quantum correlations, Mollow triplet shows great promise in engineering high-quality quantum emitters [23, 24]. Novel quantum sensing schemes have also been demonstrated based on Mollow triplet [28, 29]. In addition, Mollow triplet has been used to study the coherent dynamics of solid-state qubit systems such as quantum dots [23, 26, 27], superconducting Josephson junctions [22], and diamond color centers [25].

The analogy between photonic resonances and atomic energy levels has enabled

the investigation of complex photonic processes with established concepts of atomic physics. Prominent examples include photonic crystals [30], topological photonic systems [31], and parity–time symmetric systems [32]. It has led to the development of important photonic technologies, including optical memories [33, 34, 35], topologically protected laser [36, 37], structured light [38], etc. Atomic processes such as quantum Hall effect [39, 38], electromagnetically induced transparency [33, 34, 35], and Ramsey interference [40], have all been realized with various photonic platforms. While quantum interpretation is required to model atomic systems, it is sufficient to describe the corresponding photonic processes in the classical picture. Therefore, experimental demonstrations are also conducted with coherent optical fields [33, 34, 35, 36, 37, 38, 39, 40]. The further expansion of the analogy between photonic and atomic systems into quantum regime will be highly valuable for the future development of photonic quantum information.

### 3.2.2 Theoretical Model

Here, we demonstrate the analogue of atomic Mollow triplet with all-photonic systems in the quantum regime. With entanglement generation, the proposed photonic process cannot be interpreted in the classical picture nor realized with coherent optical fields. The schematic of a general multi-mode-coupled photonic system is shown in Fig. 3.1a. We start with a photonic ring cavity evanescently coupled to a bus waveguide. A coherent drive is launched into the cavity to initiate the spontaneous nonlinear optical process (such as parametric down-conversion and spontaneous four-wave mixing). Non-degenerate correlated photon pairs can be generated in symmetric signal and idler whispering gallery modes satisfying energy conservation. While a series of optical whispering gallery modes are supported in the photonic cavity, we focus on one signal-idler pair ( $\hat{a}_s$  and  $\hat{a}_i$ ). At the same time, the signal and idler modes are coherently coupled to the ancillary signal and idler modes ( $\hat{b}_s$  and  $\hat{b}_i$ ), respectively. The coherent coupling can be realized by additional pumps in nonlinear optical processes [41], microwave drives in electro-optic devices [40], evanescently coupled photonic resonators [42], bidirectional coherent

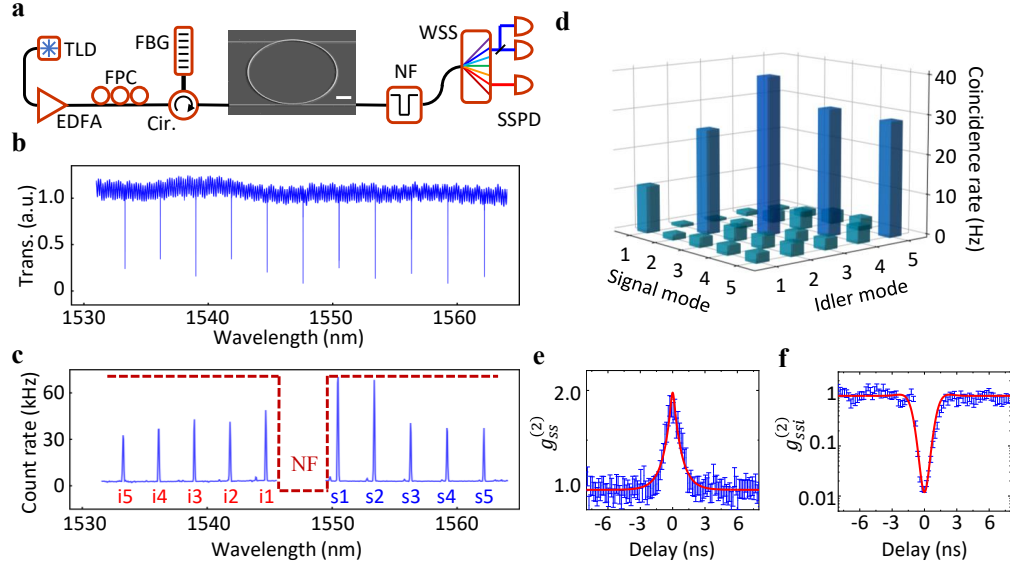


Figure 3.2: **Entangled photon pair generation.** **a.** The measurement setup. TLD, tunable laser diode; EDFA, erbium-doped fiber amplifier; FPC, fiber polarization controller; Cir., circulator; FBG, fiber Bragg grating; NF, notch filter; WSS, wavelength selective switch; SSPD, superconducting single-photon detector. The scale bar in the scanning electron microscope image is  $20 \mu\text{m}$ . **b.** Transmission spectrum of the photonic ring cavity. **c.** Single-photon spectrum. The signal (idler) modes are labeled as s1-s5 (i1-i5). The notch filter (NF) regime is labeled in red. **d.** Coincidence rates measured at all the signal/idler combinations. Strong coincidence is only visible between symmetric signal-idler modes. **e.** Self-correlation function of signal s4 mode with no heralding. The data (blue) is fitted with double-exponential decay (red). **f.** Self-correlation measurement of signal s4 mode with idler i4 mode as heralding.

coupling by back-scattering [43, 44] which is used in this work, etc. We use the following Hamiltonian to describe the coupled multimode photonic system:

$$\hat{\mathcal{H}} = \sum_{k \in (s,i)} \hbar\omega_k (\hat{a}_k^\dagger \hat{a}_k + \hat{b}_k^\dagger \hat{b}_k) + \hbar G (\hat{a}_s^\dagger \hat{a}_i^\dagger + \hat{a}_s \hat{a}_i) + \hbar g_s (\hat{a}_s^\dagger \hat{b}_s + \hat{a}_s \hat{b}_s^\dagger) + \hbar g_i (\hat{a}_i^\dagger \hat{b}_i + \hat{a}_i \hat{b}_i^\dagger). \quad (3.1)$$

Here  $G$  is the splitting-free pump-enhanced coupling rate for the parametric nonlinear process,  $g_s$  ( $g_i$ ) is the coherent coupling strength between the signal (idler) mode and the corresponding ancillary mode, and  $\omega_k$  is the angular frequency for mode  $k$  with  $k \in (s, i)$ . We also assume the signal (idler) mode and the corresponding

ancillary mode have the same resonance frequency  $\omega_s$  ( $\omega_i$ ).

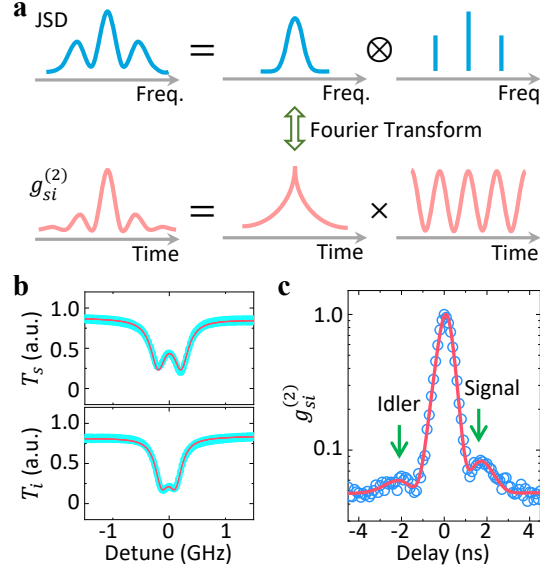


**Figure 3.3: Observation of Mollow triplet with quantum temporal correlations.** **a.** Schematic showing that the signal-idler temporal correlation is the Fourier transform of the joint spectral density. The Mollow triplet is equivalent to the convolution between one Lorentzian shape and three equal-distance delta functions in frequency (blue). In the rotating frame of the central carrier frequency, the Fourier transforms of the Lorentzian shape, and three equal-distance delta functions are double-exponential decay and sinusoidal functions, respectively. Therefore, the temporal correlation is the product of double-exponential decay and sine wave (red). **b.** Linear transmission of signal s1 and idler i1 modes (cyan). Coupling strengths  $g_s \approx 2\pi \times 219$  MHz and  $g_i \approx 2\pi \times 131$  MHz are obtained through the fitting with double Lorentzian shape (red). **c.** Temporal correlation between signal s1 and idler i1 modes (blue) shows two sidebands introduced by signal and idler coherent coupling with ancillary modes, respectively. The theoretical temporal correlation function is shown in red. This proves the Mollow triplet structure in the joint spectral density.

The coherent coupling between the signal (idler) mode and the corresponding ancillary mode leads to the re-normalization of the Hamiltonian, thus the creation of the dressed signal (idler) modes  $\hat{a}_s \pm \hat{b}_s$  ( $\hat{a}_i \pm \hat{b}_i$ ). Photon pair generation can occur with four transition paths with different combinations of the dressed signal and idler modes, shown as the four peaks in the joint spectral density (Fig. 3.1b). If a broadband pump is used, all four transition paths can be efficiently excited.

Therefore, the biphoton spectrum is proportional to the integral of the joint spectral density along the diagonal direction. With equal coupling strengths  $g_s = g_i$ , two transition paths overlap in frequency. Therefore, one central peak with two sidebands shows up in the spectrum, which is the same as the atomic Mollow triplet. If a continuous-wave pump is used, the energy conservation requires that the sum of signal and idler frequencies is constant. Therefore, the transition can only happen along the anti-diagonal direction. With proper dispersion, a triplet structure can also be observed (purple line in Fig. 3.1b, and more cases in Section 3.3.1).

In comparison, we also present the energy diagram of atomic systems resonantly driven with an optical field (Fig. 3.1c). Dressed states are generated due to the coherent coupling between degenerate states, leading to four transition paths for spontaneous photon emission. The fluorescence spectrum is proportional to the integral of transition probability density along the diagonal direction. Therefore, the Mollow triplet with a central peak and two sidebands can be observed (Fig. 3.1d). Clearly, the fluorescence emission in the atomic system shares a similar underlying physics process with parametric photon pair generation in the photonic system. The creation of dressed states and the interplay between different transition paths lead to the generation of triplet spectral structures in both systems.

### 3.2.3 Experimental Results and Discussion

In our experiment, we use integrated ring resonators fabricated from single-crystal aluminum nitride (AlN) on sapphire to demonstrate photonic Mollow triplet (Fig. 3.2a). Entangled photon pairs are generated with spontaneous four-wave mixing by launching a continuous-wave pump into the splitting-free resonance near 1547.60 nm (Fig. 3.2b). With broadband phase matching, photons are generated in multiple modes spectrally symmetric to the pump resonance (Fig. 3.2c). With energy conservation, a strong frequency correlation is only observed between symmetric signal and idler modes (Fig. 3.2d). We further isolate one signal mode and measure the corresponding self-correlation function (Fig. 3.2e). As the idler photon is discarded, the signal photon is in the single-mode thermal state showing bunching



statistics. We obtain  $g_{ss}^{(2)}(0) = 2.01 \pm 0.07$ , which is in agreement with the expected value  $g_{ss}^{(2)}(0) = 2$  for a single-mode thermal state [45]. With the strong frequency correlation, we can further use the corresponding idler photon to herald the presence of the signal photon. As shown in Fig. 3.2f, the heralded self-correlation  $g_{ssi}^{(2)}(0)$  shows non-classical anti-bunching behavior, with a minimum value close to zero. This confirms that single photons are generated from the photonic ring cavity.

The photonic ring cavity supports both clockwise (CW) and counter-clockwise (CCW) whispering gallery modes, corresponding to the original signal-idler and ancillary modes, respectively. The coherent coupling between CW and CCW modes is introduced by the coherent backscattering in the ring cavity [46]. Therefore, entangled photon pairs are generated in the dressed states consisting of CW and CCW modes. Temporal correlation function between signal and idler photons  $g_{si}^{(2)}$  is measured to verify the photonic Mollow triplet. As shown in Fig. 3.3a, Mollow triplet in joint spectral density can be considered as the convolution between a Lorentzian function with three equal-distance delta functions. The temporal correlation  $g_{si}^{(2)}$  is proportional to the Fourier transform of joint spectral density, thus the product of double-exponential decay and sinusoidal function (Section 3.3.1). As a result, sidebands can also be observed in the temporal correlation function (Fig. 3.3a). In special cases with near-zero frequency detuning, the center peak in the frequency domain can be suppressed. However, the temporal correlation still can show sidebands (Section 3.3.1). Therefore, temporal correlation can accurately reflect the coherent coupling condition for signal and idler modes. We first test the first signal-idler pair (s1 and i1 in Fig. 3.2c). From the linear transmission, we can clearly observe the mode splitting for both signal and idler modes, indicating that photonic dressed states are formed with the coherent superposition of CW and CCW modes (Fig. 3.3b). From the mode splitting amplitude, we can estimate the coupling strengths for the signal ( $g_s \approx 2\pi \times 219$  MHz) and idler ( $g_i \approx 2\pi \times 131$  MHz) modes, respectively. The temporal correlation function between signal and idler photons  $g_{si}^{(2)}$  is shown in Fig. 3.3c. In addition to the central peak, two sidebands are clearly observed, proving the Mollow triplet structure in the joint spectral density. We

further notice that the two sidebands are asymmetric in terms of both strength and frequency separation from the central peak. This is caused by the difference in the signal and idler coupling strengths.

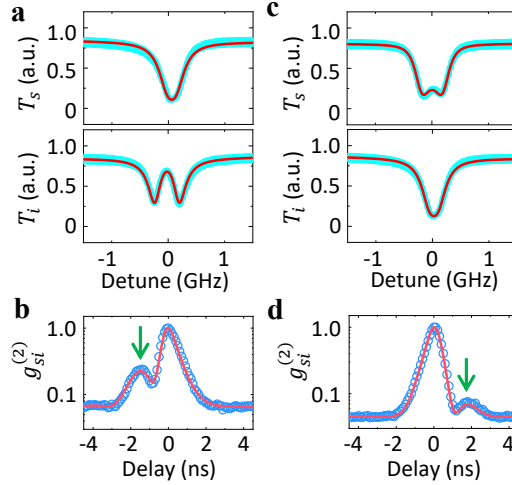


Figure 3.4: **Mollow phenomena with single sideband.** **a.** Transmission spectrum of signal s2 and idler i2 modes (cyan). Only the idler mode shows coherent coupling with  $g_i \approx 2\pi \times 247$  MHz. **b.** Measured temporal correlation between signal s2 and idler i2 modes (blue). Only the left sideband is observed. **c.** Transmission spectrum of signal s3 and idler i3 modes (cyan). Only the signal mode shows coherent coupling with  $g_s \approx 2\pi \times 175$  MHz. **d.** Measured temporal correlation between signal s3 and idler i3 modes (blue). Only the right sideband is observed. Coupling strengths are obtained through fitting linear transmission with double Lorentzian shape (red) in **a** and **c**. The theoretical temporal correlation functions are shown in red in **b** and **d**.

For example, the Mollow triplet with atomic systems is usually symmetric, as the energy splitting is the same for all energy levels [19, 20, 21]. Within our photonic system, we can select the case where the coherent coupling for the signal mode is almost absent, and only strong coupling for the idler mode is present. (s2-i2 pair in Fig. 3.2c). From the linear transmission, we can see that the signal coupling is unresolved, and the idler coupling ( $g_i \approx 2\pi \times 247$  MHz) is larger than the cavity decay rate (Fig. 3.4a). In this case, only the left sideband is observed instead of two symmetric ones, as dressed states are only formed for idler photons (Fig. 3.4b). Similarly, we can also realize strong and near-zero coupling strengths for the signal and

idler modes, respectively (s3-i3 pair in Fig. 3.2c). This configuration is confirmed through linear transmission measurement (Fig. 3.4c). Only the right sideband is observed, as dressed states are only formed for signal photons (Fig. 3.4d). By comparing two coupling configurations of signal-only splitting and idler-only splitting, we effectively conduct a reflection operation in the time domain. As a result, the sideband originally on the left (leading the central peak as in Fig. 3.4b) moves to the right (lagging the central peak as in Fig. 3.4d).

### 3.2.4 Conclusion

We have demonstrated the analogue of the atomic Mollow triplet with all-photon systems using on-chip entanglement generation in dressed photonic modes. This work expands the analogy between atomic and photonic systems into the quantum regime. It will enable the development of novel quantum photonic functions such as quantum spectro-temporal shaping [47, 48, 49, 50, 51] and high-dimensional quantum information processing [52]. Advanced coupling schemes such as dynamic coupling control with nonlinear optics [41], and microwave drives [40] can further unlock the capability to study complex physics processes with photons.

## 3.3 Supplementary Materials

### 3.3.1 Theoretical Description of Quantum Photonic Mollow Triplet

#### Dressed Photonic States

The Hamiltonian of the photonic system without the parametric nonlinear process can be written as

$$\begin{aligned} \hat{\mathcal{H}}_0 = & \hbar\omega_s(\hat{a}_s^\dagger\hat{a}_s + \hat{b}_s^\dagger\hat{b}_s) + \hbar\omega_i(\hat{a}_i^\dagger\hat{a}_i + \hat{b}_i^\dagger\hat{b}_i) \\ & + \hbar g_s(\hat{a}_s^\dagger\hat{b}_s + \hat{a}_s\hat{b}_s^\dagger) + \hbar g_i(\hat{a}_i^\dagger\hat{b}_i + \hat{a}_i\hat{b}_i^\dagger). \end{aligned} \quad (3.2)$$

Here  $\hat{a}_s$  ( $\hat{a}_i$ ) is the signal (idler) annihilation operator,  $\hat{b}_s$  ( $\hat{b}_i$ ) is the annihilation operator for the corresponding ancillary signal (idler) mode,  $\omega_s$  ( $\omega_i$ ) is the angular frequency for the signal (idler) mode,  $g_s$  ( $g_i$ ) is the coupling strength between the

signal (idler) and the corresponding ancillary mode. After re-normalization, the Hamiltonian can be written as

$$\begin{aligned} \hat{\mathcal{H}}_0 = & \hbar(\omega_s + g_s) \left( \frac{\hat{a}_s^\dagger + \hat{b}_s^\dagger}{\sqrt{2}} \right) \left( \frac{\hat{a}_s + \hat{b}_s}{\sqrt{2}} \right) + \hbar(\omega_s - g_s) \left( \frac{\hat{a}_s^\dagger - \hat{b}_s^\dagger}{\sqrt{2}} \right) \left( \frac{\hat{a}_s - \hat{b}_s}{\sqrt{2}} \right) \\ & + \hbar(\omega_i + g_i) \left( \frac{\hat{a}_i^\dagger + \hat{b}_i^\dagger}{\sqrt{2}} \right) \left( \frac{\hat{a}_i + \hat{b}_i}{\sqrt{2}} \right) + \hbar(\omega_i - g_i) \left( \frac{\hat{a}_i^\dagger - \hat{b}_i^\dagger}{\sqrt{2}} \right) \left( \frac{\hat{a}_i - \hat{b}_i}{\sqrt{2}} \right). \end{aligned} \quad (3.3)$$

Dressed modes  $(\hat{a}_s^\dagger \pm \hat{b}_s^\dagger)/\sqrt{2}$  and  $(\hat{a}_i^\dagger \pm \hat{b}_i^\dagger)/\sqrt{2}$  are generated with angular frequencies  $\omega_s \pm g_s$  and  $\omega_i \pm g_i$ , respectively.

### Linear Transmission

The equation of motion for the signal  $\hat{a}_s$  and ancillary signal  $\hat{b}_s$  modes in Eq. (3.2) can be written as

$$\frac{d\hat{a}_s}{dt} = \frac{i}{\hbar} [\hat{\mathcal{H}}_0, \hat{a}_s] - \frac{\gamma^{a_s}}{2} \hat{a}_s + \sqrt{\gamma_i^{a_s}} \hat{a}_s^{(i)} + \sqrt{\gamma_c^{a_s}} \hat{a}_{s,\text{in}}, \quad (3.4)$$

$$\frac{d\hat{b}_s}{dt} = \frac{i}{\hbar} [\hat{\mathcal{H}}_0, \hat{b}_s] - \frac{\gamma^{b_s}}{2} \hat{b}_s + \sqrt{\gamma_i^{b_s}} \hat{b}_s^{(i)} + \sqrt{\gamma_c^{b_s}} \hat{b}_{s,\text{in}}, \quad (3.5)$$

with the coupling decay rate  $\gamma_c^{a_s}$  and  $\gamma_c^{b_s}$ , intrinsic decay rate  $\gamma_i^{a_s}$  and  $\gamma_i^{b_s}$ , and total decay rate  $\gamma^{a_s} = \gamma_i^{a_s} + \gamma_c^{a_s}$  and  $\gamma^{b_s} = \gamma_i^{b_s} + \gamma_c^{b_s}$  for the  $\hat{a}_s$  and  $\hat{b}_s$  modes respectively. The inputs from the intrinsic loss channels are  $\hat{a}_s^{(i)}$  and  $\hat{b}_s^{(i)}$ , and the input modes are  $\hat{a}_{s,\text{in}}$  and  $\hat{b}_{s,\text{in}}$  for the signal and ancillary signal modes, respectively. With Fourier transform, we obtain

$$0 = \left( i\Delta_s - \frac{\gamma^{a_s}}{2} \right) \hat{a}_s(\omega) - ig_s \hat{b}_s(\omega) + \sqrt{\gamma_i^{a_s}} \hat{a}_s^{(i)}(\omega) + \sqrt{\gamma_c^{a_s}} \hat{a}_{s,\text{in}}(\omega), \quad (3.6)$$

$$0 = \left( i\Delta_s - \frac{\gamma^{b_s}}{2} \right) \hat{b}_s(\omega) - ig_s \hat{a}_s(\omega) + \sqrt{\gamma_i^{b_s}} \hat{b}_s^{(i)}(\omega) + \sqrt{\gamma_c^{b_s}} \hat{b}_{s,\text{in}}(\omega). \quad (3.7)$$

The classical equations of motion are obtained through averaging Eq. (3.6) and Eq. (3.7).

$$0 = \left( i\Delta_s - \frac{\gamma^{a_s}}{2} \right) A_s(\omega) - ig_s B_s(\omega) + \sqrt{\gamma_c^{a_s}} A_{s,\text{in}}(\omega) \quad (3.8)$$

$$0 = \left( i\Delta_s - \frac{\gamma^{b_s}}{2} \right) B_s(\omega) - ig_s A_s(\omega), \quad (3.9)$$

where  $A_s = \langle \hat{a}_s \rangle$ ,  $B_s = \langle \hat{b}_s \rangle$ ,  $A_{s,\text{in}} = \langle \hat{a}_{s,\text{in}} \rangle$ , and  $\langle \hat{a}_s^{(i)} \rangle = \langle \hat{b}_s^{(i)} \rangle = \langle \hat{b}_{s,\text{in}} \rangle = 0$ . Therefore, the intra-cavity field amplitudes can be solved as

$$A_s(\omega) = - \left[ \frac{\left( i\Delta_s - \frac{\gamma^{b_s}}{2} \right)}{\left( i\Delta_s - \frac{\gamma^{a_s}}{2} \right) \left( i\Delta_s - \frac{\gamma^{a_s}}{2} \right) + g_s^2} \right] \sqrt{\gamma_c^{a_s}} A_{s,\text{in}}(\omega) \quad (3.10)$$

$$B_s(\omega) = - \left[ \frac{ig_s}{\left( i\Delta_s - \frac{\gamma^{a_s}}{2} \right) \left( i\Delta_s - \frac{\gamma^{a_s}}{2} \right) + g_s^2} \right] \sqrt{\gamma_c^{a_s}} A_{s,\text{in}}(\omega). \quad (3.11)$$

The output field of the signal mode is

$$\begin{aligned} A_{s,\text{out}}(\omega) &= A_{s,\text{in}}(\omega) - \sqrt{\gamma_c^{a_s}} A_s(\omega) \\ &= \left\{ 1 + \gamma_c^{a_s} \left[ \frac{\left( i\Delta_s - \frac{\gamma^{b_s}}{2} \right)}{\left( i\Delta_s - \frac{\gamma^{a_s}}{2} \right) \left( i\Delta_s - \frac{\gamma^{a_s}}{2} \right) + g_s^2} \right] \right\} A_{s,\text{in}}(\omega). \end{aligned} \quad (3.12)$$

The linear transmission is

$$T_s(\Delta_s) = \left| \frac{A_{s,\text{out}}}{A_{s,\text{in}}} \right|^2 = \left| 1 + \gamma_c^{a_s} \left[ \frac{\left( i\Delta_s - \frac{\gamma^{b_s}}{2} \right)}{\left( i\Delta_s - \frac{\gamma^{a_s}}{2} \right) \left( i\Delta_s - \frac{\gamma^{a_s}}{2} \right) + g_s^2} \right] \right|^2 \quad (3.13)$$

In the special case  $\gamma^{a_s} = \gamma^{b_s} = \gamma$ , the linear transmission is reduced to the double-Lorentzian function as

$$T_s(\Delta_s) = \left| \frac{A_{s,\text{out}}}{A_{s,\text{in}}} \right|^2 = \left| 1 + \gamma_c \left[ \frac{1}{\left( i\Delta_s + g_s \right) - \frac{\gamma}{2}} + \frac{1}{\left( i\Delta_s - g_s \right) - \frac{\gamma}{2}} \right] \right|^2 \quad (3.14)$$

with the frequency separation equal to  $2g_s$ , which verifies the formation of dressed states with resonant frequencies  $\omega_s \pm g_s$  in Eq. (3.3). The derivations of linear transmission for idler are identical to the signal.

## Joint Spectral Amplitude

With the Hamiltonian  $\hat{\mathcal{H}}_0$ , the full quantum equations of motion can be written as

$$0 = \left( i\Delta_s - \frac{\gamma^{a_s}}{2} \right) \hat{a}_s(\omega) - ig_s \hat{b}_s(\omega) + \sqrt{\gamma_i^{a_s}} \hat{a}_s^{(i)}(\omega) + \sqrt{\gamma_c^{a_s}} \hat{a}_{s,\text{in}}(\omega), \quad (3.15)$$

$$0 = \left( i\Delta_i - \frac{\gamma^{a_i}}{2} \right) \hat{a}_i(\omega) - ig_i \hat{b}_i(\omega) + \sqrt{\gamma_i^{a_i}} \hat{a}_i^{(i)}(\omega) + \sqrt{\gamma_c^{a_i}} \hat{a}_{i,\text{in}}(\omega) \quad (3.16)$$

$$0 = \left( i\Delta_s - \frac{\gamma^{b_s}}{2} \right) \hat{b}_s(\omega) - ig_s \hat{a}_s(\omega) + \sqrt{\gamma_i^{b_s}} \hat{b}_s^{(i)}(\omega) + \sqrt{\gamma_c^{b_s}} \hat{b}_{s,\text{in}}(\omega) \quad (3.17)$$

$$0 = \left( i\Delta_i - \frac{\gamma^{b_i}}{2} \right) \hat{b}_i(\omega) - ig_i \hat{a}_i(\omega) + \sqrt{\gamma_i^{b_i}} \hat{b}_i^{(i)}(\omega) + \sqrt{\gamma_c^{b_i}} \hat{b}_{i,\text{in}}(\omega). \quad (3.18)$$

The intra-cavity fields are related to the input and output fields by the input-output relation

$$\begin{cases} \hat{a}_{s,\text{out}} = \hat{a}_{s,\text{in}} - \sqrt{\gamma_c^{a_s}} \hat{a}_s & \hat{a}_{i,\text{out}} = \hat{a}_{i,\text{in}} - \sqrt{\gamma_c^{a_i}} \hat{a}_i \\ \hat{a}_s^{(e)} = \hat{a}_s^{(i)} - \sqrt{\gamma_i^{a_s}} \hat{a}_s & \hat{a}_i^{(e)} = \hat{a}_i^{(i)} - \sqrt{\gamma_i^{a_i}} \hat{a}_i \\ \hat{b}_{s,\text{out}} = \hat{b}_{s,\text{in}} - \sqrt{\gamma_c^{b_s}} \hat{b}_s & \hat{b}_{i,\text{out}} = \hat{b}_{i,\text{in}} - \sqrt{\gamma_c^{b_i}} \hat{b}_i \\ \hat{b}_s^{(e)} = \hat{b}_s^{(i)} - \sqrt{\gamma_i^{b_s}} \hat{b}_s & \hat{b}_i^{(e)} = \hat{b}_i^{(i)} - \sqrt{\gamma_i^{b_i}} \hat{b}_i \end{cases} \quad (3.19)$$

Here operators  $\hat{o}_{j,\text{out}}$  and  $\hat{o}_j^{(e)}$  with  $o \in \{a, b\}$  and  $j \in \{s, i\}$  represent the output fields for the bus waveguide and intrinsic loss channel, respectively. Therefore, we can express  $\hat{a}_s$  and  $\hat{a}_i$  with output fields as

$$\hat{a}_s = - \frac{ig_s \left( \sqrt{\gamma_i^{b_s}} \hat{b}_s^{(e)} + \sqrt{\gamma_c^{b_s}} \hat{b}_{s,\text{out}} \right) + \left( i\Delta_s + \frac{\gamma^{b_s}}{2} \right) \left( \sqrt{\gamma_i^{a_s}} \hat{a}_s^{(e)} + \sqrt{\gamma_c^{a_s}} \hat{a}_{s,\text{out}} \right)}{\left( i\Delta_s + \frac{\gamma^{a_s}}{2} \right) \left( i\Delta_s + \frac{\gamma^{b_s}}{2} \right) + |g_s|^2} \quad (3.20)$$

$$\hat{a}_i = - \frac{ig_i \left( \sqrt{\gamma_i^{b_i}} \hat{b}_i^{(e)} + \sqrt{\gamma_c^{b_i}} \hat{b}_{i,\text{out}} \right) + \left( i\Delta_i + \frac{\gamma^{b_i}}{2} \right) \left( \sqrt{\gamma_i^{a_i}} \hat{a}_i^{(e)} + \sqrt{\gamma_c^{a_i}} \hat{a}_{i,\text{out}} \right)}{\left( i\Delta_i + \frac{\gamma^{a_i}}{2} \right) \left( i\Delta_i + \frac{\gamma^{b_i}}{2} \right) + |g_i|^2}. \quad (3.21)$$

The degenerate-pump four-wave mixing interaction Hamiltonian with continuous spectral basis in the cavity is at the scale of

$$\hat{\mathcal{H}}_{\text{int}} = i\hbar\kappa \int \frac{d\omega_p}{2\pi} \iint \frac{d\omega_s}{\sqrt{2\pi}} \frac{d\omega_i}{\sqrt{2\pi}} \hat{a}_s^\dagger(\omega_s) \hat{a}_i^\dagger(\omega_i) \epsilon^2(\omega_p) e^{i(\omega_s + \omega_i - 2\omega_p)t} + h.c., \quad (3.22)$$

with  $\epsilon(\omega_p)$  the intra-cavity pump profile determined by the input pump field and the pump resonance. Here we choose four-wave mixing for demonstration. With parametric down-conversion, the pump frequency and profile should be modified accordingly [6]. Photon pairs will be generated in the cavity with the bi-photon joint quantum state as

$$|\psi\rangle = e^{-\frac{i}{\hbar} \int_0^T dt \hat{\mathcal{H}}_{\text{int}}} |0, 0\rangle \approx \left[ 1 + \frac{\kappa}{2} \iint \frac{d\omega_s}{\sqrt{2\pi}} \frac{d\omega_i}{\sqrt{2\pi}} \hat{a}_s^\dagger(\omega_s) \hat{a}_i^\dagger(\omega_i) \epsilon^2\left(\frac{\omega_s + \omega_i}{2}\right) \right] |0, 0\rangle \quad (3.23)$$

By plugging Eq. (3.20) and Eq. (3.21) into Eq. (3.23) and only keeping measurable ports  $\hat{a}_{s,\text{out}}$  and  $\hat{a}_{i,\text{out}}$  terms, we obtain the output bi-photon state as

$$|\psi\rangle_{\text{out}} \propto \iint d\omega_s d\omega_i \phi(\omega_s, \omega_i) \hat{a}_{s,\text{out}}^\dagger(\omega_s) \hat{a}_{i,\text{out}}^\dagger(\omega_i) |0, 0\rangle \quad (3.24)$$

with the joint spectral amplitude  $\phi(\omega_s, \omega_i) \propto$

$$\frac{\left(-i\Delta_s + \frac{\gamma^{b_s}}{2}\right) \left(-i\Delta_i + \frac{\gamma^{b_i}}{2}\right) \epsilon^2\left(\frac{\omega_s + \omega_i}{2}\right)}{\left[\left(-i\Delta_s + \frac{\gamma^{a_s}}{2}\right) \left(-i\Delta_s + \frac{\gamma^{b_s}}{2}\right) + |g_s|^2\right] \left[\left(-i\Delta_i + \frac{\gamma^{a_i}}{2}\right) \left(-i\Delta_i + \frac{\gamma^{b_i}}{2}\right) + |g_i|^2\right]}. \quad (3.25)$$

The temporal correlation function can be further calculated from the joint spectral amplitude by

$$g_{si}^{(2)}(t_s, t_i) = \left| \iint \frac{d\omega_s}{\sqrt{2\pi}} \frac{d\omega_i}{\sqrt{2\pi}} \phi(\omega_s, \omega_i) e^{-i(\omega_s t_s + \omega_i t_i)} \right|^2 \quad (3.26)$$

### 3.3.2 Effect of Pump Frequency Detuning

In our experiment, a continuous-wave pump is used as the pump for the parametric nonlinear process. Therefore, the transition can only happen along the anti-diagonal direction. The detune between the pump frequency and the signal-idler center frequency is determined by the pump, corresponding to one anti-diagonal slice in the joint spectral density. As the pump field is always in resonance with the pump photonic mode, the frequency detune is effectively determined by the dispersion of the photonic ring cavity. With zero dispersion  $\omega_p = (\omega_s + \omega_i)/2$ , the anti-diagonal slice passes through the center of the 2D transition probability plot, and the transition

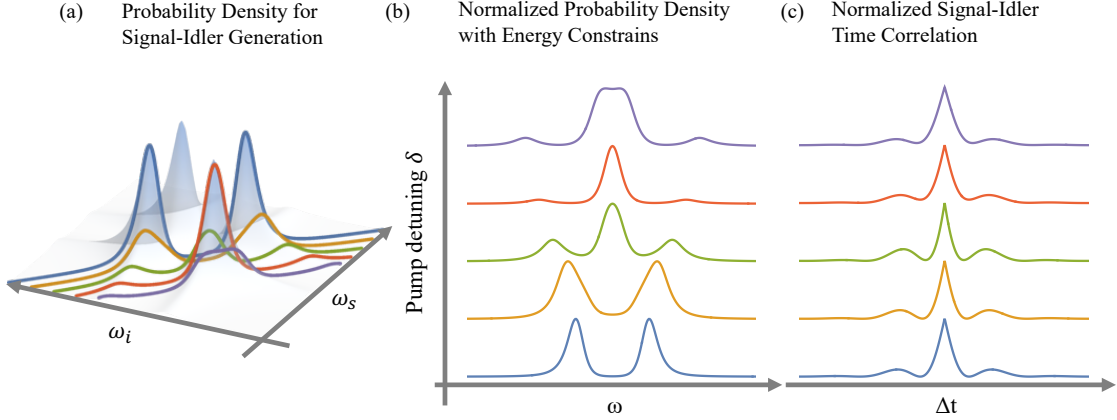


Figure 3.5: **Intepretation to the detuned photonic Mollow triplet.** **a**, The joint spectrum amplitude with different pump detuning (caused by dispersion) of the photonic cavity. **b**, Biphoton spectrums and **c**, temporal correlations with different detuning  $\delta/g=0$  (blue),  $0.75$  (orange),  $1.5$  (green),  $2.25$  (red), and  $3.0$  (purple). The simulation presets  $\delta/\gamma=1.2$ .

happens mainly between  $(\hat{a}_s^\dagger + \hat{b}_s^\dagger)/\sqrt{2}$  and  $(\hat{a}_i^\dagger - \hat{b}_i^\dagger)/\sqrt{2}$ , as well as  $(\hat{a}_s^\dagger - \hat{b}_s^\dagger)/\sqrt{2}$  and  $(\hat{a}_i^\dagger + \hat{b}_i^\dagger)/\sqrt{2}$ . As a result, the output bi-photon joint power spectrum shows two symmetric peaks (blue curves in Fig. S1). With large normal dispersion  $\omega_p < (\omega_s + \omega_i)/2$ , the transition between  $(\hat{a}_s^\dagger - \hat{b}_s^\dagger)/\sqrt{2}$  and  $(\hat{a}_i^\dagger - \hat{b}_i^\dagger)/\sqrt{2}$  will dominate with minor amplitude for transitions mainly between  $(\hat{a}_s^\dagger + \hat{b}_s^\dagger)/\sqrt{2}$  and  $(\hat{a}_i^\dagger - \hat{b}_i^\dagger)/\sqrt{2}$  as well as  $(\hat{a}_s^\dagger - \hat{b}_s^\dagger)/\sqrt{2}$  and  $(\hat{a}_i^\dagger + \hat{b}_i^\dagger)/\sqrt{2}$ . Therefore, the output bi-photon spectrum shows a triplet structure with one central peak and two sidebands (green curves in Fig. S1). With large anomalous dispersion  $\omega_p > (\omega_s + \omega_i)/2$ , the transition between  $(\hat{a}_s^\dagger + \hat{b}_s^\dagger)/\sqrt{2}$  and  $(\hat{a}_i^\dagger + \hat{b}_i^\dagger)/\sqrt{2}$  will dominate with lesser amplitude for transitions between  $(\hat{a}_s^\dagger + \hat{b}_s^\dagger)/\sqrt{2}$  and  $(\hat{a}_i^\dagger - \hat{b}_i^\dagger)/\sqrt{2}$  as well as  $(\hat{a}_s^\dagger - \hat{b}_s^\dagger)/\sqrt{2}$  and  $(\hat{a}_i^\dagger + \hat{b}_i^\dagger)/\sqrt{2}$ . The output bi-photon spectrum will be similar to the normal dispersion case. By definition, the dispersion will introduce a detuning term  $\delta = \Delta_s - \Delta_i$ .

### 3.3.3 Data for All Signal-Idler Pairs

Here we present the data for all signal-idler pairs, including the linear transmission for signal and idler modes, self-correlation of signal photons without heralding,



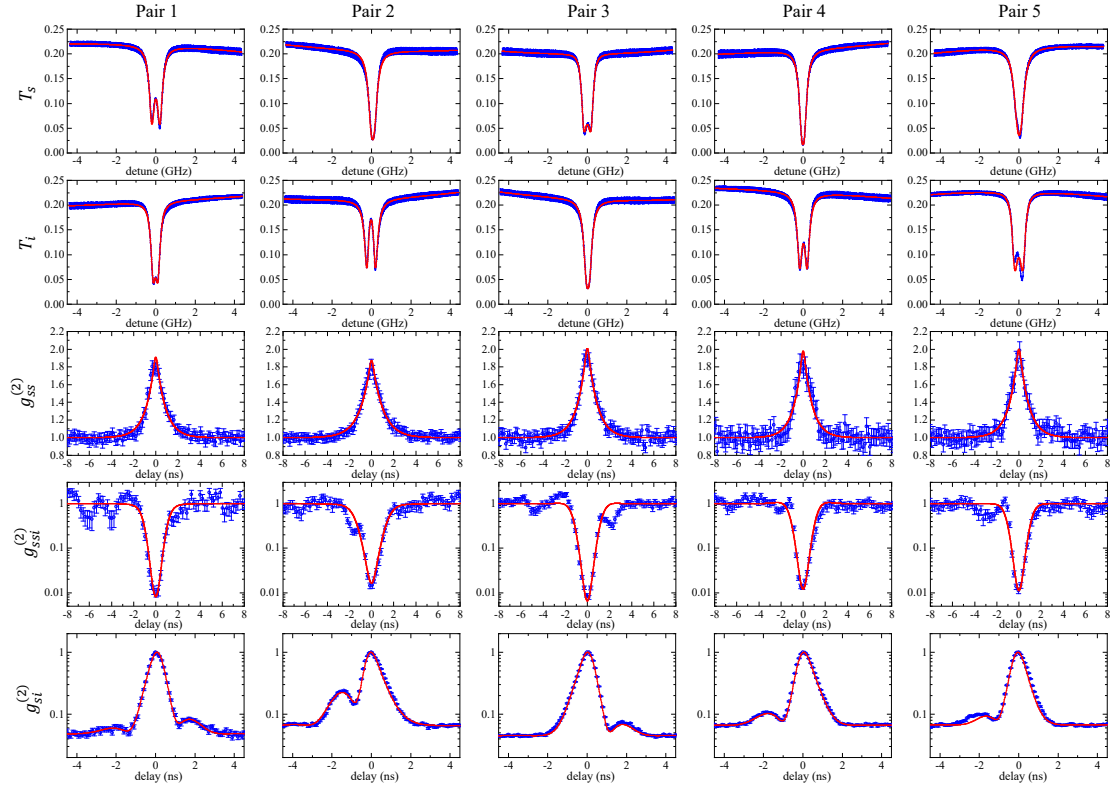


Figure 3.6: **Additional data.** First row, signal linear transmission  $T_s$ ; second row, idler linear transmission  $T_i$ ; third row, self-correlation of signal photons without heralding  $g_{ss}^{(2)}$ ; fourth row, self-correlation of signal photons heralded by idler photons  $g_{ssi}^{(2)}$ ; fifth row, the temporal correlation between signal and idler photons  $g_{si}^{(2)}$ . Data and fitting are shown in blue and red, respectively.

	Pair 1	Pair 2	Pair 3	Pair 4	Pair 5
$g_s$	210 MHz	$\approx 0$ MHz	221 MHz	82 MHz	99 MHz
$g_i$	154 MHz	217 MHz	91 MHz	188 MHz	232 MHz
$g_{ss}^{(2)}(0)$	1.91	1.87	2.01	2.01	2.00
$g_{ssi}^{(2)}(0)$	0.006	0.013	0.005	0.009	0.009

Table 3.1: **Additional parameters.** First row,  $g_s$  fitted from linear transmission  $T_s$ ; second row,  $g_i$  fitted from idler linear transmission  $T_i$ ; third row, fitted peak value of signal self-correlation without heralding; fourth row, fitted dip value of signal self-correlation heralded by idler photons.

self-correlation of signal photons heralded by idler photons, and temporal correlation between signal and idler photons (Fig. 3.6). We can first see different mode-splitting configurations and strengths for different signal-idler pairs. By fitting linear transmission with Eq. (3.13), we can obtain  $g_s$  and  $g_i$  values. We further fit the self-correlation of signal photons without heralding using double-exponential decay functions and obtain peak values close to 2, showing that the effective mode number (jitter-defined resolvable modes) is close to 1 [53]. With the self-correlation of signal photons heralded by idler photons, we obtain minimum values close to 0, which means the experiment is in the single photon regime. All values for fitted lines are summarized in Table 3.1.

## CHAPTER 4

Reconfigurable Kerr Nonlinearity Enabled by Cascaded Second-Order Nonlinear Processes<sup>†</sup>**4.1 Abstract**

Nanophotonic cavities with Kerr nonlinearities are versatile platforms both to explore fundamental physics and to develop practical photonic technologies [54, 18, 52]. This is possible because nanoscale structures allow precise dispersion control and provide significant field enhancement to improve excitation conditions. To improve the functionality and performance of photonic devices even further, direct control of the Kerr nonlinearity would be desirable. Here, we report the *in situ* control of integrated Kerr nonlinearity through its interplay with the nonlinear process of cascaded Pockels cells [55, 56, 57, 58, 59, 60]. We observe a Fano resonance in the nonlinear spectrum rather than in the linear transmission [61], confirming the quantum interference between competing optical nonlinear pathways. The Kerr nonlinearity is tuned over a dynamic range of 10 dB without modifying the photonic structure. We also demonstrate the suppression of the intrinsic material nonlinearity, and we use the tuneable nonlinearity to control the spectral brightness and coincidence-to-accidental ratio of single-photon generation.

**4.2 Main Article****4.2.1 Introduction**

The dynamic control of optical properties plays an indispensable role in a great number of fields. The linear optical properties such as refractive index and absorption can be modified in nanophotonic circuits using a wide variety of phenom-

---

<sup>†</sup>This chapter has been published previously as [2]

ena including thermal [62], electrical [63, 64], mechanical [65], and free-carrier effects [66]. It allows the modulation of optical fields with broad applications ranging from laser systems to optical communications. Recently, such linear control has also been used to demonstrate functions including the reconfigurable generation of topological photonic states [67, 68], the photonic acceleration of machine learning algorithms [69, 70], and the realization of universal photonic quantum gates [71, 72].

Similarly, the control of optical nonlinear properties will lead to significant scientific and technological advances. The enhancement of nonlinearity can obviously benefit broad photonic technologies, including all-optical information processing [73, 74, 75], quantum computing [76, 77, 78, 79], temporal-frequency conversion [80, 47, 81], etc. The full coherent control of nonlinearity beyond simple enhancement can further expand the scope of photonic technology. The nonlinearity suppression is critical to fundamentally improve the sensitivity of optical sensors [82, 83] and the capacity of optical communications [84, 85]. The phase inversion of the nonlinear interaction can enable the generation of unconventional soliton states [86, 87]. Currently, nanophotonic Kerr-type nonlinear processes are only controlled indirectly using intra-cavity photon number and dispersion. Therefore, the achievable nonlinearity and functionality are limited to the material's intrinsic properties at specific wavelengths. Cascaded second-order nonlinearity has been demonstrated as an efficient method to increase the effective third-order strength [88, 89, 90, 91, 92, 93, 94, 95]. The simultaneous implementation and coherent control of the cascaded second-order and third-order nonlinearities can further expand the capability of photonic devices [55, 56, 57, 58, 96, 59, 60]. Such advanced functions can only be realized by integrated photonic platforms with second-order nonlinearity [97, 98].

In this Letter, the complete amplitude and phase control of effective Kerr nonlinearity can be realized in a nanophotonic cavity by designing the interference with cascaded Pockels processes. Besides the enhancement of Kerr nonlinearity, we also observe unique phenomena including the nonlinearity suppression and Fano resonances in the nonlinear regime. The effective Kerr nonlinearity is highly tunable

over 10 dB dynamic range with fixed photonic structures. We further validate the control of Kerr nonlinearity in both classical and quantum regime through nonlinear frequency conversion and single-photon generation.

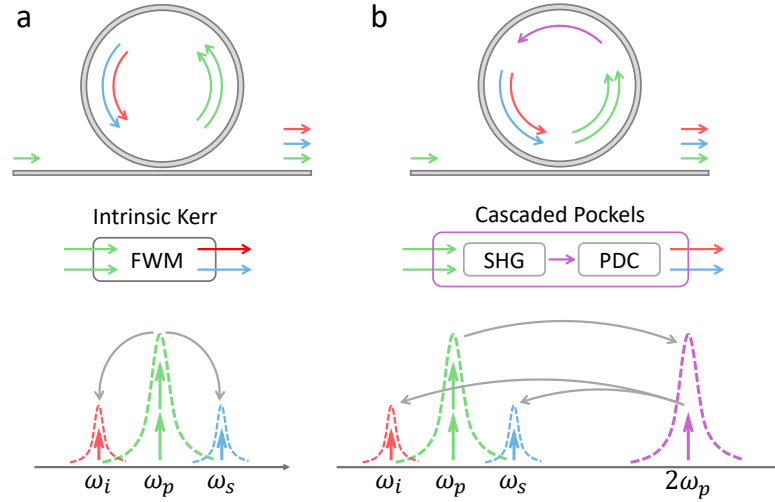


Figure 4.1: **Effective Kerr nonlinearity with cascaded Pockels process.** **a**, Intrinsic Kerr process. Two pump photons are annihilated to generate one signal and one idler photon **b**, Cascaded Pockels process. Two pump photons are annihilated to generate one second-harmonic photon, which drives the parametric down-conversion to generate one signal and one idler photon.

#### 4.2.2 Conceptual Model

In the degenerate configuration of Kerr nonlinear processes, two pump photons are annihilated to generate one signal and one idler photon, or vice versa (Fig. 4.1a). The nonlinearity is fixed by the material property and photonic structure. To modify the Kerr nonlinearity, we design a cascaded Pockels nonlinear process shown in Fig. 4.1b. In this process, two pump photons first combine to generate one second-harmonic photon. Then the second-harmonic photon drives the parametric down-conversion process in the same photonic cavity to generate one signal and one idler photon. The effective interaction Hamiltonian for the cascaded Pockels nonlinear process is

$$H_I = -\frac{1}{2}\hbar(g_c\hat{b}_p^{\dagger 2}\hat{b}_s\hat{b}_i + g_c^*\hat{b}_p^2\hat{b}_s^\dagger\hat{b}_i^\dagger), \quad (4.1)$$

with  $\hat{b}_p$ ,  $\hat{b}_s$ , and  $\hat{b}_i$  the annihilation operators of the pump, signal, and idler modes, respectively (Section 4.3.1). The effective cascaded Pockels nonlinear strength  $g_c$  at a single-photon level is defined as

$$g_c = \frac{-i|g_2|^2}{i\Delta + \gamma/2}, \quad (4.2)$$

with  $g_2$  the Pockels nonlinear strength,  $\Delta$  the frequency detune between twice the pump frequency and the second-harmonic mode, and  $\gamma$  the decay rate of the second-harmonic mode. This interaction Hamiltonian has the same form as intrinsic Kerr nonlinear processes. With highly efficient Pockels nonlinear processes, the effective Kerr nonlinearity can be significantly enhanced.

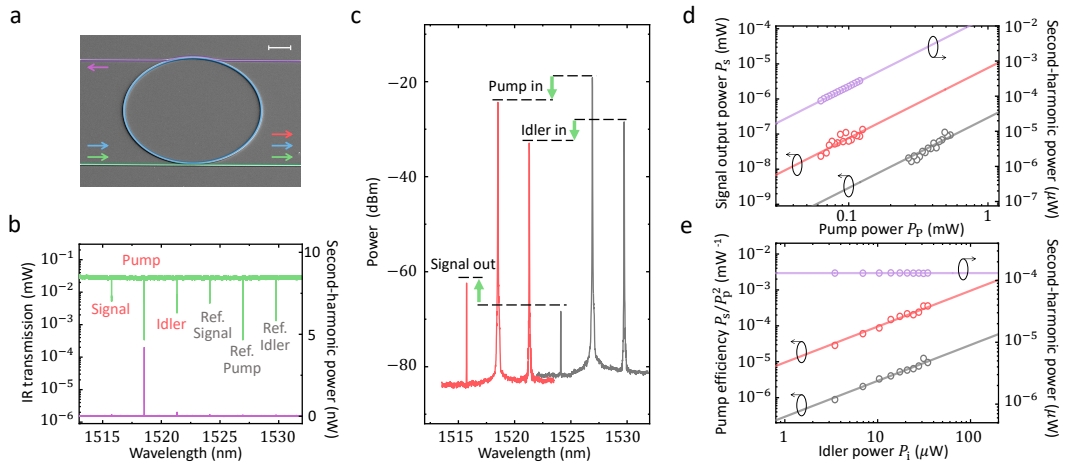


Figure 4.2: **Enhancement of Kerr nonlinearity.** **a**, Scanning electron microscope image of the fabricated aluminum nitride device with the ring cavity (blue), the bus waveguide for the second-harmonic field (purple), and the bus waveguide for the pump, idler, and signal fields (green). Scale bar 20  $\mu\text{m}$ . **b**, Pump transmission (green) and second-harmonic (purple) spectrum. Two sets of modes for FWM, with (red) and without (gray) Pockels phase-matching, are labeled. **c**, The output optical spectrum of the stimulated FWM. **d**, The output signal (red and gray) and second-harmonic power (purple) with different pump power. **e**, The pump efficiency (red and gray) and second-harmonic power (purple) with different idler input power. Results in **c**, **d**, and **e** using the reference mode set and the mode set with Pockels phase-matching are presented in red and gray, respectively. Experimental data (circles) are fitted with the theoretical model (solid lines).

To implement the cascaded Pockels nonlinear process, we use a nanophotonic

ring cavity made of aluminum nitride (Fig. 4.2a). The phase-matching condition for the Pockels nonlinear process is satisfied using a high-order transverse-magnetic (TM) second-harmonic mode and a fundamental TM pump mode (Section 4.3.2). Strong second-harmonic generation is observed with pump wavelength near 1518 nm (Fig. 4.2b). The second-harmonic generation efficiency is measured as  $\eta \approx 1800\%/W$ , leading to the estimated Pockels nonlinear strength  $g_2 \approx 2\pi \times 81$  kHz (Section 4.3.2). With the small decay rate of the second-harmonic mode ( $\gamma \approx 2\pi \times 4.5$  GHz), we can expect the enhanced Kerr nonlinearity around  $|g_c| \approx 2\pi \times 3$  Hz at zero frequency detune, which is six-fold higher than the intrinsic value ( $g_3 \approx 2\pi \times 0.5$  Hz).

The enhancement of the Kerr nonlinearity is first verified with stimulated four-wave mixing (FWM) for frequency conversion in the classical domain. With a strong pump ( $P_p$ ), we measure the conversion from the idler input ( $P_i$ ) to the signal output ( $P_s$ ). We use two sets of modes from the same nanophotonic cavity to measure the intrinsic and enhanced Kerr nonlinearity respectively. The pump mode of the reference set is not phase-matched to the Pockels nonlinear process. Therefore, only the intrinsic Kerr nonlinearity contributes to the nonlinear frequency conversion. The pump mode of the other set is phase-matched to the Pockels nonlinear process. As a result, the enhanced Kerr nonlinearity dominates the nonlinear frequency conversion. The two sets of modes share similar quality factors and coupling conditions. Consequently, the influence of different cavity-enhancement factors and extraction efficiencies can be eliminated (Section 4.3.2). The generation of the signal field is observed from the output optical spectrum with both mode sets (Fig. 4.2c). Comparing the two-mode sets, the signal output of the phase-matched set is significantly higher than the reference set, even though the smaller pump and idler inputs are used. To calibrate the enhancement factor, we fix the input idler power ( $P_i$ ) and vary the input pump power ( $P_p$ ). To achieve the same signal output ( $P_s$ ), the cascaded Pockels nonlinear process uses 7.5 dB less pump power than the intrinsic Kerr nonlinearity (Fig. 4.2d). This agrees well with the difference between the enhanced and intrinsic Kerr nonlinearity ( $|g_c/g_3| \approx 6$ ). The critical role of the Pockels nonlin-

ear process is further confirmed by the increased second-harmonic generation with respect to the pump power (Fig. 4.2d). The same conclusion is obtained from the measurement with different input idler power ( $P_i$ ). With the same pump power, the cascaded Pockels process can generate approximately 15 dB stronger signal output. The second-harmonic generation remains constant during the process, which confirms that the second-harmonic field is generated from the pump.

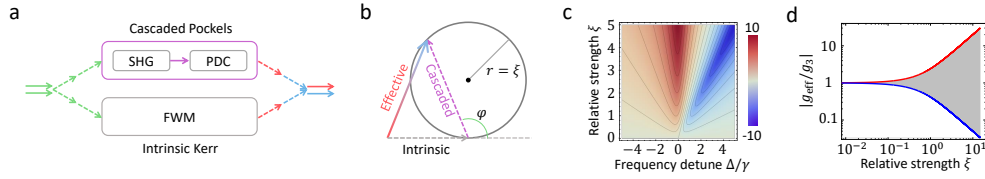


Figure 4.3: **Quantum interference between nonlinear processes.** **a**, Schematic for the quantum interference between intrinsic Kerr and cascaded Pockels process. **b**, Vector diagram showing the coherent interaction between the intrinsic Kerr and cascaded Pockels process. Phase  $\varphi$  can be controlled by the frequency detune  $\Delta$ . Intrinsic Kerr nonlinearity is normalized to 1, and the tuning range of the effective Kerr nonlinearity is bounded to the circle with radius  $\xi$ . **c**, Calculated effective Kerr nonlinearity  $|g_{\text{eff}}/g_3|$  in logarithm scale. **d**, Calculated maximum and minimum effective Kerr nonlinearity. The shaded area indicates the accessible range of the effective Kerr nonlinearity.

The coherent interaction between multiple nonlinear processes can be used to tune the overall nonlinear response. This enables complete control over the amplitude and phase of the effective Kerr nonlinearity. Taking both the intrinsic Kerr strength  $g_3$  and cascaded Pockels nonlinear rate  $g_c$  into account (Fig. 4.3a), the effective Kerr nonlinearity can be written as

$$g_{\text{eff}} = g_3 + g_c = g_3 - \frac{i|g_2|^2}{i\Delta + \gamma/2} \quad (4.3)$$

The relative phase  $\varphi$  between the two nonlinear processes can be controlled by the frequency detune  $\Delta$  (Fig. 4.3b). Both constructive and destructive interference can be realized, leading to the enhancement and suppression of the effective Kerr nonlinearity, respectively (Fig. 4.3c). Here, we define

$$\xi = |g_2|^2/(g_3\gamma), \quad (4.4)$$



so that  $2\xi$  stands for the relative strength between the two nonlinear processes at zero frequency detune. The maximum and minimum effective nonlinear strength  $|g_{\max/\min}| = g_3 \left( \frac{\sqrt{1+\xi^2 \pm \xi}}{\sqrt{1+\xi^2 \mp \xi}} \right)^{1/2}$  can be obtained at frequency detunes  $\Delta = \frac{\gamma}{2}(\xi \mp \sqrt{1+\xi^2})$ . Therefore, a larger tuning dynamic range can be achieved with more efficient Pockels nonlinear processes (Fig. 4.3d).

### 4.2.3 Experiments

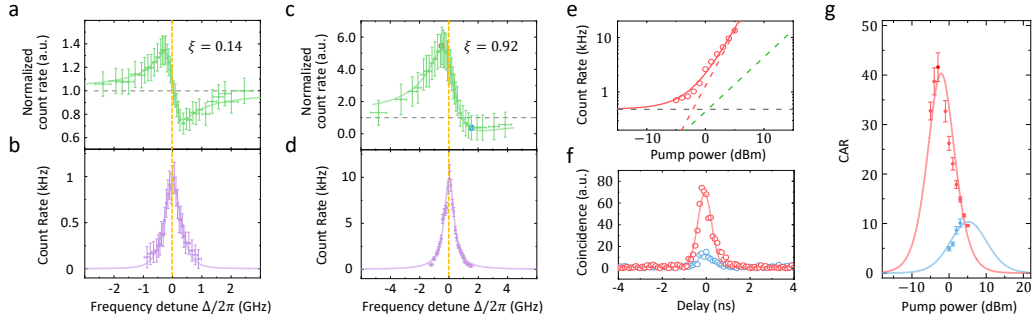


Figure 4.4: **Continuous tuning of Kerr nonlinear strength in the quantum regime.** **a, c**, Single-photon generation rate from spontaneous FWM using effective Kerr nonlinearity with  $\xi = 0.14$  and  $\xi = 0.92$  respectively. The data is normalized to the count rate with the intrinsic Kerr nonlinearity (gray dashed line). **b, d**, Single-photon generation rate from spontaneous parametric down-conversion with  $\xi = 0.14$  and  $\xi = 0.92$  respectively. **e**, Single-photon generation rate (red circle) with different pump power. Calculated background dark count (black dashed), pump-induced noise (green dashed), signal photon rate (red dashed), and total photon rate (red solid) are plotted. All photon counting data are measured from signal resonances. **f**, Signal-idler coincidence count with frequency detune  $\Delta = -2\pi \times 0.7$  GHz (red point in **c**) and  $\Delta = 2\pi \times 1.5$  GHz (blue point in **c**). The pump power is 1 mW. The accidental coincidence outside the coherent window is normalized to 1. **g**, CARs under different pump power with frequency detune  $\Delta = -2\pi \times 0.7$  GHz (red) and  $\Delta = 2\pi \times 1.5$  GHz (blue). Points: measured CARs from signal-idler coincidence. Lines: calculated CARs from the calibrated signal, idler, and noise photon rates.

To verify the quantum interference between the cascaded Pockels and the intrinsic Kerr nonlinear processes, we perform single-photon generation with spontaneous FWM. The frequency detunes  $\Delta$  is precisely controlled through the device temperature (Section 4.3.2). The pump light is tuned in resonance with the pump mode

to ensure that the intra-cavity pump photon number remains constant. The single-photon generation rate of the signal channel (proportional to  $|g_{\text{eff}}|^2$ ) is recorded to infer the effective Kerr nonlinearity. We use two different Pockels nonlinear strengths corresponding to  $\xi = 0.14$  and  $\xi = 0.92$ , respectively by selecting two different phase-matching modes (Section 4.3.2). The single-photon count rate shows Fano lineshape in both cases (Fig. 4.4a and c), indicating the coherent interaction between two competing optical nonlinear processes. A larger tuning dynamic range of the Kerr nonlinearity is achieved with the stronger Pockels nonlinear strength ( $\pm 0.6$  dB with  $\xi = 0.14$  vs.  $\pm 3.6$  dB with  $\xi = 0.92$ ), which matches our theoretical model (Fig. 4.3c). As a reference, we also measure the single-photon generation rate of the same signal channel with parametric down-conversion by pumping a visible laser into the cavity under different frequency detune (Fig. 4.4b and d), which shows Lorentzian lineshape. This confirms the quantum interference between the broad-band intrinsic Kerr process and the narrow-band cascaded Pockels nonlinear process. It is noteworthy that Fano resonances in our experiment can only be observed with a nonlinear spectrum, as the interference happens between nonlinear processes. This is in contrast to Fano resonances introduced by linear coupling between resonators, where linear transmission is sufficient to observe the asymmetric lineshape [61].

Finally, we demonstrate the control of the coincidence-to-accidental ratio (CAR) of the single-photon generation by changing the effective Kerr nonlinearity. CAR is a critical parameter to characterize the quality of single photon sources. In the low pump regime, background noise, and leaking pump dominate the total photon count. Therefore, CAR can be improved by increasing the pump power. In the high pump regime, multi-photon generation becomes the major noise source. As a result, CAR drops with increased pump power. We first set the frequency detuning  $\Delta = 2\pi \times 1.5$  GHz with  $\xi = 0.92$  to achieve the maximum nonlinearity suppression (blue point in Fig. 4.4c). We measure the cross-correlation between signal and idler photons ( $g^{(2)}$ ) to extract the dependence of CAR on the pump power (Fig. 4.4f and 4.4g). The maximum CAR of  $9 \pm 1$  is achieved using 3 dBm pump power. Next, we

set the frequency detuning  $\Delta = -2\pi \times 0.7$  GHz to realize the maximum nonlinearity enhancement (red points in Fig. 4.4c). The maximum achievable CAR is  $47 \pm 2$  with -2 dBm pump power, corresponding to more than five-fold improvement. We also calibrated photon rates of the background noise, pump-induced noise, and parametric photon pairs (Fig. 4.4e) to directly calculate CAR, which agrees with the result obtained from the coincidence measurement (Fig. 4.4f) (Section 4.3.3).

#### 4.2.4 Discussion

We have demonstrated the quantum-level coherent interaction between intrinsic Kerr and cascaded Pockels processes, leading to the *in situ* control of effective Kerr nonlinearity. This scheme can be readily implemented with other integrated photonic platforms with second-order nonlinearity [99, 100, 98]. In particular, the recent development of thin-film lithium niobate photonic devices can significantly increase the strength of the cascaded Pockels process. With the large Pockels coefficient (30 pm/V) and small visible cavity loss ( $\gamma < 2\pi \times 40$  MHz) [101], the effective Kerr nonlinearity can reach megahertz level with similar device sizes. Given that lithium niobate photonic cavities can reach linewidth below 10 MHz with telecom wavelengths [98, 102], our scheme could lead to the demonstration of single-photon strong coupling regime with Kerr nonlinearity, enabling the deterministic quantum logic operations with all-photonic systems [77, 78, 79]. While the enhancement of Kerr nonlinearity can directly find broad applications, it is also worth noting that functionalities, including the suppression and phase tuning of Kerr nonlinearity, could also open unique prospects for photonic technologies, such as eliminating nonlinear noise and improving the dynamic range of optical sensing and communication systems.

#### 4.2.5 Methods

*Device fabrication.* Devices are fabricated from 1- $\mu\text{m}$  AlN grown on sapphire substrates by MOCVD. FOx-16 resist is used for patterning photonic circuits with

electron-beam lithography. After development with TMAH, plasma etching with  $\text{Cl}_2/\text{BCl}_3/\text{Ar}$  is used to transfer the pattern to the AlN layer. Finally,  $\text{SiO}_2$  cladding is deposited by plasma-enhanced chemical vapor deposition (PECVD).

*CAR measurement.* When calculating CAR, the coincidence count is averaged within the coincidence peak ( $\pm 1$  ns) at zero delay. The accidental count is estimated by averaging the coincidence count with a large time delay outside the peak.

### 4.3 Supplementary Materials

#### 4.3.1 Theoretical Model of the Effective Kerr Nonlinearity with Cascaded Pockels Processes

The Hamiltonian describing the photonic device with both Pockels and Kerr nonlinear processes can be written as

$$H_{\text{sys}} = H_0 + H_1 + H_2 + H_3, \quad (4.5)$$

$$H_0 = \hbar\omega_p \hat{b}^\dagger \hat{b} + \hbar\omega_0 \hat{a}^\dagger \hat{a} + \hbar\omega_+ \hat{b}_+^\dagger \hat{b}_+ + \hbar\omega_- \hat{b}_-^\dagger \hat{b}_-, \quad (4.6)$$

$$H_1 = \frac{\hbar}{2} (g_2 \hat{a}^\dagger \hat{b}^2 + g_2^* \hat{a} \hat{b}^{\dagger 2}), \quad (4.7)$$

$$H_2 = \hbar (g_2 \hat{a}^\dagger \hat{b}_+ \hat{b}_- + g_2^* \hat{a} \hat{b}_+^\dagger \hat{b}_-^\dagger), \quad (4.8)$$

$$H_3 = -\frac{\hbar}{2} (g_3 \hat{b}^{\dagger 2} \hat{b}_+ \hat{b}_- + g_3^* \hat{b}^2 \hat{b}_+^\dagger \hat{b}_-^\dagger), \quad (4.9)$$

with  $a$ ,  $b$ ,  $b_+$  and  $b_-$  representing the second-harmonic field, the pump field, the signal field, and the idler field, respectively.  $H_0$  describes the free evolution of the cavity.  $H_1$  and  $H_2$  describe the Pockels process between the second-harmonic and the pump modes, as well as among the second-harmonic, signal, and idler modes.  $H_3$  describes the Kerr interaction among the pump, signal, and idler modes. The minus sign is used to match the convention of self-phase modulation [103]. The positive nonlinear strength for the Pockels and Kerr processes can be written as

$$g_2 = \sqrt{\frac{\hbar\omega_0\omega_p^2}{2\epsilon_0 V_a V_b^2}} \int_V dr^3 u_a^*(\vec{r}) \cdot \chi^{(2)} : u_b(\vec{r})^2 \quad (4.10)$$

$$g_3 = \frac{3}{2} \frac{\hbar\omega_p^2}{\epsilon_0 V_b^2} \int_V dr^3 u_b^{*2}(\vec{r}) : -\chi^{(3)} : u_b(\vec{r})^2 \quad (4.11)$$

with  $u_a(\vec{r})$  and  $u_b(\vec{r})$  the transverse mode profile of the second-harmonic and pump fields, respectively. The mode volumes are defined as  $V_a = 2\pi R n_a \iint_{\sigma} dr^2 |u_a(\vec{r})|^2$  and  $V_b = 2\pi R n_b \iint_{\sigma} dr^2 |u_b(\vec{r})|^2$ , with  $R$  the ring radius,  $n_a$  and  $n_b$  the refractive index for the second-harmonic and pump modes, and  $\sigma$  the cross-section. Here we assume that the signal and idler modes share the same transverse mode profile with the pump mode. While we do not include the interaction Hamiltonian for self-phase and cross-phase modulation, the corresponding frequency shift can be taken into account by re-defining the cavity resonance frequencies. Then the equations of motion can be written as

$$\dot{\hat{a}} = (-i\omega_0 - \frac{\gamma}{2})\hat{a} - ig_2(\frac{1}{2}\hat{b}^2 + \hat{b}_+\hat{b}_-) + \sqrt{\gamma_c}\hat{a}_{\text{in}} + \sqrt{\gamma_i}\hat{a}^{(i)} \quad (4.12)$$

$$\dot{\hat{b}} = (-i\omega_p - \frac{\kappa}{2})\hat{b} - i(g_2\hat{a} - g_3\hat{b}_+\hat{b}_-)\hat{b}^\dagger + \sqrt{\kappa_c}\hat{b}_{\text{in}} + \sqrt{\kappa_i}\hat{b}^{(i)} \quad (4.13)$$

$$\dot{\hat{b}}_+ = (-i\omega_+ - \frac{\kappa_+}{2})\hat{b}_+ - i(g_2^*\hat{a} - \frac{1}{2}g_3^*\hat{b}^2)\hat{b}_-^\dagger + \sqrt{\kappa_{c,+}}\hat{b}_{+, \text{in}} + \sqrt{\kappa_{i,+}}\hat{b}_+^{(i)} \quad (4.14)$$

$$\dot{\hat{b}}_- = (-i\omega_- - \frac{\kappa_-}{2})\hat{b}_- - i(g_2^*\hat{a} - \frac{1}{2}g_3^*\hat{b}^2)\hat{b}_+^\dagger + \sqrt{\kappa_{c,-}}\hat{b}_{-, \text{in}} + \sqrt{\kappa_{i,-}}\hat{b}_-^{(i)}. \quad (4.15)$$

with  $\gamma_c, \gamma_i, \gamma = \gamma_c + \gamma_i$  ( $\kappa_c, \kappa_i, \kappa = \kappa_c + \kappa_i$ ;  $\kappa_{c,\pm}, \kappa_{i,\pm}, \kappa_{\pm} = \kappa_{c,\pm} + \kappa_{i,\pm}$ ) the coupling, intrinsic, and total loss rate of the second-harmonic (pump; signal; idler) mode respectively. The input operators of the second-harmonic, pump, signal, and idler modes due to coupling loss (intrinsic loss) are labeled as  $\hat{a}_{\text{in}}, \hat{b}_{\text{in}}, \hat{b}_{+, \text{in}}, \hat{b}_{-, \text{in}}$  ( $\hat{a}^{(i)}, \hat{b}^{(i)}, \hat{b}_+^{(i)}, \hat{b}_-^{(i)}$ ) respectively.

With coherent input power  $P$  into the pump mode  $\hat{b}_{\text{in}} = \sqrt{\frac{P}{n_b \hbar \omega_p}} e^{-i\omega t}$ , Eq. (4.12) and Eq. (4.13) can be treated classically using the mean fields  $\langle \hat{a} \rangle = \alpha, \langle \hat{b} \rangle = \beta$ . Then the static solutions of Eq. (4.12) and Eq. (4.13) are

$$\beta = \frac{\sqrt{\kappa_c}\beta_{\text{in}}}{-i(\omega - \omega_p) + \frac{\kappa}{2} + \frac{g_2^2|\beta|^2}{-2i(2\omega - \omega_0) + \frac{\gamma}{2}}} \quad (4.16)$$

$$\alpha = \frac{-\frac{i}{2}g_2\beta^2}{-i(2\omega - \omega_0) + \frac{\gamma}{2}} \quad (4.17)$$

In the non-depletion regime, the solution is further simplified to

$$\beta = \frac{\sqrt{\kappa_c}\beta_{\text{in}}}{-i(\omega - \omega_p) + \frac{\kappa}{2}}. \quad (4.18)$$

$$\alpha = \frac{-\frac{i}{2}g_2\beta^2}{-i(2\omega - \omega_0) + \frac{\gamma}{2}}. \quad (4.19)$$

The effective interaction Hamiltonian for the signal and idler modes is

$$\begin{aligned} H_2 + H_3 &= \hbar(g_2\alpha^*\hat{b}_+\hat{b}_- + g_2^*\alpha\hat{b}_+\hat{b}_-) - \frac{\hbar}{2}(g_3\beta^{*2}\hat{b}_+\hat{b}_- + g_3^*\beta^2\hat{b}_+\hat{b}_-) \\ &= -\frac{\hbar}{2}\left[\left(g_3 - \frac{i|g_2|^2}{i(2\omega - \omega_0) + \frac{\gamma}{2}}\right)\beta^{*2}\hat{b}_+\hat{b}_- + \left(g_3^* - \frac{-i|g_2|^2}{-i(2\omega - \omega_0) + \frac{\gamma}{2}}\right)\beta^2\hat{b}_+\hat{b}_-\right]. \end{aligned} \quad (4.20)$$

$$(4.21)$$

Therefore, the overall process is equivalent to Kerr interaction Hamiltonian

$$H_I = -\frac{\hbar}{2}(g_{\text{eff}}\hat{b}_+^{\dagger 2}\hat{b}_+\hat{b}_- + g_{\text{eff}}^*\hat{b}_+^{\dagger}\hat{b}_+\hat{b}_-^{\dagger}) \quad (4.22)$$

under coherent pump  $P$  with effective Kerr nonlinearity

$$g_{\text{eff}} = g_3 - \frac{i|g_2|^2}{i(2\omega - \omega_0) + \frac{\gamma}{2}} \quad (4.23)$$

The equations of motion for the signal and idler modes are

$$\dot{\hat{b}}_+ = (-i\omega_+ - \frac{\kappa_+}{2})\hat{b}_+ + i\frac{1}{2}g_{\text{eff}}^*\beta^2\hat{b}_+^{\dagger} + \sqrt{\kappa_{c,+}}\hat{b}_{+,in} + \sqrt{\kappa_{i,+}}\hat{b}_+^{(i)} \quad (4.24)$$

$$\dot{\hat{b}}_- = (-i\omega_- - \frac{\kappa_-}{2})\hat{b}_- + i\frac{1}{2}g_{\text{eff}}^*\beta^2\hat{b}_-^{\dagger} + \sqrt{\kappa_{c,-}}\hat{b}_{-,in} + \sqrt{\kappa_{i,-}}\hat{b}_-^{(i)}, \quad (4.25)$$

with output boundary conditions:

$$\hat{b}_{+,out} = \hat{b}_{+,in} - \sqrt{\kappa_{c,+}}\hat{b}_+ \quad (4.26)$$

$$\hat{b}_{-,out} = \hat{b}_{-,in} - \sqrt{\kappa_{c,-}}\hat{b}_-. \quad (4.27)$$

For the classical stimulate four-wave mixing with idler input  $\beta_i e^{-i\omega_i t}$ , the static solution of Eq. (4.24) and Eq. (4.25) under the mean field approximation  $|\hat{b}_{+i} = \beta_+$ ,  $|\hat{b}_{-i} = \beta_-$  can be obtained

$$\beta_- = \frac{i\frac{1}{2}g_{\text{eff}}^*\beta^2\beta_+^*}{i(\omega_- - \omega_i) + \frac{\kappa_-}{2}}. \quad (4.28)$$

$$\beta_+ = \frac{\sqrt{\kappa_{c,+}}\beta_i}{i(\omega_+ - \omega_i) + \frac{\kappa_+}{2} - \frac{1}{4}\frac{|g_{\text{eff}}|^2|\beta|^4}{-i(\omega_- - \omega_i) + \frac{\kappa_-}{2}}}. \quad (4.29)$$

With on-resonance pump and idler input, the photon number conversion efficiency under perfect phase-matching  $\omega_+ + \omega_- = 2\omega_p$  is

$$\eta = \frac{|\beta_{+,out}|^2}{|\beta_i|^2} = \frac{16\kappa_{c,+}\kappa_{c,-}|g_{\text{eff}}|^2|\beta|^4}{(\kappa_+\kappa_- - |g_{\text{eff}}|^2|\beta|^4)^2} \approx \frac{16\kappa_{c,+}\kappa_{c,-}|g_{\text{eff}}|^2|\beta|^4}{\kappa_+^2\kappa_-^2} \quad (4.30)$$

For the spontaneous four-wave mixing, the output state can be written as

$$|\psi\rangle = \left[ 1 - \frac{ig_{\text{eff}}^*\beta^2}{2} \iint \frac{d\omega'}{\sqrt{2\pi}} \frac{d\omega''}{\sqrt{2\pi}} \frac{\sqrt{\kappa_{c,+}}\hat{b}_{+,out}^\dagger(\omega'')}{i(\omega_+ - \omega'') + \frac{\kappa_+}{2}} \frac{\sqrt{\kappa_{c,-}}\hat{b}_{-,out}^\dagger(\omega')}{i(\omega_- - \omega') + \frac{\kappa_-}{2}} \delta(\omega' + \omega'' - 2\omega_p) \right] |00\rangle + O\left(\frac{\kappa_{c,+}\kappa_{c,-}|g_{\text{eff}}|^2|\beta|^4}{\kappa_+^2\kappa_-^2} |22\rangle\right) \quad (4.31)$$

Therefore, the photon-pair generation rate under a weak pump can be calculated as

$$R = \langle \psi | \hat{b}_{+,out}^\dagger \hat{b}_{+,out} \hat{b}_{-,out}^\dagger \hat{b}_{-,out} | \psi \rangle \propto |g_{\text{eff}}|^2 P_{\text{in}}^2 Q_b^3, \quad (4.32)$$

with  $Q_b \approx \frac{\omega_p}{\kappa} \approx \frac{\omega_+}{\kappa_+} \approx \frac{\omega_-}{\kappa_-}$ .

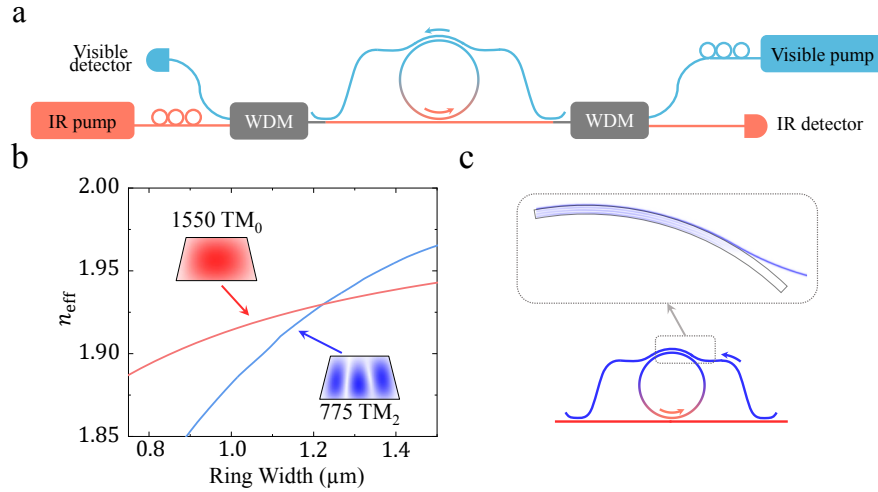


Figure 4.5: **Linear measurement setup and device design.** **a**, Measurement setup for the linear transmission of the cavity. **b**, Simulation of phase-matching condition between fundamental  $\text{TM}_0$  and second-harmonic  $\text{TM}_2$  modes. **c**, Simulation of coupling field between the visible bus waveguide  $\text{TM}_0$  mode and cavity  $\text{TM}_2$  mode.

	$\kappa_{c,+}$	$\kappa_c$	$\kappa_{c,-}$	$\kappa_+$	$\kappa$	$\kappa_-$
Phase-matched set	145 MHz	153 MHz	162 MHz	273 MHz	338 MHz	424 MHz
Reference set	150 MHz	166 MHz	124 MHz	275 MHz	365 MHz	297 MHz

Table 4.1: **Coupling rate and total loss rate for each resonance fitted from Fig. 4.6b.**

### 4.3.2 Device Characterization

The cavity loss rates and coupling conditions are obtained from the linear transmission with the setup shown in Fig. 4.5a. We use two lens fibers to couple light into and out of the device. Two on-chip wavelength-division multiplexers (WDM) are used to combine and separate the fundamental and second-harmonic fields. Two bus waveguides are designed to efficiently couple the fundamental and second-harmonic fields into the cavity respectively (Fig. 4.5b). Phase matching is realized using the fundamental transverse-magnetic (TM) field around 1550 nm wavelength and a high-order (such as  $TM_2$ ) field around 775 nm wavelength (Fig. 4.5c). Based on mode profiles and material nonlinearity,  $g_2/2\pi = 81$  kHz, and  $g_3/2\pi = 0.5$  Hz are calculated from Eq. (4.10) and (4.11).

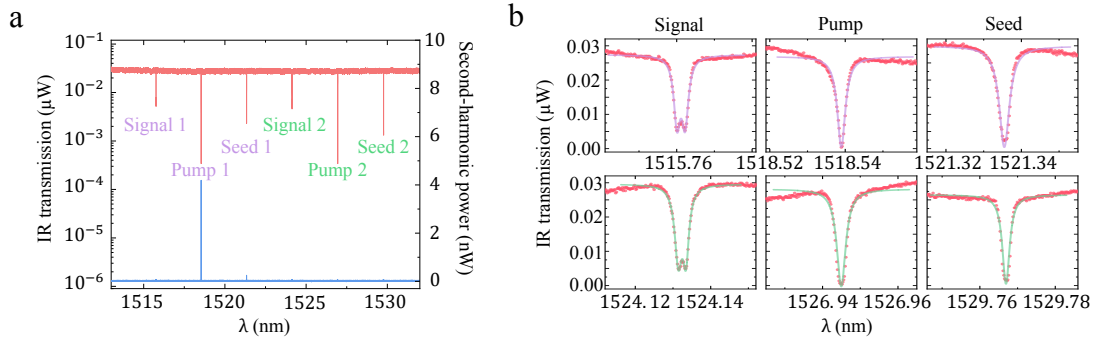


Figure 4.6: **Resonances for stimulated FWM measurement.** **a**, transmission and SHG spectrum showing Pockels phase matching near 1518 nm. **b**, zoomed-in transmission spectrum for each resonance.

To compare the FWM efficiency with the enhanced single-photon nonlinearity and the intrinsic single-photon nonlinearity, we choose two sets of modes with and



without phase-matching Pockels processes. The pump mode linewidth and the photon extraction ratios of the pump, signal, and idler modes can all affect the overall FWM efficiency

$$\eta \propto \left(\frac{\kappa_{c,+}}{\kappa_+^2}\right)\left(\frac{\kappa_{c,-}}{\kappa_-^2}\right)\left(\frac{\kappa_c}{\kappa^2}\right)^2. \quad (4.33)$$

From the device linear transmission spectrum, we can get the linewidth and extraction ratio of all resonances (Fig. 4.6 and Table 4.1). Therefore, the difference in FWM efficiency introduced by cavity conditions is less than 0.5 dB, which is much smaller than the 15 dB difference observed in the experiment. This confirms that the improved FWM efficiency is the result of the enhanced single-photon nonlinearity.

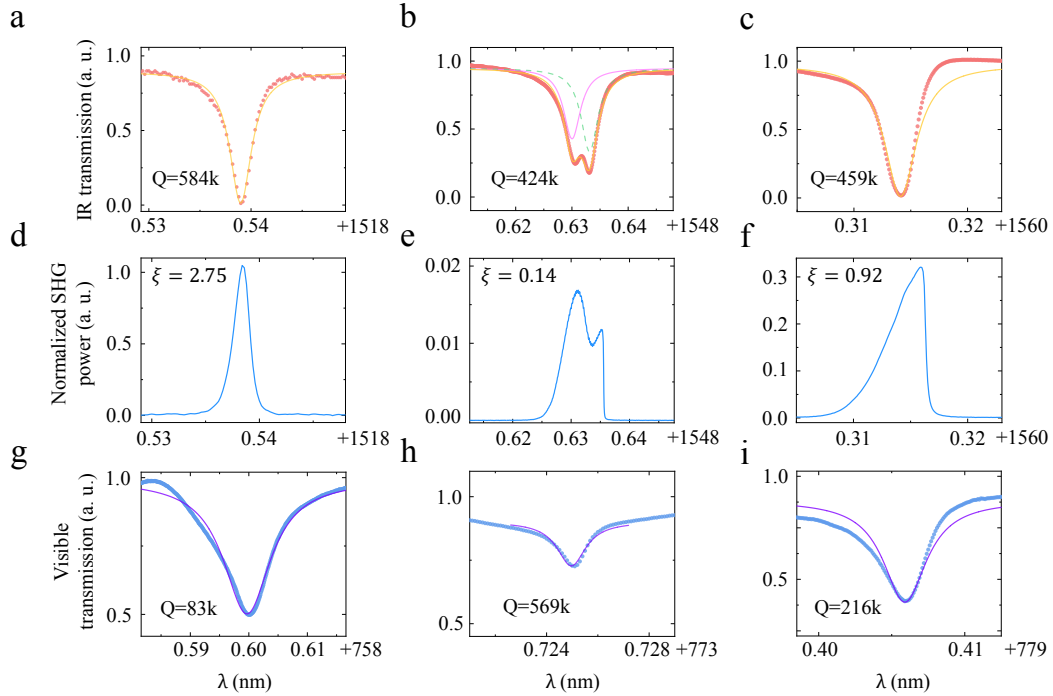


Figure 4.7: **Second-harmonic generation with different phase-matching wavelengths.** **a-c**, Fundamental mode resonances. **d-f**, Normalized SHG spectrum. **g-i** Second-harmonic mode resonances

We observed three pairs of phase-matching wavelengths ( $\sim 1518$  nm to 759 nm,  $\sim 1548$  nm to 774 nm,  $\sim 1560$  nm to 780 nm) for Pockels processes with our device (Fig. 4.7 d-f). While the fundamental fields are all  $TM_0$  modes, the second-harmonic fields can be different [104]. Therefore, the nonlinear strengths of the

Pockels processes are different. The measured second-harmonic generation efficiencies for the three phase-matching wavelengths are  $\eta = 1800\%/W$ ,  $30\%/W$ , and  $600\%/W$ , respectively. Using the cavity linewidths obtained from the linear transmission measurement (Fig. 4.7 a-c and g-i), we get the relative strengths between different Pockels processes and the intrinsic Kerr process as  $\xi = 2.75$ ,  $0.14$ , and  $0.92$  respectively.

The control of the frequency detuning between the fundamental and second-harmonic modes is realized by changing the device temperature. Both fundamental and second-harmonic modes experience red frequency shift with increased temperature but with a different thermo-optic coefficient (Fig. 4.8). The relative frequency shifts between the fundamental and second-harmonic modes for  $\xi = 0.14$  and  $\xi = 0.92$  are measured around  $0.22$  GHz and  $0.19$  GHz per Celsius degree, respectively. The device temperature is controlled with an actively stabilized oven with a temperature precision of  $0.1$  Celsius degree. Therefore, the frequency detuning can be controlled with precision around  $20$  MHz.

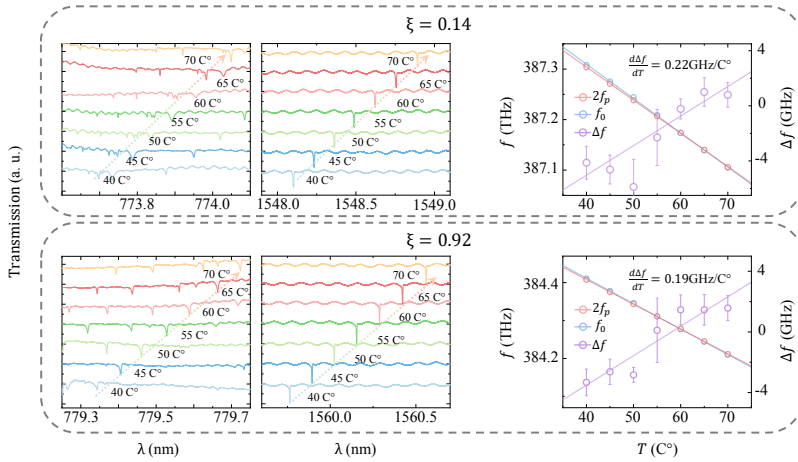


Figure 4.8: **Thermal tuning calibrations of frequency detune for two pairs of phase-matching modes.** The second-harmonic resonance (left), and pump resonance (mid) shift under different temperatures, and the linear fit of the relative frequency shift between fundamental and second-harmonic modes, corresponding to the temperature (right).

### 4.3.3 Single-Photon Measurement

Single photons generated by parametric down-conversion (PDC) processes and effective spontaneous FWM are measured with the setup shown in Fig. 4.9 a and d respectively. PDC processes are for calibrating the properties of cavity modes at visible wavelengths independently, such as the spontaneous PDC photon-pair generation efficiency. A visible pump in resonance with the second-harmonic mode is launched into the cavity. A long-pass filter with a cut-off wavelength of around 1500 nm is placed at the output to remove the residue pump. The signal and idler photons are separated by a wavelength-selective switch (WS), and only detected by superconducting nanowire single-photon detectors (SNSPD). Fig. 4.9 b and c shows count rates of the signal channel depending on the relative temperature of the device.

The main results of our experiments are obtained from the setup for measuring the photon-pair generation rate by effective spontaneous FWM. As shown in Fig. 4.9d, an IR pump in resonance with the fundamental pump mode is launched into the device. Fiber Bragg gratings and WS are used to remove the pump with a 140 dB suppression ratio. Signal and idler photons are also separated by WS, and detected by SNSPDs. The setting of WS is the same as measuring PDC, where only count rates of the signal channel are shown in Fig. 4.9 e and f. Besides, the coincidence between the single and idler photons is recorded by a time tagger with 100 ps bin size.

The coincidence-accident ratio (CAR) is obtained by two approaches. In the first approach, CAR is directly measured by the peak volume of the signal-idler coincidence near zero time delay [105].

$$\text{CAR} = \frac{\int_{-\tau/2}^{\tau/2} g^{(2)}(t) dt}{\int_{\infty-\tau/2}^{\infty+\tau/2} g^{(2)}(t) dt} \quad (4.34)$$

We use integration window  $\tau = 2$  ns, which is larger than the photon coherence time. CAR can also be calculated using the calibrated signal and noise count rates [106,

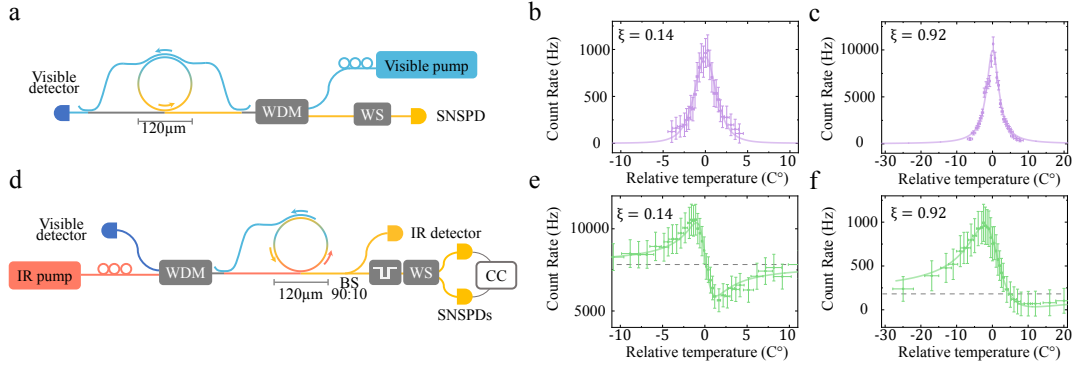


Figure 4.9: **Single photon measurement.** **a**, Experimental setup for measuring single photons with SPDC. **b-c**, Measured SPDC single-photon rates with  $\xi = 0.14$  and  $0.92$ . **d**, Experimental setup for measuring single photons with FWM. **e-f**, Measured FWM single-photon rates of signal with  $\xi = 0.14$  and  $0.92$ . Vertical error bars are estimated from the photon Poisson noise, and horizontal error bars are estimated from the error of the thermal tuning. Gray dashed lines are references for pure Kerr nonlinearity single-photon generation rate, measured at the temperature far away from the phase matching condition for Pockels nonlinear processes.

53].

$$\text{CAR} = \frac{T^2 R}{(TR + N_p + N_d)^2} + 1, \quad (4.35)$$

with  $R$ ,  $N_p$ , and  $N_d$  the intra-cavity photon-pair generation rate, noise count due to the residue pump, and the detector dark count respectively.  $T$  is the total power transmission of the measurement setup. Experimentally, dark count  $N_d$  is measured directly by SNSPD when the pump input is turned off. Power transmission  $T$  (from the cavity to SNSPDs) is calculated from the ratio between the measured signal-idler coincidence rate  $CC$  and photon rates in signal/idler channel  $R_s$  and  $R_i$  (including noise) at the highest input pump power.

$$T = \frac{CC}{\sqrt{R_s R_i}} = 3.2 \times 10^{-4}. \quad (4.36)$$

We assume that the dark count  $N_d$  is independent of pump power, residue pump noise is proportional to the pump power  $N_p \propto P$ , and the photon-pair rate is proportional to the square of the pump power  $R \propto P^2$ . By measuring the total

photon count ( $R + N_p + N_d$ ) with different pump power, we can get the

$$N_d = 480 \text{ Hz} \quad (4.37)$$

$$N_p = 436.8 \text{ Hz/mW} \times P \quad (4.38)$$

with  $P$  the on-chip input pump power. With the relative Pockels strength  $\xi = 0.92$  and frequency detune  $\Delta = -2\pi \times 0.7 \text{ GHz}$ , we get  $R = 4.1 \text{ MHz/mW}^2 \times P^2$  (maximum enhancement, red point in main text Fig. 4.4c). Therefore, we can plot the calculated CAR with different pump power (red line in the main text Fig. 4.4g). Similarly, we get  $R = 0.136 \text{ MHz/mW}^2 \times P^2$  with frequency detune  $\Delta = 2\pi \times 1.5 \text{ GHz}$  (maximum suppression, blue point in main text Fig. 4.4c), and plot the calculated CAR under maximum nonlinearity suppression (blue line in the main text Fig. 4.4g)

## CHAPTER 5

Reconfigurable Kerr Nonlinearity: Controlling the Spontaneous Symmetry  
Breaking of Photonic Chirality<sup>†</sup>**5.1 Abstract**

Spontaneous symmetry breaking in nonlinear bosonic systems provides a unified picture to understand vastly different phenomena ranging from Higgs mechanism [107] to superconductivity [108]. With intrinsic Kerr nonlinearity, photonic systems are well positioned for the technological development and basic study of spontaneous symmetry breaking [109]. However, the critical capability to control the occurrence condition and the property of spontaneous symmetry breaking remains inaccessible, as the form and magnitude of nonlinear interactions cannot be modified. Here, we report the development of reconfigurable Kerr optical nonlinearity to control spontaneous symmetry breaking. This is achieved through the interference between the intrinsic Kerr and cascaded second-order nonlinear processes. Anomalous Kerr effects, including negative self-phase modulation and strength tuning between competing nonlinear processes, have been demonstrated. With the reconfigurable Kerr nonlinearity, we realize the *in-situ* prohibition and facilitation of spontaneous symmetry breaking of photonic chirality. This work could empower the experimental study of spontaneous symmetry breaking in unexplored regimes and inspire the development of novel photonic functions.

---

<sup>†</sup>This chapter has been posted on arXiv as [3]

## 5.2 Main Article

### 5.2.1 Introduction

Photonic chirality, the asymmetric behavior of optical fields along opposite directions in photonic ring resonators, can provide complementary photonic functions from conventional spatial [110, 111], polarization [112, 113], and spectral-temporal [47, 81, 114, 115] operations. Photonic chirality is typically introduced by explicit asymmetries, including deformed photonic structures [116, 117], gain-loss modulation in non-Hermitian systems [118, 119, 120], and interaction with magnetic materials [121, 122]. Such explicit symmetry breaking of photonic chirality has been used to build optical isolators [123, 124, 125], realize topological photonic states [67, 126, 127], and develop unidirectional micro-lasers [128, 129] in the classical regime, as well as improve single-photon sources [1, 130, 131] and develop logic operations in the quantum regime [132, 133, 134].

Besides explicit approaches, the symmetry breaking of photonic chirality can also happen spontaneously with Kerr nonlinearity [135, 136, 137, 138, 139]. This is introduced by the imbalance between self- and cross-phase modulation, two fundamental Kerr nonlinear effects. In this case, photons can show propagation-direction-dependent properties even though the system configuration is completely symmetric, providing unique advantages to applications including optical isolators [140] and sensors [141, 142]. Unlike explicit approaches where symmetry breaking can be engineered conveniently by photonic structures, the capability to control the condition of spontaneous symmetry breaking remains elusive. The key challenge is the direct modification of Kerr nonlinearity, which typically has both fixed form and magnitude determined by material properties and photonic structures [18].

Here, we report the approach to break the intrinsic restriction of Kerr nonlinearity and demonstrate the controlled spontaneous symmetry breaking of photonic chirality. This is realized through the cascaded second-order nonlinearity, which is equivalent to reconfigurable artificial Kerr nonlinearity. In particular, we can selectively control the self-phase modulation coefficient without affecting the cross-phase

modulation. The capability to tune the relative strength between self- and cross-phase modulation enables the modification of the spontaneous symmetry-breaking condition for photonic chirality.

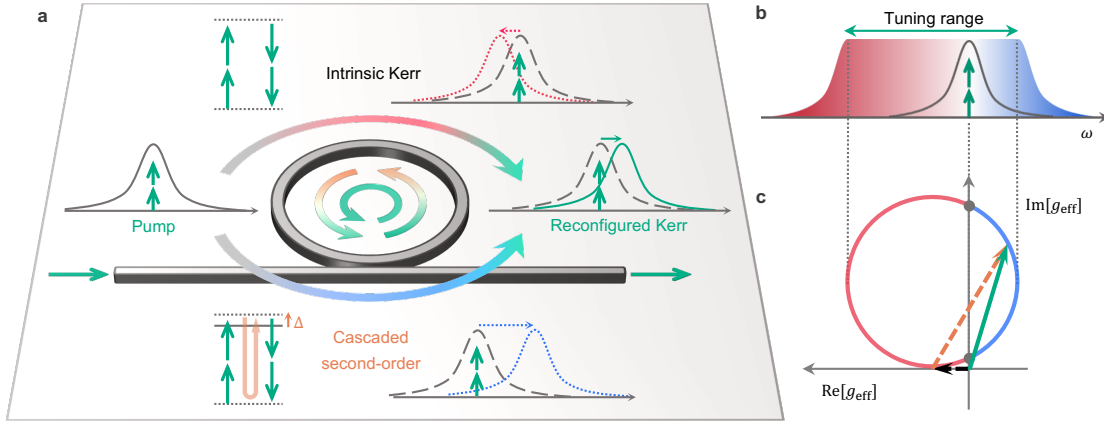


Figure 5.1: **Schematics for reconfigurable Kerr nonlinearity.** **a**, Interference between the intrinsic Kerr and the cascaded second-order nonlinear processes in the photonic ring cavity. The intrinsic Kerr nonlinearity introduces resonance shift towards lower frequency (red-shift). This can be modeled as four-wave mixing with two pump photons (green) annihilated to re-generate two photons at the same frequency. The cascaded second-order nonlinearity introduces resonance shift towards higher frequency (blue-shift) with positive cavity detune. This can be modeled as artificial four-wave mixing, where two pump photons (green) are first combined to generate one second-harmonic photon (orange), which drives the parametric down-conversion to re-generate two photons at the pump frequency. The overall frequency shift is the coherent combination of the two parallel processes. **b**, Tuning range of the frequency shift induced by self-phase modulation with anomalous Kerr nonlinearity. **c**, The vector representation of the effective Kerr nonlinear coefficient  $g_{\text{eff}}$ . By tuning the cavity detune  $\Delta$ , the effective Kerr nonlinearity can change along the circle to give the frequency shift towards lower (red) and higher (blue) frequency. Black dashed arrow: intrinsic Kerr nonlinearity; orange dashed arrow: cascaded second-order nonlinearity; green solid arrow: effective Kerr nonlinearity.

Cascaded second-order nonlinearity has been used in bulk optics to enhance Kerr nonlinearity [143, 144, 145, 146]. The recent development of novel nanophotonic materials makes it possible to demonstrate cascaded second-order nonlinearity with integrated photonic devices. With the capability to precisely engineer dispersion in nanophotonic structures, we can realize cascaded second-order nonlinearity with res-



onance enhancement for both fundamental and second-harmonic fields, in contrast to previous demonstrations with no resonance or only the fundamental resonance. This allows the observation of the interference between the cascaded second-order and intrinsic Kerr nonlinearity [2]. The approach further enables the efficient reconfiguration of the effective Kerr nonlinearity using the frequency detuning between the fundamental and second-harmonic resonances, different from bulk optics that depends on the change of the phase matching condition. Previous studies typically consider Kerr enhancement for a single pump field with cascaded second-order nonlinearity as the only dominating process [91, 144]. This work further expands the capability by demonstrating the complex interaction between multiple pump fields with the cascaded second-order nonlinearity co-existing with different nonlinear processes.

### 5.2.2 Reconfigurable Kerr Nonlinearity

Our scheme for reconfigurable Kerr nonlinearity is implemented in an integrated photonic micro-ring cavity with second-order nonlinearity [2]. We consider the cavity response to a continuous-wave pump field. The pump field is subject to two parallel nonlinear processes. The first one is the conventional self-phase modulation due to the intrinsic Kerr nonlinearity (top path in Fig. 5.1a). The cavity instantaneous resonance is shifted by  $\delta\omega \propto -g_3 \cdot N_p$ , with  $g_3$  the Kerr nonlinear coefficient and  $N_p$  the intra-cavity pump photon number. As integrated photonic materials typically have positive Kerr nonlinear coefficients [18], the resonance shifts towards a lower frequency.

In parallel with the intrinsic Kerr nonlinearity, the pump field also undergoes the cascaded second-order nonlinear process consisting of second-harmonic generation and degenerate parametric down-conversion (bottom path in Fig. 5.1a). The pump field is first doubled to generate the second-harmonic field. The second-harmonic resonance will impose an extra phase to the intra-cavity second-harmonic field depending on the frequency detuning. At the same time, the second-harmonic field drives the degenerate parametric down-conversion to re-generate the pump field.

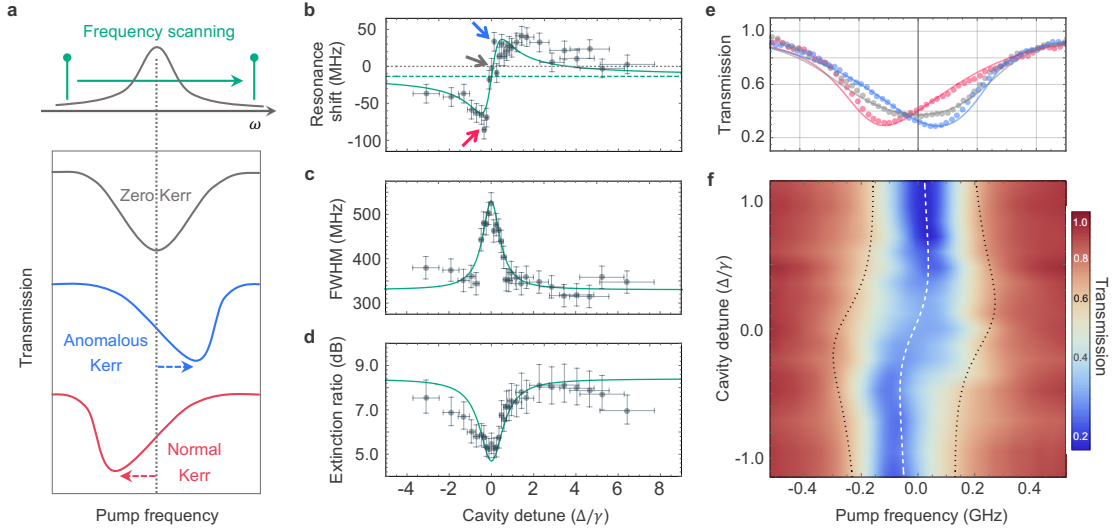


Figure 5.2: **Anomalous Kerr nonlinearity.** **a**, Calculated transmission spectrum as the pump frequency is scanned across the resonance. The transmission minimum shifts to higher (blue) and lower (red) frequencies with negative and positive Kerr nonlinear coefficients, respectively. The transmission spectrum remains symmetric (grey) if the Kerr nonlinear coefficient is zero. **b**, Measured resonance shift dependence on the cavity detune. Gray dashed line: zero frequency shift. Green dashed line: resonance shift induced by the intrinsic Kerr nonlinearity. The blue, red, and grey arrows show the condition to achieve maximum blue shift, maximum redshift, and zero shift, with the corresponding transmission spectrum shown in (e). **c**, Measured FWHM dependence on the cavity detune. **d**, Measured extinction ratio dependence on the cavity detune. **e**, Measured transmission spectrum with maximum blue shift (blue), maximum redshift (red), and zero shift (grey). **f**, Measured transmission spectrum with different cavity detune values. White dashed line: minimum transmission position; dark dashed lines: half maximum position. Solid lines in **b-e** are calculated results. Horizontal and vertical error bars in (b)-(d) are estimated based on device temperature stability and transmission variance, respectively.

Then, the extra phase is transferred back to the pump field. Therefore, the cascaded second-order nonlinearity for the pump field is equivalent to an effective Kerr nonlinearity with a non-trivial phase [2]. In this cascaded process, the second-order nonlinear strength  $g_2$ , the second-harmonic resonance linewidth  $\gamma$ , and the frequency detune  $\Delta$  between the pump and second-harmonic resonances collectively determine the effective Kerr nonlinear coefficient. The instantaneous resonance shift is  $\delta\omega \propto -\text{Re} \left[ \frac{i|g_2|^2}{-i\Delta + \gamma/2} \right] \cdot N_p$  (Section 5.3.1). With a positive detune  $\Delta > 0$ , the cascaded second-order nonlinearity can lead to the resonance shift towards a higher frequency. This is equivalent to self-phase modulation with negative Kerr nonlinear coefficients. The overall resonance shift, after the coherent combination of the intrinsic Kerr and cascaded second-order nonlinear processes, can be written as

$$\delta\omega \propto -\text{Re} \left[ g_3 + \frac{i|g_2|^2}{-i\Delta + \gamma/2} \right] \cdot N_p \stackrel{\text{def}}{=} -\text{Re} [g_{\text{eff}}] \cdot N_p \quad (5.1)$$

with  $g_{\text{eff}}$  the effective Kerr nonlinear coefficient (Fig. 5.1c). With strong second-order nonlinearity  $\xi = |g_2|^2/(g_3\gamma) > 1$ , the overall resonance shift can be reconfigured towards either lower or higher frequency depending on the cavity detune  $\Delta$  (Fig. 5.1b). A completely passive cavity without nonlinear resonance shift can also be obtained at cavity detune  $\Delta/\gamma = \frac{1}{2}(\xi \pm \sqrt{\xi^2 - 1})$ . Besides the reconfigurable resonance shift, the cascaded second-order nonlinearity also introduces extra loss for the pump field as power is converted into the second-harmonic field. This is manifested as the imaginary part of the effective Kerr nonlinearity  $g_{\text{eff}}$ .

Due to self-phase modulation, the transmission spectrum of the high-power pump field deviates from the symmetric Lorentzian shape and can be used to quantify the Kerr nonlinear coefficient (Fig. 5.2a). The speed to scan the pump frequency is sufficiently fast to avoid the frequency shift induced by the thermal effect (Section 5.3.3). The pump power is maintained below the four-wave-mixing threshold to avoid the generation of optical sidebands. With this power, the frequency difference between the minimum transmission point and the Lorentzian middle point is proportional to the real part of the effective Kerr nonlinear coefficient. The imaginary part can also be obtained through the change in the resonance's full width at half maximum

(FWHM).

The reconfigurable Kerr nonlinearity is demonstrated with an aluminum nitride ring cavity [97]. Phase-matching condition for second-order nonlinearity is first approximately satisfied by changing the ring width [147]. After determining the ring width, we realize the fine-tuning of the resonance detune  $\Delta$  by changing the device temperature, as the pump and second-harmonic resonances have different thermal-optic coefficients (Section 5.3.4). We can clearly observe the change in the pump transmission spectrum with different cavity detune values (Fig. 5.2f). The resonance shift follows a Fano shape with respect to the cavity detune (Fig. 5.2b). This agrees with the interpretation that the intrinsic Kerr and cascaded second-order nonlinear processes are coherently combined to give rise to the effective Kerr nonlinearity. The pump resonance shows a maximum shift towards higher frequency with the cavity detune  $\Delta \approx 0.5\gamma$ , proving the negative self-phase modulation (blue in Fig. 5.2e). By changing the device temperature, we can further reconfigure the pump resonance to shift towards a lower frequency and even exhibit no frequency shift (red and grey in Fig. 5.2e). In addition, we also notice that the FWHM of the pump resonance follows the Lorentzian shape with respect to the cavity detune (Fig. 5.2c). The largest FWHM is obtained with zero detune  $\Delta = 0$ , in which case maximum power is converted from the pump field to the second-harmonic field. The power conversion can be treated as an extra intrinsic loss for the pump resonance. As the cavity is weakly coupled to the bus waveguide with fixed coupling strength, the increase of the intrinsic loss leads to a drop in the resonance extinction ratio (Fig. 5.2d).

The key to realizing reconfigurable Kerr nonlinearity is the cascaded second-order nonlinear process, which requires the phase-matching condition. It provides the unique capability that we can selectively modify the target Kerr nonlinear process without affecting the others. This is achieved by designing the phase-matching condition only for the optical fields involved in the target Kerr nonlinear process. For example, we consider the same photonic ring cavity with second-order nonlinearity but pumped in both clockwise and counter-clockwise directions (Fig. 5.3a).

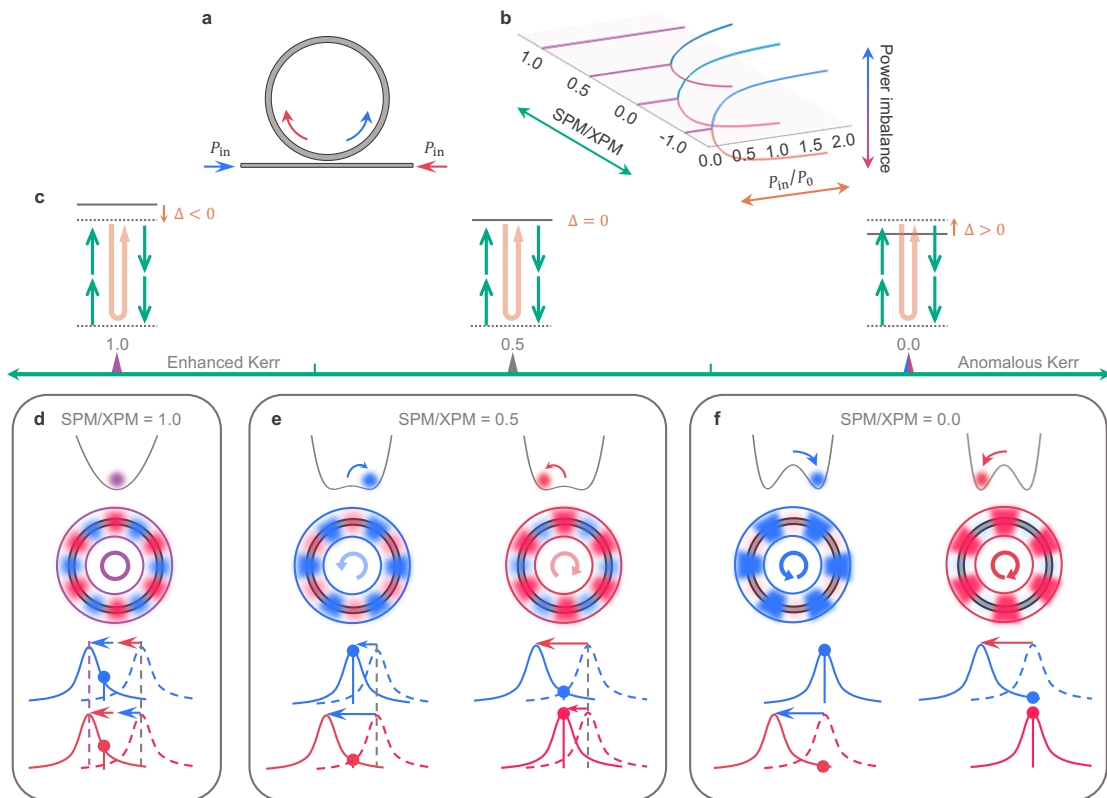


Figure 5.3: **In-situ control of spontaneous symmetry breaking of photonic chirality.** **a**, Photonic ring cavity with a bi-directional pump. **b**, Calculated spontaneous symmetry breaking condition with different relative strengths between self-phase modulation (SPM) and cross-phase modulation (XPM). **c**, Cavity detuning configuration of the cascaded second-order nonlinearity to realize different SPM/XPM relative strengths. **d**, Cavity status under the strong pump with  $SPM/XPM=1$ . The symmetric state with equal powers is always stable, as the resonance shifts are identical in two directions. **e**, Cavity status under the strong pump with  $SPM/XPM=1/2$ . The optical field in one direction dominates, as cross-phase modulation introduces twice the resonance shift than self-phase modulation. **f**, Cavity status under the strong pump with  $SPM/XPM=0$ . The power difference between different directions becomes larger as the mismatch between self- and cross-phase modulation increases.

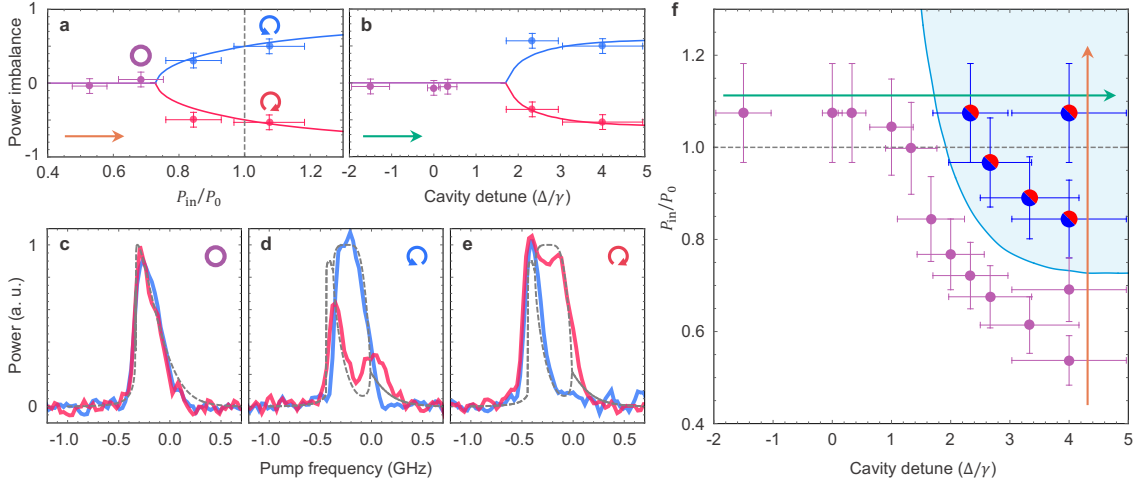


Figure 5.4: **Control of spontaneous symmetry breaking condition.** **a**, Relative power imbalance with fixed cavity detune  $\Delta \approx 4\gamma$  and varying pump power  $P_{\text{in}}$ . The threshold power for intrinsic Kerr nonlinearity is marked as the dashed black line. **b**, Relative power imbalance with varying cavity detune  $\Delta$  and fixed pump power  $P_{\text{in}} \approx 1.07P_0$ .  $P_0 \approx 51$  mW is the threshold power for spontaneous symmetry breaking with intrinsic Kerr nonlinearity. **c-e**, Measured output second-harmonic power in clockwise (blue) and counterclockwise (red) directions with cavity detune  $\Delta \approx 4\gamma$  and pump power  $P_{\text{in}} \approx 0.7P_0$ ,  $P_{\text{in}} \approx 1.07P_0$ ,  $P_{\text{in}} \approx 1.07P_0$ , corresponding to the purple, blue, and red circle points in **(a)** respectively. **f**, Cavity status with different cavity detune  $\Delta$  and pump power  $P_{\text{in}}$ . Blue solid line: calculated threshold condition for spontaneous symmetry breaking. Shaded blue area: calculated regime with asymmetric power in two directions. Black dashed line: threshold power for intrinsic Kerr nonlinearity. Purple points: measured cavity output with equal power in two directions. Blue/red points: measured cavity output with the optical field in one direction dominant. Orange arrow: the same condition change as **(a)**. Green arrow: the same condition change as **(b)**. Power and cavity detune error bars are estimated based on device temperature stability and transmission variance, respectively. Additional data for **(f)** are shown in section 5.3.5.

As the phase matching condition is only valid for optical fields along one direction, only the self-phase modulation coefficient is modified by the cascaded second-order nonlinearity. To modify the cross-phase modulation, we need sum-frequency generation between counter-propagating fields. This requires a zero wave vector for the second-harmonic field, which cannot be realized. Therefore, the cross-phase modulation coefficient remains unchanged.

### 5.2.3 Spontaneous Chiral Symmetry Breaking

The bi-directional configuration is of critical importance for numerous photonic applications, including optical gyroscope [148], single-particle detection [149], and soliton referencing [150]. It is recently realized that spontaneous symmetry breaking of photonic chirality can also be introduced in this bi-directional configuration due to the imbalance between self- and cross-phase modulation [136, 135, 137, 138, 141]. For intrinsic Kerr nonlinearity, the ratio between self- and cross-phase modulation (SPM/XPM) typically has a fixed value of 1/2 in solid-state materials without ellipticity and the polarization degeneracy [12, 10]. The optical field along one direction causes twice resonance shifts for the opposite direction. Therefore, the optical field with smaller power will experience a larger resonance shift, which further suppresses its amplitude due to the larger mismatch between the input frequency and cavity resonance. With this positive feedback mechanism, the symmetric state with equal power in both directions becomes unstable even though the input pumps have the same power (Supplementary Information II). Then the optical field in one direction becomes stronger, showing spontaneous chiral behavior (Fig. 5.3e).

Theoretically, the pump power required for spontaneous symmetry breaking depends on the frequency detuning between the pump field and cavity resonance [151, 152, 153]. However, due to the thermal effect, the frequency detuning between the pump field and cavity resonance is highly correlated with the pump power and cannot be controlled independently at high power. Therefore, pump frequency is scanned across the resonance rapidly to avoid the thermal effect in experiments [136, 135, 141]. In this case, the threshold pump power to observe

spontaneous symmetry breaking has a fixed value in photonic devices only with intrinsic Kerr effect (SPM/XPM=1/2) (Supplementary Information II).

With the capability to selectively control self-phase modulation without affecting cross-phase modulation, we can engineer a single cavity to exhibit different behaviors for spontaneous symmetry breaking (Fig. 5.3b-f). If we enhance the self-phase modulation to the same strength as cross-phase modulation (SPM/XPM=1), spontaneous symmetry breaking can be prohibited as optical fields in both directions will experience the same resonance shift regardless of the power distribution (Fig. 5.3d). If we suppress the self-phase modulation (SPM/XPM=0), spontaneous symmetry breaking can be realized more easily as the resonance shift difference is larger with lower pump power (Fig. 5.3f). Besides the resonance shift, the cascaded second-order nonlinearity can also show reconfigurable power absorption (imaginary part of  $g_{\text{eff}}$ ), which can also change the condition for spontaneous symmetry breaking.

To observe the spontaneous symmetry breaking, optical fields with identical frequency and power are coupled into the cavity in both directions (Supplementary Information III). When the optical frequency is scanned across the pump resonance, we monitor the output second-harmonic power, which is proportional to the square of the intra-cavity pump photon number (Supplementary Information III). The photonic chirality  $C$  is defined as the relative intra-cavity power imbalance

$$C = \frac{(N_p^{\text{CCW}} - N_p^{\text{CW}})}{(N_p^{\text{CCW}} + N_p^{\text{CW}})} \quad (5.2)$$

with  $N_p^{\text{CCW}}$  and  $N_p^{\text{CW}}$  the intra-cavity pump photon number along clockwise and counter-clockwise directions, respectively. A larger power imbalance indicates stronger spontaneous symmetry breaking of photonic chirality.

We first vary the pump power while fixing the device at which the self-phase modulation is suppressed (Fig. 5.4a). With low pump power, the optical fields have the same amplitude in both directions (Fig. 5.4c). By increasing the pump power, we observe the spontaneous symmetry breaking with the optical field in one direction significantly stronger than the other (Fig. 5.4d&e). Due to the suppression of the self-phase modulation, the threshold power for spontaneous symmetry breaking is



significantly lower compared to the intrinsic Kerr nonlinearity case (Fig. 5.4a). Next, we fix the pump power and vary the cavity detune  $\Delta$  for the cascaded second-order nonlinearity (Fig. 5.4b). With negative cavity detune, the self-phase modulation is enhanced. Therefore, the optical fields along both directions remain the same. By increasing the cavity detune, the imbalance between self- and cross-phase modulation becomes larger, leading to spontaneous symmetry breaking. As shown in Fig. 5.4f, the spontaneous symmetry breaking condition is collectively determined by the pump power and cavity detuning. The threshold pump power can be continuously tuned by the cavity detune. Therefore, we can either prevent or facilitate the occurrence of spontaneous symmetry breaking by increasing or decreasing the threshold pump power.

#### 5.2.4 Conclusion

In summary, we have demonstrated the capability to control the spontaneous symmetry breaking of photonic chirality. This is achieved by directly modifying Kerr nonlinear interactions with the cascaded second-order nonlinearity. Beyond the fixed intrinsic Kerr nonlinearity, we can realize reconfigurable anomalous Kerr effects, including negative self-phase modulation and strength tuning between competing Kerr nonlinear processes. This flexible mechanism can find broad applications in photonic technologies based on Kerr nonlinearity, such as frequency comb generation, quantum state generation, and frequency conversion. Moreover, the control of spontaneous symmetry-breaking conditions can provide novel insights into the study of nonlinear dynamics in broad fields ranging from condensed-matter physics to nanomechanics.

### 5.3 Supplementary Materials

#### 5.3.1 Theoretical Model for Reconfigurable Kerr Nonlinearity

The Hamiltonian describing both the second-order ( $\mathcal{H}_2$ ) and Kerr ( $\mathcal{H}_3$ ) nonlinear interactions between the second-harmonic ( $\hat{a}$ ) and fundamental ( $\hat{b}$ ) resonances in

the ring cavity can be written as

$$\mathcal{H}_{\text{sys}} = \mathcal{H}_0 + \mathcal{H}_2 + \mathcal{H}_3, \quad (5.3)$$

$$\mathcal{H}_0 = \hbar\omega_{\text{SHG}}\hat{a}^\dagger\hat{a} + \hbar\omega_0\hat{b}^\dagger\hat{b}, \quad (5.4)$$

$$\mathcal{H}_2 = \frac{\hbar}{2}(g_2\hat{a}^\dagger\hat{b}^2 + g_2^*\hat{a}\hat{b}^{\dagger 2}), \quad (5.5)$$

$$\mathcal{H}_3 = -\frac{\hbar}{4}g_3\hat{b}^{\dagger 2}\hat{b}^2, \quad (5.6)$$

with  $\omega_0$  and  $\omega_{\text{SHG}}$  the resonant frequencies for fundamental and second-harmonic resonances respectively. The second-order ( $g_2$ ) and Kerr ( $g_3$ ) single-photon nonlinearity can be expressed with device parameters

$$g_2 = \sqrt{\frac{\hbar\omega_{\text{SHG}}\omega_0^2}{2\epsilon_0 V_a V_b^2}} \int_V dr^3 u_a^*(\vec{r}) \cdot \chi^{(2)} : u_b(\vec{r})^2 \quad (5.7)$$

$$g_3 = \frac{3}{2} \frac{\hbar\omega_0^2}{\epsilon_0 V_b^2} \int_V dr^3 u_b^{*2}(\vec{r}) : \chi^{(3)} : u_b(\vec{r})^2 \quad (5.8)$$

with mode volumes  $V_a$  and  $V_b$ , mode profiles  $u_a$  and  $u_b$  for the second-harmonic and fundamental resonances, respectively. Then, the equations of motion can be derived from the Heisenberg–Langevin equation.

$$\dot{\hat{a}} = (-i\omega_{\text{SHG}} - \frac{\gamma}{2})\hat{a} - i\frac{1}{2}g_2\hat{b}^2 + \sqrt{\gamma_c}\hat{a}_{\text{in}} + \sqrt{\gamma_i}\hat{a}^{(i)} \quad (5.9)$$

$$\dot{\hat{b}} = (-i\omega_0 - \frac{\kappa}{2})\hat{b} + \frac{i}{\hbar}[\mathcal{H}_2 + \mathcal{H}_3, \hat{b}] + \sqrt{\kappa_c}\hat{b}_{\text{in}} + \sqrt{\kappa_i}\hat{b}^{(i)}, \quad (5.10)$$

where  $\gamma_c$ ,  $\gamma_i$ , and  $\gamma = \gamma_c + \gamma_i$  ( $\kappa_c$ ,  $\kappa_i$ , and  $\kappa = \kappa_c + \kappa_i$ ) represent the coupling, intrinsic, and total loss rate of the second-harmonic (pump) mode. The input operators of the second-harmonic and fundamental resonances due to coupling loss (intrinsic loss) are labeled as  $\hat{a}_{\text{in}}$  and  $\hat{b}_{\text{in}}$ , ( $\hat{a}^{(i)}$  and  $\hat{b}^{(i)}$ ) respectively. The relation between the second-harmonic and fundamental fields at steady states with the driving frequency  $\omega_p$  can be obtained from Eq. (5.9).

$$\hat{a}(2\omega_p) = \frac{-\frac{i}{2}g_2\hat{b}^2 + \sqrt{\gamma_c}\hat{a}_{\text{in}} + \sqrt{\gamma_i}\hat{a}^{(i)}}{-i\Delta + \frac{\gamma}{2}}, \quad \Delta = 2\omega_p - \omega_{\text{SHG}}. \quad (5.11)$$

Then, the mean fields,  $\alpha(2\omega_p) = \langle \hat{a}(2\omega_p) \rangle$  and  $\beta(\omega_p) = \langle \hat{b}(\omega_p) \rangle$  follow the relation

$$\alpha(2\omega_p) = \frac{-\frac{i}{2}g_2\beta(\omega_p)^2}{-i\Delta + \frac{\gamma}{2}}. \quad (5.12)$$

Here we ignore the self-phase modulation of the second-harmonic field and the cross-phase modulation influence from the second-harmonic field on the fundamental field by assuming  $\gamma \gg \kappa \approx g_3|\beta|^2 \gg g_3|\alpha|^2$ .

Then we can have the dynamics of the pump mean field in the frequency domain

$$-i(\omega_p - \omega_0)\beta(\omega_p) = -\frac{\kappa}{2}\beta(\omega_p) + \frac{ig_{\text{eff}}(\Delta)}{2}|\beta(\omega_p)|^2\beta(\omega_p) + \sqrt{\kappa_c}\beta_{\text{in}}(\omega_p). \quad (5.13)$$

The effective Kerr nonlinearity is expressed as

$$g_{\text{eff}}(\Delta) = g_3 + \frac{i|g_2|^2}{-i\Delta + \frac{\gamma}{2}} = g_3\left(1 + \frac{i\xi}{-i\Delta/\gamma + 1/2}\right) \quad (5.14)$$

Here  $\xi = |g_2|^2/g_2/\gamma$  is defined as the relative strength between the cascaded second-order nonlinearity and intrinsic Kerr nonlinearity. Due to the interference between the cascaded second-order and intrinsic Kerr processes, the amplitude of  $g_{\text{eff}}$  shows an asymmetric shape with respect to cavity detune  $\Delta$  (Fig. 5.5a). The real part of  $g_{\text{eff}}(\Delta)$  shows the power-dependent frequency shift, which exhibits a Fano lineshape with respect to cavity detune  $\Delta$  (Fig. 5.5b). The imaginary part of  $g_{\text{eff}}(\Delta)$  shows the power-dependent loss, which exhibits a Lorentzian lineshape with respect to cavity detune  $\Delta$  (Fig. 5.5c). The power-dependent loss is due to the second-harmonic generation. With a stronger fundamental field, more power will transfer to the second-harmonic field. The change in the loss can be observed with the change in the full width of the half maximum (FWHM) and extinction ratio of the transmission spectrum.

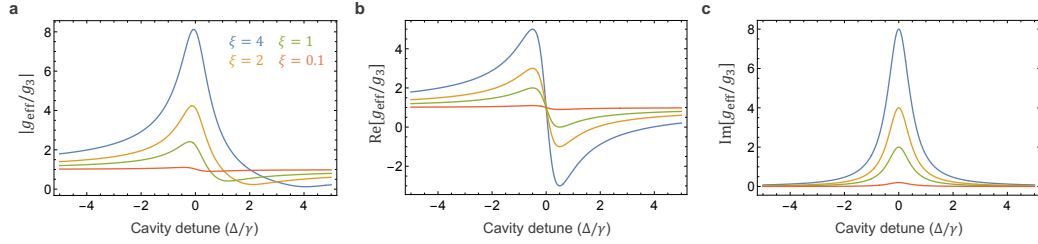


Figure 5.5: **Simulation of complex effective Kerr nonlinearity.** Calculated amplitude (a), real part (b), and imaginary part (c) of effective Kerr nonlinearity  $g_{\text{eff}}$  with respect to different cavity detune  $\Delta$  and different relative strength between cascaded second-order and intrinsic Kerr nonlinearity  $\xi$ .

### 5.3.2 Theoretical Model for Spontaneous Chiral Symmetry Breaking

#### Spontaneous Chiral Symmetry Breaking with Intrinsic Kerr Nonlinearity

When an optical ring cavity is pumped in both clockwise (CW) and counter-clockwise (CCW) directions with equal amplitudes, a standing wave will be formed if nonlinear effects are not included. There will be no difference between the CW and CCW directions, thus no chirality. However, intrinsic Kerr nonlinearity exists in all photonic materials. In particular, cross-phase modulation (XPM) is twice strong as self-phase modulation (SPM). The imbalance between XPM and SPM can cause spontaneous symmetry breaking between the CW and CCW directions, which shows chiral behavior. The equation of motion for the ring cavity with a bi-directional pump can be written as

$$\dot{\hat{b}}_r = \left(-i\omega_0 - \frac{\kappa}{2}\right)\hat{b}_r + \frac{ig_3}{2}(\hat{b}_r^\dagger\hat{b}_r + 2\hat{b}_l^\dagger\hat{b}_l)\hat{b}_r + \sqrt{\kappa_c}\hat{b}_{r,\text{in}} + \sqrt{\kappa_i}\hat{b}_r^{(i)} \quad (5.15)$$

$$\dot{\hat{b}}_l = \left(-i\omega_0 - \frac{\kappa}{2}\right)\hat{b}_l + \frac{ig_3}{2}(2\hat{b}_r^\dagger\hat{b}_r + \hat{b}_l^\dagger\hat{b}_l)\hat{b}_l + \sqrt{\kappa_c}\hat{b}_{l,\text{in}} + \sqrt{\kappa_i}\hat{b}_l^{(i)} \quad (5.16)$$

The subscripts  $r$  and  $l$  represent CCW and CW directions, respectively. The mean field dynamics ( $\beta_r(\omega) = \langle \hat{b}_r(\omega) \rangle$ ,  $\beta_l(\omega) = \langle \hat{b}_l(\omega) \rangle$ ) is

$$\dot{\beta}_r = \left(-i\omega_0 - \frac{\kappa}{2}\right)\beta_r + \frac{ig_3}{2}(|\beta_r|^2 + 2|\beta_l|^2)\beta_r + \sqrt{\kappa_c}\beta_{r,\text{in}} \quad (5.17)$$

$$\dot{\beta}_l = \left(-i\omega_0 - \frac{\kappa}{2}\right)\beta_l + \frac{ig_3}{2}(2|\beta_r|^2 + |\beta_l|^2)\beta_l + \sqrt{\kappa_c}\beta_{l,\text{in}} \quad (5.18)$$

Assuming the pump power in CCW and CW direction has the same value  $\beta_{r,\text{in}} = \beta_{l,\text{in}} = \sqrt{\frac{P_{\text{in}}}{\hbar\omega_p}} e^{-i\omega_p t}$ , with  $P_{\text{in}}$  the pump power and  $\omega_p$  the pump frequency, we can obtain the steady-state equations

$$0 = (i\Delta_p - \frac{\kappa}{2})\beta_r + \frac{ig_3}{2}(|\beta_r|^2 + 2|\beta_l|^2)\beta_r + \sqrt{\frac{\kappa_c P_{\text{in}}}{\hbar\omega_p}} \quad (5.19)$$

$$0 = (i\Delta_p - \frac{\kappa}{2})\beta_l + \frac{ig_3}{2}(2|\beta_r|^2 + |\beta_l|^2)\beta_l + \sqrt{\frac{\kappa_c P_{\text{in}}}{\hbar\omega_p}}. \quad (5.20)$$

with  $\Delta_p = \omega_p - \omega_0$  the frequency difference between the pump field and fundamental resonance. We can further define the intra-cavity photon number for optical fields in CCW and CW directions  $N_r = |\beta_r|^2$  and  $N_l = |\beta_l|^2$ , which are real numbers. Then we can solve the cavity status in the real number domain.

$$\frac{\kappa^2}{4}N_r + \left[ \Delta_p + \frac{g_3(N_r + 2N_l)}{2} \right]^2 N_r = \frac{\kappa_c P_{\text{in}}}{\hbar\omega_p} \quad (5.21)$$

$$\frac{\kappa^2}{4}N_l + \left[ \Delta_p + \frac{g_3(2N_r + N_l)}{2} \right]^2 N_l = \frac{\kappa_c P_{\text{in}}}{\hbar\omega_p} \quad (5.22)$$

We are interested in the imbalance between the two directions. Therefore, we further define the photon number difference  $N_- = N_r - N_l$  and the total photon number  $N_+ = N_r + N_l$ . Then, the steady-state equations become

$$N_- \left[ g_3^2 N_-^2 + 4\kappa^2 + (3g_3 N_+ + 4\Delta_p)(g_3 N_+ + 4\Delta_p) \right] = 0 \quad (5.23)$$

$$N_+ \left[ 4\kappa^2 + (3g_3 N_+ + 4\Delta_p)^2 \right] = 32 \frac{\kappa_c P_{\text{in}}}{\hbar\omega_p} + (5g_3 N_+ + 8\Delta_p)g_3 N_-^2 \quad (5.24)$$

The behavior of the cavity can be qualitatively obtained by analyzing Eq. (5.23). At low pump power, both  $N_+$  and  $N_-$  are small. The term in the square brackets in Eq. (5.23) is dominated by  $\kappa^2$  or  $\Delta_p^2$ , which always has positive values. Therefore, the only possible real solution for Eq. (5.23) is  $N_- = 0$ . The optical fields in CCW and CW directions have the same power, and thus do not show chirality.

With a large pump power,  $N_+$  increases. The term in the square brackets in Eq. (5.23) is dominated by  $(3g_3 N_+ + 4\Delta_p)(g_3 N_+ + 4\Delta_p)$ , which can show negative value with negative frequency detune  $\Delta_p \in (-3g_3 N_+/4, -g_3 N_+/4)$ . If the cavity

loss  $\kappa$  is small, we can have three real solutions to Eq. (5.23)

$$N_- = 0, \pm \sqrt{-4\kappa^2 - (3g_3N_+ + 4\Delta_p)(g_3N_+ + 4\Delta_p)} \quad (5.25)$$

In this case, the  $N_- = 0$  is not stable, while the other non-zero solutions are stable. Therefore, the optical fields in CCW and CW directions will have power differences, showing chiral behavior (Fig. 5.6a). The transition condition between the single-solution and triple-solution regime can be obtained by setting the term in the square brackets in Eq. (5.23) to be zero under the condition  $N_- = 0$ , which gives

$$4\kappa^2 + (3g_3N_+ + 4\Delta_p)(g_3N_+ + 4\Delta_p) = 0 \quad (5.26)$$

The corresponding input pump power can also be obtained from Eq. (5.24)

$$P_{\text{in}} = \frac{\hbar\omega_p}{32\kappa_c} \cdot N_+ [4\kappa^2 + (3g_3N_+ + 4\Delta_p)^2] \quad (5.27)$$

In our experiment, the input pump frequency is scanned across the resonance. Therefore, the occurrence of spontaneous symmetry breaking is determined by the smallest pump power for all possible frequency detune values. At frequency detune  $\Delta_p = -\frac{5\sqrt{3}}{6}\kappa$ , we have the smallest pump power for Eq. (5.27)

$$P_0 = \min P_{\text{in}} = \frac{2\hbar\omega_p\kappa^3}{3\sqrt{3}\kappa_c g_3} \quad (5.28)$$

which is defined as the threshold power. Obviously, the threshold power is completely determined by the intrinsic properties of the nonlinear systems.

### Spontaneous Chiral Symmetry Breaking with Reconfigurable Kerr Nonlinearity

With reconfigurable Kerr nonlinearity, the equation of motion for CCW and CW optical fields should be rewritten as

$$\dot{\beta}_r = \left\{ -i\omega_0 - \frac{\kappa - ig_{\text{eff}}|\beta_r|^2}{2} + ig_3|\beta_l|^2 \right\} \beta_r + \sqrt{\kappa_c}\beta_{r,\text{in}} \quad (5.29)$$

$$\dot{\beta}_l = \left\{ -i\omega_0 - \frac{\kappa - ig_{\text{eff}}|\beta_l|^2}{2} + ig_3|\beta_r|^2 \right\} \beta_l + \sqrt{\kappa_c}\beta_{l,\text{in}}, \quad (5.30)$$

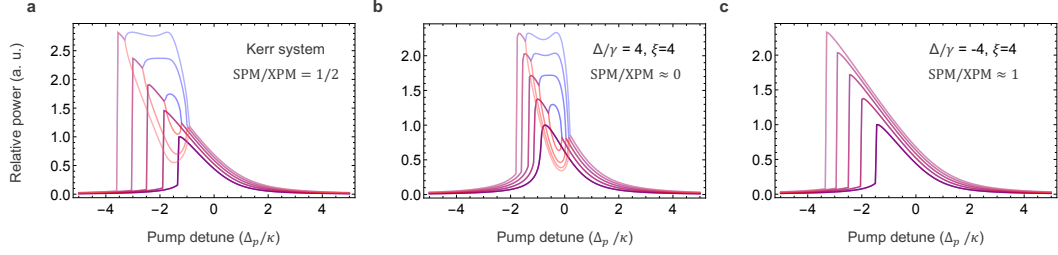


Figure 5.6: **Spontaneous symmetry breaking of photonic chirality.** **a**, Calculated intra-cavity power in CCW and CW directions with intrinsic Kerr nonlinearity,  $\text{SPM/XPM} = 1/2$ . **b**, Calculated intra-cavity power in CCW and CW directions with reconfigurable Kerr nonlinearity,  $\text{SPM/XPM} = 0$ . **c**, Calculated intra-cavity power in CCW and CW directions with reconfigurable Kerr nonlinearity,  $\text{SPM/XPM} = 1$ . For comparing threshold power for all figures, pump power is increased from  $0.55P_0$  to  $1.55P_0$  from bottom to up curves with  $0.25P_0$  steps. Symmetric power is shown in purple. The two branches of asymmetric power are shown in blue and red, respectively.

Following the same procedure, we can obtain the steady-state equation for intra-cavity photon numbers  $N_r = |\beta_r|^2$  and  $N_l = |\beta_l|^2$

$$\left\{ \left[ \frac{\kappa + g_{\text{eff}}^{\text{im}} N_r}{2} \right]^2 + \left[ \Delta_p + \frac{2g_3 N_l + g_{\text{eff}}^{\text{re}} N_r}{2} \right]^2 \right\} N_r = \frac{\kappa_c P_{\text{in}}}{\hbar \omega_p} \quad (5.31)$$

$$\left\{ \left[ \frac{\kappa + g_{\text{eff}}^{\text{im}} N_l}{2} \right]^2 + \left[ \Delta_p + \frac{2g_3 N_r + g_{\text{eff}}^{\text{re}} N_l}{2} \right]^2 \right\} N_l = \frac{\kappa_c P_{\text{in}}}{\hbar \omega_p} \quad (5.32)$$

with  $g_{\text{eff}}^{\text{re}} = \text{Re}[g_{\text{eff}}]$  and  $g_{\text{eff}}^{\text{im}} = \text{Im}[g_{\text{eff}}]$  the real and imaginary parts of the effective Kerr nonlinearity, respectively. If we control the cavity detuning such that  $g_{\text{eff}} = 0$ , the imbalance between SPM and XPM becomes larger. Therefore, spontaneous symmetry breaking can happen with lower power (Fig. 5.6b). If we control the cavity detuning to  $g_{\text{eff}} = 2g_3$ , the imbalance between SPM and XPM vanishes. Therefore, spontaneous symmetry breaking is prohibited regardless of the pump power (Fig. 5.6c).

### 5.3.3 Experimental Setups

The transmission spectrum of the pump field is recorded to measure the self-phase modulation effect. The measurement setup is shown in Fig. 5.7a. We use

a single-sideband modulation method to scan the frequency of the pump field with high speed [154, 155]. The single-sideband modulation module consists of a high-bandwidth optical IQ modulator. The two arms of the IQ modulator are driven with the same microwave frequency and power, but a  $90^\circ$  phase shift. The DC bias is tuned such that both the carrier and low-frequency sideband are suppressed, and only the high-frequency sideband is maintained. The microwave signal is derived from the voltage-controlled oscillator (VCO). By linearly changing the input voltage of VCO from 0 to 10 V, the output microwave frequency, thus the frequency offset of the optical sideband, is changed from 6 to 12 GHz. The frequency scan is repeated with a 3 MHz rate. The single optical sideband is further amplified with an erbium-doped fiber amplifier (EDFA) to serve as the pump field.

A small portion of the pump field is tapped to monitor the power stability. After the wavelength-division multiplexer (WDM), the pump field is coupled into the cavity. The output pump field is collected by an infrared (IR) photodetector and an optical spectrum analyzer. The second-harmonic field is separated from the pump field with WDM and detected by a visible photodetector. Output signals from IR and visible photodetectors are sent into an oscilloscope, which is triggered by the linear voltage signal. Optical attenuators (OA) are added before photodetectors to prevent power saturation. The IR and visible photodetectors have bandwidths of 1 GHz and 125 MHz, respectively, which are sufficient to capture fast frequency modulation.

To observe the spontaneous symmetry breaking, we use a symmetric setup to measure the pump and second-harmonic fields in both directions at the same time (Fig. 5.7b). The pump field is split equally into two paths after EDFA. Tunable optical attenuators are used to control the pump power difference below 1% between the two directions. Optical circulators are used on both sides to separate the input and output pump fields. Second-harmonic fields are separated from pump fields by WDMs. Output signals from IR and visible photodetectors are recorded by an oscilloscope for post-processing.



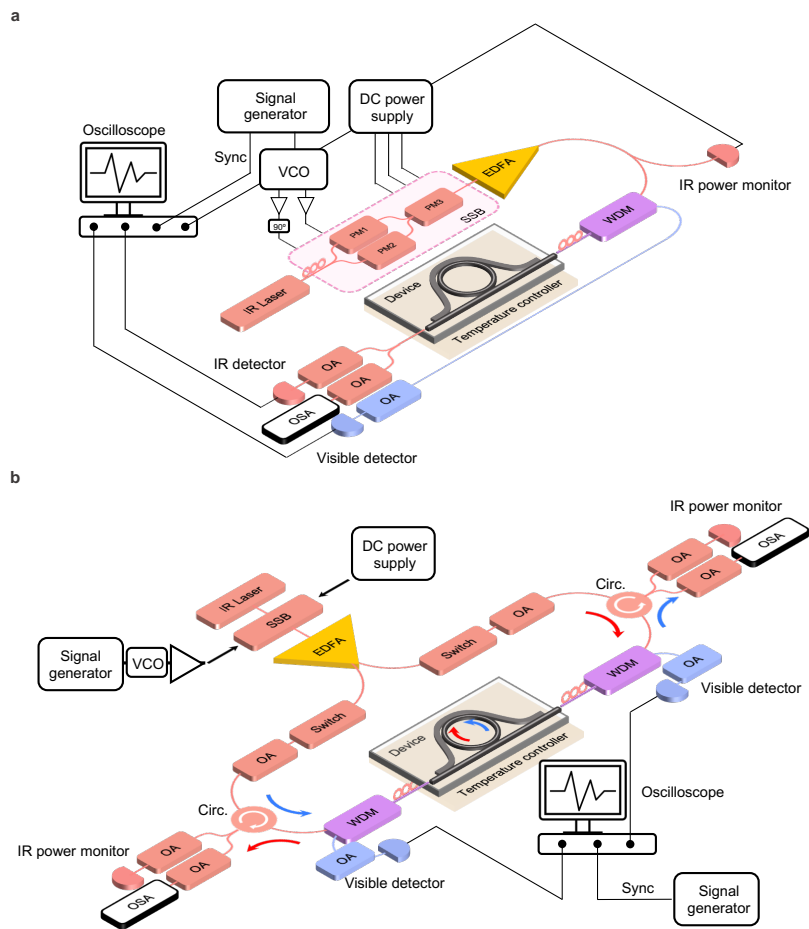


Figure 5.7: **Experimental setups.** **a**, The experimental setup for transmission measurement with fast frequency scan. **b**, The experimental setup for the measurement of spontaneous symmetry breaking. PM: phase modulator; EDFA: erbium-doped fiber amplifier; OA: optical attenuator; OSA: optical spectrum analyzer; VCO: voltage-controlled oscillator. WDM: wavelength-division multiplexer. Circ.: Optical circulator.

### 5.3.4 Basic Device Parameters

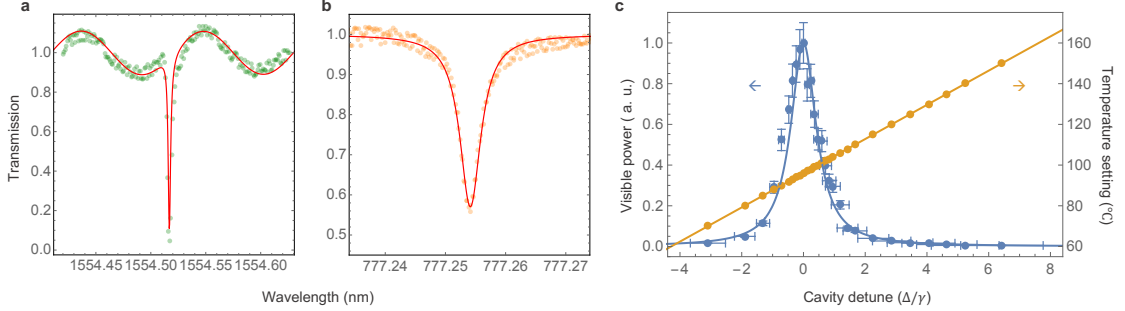


Figure 5.8: **Linear and nonlinear properties of the target cavities.** **a**, Fundamental resonance transmission spectrum. **b**, Second-harmonic resonance transmission spectrum. **c**, Normalized second-harmonic power with different cavity detuning and device temperature.

The aluminum nitride ring cavity has a radius of  $60 \mu\text{m}$ , a thickness of  $1 \mu\text{m}$ , and a width of  $1.1 \mu\text{m}$ . The quality factor of the fundamental resonance is  $5.82 \times 10^5$ , corresponding to the resonance total loss rate  $\kappa \approx 2\pi \times 330 \text{ MHz}$ . Assuming under-coupled resonance, the coupling rate of  $\kappa_c \approx 0.33\kappa$  is obtained from the extinction ratio  $\approx 0.15$ . The quality factor of the second-harmonic resonance is  $1.83 \times 10^5$ , corresponding to the resonance total loss rate  $\gamma \approx 2\pi \times 2.0 \text{ GHz}$ . With aluminum nitride Pockels nonlinear coefficient  $\chi^{(2)} \approx 1 \text{ pm/V}$ , we can calculate the second-order nonlinear strength  $g_2 = 2\pi \times 122 \text{ kHz}$  from Eq. 2.184 [97]. With aluminum nitride Kerr nonlinear coefficient  $n_2 \approx 2.8 \times 10^{-19} \text{ m}^2/\text{W}$ , we can calculate the Kerr nonlinear strength  $g_3 = 2\pi \times 2 \text{ Hz}$ . Therefore, we can get the relative strength between cascaded and intrinsic Kerr nonlinearity  $\xi = |g_2|^2/(g_3\gamma) \approx 3.7$ . The threshold power for spontaneous symmetry breaking with intrinsic Kerr nonlinearity  $P_0 = \frac{2\hbar\omega_p\kappa^3}{3\sqrt{3}\kappa_c g_3} \approx 51 \text{ mW}$ .

During the experiment, the cavity detuning between fundamental and second-harmonic resonances is controlled by changing the device temperature. The actively stabilized heater can maintain the temperature with the precision of  $0.1 \text{ Celsius}$  degree. The tuning sensitivity is  $0.2 \text{ GHz per degree}$  (Fig. 5.8a). Therefore, the cavity detune resolution is  $20 \text{ MHz}$ , which is much smaller than the fundamental

resonance linewidth  $\kappa \approx 2\pi \times 330$  MHz and second-harmonic resonance linewidth  $\gamma \approx 2\pi \times 2.0$  GHz.

### 5.3.5 Additional Data for Spontaneous Chiral Symmetry Breaking

Here we present the additional data of the selected output second harmonic power spectrum under the bi-directional pump used in Fig. 5.4f of the main text.

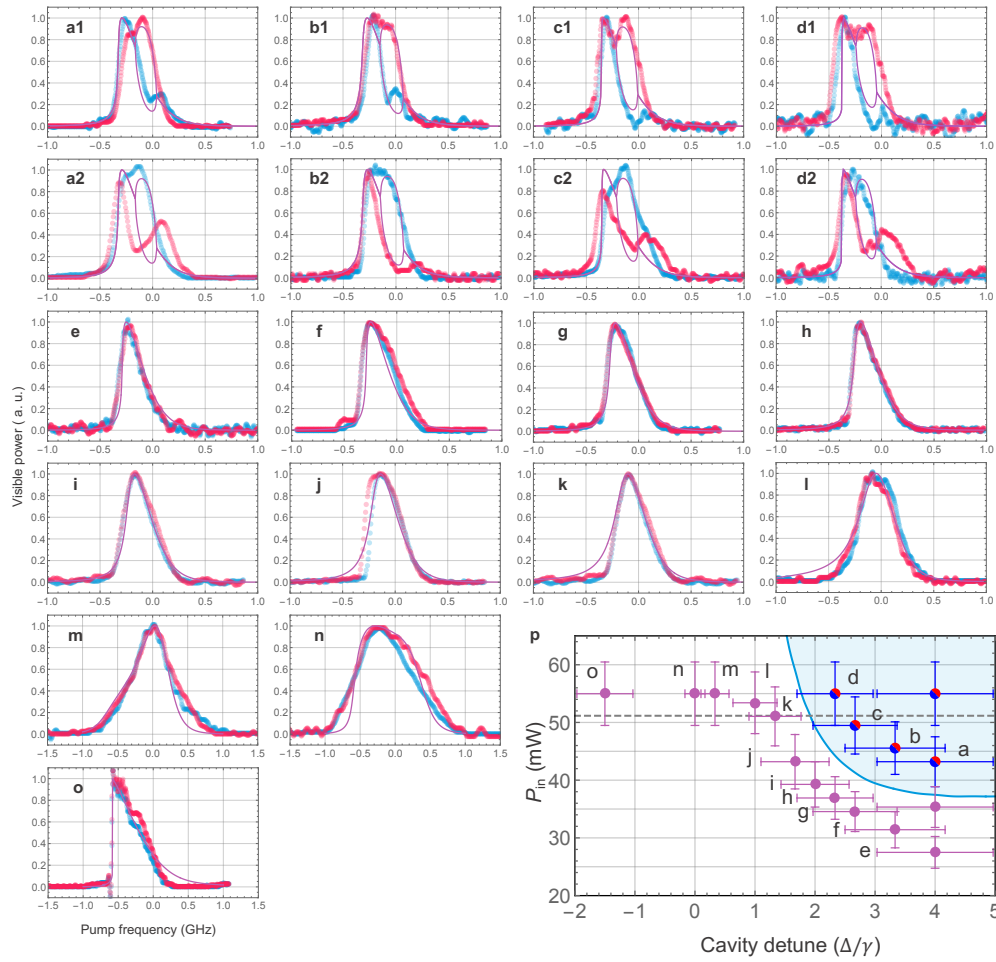


Figure 5.9: **Additional data.** **a1-o** Additional data for Fig. 5.4f in the main text. Measured output second-harmonic power in clockwise and counterclockwise directions are shown in blue and red, respectively. The corresponding cavity detuning and power conditions are labeled in **p**, a copy of Fig. 5.4 in the main text. The Blue shaded area corresponds to the condition for spontaneous symmetry breaking.

## CHAPTER 6

High-Purity Pulsed Squeezing Generation in Integrated Photonics<sup>†</sup>**6.1 Abstract**

Squeezed light has evolved into a powerful tool for quantum technology, ranging from quantum-enhanced sensing and quantum state engineering based on partial post-selection techniques. The pulsed generation of squeezed light is of particular interest, as it can provide accurate time stamps and a physically defined temporal mode, which are highly preferred in complex communication networks and large-scale information processing. However, the multi-mode feature of pulsed squeezing limits the purity of the output state, negatively impacting its application in quantum technology. Previous demonstrations and analysis of pulsed squeezing focus on single-pass configuration and synchronously pumped free-space cavities. In this Letter, we propose a new approach to generate pulsed squeezing with high temporal purity. Parametric down-conversion in integrated photonic cavities is pumped by single-pass pulses. We show that the effective mode number of the output pulsed squeezing approaches unity. Such a high-purity squeezed light can be realized with broad parameters and low pump power, providing a robust approach to generating large-scale quantum resources.

**6.2 Main Article****6.2.1 Introduction**

Non-Gaussian states are indispensable resources required by quantum information processing to demonstrate quantum advantage [156]. Partial detection of

---

<sup>†</sup>This chapter has been published previously as [6]

squeezed light is one of the most important optical approaches to generate non-Gaussian states [157, 158, 159, 160, 161]. Optical cat and kitten states have been generated based on photon-number subtraction from a single-mode squeezed vacuum [162, 163, 164, 165]. In principle, arbitrary non-Gaussian states, including the Gottesman-Kitaev-Preskill (GKP) state for cluster-modal quantum computing [166, 167, 168, 169, 170, 171, 6], can be generated based on the Gaussian-Boson-Sampling (GBS) configuration and the photon-number-resolving (PNR) detection [172, 173]. One critical requirement to implement partial detection of squeezed light is that all photons must be in the same spectral-temporal mode. Otherwise, unconditioned Gaussian modes will be mixed with the target non-Gaussian mode, thus decreasing the purity of the output state. Common techniques utilized for single photons, such as spectral filtering and post-selection within a small time window, cannot be applied for the squeezed light due to the excess loss. Improved pulsed squeezing also finds applications beyond the engineering of non-Gaussian states of light. For example, imaging of delicate biological samples can benefit from pulsed squeezing by improving the sensitivity beyond standard quantum limit [174].

The standard configuration to implement pulsed squeezing is single-pass parametric down-conversion [175, 176, 177, 178, 179]. This process intrinsically involves multiple modes in both space and time, which all have significant squeezing and energy [180]. Synchronously-pumped parametric down-conversion in free-space cavities has also been proposed for pulsed squeezing [181, 182]. However, the generated squeezing still contains significant multi-mode contributions. It also requires that the pump repetition rate matches the cavity free-spectra-range (FSR), which is challenging for integrated cavities with a large FSR. While the complex shaping of local oscillators can be utilized to improve the measured squeezing level [183], it does not work well on non-Gaussian state generation through partial detection, which requires the separation of different modes. Therefore, a new approach to generating pulsed squeezing with high purity is highly desired to further improve the capability of photonic quantum information processing.

In this Letter, we analyze pulsed squeezing with an unexplored configuration,

cavity-enhanced parametric down-conversion with single-pass pulse pumps. Such configuration is well-positioned for pulsed squeezing generation with integrated photonic cavities, with FSR much larger than the pulse pump bandwidth. The Bloch-Messiah approach is used to decompose the input-output relation into independent squeezing modes [184, 185]. We demonstrate that the effective mode number at the output can approach unity, showing there is only one dominant spectral-temporal mode. Unlike the single-pass pulsed squeezing [180], this approach does not require the delicate shaping of the pump, making its experimental implementation robust.

### 6.2.2 Theoretical Model

The proposed configuration is shown in Fig. 6.1 and consists of a photonic ring cavity evanescently coupled to a bus waveguide. Phase-matching condition is satisfied for degenerate parametric down-conversion between the pump mode centering at frequency  $2\omega_0$  and the signal mode centering at frequency  $\omega_0$ . The input pump pulse with a center frequency  $2\omega_0$  is launched into the cavity through the bus waveguide.

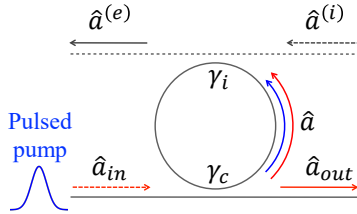


Figure 6.1: **Proposed configuration for high-purity pulsed squeezing generation: parametric down-conversion in a photonic ring cavity with a pulsed pump.** The solid line represents the bus waveguide with signal coupling rate  $\gamma_c$ , input mode  $\hat{a}_{\text{in}}$ , and output mode  $\hat{a}_{\text{out}}$ ; the dotted line represents the virtual waveguide for the intrinsic loss channel with loss rate  $\gamma_i$ , input mode  $\hat{a}^{(i)}$ , and output mode  $\hat{a}^{(e)}$ .

The dynamics of the intra-cavity signal mode  $\hat{a}$  can be described by the equation of motion [11, 186],

$$\frac{d\hat{a}}{dt} = \frac{i}{\hbar}[\hat{H}, \hat{a}] - \frac{\gamma}{2}\hat{a} + \sqrt{\gamma_i}\hat{a}^{(i)} + \sqrt{\gamma_c}\hat{a}_{\text{in}} \quad (6.1)$$

with intrinsic loss rate  $\gamma_i$ , bus waveguide coupling rate  $\gamma_c$ , total cavity decay  $\gamma = \gamma_i + \gamma_c$ , and noise operators due to intrinsic loss  $\hat{a}^{(i)}$  and bus waveguide  $\hat{a}_{\text{in}}$ . The Hamiltonian  $\hat{H}$  can be written as

$$\begin{aligned} \hat{H} = & \hbar\omega_0 \int d\omega \hat{a}^\dagger(\omega) \hat{a}(\omega) \\ & + \frac{i\hbar\kappa}{2} \iint d\omega d\omega' \hat{a}^\dagger(\omega) \hat{a}^\dagger(\omega') \varepsilon(\omega + \omega') + h.c. \end{aligned} \quad (6.2)$$

with  $\kappa$  the single photon coupling rate for parametric down-conversion. The intra-cavity pump field  $\varepsilon(\omega)$  is written as

$$\varepsilon(\omega) = E_p(\omega) \frac{\sqrt{\gamma_{pc}}}{-i(\omega - 2\omega_0) + \gamma_p/2} \quad (6.3)$$

with the bus waveguide coupling rate  $\gamma_{pc}$  and total decay rate  $\gamma_p$  for the pump mode, and  $E_p(\omega)$  the spectrum amplitude of the input pulse. Utilizing Fourier transformation, Eq. (6.1) can be further expressed in the frequency domain

$$\begin{aligned} 0 = & \int d\omega' [i(\omega - \omega_0) - \frac{\gamma}{2}] \delta(\omega - \omega') \hat{a}(\omega') \\ & + \int d\omega' \kappa \varepsilon(\omega + \omega') \hat{a}^\dagger(\omega') + \sqrt{\gamma_i} \hat{a}^{(i)}(\omega) + \sqrt{\gamma_c} \hat{a}_{\text{in}}(\omega). \end{aligned} \quad (6.4)$$

By including the complex-conjugation, we can rewrite Eq. (6.4) into the following equivalent matrix form

$$0 = \begin{pmatrix} D & E \\ E^\dagger & D^\dagger \end{pmatrix} \begin{pmatrix} \hat{a}(\omega) \\ \hat{a}^\dagger(\omega) \end{pmatrix} + \sqrt{\gamma_i} \begin{pmatrix} \hat{a}^{(i)}(\omega) \\ \hat{a}^{(i)\dagger}(\omega) \end{pmatrix} + \sqrt{\gamma_c} \begin{pmatrix} \hat{a}_{\text{in}}(\omega) \\ \hat{a}_{\text{in}}^\dagger(\omega) \end{pmatrix} \quad (6.5)$$

where the diagonal matrix  $D(\omega, \omega') = [i(\omega - \omega_0) - \gamma/2] \cdot \delta(\omega - \omega')$  shows the effect of frequency detuning and energy decay, and the matrix  $E(\omega, \omega') = \kappa \varepsilon(\omega + \omega')$  shows the nonlinear interaction enhanced by the pump. The output field can then be derived based on the input-output theory

$$\begin{aligned} \begin{pmatrix} \hat{a}_{\text{out}}(\omega) \\ \hat{a}_{\text{out}}^\dagger(\omega) \end{pmatrix} = & \left[ \begin{pmatrix} I & \\ & I \end{pmatrix} + \gamma_c \begin{pmatrix} D & E \\ E^\dagger & D^\dagger \end{pmatrix}^{-1} \right] \begin{pmatrix} \hat{a}_{\text{in}}(\omega) \\ \hat{a}_{\text{in}}^\dagger(\omega) \end{pmatrix} \\ & + \sqrt{\gamma_c \gamma_i} \begin{pmatrix} D & E \\ E^\dagger & D^\dagger \end{pmatrix}^{-1} \begin{pmatrix} \hat{a}^{(i)}(\omega) \\ \hat{a}^{(i)\dagger}(\omega) \end{pmatrix}. \end{aligned} \quad (6.6)$$

Here we assume that the intrinsic loss of the photonic cavity is Markovian, and can be modeled as a virtual waveguide with the input mode  $\hat{a}^{(i)}$  and output mode  $\hat{a}^{(e)}$  (dashed line in Fig. 6.1) [9, 186]. Then Eq. (6.6) is converted to the symplectic form

$$\begin{aligned} \begin{pmatrix} \hat{a}_{\text{out}}(\omega) \\ \hat{a}_{\text{out}}^\dagger(\omega) \\ \hat{a}^{(e)}(\omega) \\ \hat{a}^{(e)\dagger}(\omega) \end{pmatrix} &= \begin{pmatrix} \left[ \begin{pmatrix} I & \\ & I \end{pmatrix} + \gamma_c \begin{pmatrix} D & E \\ E^\dagger & D^\dagger \end{pmatrix}^{-1} \right] & \sqrt{\gamma_c \gamma_i} \begin{pmatrix} D & E \\ E^\dagger & D^\dagger \end{pmatrix}^{-1} \\ \sqrt{\gamma_c \gamma_i} \begin{pmatrix} D & E \\ E^\dagger & D^\dagger \end{pmatrix}^{-1} & \left[ \begin{pmatrix} I & \\ & I \end{pmatrix} + \gamma_i \begin{pmatrix} D & E \\ E^\dagger & D^\dagger \end{pmatrix}^{-1} \right] \end{pmatrix} \begin{pmatrix} \hat{a}_{\text{in}}(\omega) \\ \hat{a}_{\text{in}}^\dagger(\omega) \\ \hat{a}^{(i)}(\omega) \\ \hat{a}^{(i)\dagger}(\omega) \end{pmatrix} \\ &= \begin{pmatrix} \sqrt{\frac{\gamma_c}{\gamma}} & -\sqrt{\frac{\gamma_i}{\gamma}} \\ \sqrt{\frac{\gamma_i}{\gamma}} & \sqrt{\frac{\gamma_c}{\gamma}} \end{pmatrix} \begin{pmatrix} \left[ \begin{pmatrix} I & \\ & I \end{pmatrix} + \gamma \begin{pmatrix} D & E \\ E^\dagger & D^\dagger \end{pmatrix}^{-1} \right] & 0 \\ 0 & \begin{pmatrix} I & \\ & I \end{pmatrix} \end{pmatrix} \begin{pmatrix} \sqrt{\frac{\gamma_c}{\gamma}} & \sqrt{\frac{\gamma_i}{\gamma}} \\ -\sqrt{\frac{\gamma_i}{\gamma}} & \sqrt{\frac{\gamma_c}{\gamma}} \end{pmatrix} \begin{pmatrix} \hat{a}_{\text{in}}(\omega) \\ \hat{a}_{\text{in}}^\dagger(\omega) \\ \hat{a}^{(i)}(\omega) \\ \hat{a}^{(i)\dagger}(\omega) \end{pmatrix}. \end{pmatrix} \quad (6.7) \end{aligned}$$

The Bloch-Messiah decomposition means that an arbitrary Gaussian transformation can be represented by two passive linear-optical interferometers ( $P$  and  $Q$  in our case) intermitted by parallel squeezing transformations. This allows us to rewrite the core matrix  $\left[ \begin{pmatrix} I & \\ & I \end{pmatrix} + \gamma \begin{pmatrix} D & E \\ E^\dagger & D^\dagger \end{pmatrix}^{-1} \right]$  into a combination of a set of single-mode squeezers (Bogoliubov transformations) placed between two multi-port interferometers [184, 185].

$$\begin{aligned} &\left[ \begin{pmatrix} I & \\ & I \end{pmatrix} + \gamma \begin{pmatrix} D & E \\ E^\dagger & D^\dagger \end{pmatrix}^{-1} \right] \\ &= \begin{pmatrix} P & \\ & P^* \end{pmatrix} \begin{pmatrix} \cosh \xi_1 & & e^{i\theta_1} \sinh \xi_1 & \\ & \dots & & \dots \\ & & \cosh \xi_n & e^{i\theta_n} \sinh \xi_n \\ e^{-i\theta_1} \sinh \xi_1 & & & \cosh \xi_1 \\ & \dots & & \dots \\ & & e^{-i\theta_n} \sinh \xi_n & \cosh \xi_n \end{pmatrix} \begin{pmatrix} Q^\dagger \\ & Q^T \end{pmatrix} \quad (6.8) \end{aligned}$$

Therefore, the overall input-output relation is modeled as a multi-mode optical parametric amplifier sandwiched by two beamsplitters with reflection  $R = \gamma_c/\gamma$



(Fig. 6.2). The spectral-temporal shape of the characteristic input modes of each single-mode squeezer ( $b_{\text{in},k}$ ) is determined by the unitary transformation  $Q$ .

$$\hat{b}_{\text{in}} = Q^\dagger \left( \sqrt{\frac{\gamma_c}{\gamma}} \hat{a}_{\text{in}}(\omega) + \sqrt{\frac{\gamma_i}{\gamma}} \hat{a}^{(i)}(\omega) \right). \quad (6.9)$$

Each characteristic mode undergoes independent squeezing

$$\hat{b}_{\text{out},k} = \cosh \xi_k \hat{b}_{\text{in},k} + e^{i\theta_k} \sinh \xi_k \hat{b}_{\text{in},k}^\dagger \quad (6.10)$$

where  $\xi_k$  and  $\theta_k$  are the squeezing amplitude and phase of the  $k$ th mode. After mixing with the vacuum at the second beamsplitter, the variance of the squeezed quadrature of the  $k$ th mode is

$$\langle (\Delta X_k(\frac{\theta_k - \pi}{2}))^2 \rangle = \frac{1}{2} \left( \frac{\gamma_i}{\gamma} + \frac{\gamma_c}{\gamma} e^{-2\xi_k} \right). \quad (6.11)$$

This result is identical to the CW-squeezing process [11], where the maximum squeezing is limited by the intrinsic loss of the cavity. Over-coupled cavity ( $\gamma_c \gg \gamma_i$ ) is required to realize high squeezing. The effective mode number  $K$  can be directly calculated from the squeezing amplitude  $\xi_k$ .

$$K = \frac{(\sum_k \sinh^2 \xi_k)^2}{\sum_k \sinh^4 \xi_k} \quad (6.12)$$

Higher mode number  $K$  infers a lower purity [45]. Since the squeezed light includes multi-photon components, the definition of purity is more general than the one for the single-photon case, where only the first-order term is considered.

Our derivation assumes that the pump is below the threshold so that all the output modes are still squeezed vacuum. The pump threshold can be determined when the gain for any intra-cavity mode is equal to the amplitude loss rate  $\gamma/2$ . By rewriting Eq. (6.1) into the rotation frame  $\hat{a} \rightarrow \hat{a} \cdot e^{i\omega_0 t}$  and taking the average on the initial vacuum state, we can express the classical dynamics of the intra-cavity field as

$$\langle \dot{\hat{a}} \rangle = -\frac{\gamma}{2} \langle \hat{a} \rangle + E \langle \hat{a} \rangle^*. \quad (6.13)$$

The solution to Eq. (6.13) has the form  $\langle \hat{a} \rangle_k = S_k \cdot e^{\lambda_k t}$ , where  $\lambda_k$  and  $S_k$  are the  $k$ th eigenvalue and eigenstate of matrix  $E$  [181]. We label the eigenvalue with

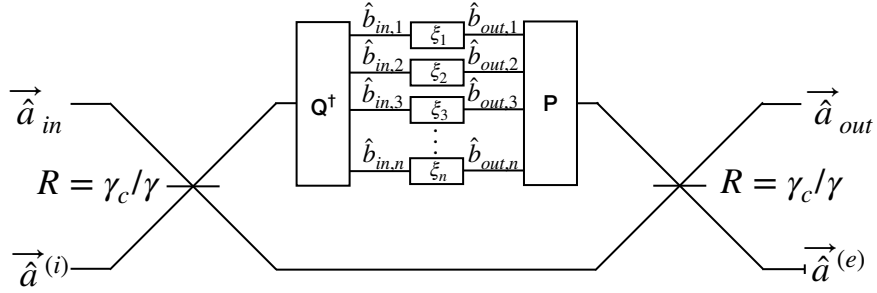


Figure 6.2: **Equivalent photonic circuit of parametric down-conversion in a photonic cavity with pulsed pump.**

the largest modulus as  $\lambda_0$ . As  $\lambda_0$  can always be made a real number by adjusting the global phase, the criteria for the threshold pump becomes  $\lambda_0 = \gamma/2$ . It is noteworthy that the eigenstates of the intra-cavity modes (decomposition of matrix  $E$ ) are different from the characteristic modes obtained at the output with the Bloch-Messiah decomposition of the core matrix in Eq. (6.7).

### 6.2.3 Numerical Simulation

As can be seen from the last section, all critical properties of the output state depend on the distribution of squeezing amplitude  $\xi_k$ . In order to get further insight, the generation of pulsed squeezing in photonic ring cavities is investigated numerically. Without loss of generality, we assume the input pump has a Gaussian spectrum shape  $E_p(\omega) \propto e^{-(4 \ln 2)(\omega - \omega_0)^2/\delta^2}$  with full-width-half-maximum (FWHM)  $\delta$ . The threshold condition needs to be determined first. Using the condition  $\lambda_0 = \gamma/2$ , we obtain the relation between the intra-cavity threshold power  $P_{th}$  and the pump bandwidth  $\delta$  (Fig. 6.3). Here we assume that the pump and signal modes have the same quality factor, thus  $\gamma_p = 2\gamma$ . Monotonic decay of the intra-cavity threshold power  $P_{th}$  with respect to the pump bandwidth  $\delta$  can be observed, due to the contribution from multiple pump frequency components. Compared with a CW pump, the intra-cavity threshold power can be decreased by three orders of magnitude, making this scheme highly power efficient.

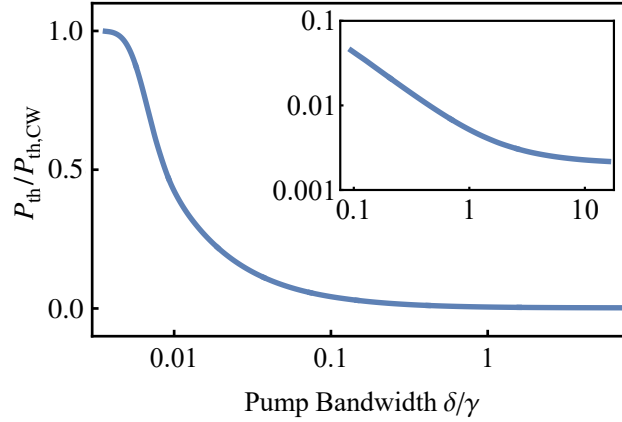


Figure 6.3: **The intra-cavity pump threshold power  $P_{\text{th}}$  with dependence on the pump bandwidth  $\delta$ .** The power is normalized with CW intra-cavity threshold  $P_{\text{th,CW}} = \epsilon\gamma^2/8\kappa^2$ , with  $\epsilon$  the absolute permittivity. The inset is the log scale plot. This figure assumes  $\gamma_p = 2\gamma$ .

Through the Bloch-Messiah decomposition of Eq. (6.7), we can obtain the spectral shape (Fig. 6.4) and squeezing amplitude (Fig. 6.5) of each characteristic mode. Then the squeezing level can be estimated with Eq. (6.11). The squeezing level of the first characteristic mode is plotted in Fig. 6.5(a). As expected, the squeezing level increases with pump power below the threshold, and lower intrinsic loss leads to higher squeezing. We further plot the squeezing level for high-order modes. Due to smaller optical gain, the squeezing level for high-order modes decreases rapidly (Fig. 6.5(b)). Based on Eq. (6.12), this indicates the output field will have a small effective mode number and high purity without any filtering and post-selection. When pump power is small, the effective mode number stays constant where entangled photon pairs are generated. With the pump power approaching the threshold, the effective mode number drops to a value limited by the pump bandwidth (Fig. 6.6(a)).

We further observe that the effective mode number decreases monotonically with both the input pump bandwidth  $\delta$  and the pump cavity linewidth  $\gamma_p$  (Fig. 6.6(b)&(c)). The signal cavity with a small linewidth  $\gamma$  will function as a spectral-temporal filter to enhance the first characteristic mode and suppress high-

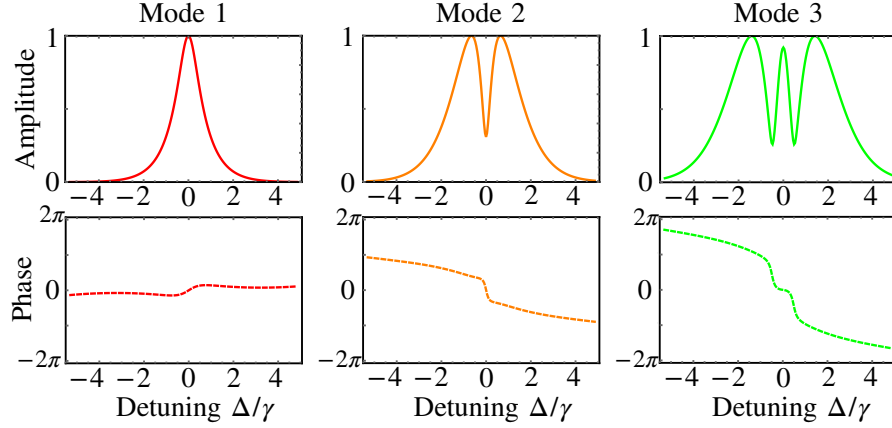


Figure 6.4: **The spectral amplitude (solid) and phase (dash) of the first three characteristic modes near the pump threshold.** This figure assumes  $\gamma_p = 2\gamma$  and  $\delta = 2\gamma_p$ .

order characteristic modes. With a larger input pump bandwidth  $\delta$  and pump cavity linewidth  $\gamma_p$ , the filtering effect is more significant, thus leading to a smaller effective mode number. This filtering effect is different from adding narrow filters after the squeezing generation, as the parametric down-conversion and the filtering happen simultaneously in the same cavity. Therefore, no extra loss will be introduced. This filtering effect can be clearly observed in Fig. 6.6(d), where the FWHM of the first characteristic mode increases rapidly with small pump bandwidths but saturate at large pump bandwidths.

In order to access the maximum squeezing, the spectral-temporal shape of the local oscillator must match the first characteristic mode. Based on the fact that the first characteristic mode shape is critically dependent on the filter effect of the signal cavity (Fig. 6.6(d)), we further design an easy and efficient method for the local oscillator shaping.

As shown in Fig. 6.7, the generation of the pulsed squeezing follows the standard configuration, where a strong optical pulse at the signal frequency is used to generate the pump pulse for parametric down-conversion. A small portion of the optical pulse is tapped to serve as the local oscillator. In order to match the spectral-temporal shape of the first characteristic mode, the optical pulse can simply go through an

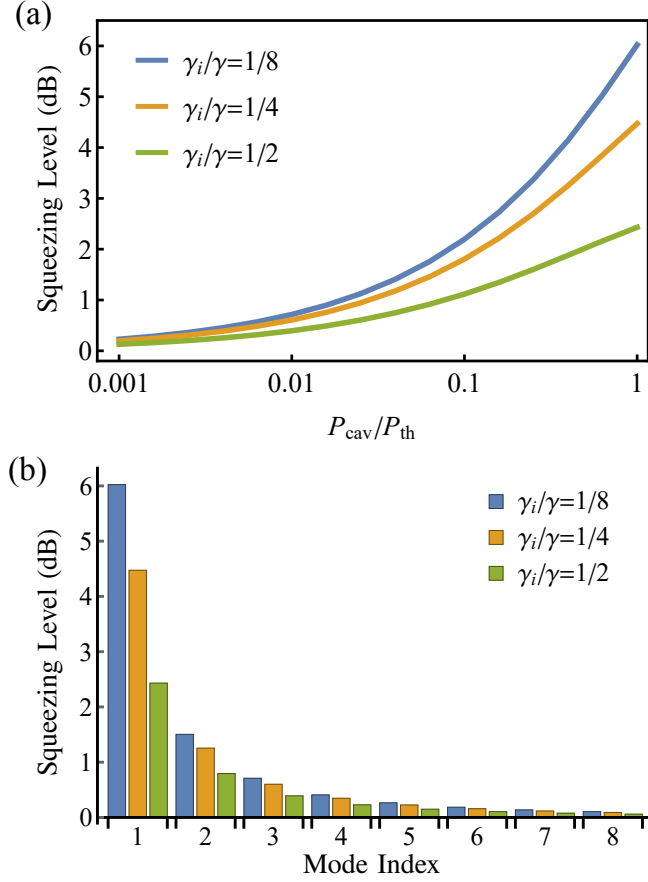


Figure 6.5: **Squeezing levels.** (a) Squeezing level of the first characteristic mode with different intra-cavity power  $P_{cav}$  and intrinsic loss  $\gamma_i$ . (b) Squeezing level of high-order characteristic modes with intra-cavity pump power at  $P_{cav} = 0.99P_{th}$ . This figure assumes  $\gamma_p = 2\gamma$  and  $\delta = 2\gamma_p$ .

optical cavity with Lorentzian lineshape. The cavity linewidth  $\gamma_f$  is optimized to obtain the maximum mode overlap and squeezing level (Fig. 6.8). With a small pump bandwidth, the system is in the quasi-CW regime, and a local oscillator without any mode shaping can achieve near-perfect mode matching. With a large pump bandwidth, the filter effect of the signal cavity is significant. A proper filter cavity for the local oscillator is required, and near-perfect matching can be achieved. As a small effective mode number is obtained only with a large pump bandwidth, this approach for the local oscillator shaping should be sufficient.

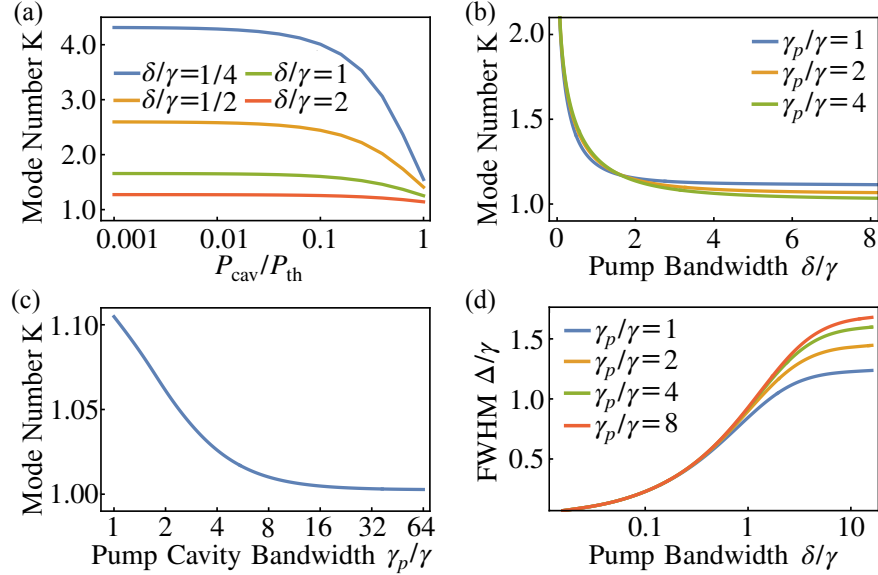


Figure 6.6: **Effective mode numbers.** (a) Effective mode number  $K$  as a function of intra-cavity pump power  $P_{\text{cav}}/P_{\text{th}}$  with different pump bandwidth  $\delta/\gamma$ . This figure assumes  $\gamma_p = 2\gamma$ . (b) Effective mode number  $K$  as a function of pump bandwidth  $\delta/\gamma$  with different pump cavity bandwidth  $\gamma_p$ . This figure assumes  $P_{\text{cav}} = 0.99P_{\text{th}}$ . (c) Effective mode number  $K$  as a function of pump cavity bandwidth  $\gamma_p$ . This figure assumes  $P_{\text{cav}} = 0.99P_{\text{th}}$  and  $\delta = 16\gamma$ . (d) FWHM of the first characteristic mode  $\Delta$  as a function of pump bandwidth  $\delta$  with different pump cavity linewidth  $\gamma_p$ . This figure assumes  $P_{\text{cav}} = 0.99P_{\text{th}}$ .

#### 6.2.4 Discussion

While the current analysis is based on degenerate parametric down-conversion, the generalization to non-degenerate cases is straightforward. The dynamics of intra-cavity modes for signal  $\hat{a}_1$  and idler  $\hat{a}_2$  can be written as

$$\begin{aligned}
 0 = & \int d\omega' [i(\omega - \omega_k) - \frac{\gamma}{2}] \delta(\omega - \omega') \hat{a}_k(\omega') \\
 & + \int d\omega' \kappa \varepsilon(\omega + \omega') \hat{a}_l^\dagger(\omega') + \sqrt{\gamma_i} \hat{a}_k^{(i)}(\omega) + \sqrt{\gamma_c} \hat{a}_{k,\text{in}}(\omega)
 \end{aligned} \tag{6.14}$$

with the index  $(k, l) = (1, 2)$  or  $(2, 1)$ . The Bloch-Messiah decomposition needs to be applied to the signal and idler modes simultaneously. All conclusions for degenerate cases remain valid for non-degenerate cases. The pulsed squeezing generation with non-degenerate configuration can be realized with both parametric down-conversion

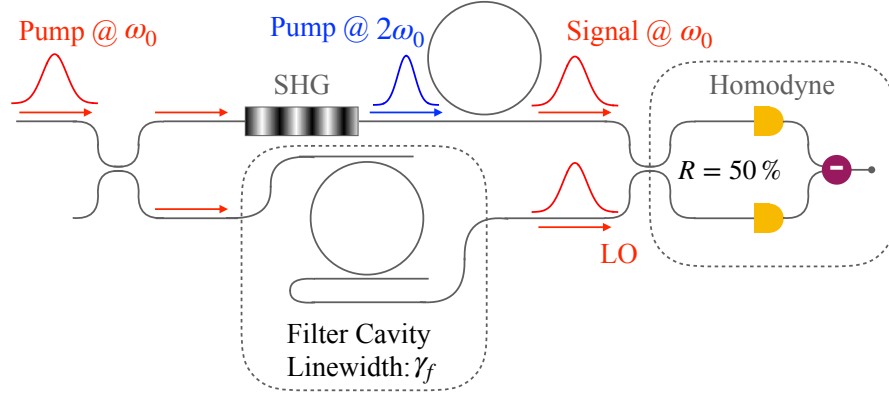


Figure 6.7: **Proposed setup for local oscillator shaping.**

[187] and four-wave-mixing [52]. For parametric down-conversion, it is easier to achieve a pump cavity linewidth much larger than a signal cavity linewidth ( $\gamma_p \gg \gamma$ ), due to the vastly different wavelengths. This is beneficial to achieve a small effective mode number. The recent development of aluminum nitride [97, 47, 187, 188], gallium arsenide [189], and lithium niobate [190, 191, 192] photonics has made it possible to demonstrate pulse squeezing with the proposed method<sup>1</sup>. On the other hand, four-wave-mixing has a wider collection of materials as it does not require non-centro-symmetric crystal structures. For four-wave-mixing, pump field in Eq. (6.3) needs to be modified as

$$\varepsilon(\omega) = \int d\omega' \frac{\sqrt{\gamma_{pc}} E_p(\omega - \omega')}{-i(\omega - \omega' - \omega_0) + \frac{\gamma_p}{2}} \frac{\sqrt{\gamma_{pc}} E_p(\omega')}{-i(\omega' - \omega_0) + \frac{\gamma_p}{2}}. \quad (6.15)$$

Based on Hydrex silica glass, single photons have been generated from degenerate four-wave-mixing with pulsed pumps. This corresponds to pump power being far below the threshold (Fig. 6.6a). Therefore, the experimental result matches our theoretical calculation well<sup>2</sup>. Recently, the CW-squeezed light has also been achieved

<sup>1</sup>Degenerate parametric down-conversion has been realized based on AlN ring cavities [193]. The linewidths for the signal and pump resonances are 192 MHz and 960 MHz, respectively. If pumped by Gaussian pulses with bandwidth  $\delta = 1$  GHz, our model predicts that the output mode could have an effective mode number  $K = 1.038$ .

<sup>2</sup>In Ref. [194], Hydrex silica cavity with  $\gamma_p = \gamma = 0.803$  GHz is pumped with a pulse (duration 0.6 ns and bandwidth 1.67 GHz). The effective mode number is measured to be 1.086. Based

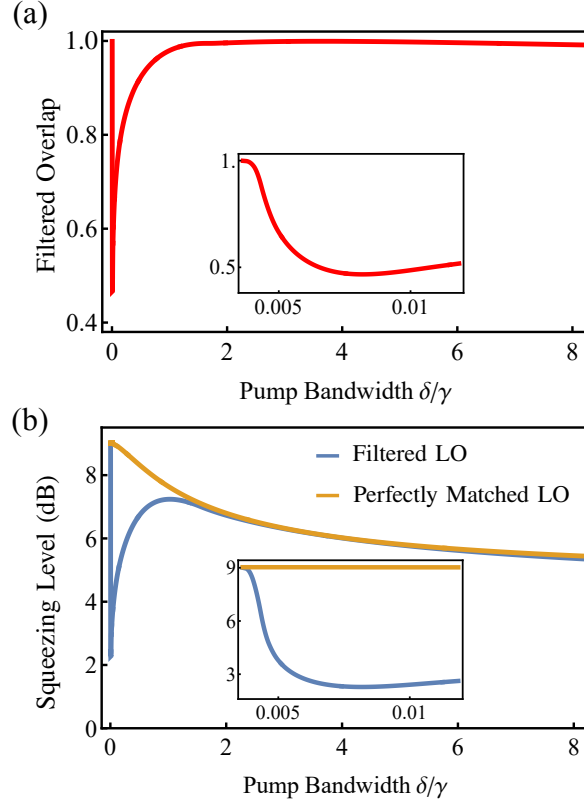


Figure 6.8: **Simulations of different pulsed pumps.** (a) The overlap between the first characteristic mode and the filtered local oscillator with dependence on  $\delta$  (b) Measured squeezing level as a function of  $\delta$  with filtered (blue) and perfectly matched local oscillator (orange). Insets are zoom-in of the intermediate region between the quasi-CW pump and the pulsed pump. This figure assumes  $P_{\text{cav}} = 0.99P_{\text{th}}$ ,  $\gamma_p = 2\gamma$ , and  $\gamma_i = 1/8\gamma$ .

with photonic ring cavities [195, 196], which brightens the way towards integrated pulsed squeezing generation.

### 6.2.5 Conclusion

In conclusion, we have proposed a novel approach to generate pulsed squeezing with high temporal purity. Parametric down-conversion in photonic cavities with a single on our theoretical mode, the effective mode number of  $K = 1.092$  is calculated in the low power regime, which matches the experiment.



pulsed pump is analyzed based on the Bloch-Messiah decomposition. We show that a near-unity effective mode number can be obtained. A large pump cavity linewidth and a pump bandwidth are preferred to decrease the effective mode number. As the dependence of the effective mode number on pump cavity linewidth and pump bandwidth is monotonic, no delicate balance between the pump power and linewidth is required, making the approach robust. An additional benefit is the low pump threshold due to the contribution from multiple frequency components, leading to the high power efficiency of this approach. We further designed an easy method to realize optimum matching between the local oscillator and output characteristic mode for maximum squeezing measurement. The robustness, high efficiency, and easy match make this approach promising for large-scale quantum networks and complex quantum state generation.

## CHAPTER 7

Customized Poling for High-Purity Indistinguishable Photon-Pair Generation <sup>†</sup>**7.1 Abstract**

Indistinguishable single photons are key ingredients for a plethora of quantum information processing applications ranging from quantum communications to photonic quantum computing. A mainstream platform to produce indistinguishable single photons over a wide spectral range is based on bi-photon generation through spontaneous parametric down-conversion (SPDC) in nonlinear crystals. The purity of the SPDC bi-photons, however, is limited by their spectral correlations. Here, we present a design recipe, based on a machine-learning framework, for the engineering of bi-photon joint spectrum amplitudes over a wide spectral range. By customizing the poling profile of the  $\text{KTiOPO}_4$  (KTP) crystal, we show, numerically, that spectral purities of 99.22%, 99.99%, and 99.82% can be achieved, respectively, in the 1310-nm, 1550-nm, and 1600-nm bands after applying a moderate 8-nm filter. The machine-learning framework thus enables the generation of near-indistinguishable single photons over the entire telecommunication band without resorting to KTP crystal's group-velocity-matching wavelength window near 1582 nm.

**7.2 Main Article****7.2.1 Introduction**

Quantum information science is an emerging area of study that creates new opportunities for next-generation communication, computing, and sensing applications. Photons are unique quantum-information carriers as they can be transmitted over long distances for entanglement distribution [197, 198], secure communication

---

<sup>†</sup>This chapter has been published previously as [5]

[199, 200], and sensing [201, 202, 203]. In addition, single photons would be critical resources in near-term quantum-computing devices for, e.g., Boson Sampling [204, 205, 206, 207, 208], to demonstrate a performance advantage over any classical computing platforms, a.k.a., the quantum supremacy.

Specifically, the quantum internet [209, 210] will be empowered by single photons that herald the creation of entanglement between network nodes at a distance [211]. Such a capability underpins distributed quantum computing [212, 213, 214] and distributed quantum sensing [215, 216, 217, 218]. The quality of the heralded entanglement, produced by interfering two single photons on a beamsplitter to erase the which-way information, is critically dependent on the indistinguishability and the purity of the two photons. To ensure high performance for quantum-information applications, the interfering photons need to share the same spectral, temporal, spatial, and polarization states [219, 220]. In addition, it is desirable that the single photons situate in the telecommunication band to leverage the abundant modulation, transmission, and detection devices for long-distance quantum communications.

Nonlinear crystals are widely employed to produce entangled and heralded single photons [221, 222, 223, 224]. Compared to solid-state single-photon emitters such as quantum dots and nitrogen-vacancy centers, nonlinear crystals enjoy room-temperature operations, the capability of generating photons in the telecommunication band, and the absence of spectral diffusion that degrades the purity of the produced photons.  $\text{KTiOPO}_4$  (KTP), in this regard, is a widely used nonlinear crystal material by virtue of its high nonlinearity and broad transparency window. In particular, KTP possesses a group-velocity-matching (GVM) wavelength around 1582 nm [222] vouchsafed by its material dispersion in type-II SPDC processes. Such a unique property has been harnessed to generate spectrally-uncorrelated bi-photons near the telecommunication c-band at 1550 nm. To achieve phase matching, two crystal poling strategies have been pursued. In the conventional periodic poling strategy, shown in Fig. 7.1 (top), the positive and negative polarities each constitutes half of the duty cycle in each poling period, resulting in a *sinc* phase-matching profile whose side lobes limit the spectral purity. As a result, a narrowband filter

is typically employed to cut off the side lobes, at the cost of reducing the flux and the heralding efficiency. To mitigate the limitation of periodic poling, Brańczyk *et al.* gave a solution by adding another type of poling [224]. Then Dixon *et al.* introduced a customized aperiodic poling profile, illustrated in Fig. 7.1 (bottom), to achieve a Gaussian phase-matching profile at the GVM wavelength more practically [225]. In conjunction with a Gaussian spectrum pump, a 99.5% spectral purity was measured after applying an 8.5-nm full width at half maximum Gaussian spectral filter. The spectral purity of the bi-photons produced in Dixon *et al.*'s scheme, however, degrades to 97.12% after applying a 40-nm filter in the 1550-nm band due to the higher-order terms, e.g. group-velocity-dispersion [226]. In follow-up works [227, 228, 229, 230, 231, 49], several poling-design optimization approaches were introduced to improve upon Ref. [225]'s spectral purity. Like Dixon *et al.*'s scheme, these approaches require operating under the validity of first-order approximation. Since the KTP crystal has a smooth group-velocity-mismatch around the GVM wavelength, the former designs can still be valid for spectrally-uncorrelated bi-photon generation over the entire telecommunication window from  $\sim 1300$  nm to 1600 nm [226]. However, the purity is confined as a result of first-order approximation, which is no longer efficient. In addition, these approaches rely on binary optimization that limits the achievable purity, due to a lack of access to the full parameter space. To generate high-purity bi-photons at wavelengths away from 1582 nm, period-poled KTP's output spectral purity is limited to merely  $\sim 81\%$  [232], which is insufficient for many applications. Apart from KTP, references [233, 234, 235] compiled a list of other nonlinear materials, each operating at a specific wavelength dictated by its GVM property. However, a scheme for generating high spectrally-uncorrelated bi-photons at any target wavelength remains elusive.

Here, we present a general machine-learning framework that seeks the optimum poling design for the generation of spectrally-uncorrelated bi-photons. Unlike prior works, our approach exploits an optimization fully empowered by machine learning to obviate the need for either the first-order approximation or the GVM property of nonlinear crystals. This yields a purity in excess of 99.8% with an 8-nm filter over

1310 nm to 1600 nm. In particular, a 99% spectral purity in the 1550-nm band is achieved after applying a 40-nm wideband filter that nicely maintains the flux and the heralding efficiency. Our result demonstrates the power of machine learning in tackling hard quantum information problems.

In this paper, we focus on optimizing KTP's type-II phase matching to generate spectrally-pure bi-photons, but our method can be applied to other phase-matching types.

### 7.2.2 Bi-Photon JSA and Phase Matching

In spontaneous parametric down-conversion (SPDC), the generated bi-photons can be represented in the frequency domain as a superposition of different frequency modes:

$$|\psi\rangle_{SI} = \iint d\omega_s d\omega_i f(\omega_s, \omega_i) \hat{a}_{\omega_s}^\dagger \hat{b}_{\omega_i}^\dagger |0\rangle_s |0\rangle_i. \quad (7.1)$$

Here,  $\hat{a}_{\omega_s}^\dagger$  is the creation operator for the signal photon,  $\hat{b}_{\omega_i}^\dagger$  is the creation operator for the idler photon, and  $f(\omega_s, \omega_i)$  is the bi-photon joint spectrum amplitude (JSA) that entails complete information about the spectral-temporal properties of the photon pair. The bi-photon JSA is determined by the pump spectrum and the properties of the nonlinear crystal by  $f(\omega_s, \omega_i) \propto \alpha(\omega_p)G(\Delta k)$ , where  $\omega_p = \omega_s + \omega_i$  relates the pump, signal, and idler frequencies by energy conservation,  $\alpha(\omega_p)$  describes the pump spectral profile, and  $G(\Delta k)$  encompasses information about the phase-matching properties of the nonlinear crystal [222]. Specifically, the phase-matching function

$$G(\Delta k) = \frac{1}{L} \int_0^L dz g(z) \exp(-i\Delta k z), \quad (7.2)$$

where  $g(z) = \{1, -1\}$  describes the poling profile along the propagation  $z$  axis. The phase mismatch

$$\begin{aligned} \Delta k(\omega_s, \omega_i) &= k_p(\omega_p) - k_s(\omega_s) - k_i(\omega_i) \\ &= 2\pi n(\omega_p)/\lambda_p - 2\pi n(\omega_s)/\lambda_s - 2\pi n(\omega_i)/\lambda_i, \end{aligned} \quad (7.3)$$

where  $n(\omega)$  is the frequency-dependent refractive index that determines the material dispersion, and  $\lambda_p$ ,  $\lambda_s$ , and  $\lambda_i$  are the pump, signal, and idler wavelengths [222, 225,

231]. To quantitatively describe the spectral correlation between the signal and idler photons, their JSA is decomposed [225, 49] as  $f(\omega_s, \omega_i) = \sum_n \xi_n \beta_{S,n}(\omega_s) \beta_{I,n}(\omega_i)$ , where  $\{\beta_{S,n}(\omega_s)\}$  and  $\{\beta_{I,n}(\omega_i)\}$  are two sets of orthogonal functions, viz.

$$\int d\omega \beta_{j,n}^*(\omega) \beta_{j,m}(\omega) = \delta_{n,m}, \quad (7.4)$$

where  $j \in \{S, I\}$ . The purity is then defined as

$$\mathcal{P} = \sum_n |\xi_n|^4 / (\sum_n |\xi_n|^2)^2. \quad (7.5)$$

Equivalently,  $\mathcal{P} = \text{Tr}(\text{Tr}_i(|\psi\rangle\langle\psi|_{SI}))^2$ , which quantifies how pure the signal-photon state is after tracing out the idler photon. If  $f(\omega_s, \omega_i) = \beta_s(\omega_s) \beta_i(\omega_i)$ , i.e.,  $\mathcal{P} = 1$ , the JSA then describes a product state of spectrally-uncorrelated two photons particularly useful for Boson sampling, entanglement distribution, and photonic quantum information processing [207, 236, 223].

Another quantitative property of a bi-photon JSA is the spectral indistinguishability defined as

$$\mathcal{I} = \text{Re} \left[ \iint d\omega_s d\omega_i f^*(\omega_s, \omega_i) f(\omega_i, \omega_s) \right] \quad (7.6)$$

$\mathcal{I}$  quantifies the difference in the spectra of two photons [237, 238, 239, 240, 241, 242] and equals the visibility of Hong-Ou-Mandel interference.  $\mathcal{I}$  is a useful metric for single-photon sources such as quantum dots for which spectral diffusion is a practical limitation. This paper considers broadband heralded single photons from independent SPDC sources, so purity is a more appropriate performance metric (see Section 7.3.1 for more information). We will, however, calculate the indistinguishability for the signal and idler photons.

To engineer a desired bi-photon JSA  $f(\omega_s, \omega_i)$ , one has two tunable knobs: the pump spectral profile  $\alpha(\omega_p)$  and the crystal poling profile  $g(z)$ . In this paper, we introduce a general recipe that harnesses a machine-learning framework to automate the design for  $\alpha(\omega_p)$  and  $g(z)$ . Let us first formulate the JSA engineering problem and provide some insights into its connection with machine learning.

The poling profile embedded in  $g(z)$  involves the poling period  $\Lambda$  and an array  $\mathbf{A} = \{A_i\}$  that specifies the duty cycle in each of the  $N$  periods.  $\Lambda$  is given by the

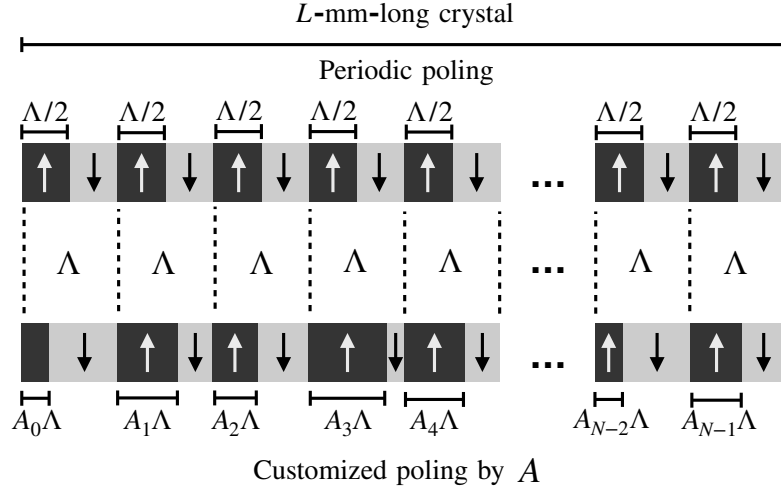


Figure 7.1: **Poling profiles for a  $L$ -mm-long nonlinear crystal with  $N$  poling periods.** Top: periodic poling with a period of  $\Lambda$ . Bottom: customized poling with a profile embedded in the array  $\mathbf{A}$ .

phase-matching condition at the pump's central frequency  $\omega_{P_0}$  when signal and idler photons are wavelength degenerate at  $\omega_{P_0}/2$ :  $\Lambda = 2\pi/\Delta k_0$ , where  $\Delta k_0 = \Delta k(\omega_s = \omega_i = \omega_{P_0}/2)$ .  $g(z)$  thus relates to  $\Lambda$  and  $\mathbf{A}$  by

$$g(z, \mathbf{A}) = -1 + 2 \sum_{j=0}^{N-1} [\Theta(z - j\Lambda) - \Theta(z - (j + A_j)\Lambda)] \quad (7.7)$$

where  $\Theta$  is the unit step function (see Fig. 7.1). Plugging  $g(z)$ , given by Eq. (7.7), into the phase-matching function yields

$$G(\Delta k, \mathbf{A}) = \frac{1}{iL\Delta k} \sum_{j=0}^{N-1} [e^{-i\Lambda j\Delta k} + e^{-i\Lambda(j+1)\Delta k} - 2e^{-i\Lambda(j+A_j)\Delta k}] \quad (7.8)$$

In practice, the design of  $g(z)$  is limited by the minimum poling length  $\Lambda_{\min}$ . To accommodate the practical limitation, we modify the duty cycles as  $A_i \in [\Lambda_{\min}/\Lambda, 1 - \Lambda_{\min}/\Lambda]$  (the ratio of the positive polarity portion within each poling period) in tuning the JSA.

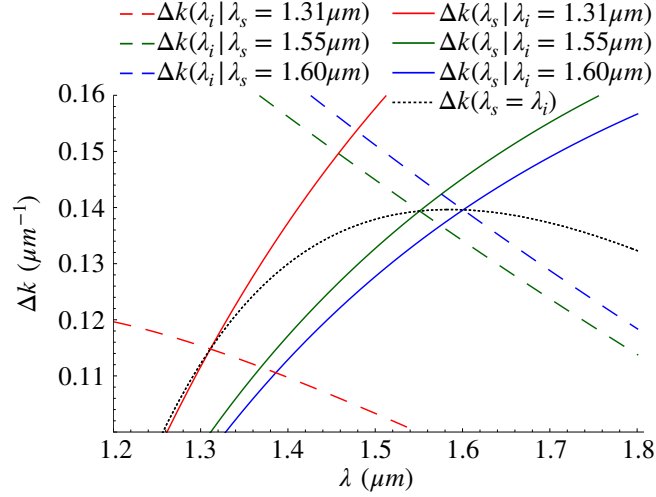


Figure 7.2: **KTP's Type-II SPDC phase mismatch  $\Delta k(\omega_s, \omega_i)$  with fixed idler (solid) or signal (dashed) wavelengths in the 1200-nm to 1800-nm range.** The intersection points between the solid and the dashed lines of the same color are where a first-order approximation for the phase mismatch is performed. The black dotted line is formed by all intersections at different wavelengths, giving the phase mismatch,  $\Delta k_0$ , at the degenerate wavelengths.

### 7.2.3 The GVM Condition and Gaussian Phase-Matching Profile

To generate spectrally-uncorrelated bi-photons, we desire  $f(\omega_s, \omega_i) = \alpha(\omega_s + \omega_i)G(\Delta k(\omega_s, \omega_i)) = \beta_s(\omega_s)\beta_i(\omega_i)$ . A conventional approach to engineer such a product-state wave function is picking the signal and idler wavelengths,  $\omega_{s_0}$  and  $\omega_{i_0}$ , that satisfy  $\partial\Delta k/\partial\omega_s|_{\omega_{s_0}} = -\partial\Delta k/\partial\omega_i|_{\omega_{i_0}} = \gamma_{\text{GVM}}$ , known as the GVM condition. Around  $\omega_{s_0}$  and  $\omega_{i_0}$ , the phase mismatch is fully determined by the frequency difference between the signal and idler photons, i.e.,  $\Delta k \approx \Delta k_0 + \gamma_{\text{GVM}}(\omega_s - \omega_i)$ . This leads to a phase-matching function  $G(\Delta k)$  that is solely a function of  $\omega_s - \omega_i$ , viz.  $G(\omega_s - \omega_i)$ . Under the GVM condition, it is possible to engineer a Gaussian phase-matching function[226]

$$G(\omega_s - \omega_i) \approx G_0 \exp \left[ -\frac{(\omega_s - \omega_i)^2}{\sigma_C^2} \right], \quad (7.9)$$



where  $\sigma_C$  is determined by the poling profile  $g(z|\mathbf{A}_{\text{GVM}})$ . In conjunction with a Gaussian pump spectral profile

$$\alpha(\omega_p) = a_0 \exp \left[ -\frac{(\omega_s + \omega_i - \omega_{P_0})^2}{\sigma_p^2} \right] \quad (7.10)$$

and by choosing  $\sigma_p = \sigma_C$ , one obtains

$$\begin{aligned} f(\omega_s, \omega_i) &= \alpha(\omega_s + \omega_i) G(\omega_s - \omega_i) \\ &\propto \exp \left[ -\frac{2(\omega_s - \omega_{s_0})^2}{\sigma_p^2} \right] \exp \left[ -\frac{2(\omega_i - \omega_{i_0})^2}{\sigma_p^2} \right], \end{aligned} \quad (7.11)$$

i.e., a spectrally-uncorrelated product state of bi-photons.

The JSA engineering approach based on GVM and Gaussian phase matching, albeit ingenious, is limited by the dispersion properties of the nonlinear materials, resulting in only a handful of GVM wavelengths, each associated with a specific nonlinear optical material. For example, the GVM wavelengths are  $\sim 1582$  nm for KTP,  $\sim 830$  nm for KDP ( $\text{KH}_2\text{PO}_4$ ), and  $\sim 922$  nm for ADA ( $\text{NH}_4\text{H}_2\text{AsO}_4$ ) [235]. Such a restriction impedes the generation of spectrally-uncorrelated bi-photons that covers the entire telecommunication band from  $\sim 1300$  nm to  $\sim 1600$  nm and precludes interfacing SPDC photons with solid-state quantum emitters in the visible to near-infrared wavelength range, as a means to entangle qubits at a distance. To engineer spectrally-uncorrelated bi-photon JSAs over a wide spectral range, let us further understand the limitations of the GVM approach.

#### 7.2.4 General Phase Matching without the GVM Condition

Let us now consider working at non-GVM wavelengths. Let the phase mismatch at the degenerate wavelength be  $\Delta k_0$ . The phase mismatch at any wavelengths in the vicinity of the degenerate wavelength can be expressed, in a first-order approximation, as  $\Delta k - \Delta k_0 \approx \gamma_s \omega_s - \gamma_i \omega_i$ , where  $\gamma_s \neq \gamma_i$  for a non-GVM case. Without loss of generality, both  $\gamma_s$  and  $\gamma_i$  are chosen to be positive. The validity of the first-order approximation is verified in Fig. 7.2, which shows the linearity of  $\Delta k$  around the degenerate wavelengths at the intersections between the solid and dashed lines.

Applying the poling profile  $\mathbf{A}_{\text{GVM}}$  which is developed at the GVM wavelengths, we have

$$\begin{aligned} G(\Delta k, \mathbf{A}_{\text{GVM}}) &\approx G'_0 \exp \left[ -\frac{(\Delta k - \Delta k_0)^2}{\gamma_{\text{GVM}}^2 \sigma_C^2} \right] \times \left[ 1 + \frac{\Delta k - \Delta k_0}{\Delta k_0} + \mathcal{O}((\Delta k - \Delta k_0))^2 \right] \\ &\approx G'_0 \exp \left[ -\frac{(\gamma_s \omega_s - \gamma_i \omega_i)^2}{\gamma_{\text{GVM}}^2 \sigma_C^2} \right] \times \left[ 1 + \frac{\gamma_s \omega_s - \gamma_i \omega_i}{\Delta k_0} + \mathcal{O}((\gamma_s \omega_s - \gamma_i \omega_i)^2) \right], \end{aligned} \quad (7.12)$$

where the second term includes high-order contributions. Since  $(\gamma_s \omega_s - \gamma_i \omega_i)/\Delta k_0$  is small but not negligible, it causes a reduced spectral purity. The spectral purity will, nonetheless, still be high after applying narrowband filters as the higher-order term primarily contribute to areas of large detuning from the central wavelength. It appears that by choosing the pump bandwidth  $\sigma_p = \gamma_{\text{GVM}} \sigma_C / \sqrt{\gamma_s \gamma_i}$ , one obtains, in a non-GVM regime, a product-state JSA  $f(\omega_s, \omega_i) \propto \exp \left[ -\frac{(\omega_s - \omega_{s0})^2}{\sigma_s^2} \right] \exp \left[ -\frac{(\omega_i - \omega_{i0})^2}{\sigma_i^2} \right]$ , where

$$\sigma_s = \frac{\sigma_C \gamma_{\text{GVM}}}{\sqrt{\gamma_s (\gamma_s + \gamma_i)}}, \quad \sigma_i = \frac{\sigma_C \gamma_{\text{GVM}}}{\sqrt{\gamma_i (\gamma_s + \gamma_i)}}. \quad (7.13)$$

However, a number of caveats about this result need to be noted. First, a practical phase-matching function  $G(\Delta k, \mathbf{A}_{\text{GVM}})$  is only approximately Gaussian due to the finite number of periods and the minimum duty cycle  $\Lambda_{\text{min}}$  that induces discretization errors; and second, the higher-order Hermit-Gaussian terms in Eq. 7.12 generate side lobes, which should be accounted for in an effective design. As a result, a 99.5% filtered spectral purity [225] at the GVM wavelength with Gaussian phase matching reduces to 97.13% in the 1550-nm band after switching to a 40-nm filter.

### 7.2.5 The Machine-Learning Framework

We introduce a machine-learning framework to cope with the limitations associated with the GVM and Gaussian-phase-matching approach. The machine-learning framework enables the suppression of higher-order terms and compensations for discretization errors, leading to high-spectral-purity bi-photons over a wide range of wavelengths. In addition, the machine-learning framework is capable of designing a poling profile that corrects deviations from a perfect Gaussian-spectrum pump.

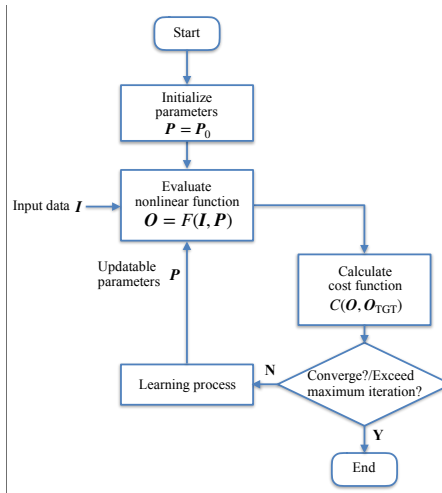


Figure 7.3: **A general machine-learning model.**  $\mathbf{I}$ : input data;  $\mathbf{O}$ : output data;  $\mathbf{P}$ : updatable parameters;  $\mathbf{P}_0$ : initial parameters;  $F(\mathbf{I}, \mathbf{P})$  nonlinear function;  $\mathbf{O}_{\text{TGT}}$ : target output data;  $C(\mathbf{O}, \mathbf{O}_{\text{TGT}})$ : cost function that determines the distance between the present output data and the target output data; the learning process is an algorithm that updates the parameters based on the cost.

A general machine-learning framework is comprised of multiple building blocks, as illustrated in Fig. 7.3. A nonlinear function  $F$  is characterized by a set of updatable parameters  $\mathbf{P}$ .  $F$  takes input data  $\mathbf{I}$  and produces output data  $\mathbf{O} = F(\mathbf{I}, \mathbf{P})$ . The objective of learning is to seek the optimum  $\mathbf{P}$  so that  $\mathbf{O}$  converges to the target output data  $\mathbf{O}_{\text{TGT}}$  for different  $\mathbf{I}$ . To this end, we define a cost function,  $C(\mathbf{O}, \mathbf{O}_{\text{TGT}})$ , that quantifies the distance between  $\mathbf{O}$  and  $\mathbf{O}_{\text{TGT}}$ .  $\mathbf{P}$  is initialized by a preset of parameters  $\mathbf{P}_0$  and updated by a learning process supplied with the calculated cost in each iteration.

The most common class of learning processes is based on gradient descent, in which  $\mathbf{P}$  is updated based on a linear scaling of the negativity of the gradient of the cost function [243, 244]. Linear scaling is defined as the learning rate. *Adam* is an upgraded version of the gradient-descent learning process. *Adam* introduces the adaptive momentum method that adjusts the learning rate based on the learning history [245, 246]. Such a feature differentiates *Adam* from a conventional gradient-descent learning process with a fixed learning rate.

To date, several optimization approaches based on *forwardpropagation* have been

employed to design the poling profile for JSA engineering [227, 228, 229]. These approaches rest upon equal poling periods and static strategies to optimize the poling profile. In contrast, gradient descent and *Adam* fall into *backpropagation* learning processes because the gradient of the cost function is calculated as a partial derivative over elements in  $\mathbf{P}$ . Critically, the backpropagation approach in our machine-learning framework automates the optimization procedure. Moreover, the search time in the parameter space is significantly reduced by virtue of *Adam*'s adaptive parameter update strategy.

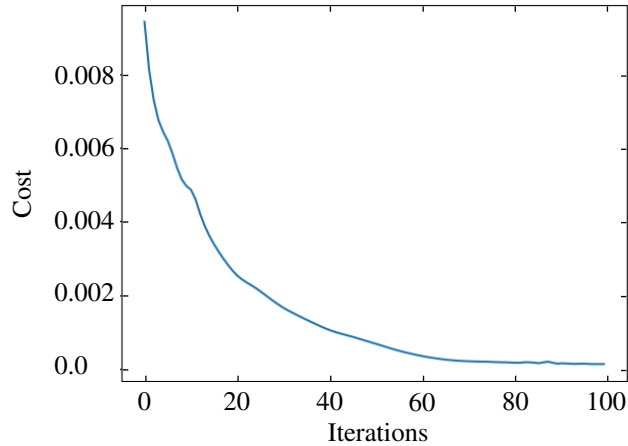


Figure 7.4: **The evolution of the cost during poling optimization for the generation of spectrally-uncorrelated bi-photons in the 1550-nm band.** The cost approaches 0 after 100 iterations, indicating near-spectrally-uncorrelated bi-photons can be produced with the optimized crystal poling.

To utilize the machine-learning framework to engineer the JSAs for spectrally-uncorrelated bi-photons, we assume that a pump with an ideal Gaussian spectrum and bandwidth is available at the desired wavelength, with the understanding that deviations from the ideal conditions can be accommodated by the machine-learning framework. Consider the function  $H(\omega_s, \mathbf{A}) \equiv |G(\Delta k(\omega_s, \omega_{P_0} - \omega_i), \mathbf{A})|$ , i.e., a slice of the phase-matching function  $|G(\Delta k(\omega_s, \omega_i), \mathbf{A})|$  along the  $\omega_s + \omega_i = \omega_{P_0}$  axis, where  $\omega_{P_0}$  is the central frequency for the pump. If  $H(\omega_s, \mathbf{A})$  is Gaussian,  $|G(\Delta k(\omega_s, \omega_i), \mathbf{A})|$  will have the form as the first term in Eq. 7.12. Therefore, Our objective is to seek the optimum poling profile  $\mathbf{A}$  such that  $H(\omega_s, \mathbf{A}) \rightarrow$

$H_0 \exp \left[ -\frac{(\omega_s - \omega_{t_0})^2}{2\sigma_t^2} \right]$ , where  $\omega_{t_0}$  and  $\sigma_t$  is the central frequency and the standard deviation for this Gaussian target. The purity of the bi-photons ties to the distance between  $H(\omega_s, \mathbf{A})$  and an ideal Gaussian form. In the machine-learning framework, the input data  $\mathbf{I}$  consist of an array of sampled signal frequencies:  $\boldsymbol{\omega}_s = \{\omega_{s_1}, \omega_{s_2}, \dots, \omega_{s_k}\}$ . The updatable parameters  $\mathbf{P}$  include the duty cycle array  $\mathbf{A}$ , the target central frequency  $\omega_{t_0}$ , and the target bandwidth  $\sigma_t$ . With the updatable parameters, the nonlinear function returns the output data  $\mathbf{O} = F(\mathbf{I}, \mathbf{P}) = H(\boldsymbol{\omega}_s, \mathbf{A})$ , which aims to approach the target output data

$$\mathbf{O}_{\text{TGT}} = H_0 \exp \left[ -\frac{(\boldsymbol{\omega}_s - \omega_{t_0})^2}{2\sigma_t^2} \right] \quad (7.14)$$

The cost is then defined as the distance between the output data and an ideal Gaussian function as

$$C(\mathbf{O}, \mathbf{O}_{\text{TGT}}) = \sum_{l=1}^k \left\{ H(\omega_{s_l}, \mathbf{A}) - H_0 \exp \left[ -\frac{(\omega_{s_l} - \omega_{t_0})^2}{2\sigma_t^2} \right] \right\}^2 \quad (7.15)$$

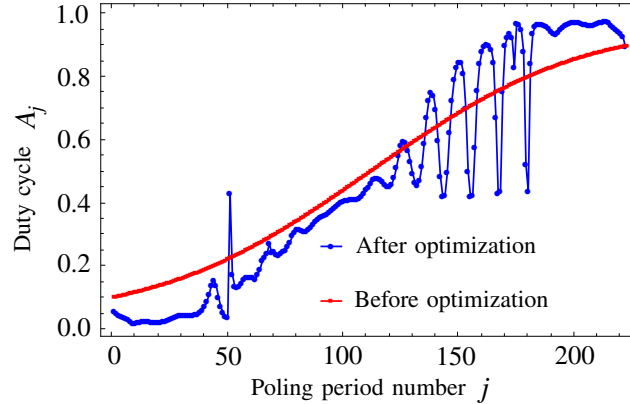


Figure 7.5: **Poling profiles for the generation of spectrally-uncorrelated bi-photons in the 1550-nm band.** Red curve: the initial poling profile prior to applying machine learning, obtained from the GVM condition and Gaussian phase matching [225]; Blue dots: the optimized poling profile obtained by the machine-learning framework.

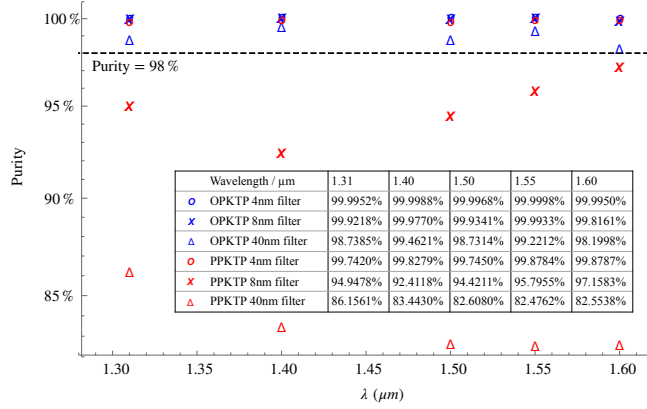


Figure 7.6: **Simulated purities at different wavelengths after applying filters of different bandwidths.** Circles: purities with our machine-learning-based poling design; Crosses: purities with periodic poling. Inset: a table that summarizes the purities for both optimized-poling KTP (OPKTP) and periodically-poled KTP (PPKTP). For PPKTP, a longer wavelength yields larger bandwidth for the bi-photons. An 8-nm filter then eliminates the first side lobe to increase the purity. The dashed line corresponds to a 98% purity. The purities obtained by our poling-design recipe in conjunction with the 40-nm filter all sit above the dashed line. The relation between the purity and the filter bandwidth is discussed in detail in the main text.

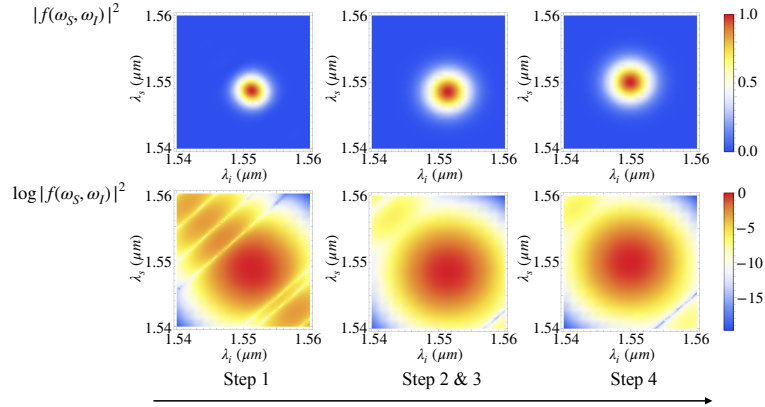


Figure 7.7: **Bi-photon joint-power spectrum after each design step.** Step 1 takes a prior poling design, which, without any optimization, suffers from side lobes that degrade the purity. After Steps 2 & 3, the side lobes are suppressed by the machine-learning framework while leaving the bi-photons non-degenerate. After Step 4, the bi-photons become degenerate at 1550 nm. The logarithm scale amplifies the visibility of the side lobes.

### 7.2.6 Poling-Design Recipe

We customize the poling for an  $L = 10$ -mm KTP crystal comprised of  $\sim 200$  poling periods. Such a size of the parameter space would be a challenge for any analytic attempt to devise the optimum poling profile. The machine-learning framework, by contrast, optimizes the duty cycle array  $\mathbf{A}$  by gradually minimizing the cost function over each iteration. In doing so, the optimization does not rely on any approximation, nor does it place any requirement on the pump profile. It can thus cope with any target output data under any pump profile. In what follows, we describe the four main steps of our poling-design recipe.

**Step 1: Initialization** Set the target wavelength and the bandwidth of interest. Set the poling period  $\Lambda = 2\pi/\Delta k_0$  at the target wavelength. Set the minimum poling length  $A_{\min}$  allowed by the fabrication processes. As a reference,  $A_{\min} = 0$  is an upper bound for the performance. Initialize  $\mathbf{A} = \mathbf{A}_{\text{GVM}}$  and choose the maximum number of machine-learning iterations.

**Step 2: Cost function calculation** Obtain and normalize  $\mathbf{O} = H(\boldsymbol{\omega}_s, \mathbf{A})$ . Calculate the cost function  $C(\mathbf{O}, \mathbf{O}_{\text{TGT}})$ .

**Step 3a: Pump optimization** Use *Adam* with learning rate  $r_a$  to update  $\omega_{t_0}$  and  $\sigma_t$  and reduce the cost function.

**Step 3b: Poling optimization** Use *Adam* with learning rate  $r_b$  to update  $\mathbf{A}$  and reduce the cost function. Repeat from **Step 2** until the maximum number of iterations is reached, or the cost function converges to the minimum.

**Step 4: Poling period adjustment** Fine tune  $\Lambda$  without modifying  $\mathbf{A}$  to eliminate the non-degeneracy between the signal and idler photons.

### 7.2.7 Simulation Results

The machine-learning framework for the poling design is realized in Python with the TensorFlow library. The material dispersion profile of KTP is derived by the Sellmeier equation reported in Ref. [247]. The employed learning rates are  $r_a = 0.005$  and  $r_b = 0.015$ .

Working in the 1550-nm band, the cost converges after 100 machine-learning iterations, shown in Fig. 7.4. Fig. 7.5 displays the initial poling profile and the optimized poling profile obtained by the machine-learning framework. The simulation derives a minimum poling length of  $\sim 0.9 \mu\text{m}$  (2.04% of a poling period), even though we set  $A_{\min} = 0$  to obtain the optimum poling profile. The periodic peaks in the machine-learned poling profile may be responsible for the compensation of discretization errors.

Since our main focus is on broadband heralded single photons from independent SPDC sources, the visibility of the Hong-Ou-Mandel (HOM) interference is primarily determined by the purity [237, 240, 241, 242, 220] (see also Sec. 7.3.1). As such, we use purity as a main performance metric to compare our design with others <sup>1</sup>.

After applying ideal rectangular filters with various bandwidths, the spectral purity of the produced bi-photons is calculated by the coefficients of Schmidt decomposition [225, 49] and Eq. (7.5). We apply our recipe to generating spectrally-uncorrelated bi-photons in the 1310-nm, 1400-nm, 1500-nm, and 1600-nm bands. The spectral purities with filters of various bandwidths are derived for both optimized-poling KTP (OPKTP) and periodically-poled KTP (PPKTP), as depicted in Fig. 7.6 and summarized in the inset. Even with a 40-nm filter, our machine-learning-based poling design achieves purities in excess of 98%, marked as the dashed line in Fig. 7.6) [206]<sup>2</sup>.

<sup>1</sup>We calculated the indistinguishability defined in Ref. [240] in the 1550-nm band. After applying a 4-nm filter, the indistinguishability between signal and idler is 99.4%, decreasing to 98.7% (98.1%) with an 8-nm (40-nm) filter. The decrease in the indistinguishability is caused by the asymmetry between the signal and the idler's spectra at non-GVM wavelengths.

<sup>2</sup>In addition, Fig. 4 of Ref. [206] shows that with assumptions, the minimum indistinguishability



The filters cut the JSA at finite wavelengths and thus simplify the numerical estimation for purity. The filter bandwidths are critical parameters: Fig. 7.6 shows that a narrower filter bandwidth leads to a higher purity. A narrowband filter, however, decreases the photon flux and the heralding efficiency due to its increased insertion loss compared to that of a wideband filter. In our simulation at 1550 nm, the output signal’s full width at half maximum (FWHM) is about 4.5 nm, so we choose 4 nm, 8 nm, and 40 nm to keep  $\sim 68\%$ ,  $\sim 95\%$ , and  $\sim 100\%$  of the photon flux. Filters of the same linewidths are used at other wavelengths. To achieve high heralding efficiency, our customized poling crystals need to be pumped by loosely focused beams [248, 249] in conjunction with high-efficiency detectors [250, 251]. Since the signal photon and the idler photon are nearly spectrally separable, the heralding efficiency is close to the system efficiency of either arm. Assuming a 5% insertion loss for the optical filter and a 90% quantum efficiency for the detector, the heralding efficiency will then be close to 85%.

To further illustrate the poling optimization procedure, Fig. 7.7 shows the joint spectral intensity, defined as  $|f(\omega_s, \omega_i)|^2$ , in the 1550-nm band after each step. One observes that side lobes are suppressed after Steps 2 & 3, and Step 4 eliminates the non-degeneracy between the bi-photons.

Table 7.1 collects key metrics reported in this and prior works of poling design for spectrally-uncorrelated photon generation. Since different works employ filters of different bandwidths and set different resolutions for JSAs in calculating the purity, the highest purity numbers do not accurately reflect the performance for different schemes. Notably, our machine-learning framework is able to compensate higher-order terms by direct calculating the cost function from the sampled bi-photon JSA, whereas prior works are all based on first-order approximations, as discussed in Sec. 7.2.4. Because our machine-learning framework relies on neither a first-order 

---

 required for quantum advantages in Boson Sampling is asymptotically approaching around 98% in its black-dotted line. The indistinguishability of photons from independent heralded SPDC sources is dominated by the purity of each photon. As such, we set 98% as a baseline to compare the performance of our design recipe with others.

approximation nor the GVM condition, high spectral purity can be achieved over the entire telecommunication band from 1300 nm to 1600 nm. We should note that the bi-photon JSA centered at non-GVM wavelengths, e.g., a central wavelength at 1310 nm, is elliptical since  $\sigma_s \neq \sigma_i$ . The unequal bandwidth of the signal and idler photons, however, does not prevent signal or idler photons from independent sources from interfering, as a building block for entanglement swapping and quantum teleportation.

Reference	Poling strategy	Optimization method	Central wavelength	Number of domains	Crystal length	Filter type & bandwidth	Achieved highest purity
A. M. Brańczyk <i>et al.</i> [224]	Customized poling order	Analytic design	1576 nm	~900	24.2 mm	N/A	99.0%
P. B. Dixon <i>et al.</i> [225]	Customized duty cycle	Analytic design	1582 nm	~520	12 mm	Gaussian 8.5 nm	99.5%
J. Tambasco <i>et al.</i> [228]	Customized orientation	Binary coordinate descent	1550 nm	~532	12 mm	Rectangular ~16 nm <sup>3</sup>	99.6%
A. Dosseva <i>et al.</i> [227]	Customized orientation	Binary simulated annealing	1582 nm	1300	~14.1 mm	Rectangular ~10 nm <sup>4</sup>	99.9%
F. Graffitti <i>et al.</i> [229]	Customized orientation + tuning periods	Binary coordinate descent & simulated annealing	1582 nm	~870 (60)	2 mm	Rectangular 107 nm	99.0%
F. Graffitti <i>et al.</i> [229]	Sub-coherence engineering	Binary coordinate descent	1582 nm	~870 (502)	2 mm	Rectangular 107 nm	99.4%
This work	Customized duty cycle + tuning periods	<i>Adam</i>	1300nm -1600 nm	~400 -~500	10 mm	Rectangular 8 nm	>99.8%

Table 7.1: **Comparison of the performance metrics between prior works and the present work.** Numbers with the ‘~’ symbol are inferred based on the context of the references. The number of domains equals the total number of free variables being optimized. The numbers in the parenthesis denote the final numbers of domains after combining domains with the same polarity after optimization. The phase-matching bandwidth is determined by the crystal length. As such, the comparison of the filter bandwidths should be made among crystals with similar lengths.

## 7.2.8 Discussion

The machine-learning framework represents a general optimization strategy particularly suitable for complex problems that have clear objectives but cannot be tackled

by approximation methods due to the sensitivity to small variations in their solutions. This kind of problem typically involves a large parameter space that is hard to solve by conventional optimization methods. Intriguingly, the solutions sought by the machine-learning framework may, in turn, offer new insights into the complex problems at hand.

The machine-learning framework utilizes *Adam* as the learning process. Since *Adam* converges at a zero-gradient minimum point, the poling profile is robust against small fabrication errors. *Adam* has shown great performance in many non-convex optimization problems. To fully unleash the potential of *Adam*, it sometimes requires careful choice of the learning rate. Since one cannot ensure the convergence of the machine-learning algorithm to the global optimum, it is recommended to set initial parameters based on a good existing design and subsequently leverage machine learning to achieve substantial improvement. In this work, we set a known Gaussian poling profile obtained at the GVM wavelength as the initial parameters for the machine-learning framework. In the learning process, a finer sampling resolution will slightly improve the performance at the cost of requiring more computational resources. Apart from the KTP, our machine-learning-based design recipe is applicable to nonlinear crystals, as long as the first-order approximation dominates higher-order terms in the phase-mismatch function at the working wavelength.

The machine-learning framework can also be used for seeking poling profiles for other forms of bi-photon JSAs by simply modifying the target JSA in the cost function. For example, non-degenerate bi-photon states and non-Gaussian states can be engineered by our approach, as a means for entangling solid-state qubits at a distance [252, 253, 254]. To engineer an arbitrary bi-photon JSA, a learning process solely based on sampling the signal frequencies becomes insufficient. In such a general situation, one should sample both the signal's and the idler's frequencies, in  $\omega_s$  and  $\omega_i$ , and feed to the nonlinear function to obtain  $H(\omega_s, \omega_i|\mathbf{A})$  as the output. The cost function should also be modified accordingly. There is, however, no fundamental constraint that prevents the machine-learning framework from engineering an arbitrary bi-photon JSA but given a finite number of poling periods, the

machine-learning framework may only approach a target bi-photon JSA down to a certain precision [255].

### 7.2.9 Conclusions

We have developed a machine-learning framework to solve the problem of the generation of indistinguishable bi-photons in the telecommunication band over 1300 nm to 1600 nm. Our approach leads to a spectral purity in excess of 99.99% for bi-photons in the 1550-nm band after applying an 8-nm filter and in excess of 98% over the entire telecommunication band while maintaining a high photon flux and heralding efficiency by using a wide 40-nm filter. This work demonstrates machine learning's potential to advance quantum information science. We hope that this work will spur the pursuits of other machine-learning-enhanced quantum communication, sensing, and information processing applications.

## 7.3 Supplementary Materials

### 7.3.1 Definition of the Purity of a Bi-Photon State

In general, a bi-photon state can be described by a density matrix  $\rho_{12}$ . A common definition for the bi-photon spectral purity is the purity of one photon after tracing out the other:

$$\mathcal{P} \equiv \text{Tr} [(\text{Tr}_2(\rho_{12}))^2] \quad (7.16)$$

In our cases, a bi-photon pure state with a JSA  $f(\omega_s, \omega_i)$  is described as

$$|\psi\rangle_{SI} \equiv \iint d\omega_s d\omega_i f(\omega_s, \omega_i) \hat{a}_{\omega_s}^\dagger \hat{b}_{\omega_i}^\dagger |0\rangle_s |0\rangle_i. \quad (7.17)$$

Since  $f(\omega_s, \omega_i)$  can be Schmidt decomposed to  $f(\omega_s, \omega_i) = \sum_n \xi_n \beta_{s,n}(\omega_s) \beta_{i,n}(\omega_i)$ , where  $\{\beta_{s,n}\}$  and  $\{\beta_{i,n}\}$  are two sets of orthogonal functions:

$$\int d\omega \beta_{j,n}^*(\omega) \beta_{j,m}(\omega) = \delta_{n,m}, \quad (7.18)$$

where  $j \in \{S, I\}$ . We can then rewrite the bi-photon pure state as

$$|\psi\rangle_{SI} = \frac{\sum_n \xi_n \hat{a}_{s,n}^\dagger \hat{b}_{i,n}^\dagger |0\rangle_s |0\rangle_i}{\sqrt{\sum_n |\xi_n|^2}}, \quad (7.19)$$

in which the operators obey

$$\begin{aligned}\hat{a}_n^\dagger &= \int d\omega_s \beta_{s,n}(\omega_s) \hat{a}_{\omega_s}^\dagger, \quad [\hat{a}_m, \hat{a}_n^\dagger] = \delta_{m,n}, \\ \hat{b}_n^\dagger &= \int d\omega_i \beta_{i,n}(\omega_i) \hat{b}_{\omega_i}^\dagger, \quad [\hat{b}_m, \hat{b}_n^\dagger] = \delta_{m,n}.\end{aligned}\tag{7.20}$$

Finally, the purity of this bi-photon pure state turns out to be

$$\begin{aligned}\mathcal{P} &\equiv \text{Tr} [(\text{Tr}_i(|\psi\rangle\langle\psi|_{SI}))^2] \\ &= \text{Tr} \left[ \left( \frac{\sum_n |\xi_n|^2 \hat{a}_{s,n}^\dagger |0\rangle\langle 0| \hat{a}_{s,n}}{\sum_n |\xi_n|^2} \right)^2 \right] = \sum_n |\xi_n|^4 / \left( \sum_n |\xi_n|^2 \right)^2,\end{aligned}\tag{7.21}$$

which agrees with the definition in Eq. (7.5).

### 7.3.2 Definition of the Indistinguishability of a Bi-Photon State

Indistinguishability, on the other hand, is usually defined as the visibility of Hong-Ou-Mandel (HOM) interference:  $\mathcal{I} \equiv (R_{\max} - R_{\min})/R_{\max}$ . Here,  $R_{\max}$  ( $R_{\min}$ ) is the maximum (minimum) coincidence rate at different time delays between the signal and idler photons [237, 238, 239, 240, 241, 242, 220].  $R_{\max}$  occurs when the two photons arrive at the beamsplitter at completely different times while  $R_{\min}$  arises when they arrive at the same time. Therefore, given photon-pair flux  $R_{\text{in}}$ ,  $R_{\max} = R_{\text{in}}/2$  because no quantum interference takes place, and the two photons randomly take the two output ports of the beamsplitter. Assuming ideal detectors and constant bi-photon flux, the coincidence rate at zero time delay depends only on the JSA of the bi-photon. The two detection events can be written as two projection measurements:

$$\begin{aligned}\langle M_1 | &= \langle 0 | \frac{1}{\sqrt{2}} \int d\omega (a_\omega + b_\omega) \\ \langle M_2 | &= \langle 0 | \frac{1}{\sqrt{2}} \int d\omega (a_\omega - b_\omega).\end{aligned}\tag{7.22}$$

The minimal coincidence rate is then derived as

$$R_{\min} \equiv R_{\text{in}} \text{Tr}(|M_1\rangle\langle M_1| \otimes |M_2\rangle\langle M_2| \rho_{12}).\tag{7.23}$$

We have estimated indistinguishability for the two states. The first one is the post-selected bi-photon pure state, i.e., Eq. 7.19 from the SPDC process. The indistinguishability, in this case, equals the visibility of HOM interference between the signal and the idler photons from the same source. The minimum coincidence rate is derived as

$$\begin{aligned}
R_{\min} &\equiv R_{\text{in}} \text{Tr}(|M_1\rangle\langle M_1| \otimes |M_2\rangle\langle M_2| |\psi\rangle\langle\psi|_{SI}) \\
&= \frac{1}{4} R_{\text{in}} \iint d\omega d\omega' |f(\omega, \omega') - f(\omega', \omega)|^2 \\
&= \frac{1}{2} R_{\text{in}} \left\{ 1 - \text{Re} \left[ \iint d\omega d\omega' f^*(\omega, \omega') f(\omega', \omega) \right] \right\}.
\end{aligned} \tag{7.24}$$

The indistinguishability between such a pair of signal and idler photons is, in turn

$$\mathcal{I} \equiv (R_{\max} - R_{\min})/R_{\max} = \text{Re} \left[ \iint d\omega_s d\omega_i f^*(\omega_s, \omega_i) f(\omega_i, \omega_s) \right] \tag{7.25}$$

A more helpful scenario, e.g., in a quantum network, is the interference between two photons from two independent sources, e.g., two heralded single-photon sources or two quantum dots. In this case, the bi-photon state is in the form of a product state, i.e.,  $\rho_{12} = \rho_1 \otimes \rho_2$  in which  $\rho_1$  ( $\rho_2$ ) is the density matrix of the first (second) photon. The minimum coincidence rate in the HOM interference is

$$\begin{aligned}
R_{\min} &\equiv R_{\text{in}} \text{Tr}(|M_1\rangle\langle M_1| \otimes |M_2\rangle\langle M_2| \rho_1 \otimes \rho_2) \\
&= \frac{1}{2} R_{\text{in}} [1 - \text{Tr}(\rho_1 \rho_2)] = \frac{1}{4} R_{\text{in}} [2 + \|\rho_1 - \rho_2\|^2 - \text{Tr}(\rho_1^2) - \text{Tr}(\rho_2^2)],
\end{aligned} \tag{7.26}$$

where  $\|\rho\|^2 \equiv \text{Tr}(\rho^\dagger \rho)$  [223, 241]. The indistinguishability turns out to be

$$\mathcal{I} \equiv (R_{\max} - R_{\min})/R_{\max} = \frac{1}{2} [\text{Tr}(\rho_1^2) + \text{Tr}(\rho_2^2) - \|\rho_1 - \rho_2\|^2]. \tag{7.27}$$

Because of the broad spectrum of single photons generated from heralded SPDC sources,  $\|\rho_1 - \rho_2\|^2$  is much smaller than each photon's purity  $\text{Tr}(\rho_1^2)$  and  $\text{Tr}(\rho_2^2)$ . So the HOM visibility of heralded single photons from SPDC sources is primarily limited by the purity of each photon. As such, we take purity as the principal performance metric to compare our customized poling source with others. In contrast, the indistinguishability of single photons generated from quantum dots is primarily constrained by  $\|\rho_1 - \rho_2\|^2$  due to spectral wandering and spectral diffusion.

## Bibliography

- [1] Chaohan Cui, Liang Zhang, and Linran Fan. Photonic analog of mollow triplet with on-chip photon-pair generation in dressed modes. *Optics Letters*, 46(19):4753–4756, 2021.
- [2] Chaohan Cui, Liang Zhang, and Linran Fan. In situ control of effective kerr nonlinearity with pockels integrated photonics. *Nature Physics*, 18(5):497–501, 2022.
- [3] Chaohan Cui, Liang Zhang, and Linran Fan. Control spontaneous symmetry breaking of photonic chirality with reconfigurable anomalous nonlinearity. *arXiv preprint arXiv:2208.04866*, 2022.
- [4] Chaohan Cui, Christos N Gagatsos, Saikat Guha, and Linran Fan. High-purity pulsed squeezing generation with integrated photonics. *Physical Review Research*, 3(1):013199, 2021.
- [5] Chaohan Cui, Reeshad Arian, Saikat Guha, N Peyghambarian, Quntao Zhuang, and Zheshen Zhang. Wave-function engineering for spectrally uncorrelated biphotons in the telecommunication band based on a machine-learning framework. *Physical Review Applied*, 12(3):034059, 2019.
- [6] Chaohan Cui, Kaushik P Seshadreesan, Saikat Guha, and Linran Fan. High-dimensional frequency-encoded quantum information processing with passive photonics and time-resolving detection. *Physical Review Letters*, 124(19):190502, 2020.
- [7] Chaohan Cui, William Horrocks, Shuhong Hao, Saikat Guha, Nasser Peyghambarian, Quntao Zhuang, and Zheshen Zhang. Quantum receiver enhanced by adaptive learning. *Light: Science & Applications*, 11(1):344, 2022.
- [8] Walter Greiner, Joachim Reinhardt, et al. *Field quantization*. Springer Science & Business Media, 1996.
- [9] Peter D Drummond and Zbigniew Ficek. *Quantum squeezing*, volume 27. Springer Science & Business Media, 2013.
- [10] Robert W Boyd. *Nonlinear optics*. Academic press, 2020.
- [11] Daniel F Walls and Gerard J Milburn. *Quantum optics*. Springer Science & Business Media, 2007.

- [12] Govind P Agrawal. Nonlinear fiber optics. In *Nonlinear Science at the Dawn of the 21st Century*, pages 195–211. Springer, 2000.
- [13] Bahaa EA Saleh and Malvin Carl Teich. *Fundamentals of photonics*. John Wiley & Sons, 2019.
- [14] KJ Blow, Rodney Loudon, Simon JD Phoenix, and TJ Shepherd. Continuum fields in quantum optics. *Physical Review A*, 42(7):4102, 1990.
- [15] JR Jeffers, N Imoto, and R Loudon. Quantum optics of traveling-wave attenuators and amplifiers. *Physical Review A*, 47(4):3346, 1993.
- [16] Crispin W Gardiner and Matthew J Collett. Input and output in damped quantum systems: Quantum stochastic differential equations and the master equation. *Physical Review A*, 31(6):3761, 1985.
- [17] Mark Hillery and Leonard D Mlodinow. Quantization of electrodynamics in nonlinear dielectric media. *Physical Review A*, 30(4):1860, 1984.
- [18] Alexander L Gaeta, Michal Lipson, and Tobias J Kippenberg. Photonic-chip-based frequency combs. *Nature Photonics*, 13(3):158–169, 2019.
- [19] BR Mollow. Power spectrum of light scattered by two-level systems. *Physical Review*, 188(5), 1969.
- [20] F Schuda, CR Stroud Jr, and M Hercher. Observation of the resonant stark effect at optical frequencies. *Journal of Physics B: Atomic and Molecular Physics*, 7(7):L198, 1974.
- [21] A Aspect, G Roger, S Reynaud, J Dalibard, and C Cohen-Tannoudji. Time correlations between the two sidebands of the resonance fluorescence triplet. *Physical Review Letters*, 45(8):617, 1980.
- [22] M Baur, Stefan Filipp, R Bianchetti, JM Fink, M Göppl, L Steffen, Peter J Leek, Alexandre Blais, and Andreas Wallraff. Measurement of autler-townes and mollow transitions in a strongly driven superconducting qubit. *Physical Review Letters*, 102(24):243602, 2009.
- [23] Edward B Flagg, Andreas Muller, JW Robertson, Sebastien Founta, DG Deppe, Min Xiao, Wenquan Ma, GJ Salamo, and Chih-Kang Shih. Resonantly driven coherent oscillations in a solid-state quantum emitter. *Nature Physics*, 5(3):203–207, 2009.
- [24] Ata Ulhaq, Stefanie Weiler, Sven M Ulrich, Robert Roßbach, Michael Jetter, and Peter Michler. Cascaded single-photon emission from the mollow triplet sidebands of a quantum dot. *Nature Photonics*, 6(4):238–242, 2012.



- [25] Benjamin Pigeau, Sven Rohr, L Mercier De Lépinay, Arnaud Gloppe, Vincent Jacques, and Olivier Arcizet. Observation of a phononic mollow triplet in a multimode hybrid spin-nanomechanical system. *Nature Communications*, 6(1):1–7, 2015.
- [26] Kevin A Fischer, Kai Müller, Armand Rundquist, Tomas Sarmiento, Alexander Y Piggott, Yousif Kelaita, Constantin Dory, Konstantinos G Lagoudakis, and Jelena Vučković. Self-homodyne measurement of a dynamic mollow triplet in the solid state. *Nature Photonics*, 10(3):163–166, 2016.
- [27] KG Lagoudakis, KA Fischer, T Sarmiento, PL McMahon, M Radulaski, JL Zhang, Y Kelaita, C Dory, K Müller, and J Vučković. Observation of mollow triplets with tunable interactions in double lambda systems of individual hole spins. *Physical Review Letters*, 118(1):013602, 2017.
- [28] Timo Joas, Andreas M Waeber, Georg Braunbeck, and Friedemann Reinhard. Quantum sensing of weak radio-frequency signals by pulsed mollow absorption spectroscopy. *Nature Communications*, 8(1):1–6, 2017.
- [29] Jonas Meinel, Vadim Vorobyov, Boris Yavkin, Durga Dasari, Hitoshi Sumiya, Shinobu Onoda, Junichi Isoya, and Jörg Wrachtrup. Heterodyne sensing of microwaves with a quantum sensor. *arXiv preprint arXiv:2008.10068*, 2020.
- [30] John D Joannopoulos, Pierre R Villeneuve, and Shanhui Fan. Photonic crystals: putting a new twist on light. *Nature*, 386(6621):143–149, 1997.
- [31] Tomoki Ozawa, Hannah M Price, Alberto Amo, Nathan Goldman, Mohammad Hafezi, Ling Lu, Mikael C Rechtsman, David Schuster, Jonathan Simon, Oded Zilberberg, et al. Topological photonics. *Reviews of Modern Physics*, 91(1):015006, 2019.
- [32] Şahin Kaya Özdemir, Stefan Rotter, Franco Nori, and L Yang. Parity–time symmetry and exceptional points in photonics. *Nature Materials*, 18(8):783–798, 2019.
- [33] Amir H Safavi-Naeini, TP Mayer Alegre, Jasper Chan, Matt Eichenfield, Martin Winger, Qiang Lin, Jeff T Hill, Darrick E Chang, and Oskar Painter. Electromagnetically induced transparency and slow light with optomechanics. *Nature*, 472(7341):69–73, 2011.
- [34] Stefan Weis, Rémi Rivière, Samuel Deléglise, Emanuel Gavartin, Olivier Arcizet, Albert Schliesser, and Tobias J Kippenberg. Optomechanically induced transparency. *Science*, 330(6010):1520–1523, 2010.

- [35] Linran Fan, King Y Fong, Menno Poot, and Hong X Tang. Cascaded optical transparency in multimode-cavity optomechanical systems. *Nature Communications*, 6(1):1–6, 2015.
- [36] Liang Feng, Zi Jing Wong, Ren-Min Ma, Yuan Wang, and Xiang Zhang. Single-mode laser by parity-time symmetry breaking. *Science*, 346(6212):972–975, 2014.
- [37] P St-Jean, V Goblot, E Galopin, A Lemaître, T Ozawa, L Le Gratiet, I Sagnes, J Bloch, and A Amo. Lasing in topological edge states of a one-dimensional lattice. *Nature Photonics*, 11(10):651–656, 2017.
- [38] Babak Bahari, Liyi Hsu, Si Hui Pan, Daryl Preece, Abdoulaye Ndao, Abdelkrim El Amili, Yeshaiahu Fainman, and Boubacar Kanté. Photonic quantum hall effect and multiplexed light sources of large orbital angular momenta. *Nature Physics*, pages 1–4, 2021.
- [39] Zheng Wang, Yidong Chong, John D Joannopoulos, and Marin Soljačić. Observation of unidirectional backscattering-immune topological electromagnetic states. *Nature*, 461(7265):772–775, 2009.
- [40] Mian Zhang, Cheng Wang, Yaowen Hu, Amirhassan Shams-Ansari, Tianhao Ren, Shanhui Fan, and Marko Lončar. Electronically programmable photonic molecule. *Nature Photonics*, 13(1):36–40, 2019.
- [41] Xiang Guo, Chang-Ling Zou, Liang Jiang, and Hong X Tang. All-optical control of linear and nonlinear energy transfer via the zeno effect. *Physical Review Letters*, 120(20):203902, 2018.
- [42] Bo Peng, Şahin Kaya Özdemir, Weijian Chen, Franco Nori, and Lan Yang. What is and what is not electromagnetically induced transparency in whispering-gallery microcavities. *Nature Communications*, 5(1):1–9, 2014.
- [43] Xiyuan Lu, Steven Rogers, Wei C Jiang, and Qiang Lin. Selective engineering of cavity resonance for frequency matching in optical parametric processes. *Applied Physics Letters*, 105(15):151104, 2014.
- [44] Yuntao Xu, Ayed Al Sayem, Linran Fan, Changling Zou, and Hong X Tang. Bidirectional electro-optic conversion reaching 1% efficiency with thin film lithium niobate. In *CLEO: Science and Innovations*, pages SM4L–4. Optical Society of America, 2021.
- [45] Andreas Christ, Kaisa Laiho, Andreas Eckstein, Katiúscia N Casseiro, and Christine Silberhorn. Probing multimode squeezing with correlation functions. *New Journal of Physics*, 13(3):033027, 2011.

- [46] Ang Li, Thomas Van Vaerenbergh, Peter De Heyn, Peter Bienstman, and Wim Bogaerts. Backscattering in silicon microring resonators: a quantitative analysis. *Laser & Photonics Reviews*, 10(3):420–431, 2016.
- [47] Linran Fan, Chang-Ling Zou, Menno Poot, Risheng Cheng, Xiang Guo, Xu Han, and Hong X Tang. Integrated optomechanical single-photon frequency shifter. *Nature Photonics*, 10(12):766–770, 2016.
- [48] Michał Karpiński, Michał Jachura, Laura J Wright, and Brian J Smith. Bandwidth manipulation of quantum light by an electro-optic time lens. *Nature Photonics*, 11(1):53–57, 2017.
- [49] Vahid Ansari, John M Donohue, Benjamin Brecht, and Christine Silberhorn. Tailoring nonlinear processes for quantum optics with pulsed temporal-mode encodings. *Optica*, 5(5):534–550, 2018.
- [50] Steven D Rogers, Austin Graf, Usman A Javid, and Qiang Lin. Coherent quantum dynamics of systems with coupling-induced creation pathways. *Communications Physics*, 2(1):1–9, 2019.
- [51] Usman A Javid, Steven D Rogers, Austin Graf, and Qiang Lin. Temporally asymmetric biphoton states in cavity-enhanced optical parametric processes. *Physical Review Applied*, 12(5):054019, 2019.
- [52] Michael Kues, Christian Reimer, Joseph M Lukens, William J Munro, Andrew M Weiner, David J Moss, and Roberto Morandotti. Quantum optical microcombs. *Nature Photonics*, 13(3):170–179, 2019.
- [53] Christian Reimer, Lucia Caspani, Matteo Clerici, Marcello Ferrera, Michael Kues, Marco Peccianti, Alessia Pasquazi, Luca Razzari, Brent E Little, Sai T Chu, et al. Integrated frequency comb source of heralded single photons. *Optics Express*, 22(6):6535–6546, 2014.
- [54] Tobias J Kippenberg, Alexander L Gaeta, Michal Lipson, and Michael L Gorodetsky. Dissipative kerr solitons in optical microresonators. *Science*, 361(6402), 2018.
- [55] Roland Schiek. Nonlinear refraction caused by cascaded second-order nonlinearity in optical waveguide structures. *Journal of the Optical Society of America B*, 10(10):1848–1855, 1993.
- [56] AG White, J Mlynek, and S Schiller. Cascaded second-order nonlinearity in an optical cavity. *Europhysics Letters*, 35(6):425, 1996.
- [57] Ivan Biaggio. Degenerate four-wave mixing in noncentrosymmetric materials. *Physical Review A*, 64(6):063813, 2001.

- [58] Christian Kolleck. Cascaded second-order contribution to the third-order nonlinear susceptibility. *Physical Review A*, 69(5):053812, 2004.
- [59] Ming Li, Chang-Ling Zou, Chun-Hua Dong, and Dao-Xin Dai. Optimal third-harmonic generation in an optical microcavity with  $\chi^{(2)}$  and  $\chi^{(3)}$  nonlinearities. *Optics Express*, 26(21):27294–27304, 2018.
- [60] Ming Li, Chang-Ling Zou, Chun-Hua Dong, Xi-Feng Ren, and Dao-Xin Dai. Enhancement of second-harmonic generation based on the cascaded second- and third-order nonlinear processes in a multimode optical microcavity. *Physical Review A*, 98(1):013854, 2018.
- [61] Mikhail F Limonov, Mikhail V Rybin, Alexander N Poddubny, and Yuri S Kivshar. Fano resonances in photonics. *Nature Photonics*, 11(9):543–554, 2017.
- [62] Nicholas C Harris, Yangjin Ma, Jacob Mower, Tom Baehr-Jones, Dirk Englund, Michael Hochberg, and Christophe Galland. Efficient, compact and low loss thermo-optic phase shifter in silicon. *Optics Express*, 22(9):10487–10493, 2014.
- [63] Cheng Wang, Mian Zhang, Brian Stern, Michal Lipson, and Marko Lončar. Nanophotonic lithium niobate electro-optic modulators. *Optics Express*, 26(2):1547–1555, 2018.
- [64] Cheng Wang, Mian Zhang, Xi Chen, Maxime Bertrand, Amirhassan Shams-Ansari, Sethumadhavan Chandrasekhar, Peter Winzer, and Marko Lončar. Integrated lithium niobate electro-optic modulators operating at cmos-compatible voltages. *Nature*, 562(7725):101–104, 2018.
- [65] Po Dong, Wei Qian, Hong Liang, Roshanak Shafiiha, Ning-Ning Feng, Dazeng Feng, Xuezhe Zheng, Ashok V Krishnamoorthy, and Mehdi Asghari. Low power and compact reconfigurable multiplexing devices based on silicon microring resonators. *Optics Express*, 18(10):9852–9858, 2010.
- [66] Graham T Reed, G Mashanovich, F Yand Gardes, and DJ Thomson. Silicon optical modulators. *Nature Photonics*, 4(8):518–526, 2010.
- [67] Han Zhao, Xingdu Qiao, Tianwei Wu, Bikashkali Midya, Stefano Longhi, and Liang Feng. Non-hermitian topological light steering. *Science*, 365(6458):1163–1166, 2019.
- [68] Zhifeng Zhang, Xingdu Qiao, Bikashkali Midya, Kevin Liu, Jingbo Sun, Tianwei Wu, Wenjing Liu, Ritesh Agarwal, Josep Miquel Jornet, Stefano Longhi, et al. Tunable topological charge vortex microlaser. *Science*, 368(6492):760–763, 2020.

- [69] Yichen Shen, Nicholas C Harris, Scott Skirlo, Mihika Prabhu, Tom Baehr-Jones, Michael Hochberg, Xin Sun, Shijie Zhao, Hugo Larochelle, Dirk Englund, et al. Deep learning with coherent nanophotonic circuits. *Nature Photonics*, 11(7):441–446, 2017.
- [70] Johannes Feldmann, Nathan Youngblood, C David Wright, Harish Bhaskaran, and Wolfram HP Pernice. All-optical spiking neurosynaptic networks with self-learning capabilities. *Nature*, 569(7755):208–214, 2019.
- [71] Jacques Carolan, Christopher Harrold, Chris Sparrow, Enrique Martín-López, Nicholas J Russell, Joshua W Silverstone, Peter J Shadbolt, Nobuyuki Matsuda, Manabu Oguma, Mikitaka Itoh, et al. Universal linear optics. *Science*, 349(6249):711–716, 2015.
- [72] Jianwei Wang, Fabio Sciarrino, Anthony Laing, and Mark G Thompson. Integrated photonic quantum technologies. *Nature Photonics*, 14(5):273–284, 2020.
- [73] Alan E Willner, Salman Khaleghi, Mohammad Reza Chitgarha, and Omer Faruk Yilmaz. All-optical signal processing. *Journal of Lightwave Technology*, 32(4):660–680, 2013.
- [74] Mingxiao Li, Hanxiao Liang, Rui Luo, Yang He, Jingwei Ling, and Qiang Lin. Photon-level tuning of photonic nanocavities. *Optica*, 6(7):860–863, 2019.
- [75] Anton V Zasedatelev, Anton V Baranikov, Denis Sannikov, Darius Urbonas, Fabio Scafirimuto, Vladislav Yu Shishkov, Evgeny S Andrianov, Yurii E Lozovik, Ullrich Scherf, Thilo Stöferle, et al. Single-photon nonlinearity at room temperature. *Nature*, 597(7877):493–497, 2021.
- [76] Jeremy L O’Brien, Akira Furusawa, and Jelena Vučković. Photonic quantum technologies. *Nature Photonics*, 3(12):687–695, 2009.
- [77] Gerard J Milburn. Quantum optical fredkin gate. *Physical Review Letters*, 62(18):2124, 1989.
- [78] Daniel J Brod and Joshua Combes. Passive cphase gate via cross-kerr nonlinearities. *Physical Review Letters*, 117(8):080502, 2016.
- [79] Mikkel Heuck, Kurt Jacobs, and Dirk R Englund. Controlled-phase gate using dynamically coupled cavities and optical nonlinearities. *Physical Review Letters*, 124(16):160501, 2020.
- [80] Mark A Foster, Reza Salem, David F Geraghty, Amy C Turner-Foster, Michal Lipson, and Alexander L Gaeta. Silicon-chip-based ultrafast optical oscilloscope. *Nature*, 456(7218):81–84, 2008.

- [81] Linran Fan, Chang-Ling Zou, Na Zhu, and Hong X Tang. Spectrotemporal shaping of itinerant photons via distributed nanomechanics. *Nature Photonics*, 13(5):323–327, 2019.
- [82] Katsumi Iwatsuki, Kazuo Hotate, and Minoru Higashiguchi. Kerr effect in an optical passive ring-resonator gyro. *Journal of Lightwave Technology*, 4(6):645–651, 1986.
- [83] Wei Liang, Vladimir S Ilchenko, Anatoliy A Savchenkov, Elijah Dale, Danny Eliyahu, Andrey B Matsko, and Lute Maleki. Resonant microphotonic gyroscope. *Optica*, 4(1):114–117, 2017.
- [84] Andrew D Ellis, Jian Zhao, and David Cotter. Approaching the non-linear shannon limit. *Journal of Lightwave Technology*, 28(4):423–433, 2009.
- [85] Son Thai Le, Vahid Aref, and Henning Buelow. Nonlinear signal multiplexing for communication beyond the kerr nonlinearity limit. *Nature Photonics*, 11(9):570–576, 2017.
- [86] Xiaoxiao Xue, Yi Xuan, Yang Liu, Pei-Hsun Wang, Steven Chen, Jian Wang, Dan E Leaird, Minghao Qi, and Andrew M Weiner. Mode-locked dark pulse kerr combs in normal-dispersion microresonators. *Nature Photonics*, 9(9):594–600, 2015.
- [87] Óskar B Helgason, Francisco R Arteaga-Sierra, Zhichao Ye, Krishna Twayana, Peter A Andrekson, Magnus Karlsson, Jochen Schröder, and Victor Torres-Company. Dissipative solitons in photonic molecules. *Nature Photonics*, 15(4):305–310, 2021.
- [88] Ch Bosshard, I Biaggio, S Follonier, P Günter, et al. Cascaded contributions to degenerate four-wave mixing in an acentric organic crystal. *Optics Letters*, 24(4):196–198, 1999.
- [89] Hua-Tang Tan and He Huang. Bright quadripartite entanglement from competing  $\chi$  (2) nonlinearities. *Physical Review A*, 83(1):015802, 2011.
- [90] Kiyotaka Sasagawa and Masahiro Tsuchiya. Highly efficient third harmonic generation in a periodically poled MgO : LiNbO<sub>3</sub> disk resonator. *Applied Physics Express*, 2(12):122401, 2009.
- [91] Ville Ulvila, Christopher R Phillips, Lauri Halonen, and Markku Vainio. Frequency comb generation by a continuous-wave-pumped optical parametric oscillator based on cascading quadratic nonlinearities. *Optics Letters*, 38(21):4281–4284, 2013.

- [92] Guang-Zhen Li, Yu-Ping Chen, Hao-Wei Jiang, and Xian-Feng Chen. Enhanced kerr electro-optic nonlinearity and its application in controlling second-harmonic generation. *Photonics Research*, 3(4):168–172, 2015.
- [93] Shijie Liu, Yuanlin Zheng, and Xianfeng Chen. Cascading second-order nonlinear processes in a lithium niobate-on-insulator microdisk. *Optics Letters*, 42(18):3626–3629, 2017.
- [94] Richard Wolf, Ingo Breunig, Hans Zappe, and Karsten Buse. Cascaded second-order optical nonlinearities in on-chip micro rings. *Optics Express*, 25(24):29927–29933, 2017.
- [95] Li Zhang, Zhenzhong Hao, Qiang Luo, Ang Gao, Ru Zhang, Chen Yang, Feng Gao, Fang Bo, Guoquan Zhang, and Jingjun Xu. Dual-periodically poled lithium niobate microcavities supporting multiple coupled parametric processes. *Optics Letters*, 45(12):3353–3356, 2020.
- [96] C Dorrer, RG Roides, J Bromage, and JD Zuegel. Self-phase modulation compensation in a regenerative amplifier using cascaded second-order nonlinearities. *Optics Letters*, 39(15):4466–4469, 2014.
- [97] Chi Xiong, Wolfram HP Pernice, Xiankai Sun, Carsten Schuck, King Y Fong, and Hong X Tang. Aluminum nitride as a new material for chip-scale optomechanics and nonlinear optics. *New Journal of Physics*, 14(9):095014, 2012.
- [98] Di Zhu, Linbo Shao, Mengjie Yu, Rebecca Cheng, Boris Desiatov, CJ Xin, Yaowen Hu, Jeffrey Holzgrafe, Soumya Ghosh, Amirhassan Shams-Ansari, et al. Integrated photonics on thin-film lithium niobate. *Advances in Optics and Photonics*, 13(2):242–352, 2021.
- [99] Ali W Elshaari, Wolfram Pernice, Kartik Srinivasan, Oliver Benson, and Val Zwiller. Hybrid integrated quantum photonic circuits. *Nature Photonics*, 14(5):285–298, 2020.
- [100] Juanjuan Lu, Ming Li, Chang-Ling Zou, Ayed Al Sayem, and Hong X Tang. Toward 1% single-photon anharmonicity with periodically poled lithium niobate microring resonators. *Optica*, 7(12):1654–1659, 2020.
- [101] Boris Desiatov, Amirhassan Shams-Ansari, Mian Zhang, Cheng Wang, and Marko Lončar. Ultra-low-loss integrated visible photonics using thin-film lithium niobate. *Optica*, 6(3):380–384, 2019.
- [102] Vladimir S Ilchenko, Anatoliy A Savchenkov, Andrey B Matsko, and Lute Maleki. Nonlinear optics and crystalline whispering gallery mode cavities. *Physical Review Letters*, 92(4):043903, 2004.

- [103] Yanne K Chembo and Curtis R Menyuk. Spatiotemporal lugiato-lefever formalism for kerr-comb generation in whispering-gallery-mode resonators. *Physical Review A*, 87(5):053852, 2013.
- [104] Ian Briggs, Songyan Hou, Chaohan Cui, and Linran Fan. Simultaneous type-i and type-ii phase matching for second-order nonlinearity in integrated lithium niobate waveguide. *Optics Express*, 29(16):26183–26190, 2021.
- [105] Lucia Caspani, Chunle Xiong, Benjamin J Eggleton, Daniele Bajoni, Marco Liscidini, Matteo Galli, Roberto Morandotti, and David J Moss. Integrated sources of photon quantum states based on nonlinear optics. *Light: Science & Applications*, 6(11):e17100–e17100, 2017.
- [106] Erman Engin, Damien Bonneau, Chandra M Natarajan, Alex S Clark, Michael G Tanner, Robert H Hadfield, Sanders N Dorenbos, Val Zwiller, Kazuya Ohira, Nobuo Suzuki, et al. Photon pair generation in a silicon micro-ring resonator with reverse bias enhancement. *Optics Express*, 21(23):27826–27834, 2013.
- [107] Jeremy Bernstein. Spontaneous symmetry breaking, gauge theories, the higgs mechanism and all that. *Reviews of Modern Physics*, 46(1):7, 1974.
- [108] G Baskaran and Philip W Anderson. Gauge theory of high-temperature superconductors and strongly correlated fermi systems. *Physical Review B*, 37(1):580, 1988.
- [109] Boris A Malomed. *Spontaneous symmetry breaking, self-trapping, and Josephson oscillations*. Springer, 2013.
- [110] Uzi Efron. *Spatial light modulator technology: materials, devices, and applications*, volume 47. CRC press, 1994.
- [111] Ningbo Zhao, Xiaoying Li, Guifang Li, and Joseph M Kahn. Capacity limits of spatially multiplexed free-space communication. *Nature Photonics*, 9(12):822–826, 2015.
- [112] Yan Han and Guifang Li. Coherent optical communication using polarization multiple-input-multiple-output. *Optics Express*, 13(19):7527–7534, 2005.
- [113] Andrea Crespi, Roberta Ramponi, Roberto Osellame, Linda Sansoni, Irene Bongioanni, Fabio Sciarrino, Giuseppe Vallone, and Paolo Mataloni. Integrated photonic quantum gates for polarization qubits. *Nature Communications*, 2(1):1–6, 2011.
- [114] Joseph M Lukens and Pavel Lougovski. Frequency-encoded photonic qubits for scalable quantum information processing. *Optica*, 4(1):8–16, 2017.



- [115] Michael G Raymer and Ian A Walmsley. Temporal modes in quantum optics: then and now. *Physica Scripta*, 95(6):064002, 2020.
- [116] Brandon Redding, Li Ge, Qinghai Song, Jan Wiersig, Glenn S Solomon, and Hui Cao. Local chirality of optical resonances in ultrasmall resonators. *Physical Review Letters*, 108(25):253902, 2012.
- [117] Hui Cao and Jan Wiersig. Dielectric microcavities: Model systems for wave chaos and non-hermitian physics. *Reviews of Modern Physics*, 87(1):61, 2015.
- [118] Pei Miao, Zhifeng Zhang, Jingbo Sun, Wiktor Walasik, Stefano Longhi, Natalia M Litchinitser, and Liang Feng. Orbital angular momentum microlaser. *Science*, 353(6298):464–467, 2016.
- [119] Liang Feng, Ramy El-Ganainy, and Li Ge. Non-hermitian photonics based on parity–time symmetry. *Nature Photonics*, 11(12):752–762, 2017.
- [120] Ramy El-Ganainy, Konstantinos G Makris, Mercedeh Khajavikhan, Ziad H Musslimani, Stefan Rotter, and Demetrios N Christodoulides. Non-hermitian physics and pt symmetry. *Nature Physics*, 14(1):11–19, 2018.
- [121] M Decker, MW Klein, M Wegener, and S Linden. Circular dichroism of planar chiral magnetic metamaterials. *Optics Letters*, 32(7):856–858, 2007.
- [122] Mingkai Liu, David A Powell, Ilya V Shadrivov, Mikhail Lapine, and Yuri S Kivshar. Spontaneous chiral symmetry breaking in metamaterials. *Nature Communications*, 5(1):4441, 2014.
- [123] Clément Sayrin, Christian Junge, Rudolf Mitsch, Bernhard Albrecht, Danny O’Shea, Philipp Schneeweiss, Jürgen Volz, and Arno Rauschenbeutel. Nanophotonic optical isolator controlled by the internal state of cold atoms. *Physical Review X*, 5(4):041036, 2015.
- [124] Keyu Xia, Franco Nori, and Min Xiao. Cavity-free optical isolators and circulators using a chiral cross-kerr nonlinearity. *Physical Review Letters*, 121(20):203602, 2018.
- [125] Donggyu B Sohn, Oğulcan E Örsel, and Gaurav Bahl. Electrically driven optical isolation through phonon-mediated photonic autler–townes splitting. *Nature Photonics*, 15(11):822–827, 2021.
- [126] Srinivas Raghu and Frederick Duncan Michael Haldane. Analogs of quantum-hall-effect edge states in photonic crystals. *Physical Review A*, 78(3):033834, 2008.

- [127] Mohammad Hafezi, Eugene A Demler, Mikhail D Lukin, and Jacob M Taylor. Robust optical delay lines with topological protection. *Nature Physics*, 7(11):907–912, 2011.
- [128] Bo Peng, Şahin Kaya Özdemir, Matthias Liertzer, Weijian Chen, Johannes Kramer, Huzeyfe Yilmaz, Jan Wiersig, Stefan Rotter, and Lan Yang. Chiral modes and directional lasing at exceptional points. *Proceedings of the National Academy of Sciences*, 113(25):6845–6850, 2016.
- [129] Nicola Carlon Zambon, Philippe St-Jean, Marijana Milićević, Aristide Lemaître, Abdelmounaim Harouri, Luc Le Gratiet, Olivier Bleu, DD Solnyshkov, Guillaume Malpuech, Isabelle Sagnes, et al. Optically controlling the emission chirality of microlasers. *Nature Photonics*, 13(4):283–288, 2019.
- [130] R Mitsch, C Sayrin, B Albrecht, P Schneeweiss, and A Rauschenbeutel. Quantum state-controlled directional spontaneous emission of photons into a nanophotonic waveguide. *Nature Communications*, 5(1):1–5, 2014.
- [131] Immo Söllner, Sahand Mahmoodian, Sofie Lindskov Hansen, Leonardo Midolo, Alisa Javadi, Gabija Kiršanskė, Tommaso Pregnolato, Haitham El-Ella, Eun Hye Lee, Jin Dong Song, et al. Deterministic photon–emitter coupling in chiral photonic circuits. *Nature Nanotechnology*, 10(9):775–778, 2015.
- [132] Christian Junge, Danny O’shea, Jürgen Volz, and Arno Rauschenbeutel. Strong coupling between single atoms and nontransversal photons. *Physical Review Letters*, 110(21):213604, 2013.
- [133] Itay Shomroni, Serge Rosenblum, Yulia Lovsky, Orel Bechler, Gabriel Guelandelman, and Barak Dayan. All-optical routing of single photons by a one-atom switch controlled by a single photon. *Science*, 345(6199):903–906, 2014.
- [134] Peter Lodahl, Sahand Mahmoodian, Søren Stobbe, Arno Rauschenbeutel, Philipp Schneeweiss, Jürgen Volz, Hannes Pichler, and Peter Zoller. Chiral quantum optics. *Nature*, 541(7638):473–480, 2017.
- [135] Qi-Tao Cao, Heming Wang, Chun-Hua Dong, Hui Jing, Rui-Shan Liu, Xi Chen, Li Ge, Qihuang Gong, and Yun-Feng Xiao. Experimental demonstration of spontaneous chirality in a nonlinear microresonator. *Physical Review Letters*, 118(3):033901, 2017.
- [136] Leonardo Del Bino, Jonathan M Silver, Sarah L Stebbings, and Pascal Del’Haye. Symmetry breaking of counter-propagating light in a nonlinear resonator. *Scientific Reports*, 7(1):1–6, 2017.

- [137] Bruno Garbin, Julien Fatome, Gian-Luca Oppo, Miro Erkintalo, Stuart G Murdoch, and Stéphane Coen. Asymmetric balance in symmetry breaking. *Physical Review Research*, 2(2):023244, 2020.
- [138] Qi-Tao Cao, Ruishan Liu, Heming Wang, Yu-Kun Lu, Cheng-Wei Qiu, Stefan Rotter, Qihuang Gong, and Yun-Feng Xiao. Reconfigurable symmetry-broken laser in a symmetric microcavity. *Nature Communications*, 11(1):1–7, 2020.
- [139] Gang Xu, Alexander U Nielsen, Bruno Garbin, Lewis Hill, Gian-Luca Oppo, Julien Fatome, Stuart G Murdoch, Stéphane Coen, and Miro Erkintalo. Spontaneous symmetry breaking of dissipative optical solitons in a two-component kerr resonator. *Nature Communications*, 12(1):1–9, 2021.
- [140] Leonardo Del Bino, Jonathan M Silver, Michael TM Woodley, Sarah L Stebbings, Xin Zhao, and Pascal Del’Haye. Microresonator isolators and circulators based on the intrinsic nonreciprocity of the kerr effect. *Optica*, 5(3):279–282, 2018.
- [141] Jonathan M Silver, Leonardo Del Bino, Michael TM Woodley, George N Ghalanos, Andreas Ø Svela, Niall Moroney, Shuangyou Zhang, Kenneth TV Grat-tan, and Pascal Del’Haye. Nonlinear enhanced microresonator gyroscope. *Op-tica*, 8(9):1219–1226, 2021.
- [142] Yi-Yi Li, Qi-Tao Cao, Jin-hui Chen, Xiao-Chong Yu, and Yun-Feng Xiao. Mi-crocavity sensor enhanced by spontaneous chiral symmetry breaking. *Physical Review Applied*, 16(4):044016, 2021.
- [143] Alexander V Buryak, Paolo Di Trapani, Dmitry V Skryabin, and Stefano Trillo. Optical solitons due to quadratic nonlinearities: from basic physics to futuristic applications. *Physics Reports*, 370(2):63–235, 2002.
- [144] Simona Mosca, Iolanda Ricciardi, Maria Parisi, Pasquale Maddaloni, Luigi Santamaria, Paolo De Natale, and Maurizio De Rosa. Direct generation of optical frequency combs in  $\chi^{(2)}$  nonlinear cavities. *Nanophotonics*, 5(2):316–331, 2016.
- [145] Morten Bache. Cascaded nonlinearities for ultrafast nonlinear optical science and applications, 2017. Doctor Technices Thesis, Danmarks Tekniske Univer-sitet.
- [146] BB Zhou, Xing Liu, HR Guo, XL Zeng, XF Chen, HP Chung, Yen-Hung Chen, and Morten Bache. Parametrically tunable soliton-induced resonant radiation by three-wave mixing. *Physical Review Letters*, 118(14):143901, 2017.

- [147] Liang Zhang, Chaohan Cui, Jianchang Yan, Yanan Guo, Junxi Wang, and Linran Fan. On-chip parallel processing of quantum frequency combs for high-dimensional hyper-entanglement generation. *arXiv preprint arXiv:2111.12784*, 2021.
- [148] Yu-Hung Lai, Yu-Kun Lu, Myoung-Gyun Suh, Zhiquan Yuan, and Kerry Vahala. Observation of the exceptional-point-enhanced sagnac effect. *Nature*, 576(7785):65–69, 2019.
- [149] Weijian Chen, Şahin Kaya Özdemir, Guangming Zhao, Jan Wiersig, and Lan Yang. Exceptional points enhance sensing in an optical microcavity. *Nature*, 548(7666):192–196, 2017.
- [150] Qi-Fan Yang, Xu Yi, Ki Youl Yang, and Kerry Vahala. Counter-propagating solitons in microresonators. *Nature Photonics*, 11(9):560–564, 2017.
- [151] AE Kaplan and P Meystre. Directionally asymmetrical bistability in a symmetrically pumped nonlinear ring interferometer. *Optics Communications*, 40(3):229–232, 1982.
- [152] Michael TM Woodley, Jonathan M Silver, Lewis Hill, François Copie, Leonardo Del Bino, Shuangyou Zhang, Gian-Luca Oppo, and Pascal Del’Haye. Universal symmetry-breaking dynamics for the kerr interaction of counterpropagating light in dielectric ring resonators. *Physical Review A*, 98(5):053863, 2018.
- [153] Lewis Hill, Gian-Luca Oppo, Michael TM Woodley, and Pascal Del’Haye. Effects of self-and cross-phase modulation on the spontaneous symmetry breaking of light in ring resonators. *Physical Review A*, 101(1):013823, 2020.
- [154] S Shimotsu, S Oikawa, T Saitou, N Mitsugi, K Kubodera, T Kawanishi, and M Izutsu. Single side-band modulation performance of a linbo 3 integrated modulator consisting of four-phase modulator waveguides. *IEEE Photonics Technology Letters*, 13(4):364–366, 2001.
- [155] Zheng Gong, Alexander Bruch, Mohan Shen, Xiang Guo, Hojoong Jung, Linran Fan, Xianwen Liu, Liang Zhang, Junxi Wang, Jinmin Li, et al. High-fidelity cavity soliton generation in crystalline aln micro-ring resonators. *Optics Letters*, 43(18):4366–4369, 2018.
- [156] Christian Weedbrook, Stefano Pirandola, Raúl García-Patrón, Nicolas J Cerf, Timothy C Ralph, Jeffrey H Shapiro, and Seth Lloyd. Gaussian quantum information. *Reviews of Modern physics*, 84(2):621, 2012.

- [157] T Opatrny, G Kurizki, and D-G Welsch. Improvement on teleportation of continuous variables by photon subtraction via conditional measurement. *Physical Review A*, 61(3):032302, 2000.
- [158] Alexei Ourjoumtsev, Aurelien Dantan, Rosa Tualle-Brouri, and Philippe Grangier. Increasing entanglement between gaussian states by coherent photon subtraction. *Physical Review Letters*, 98(3):030502, 2007.
- [159] Kentaro Wakui, Hiroki Takahashi, Akira Furusawa, and Masahide Sasaki. Photon subtracted squeezed states generated with periodically poled ktiopo 4. *Optics Express*, 15(6):3568–3574, 2007.
- [160] Naoto Namekata, Yuta Takahashi, Go Fujii, Daiji Fukuda, Sunao Kurimura, and Shuichiro Inoue. Non-gaussian operation based on photon subtraction using a photon-number-resolving detector at a telecommunications wavelength. *Nature Photonics*, 4(9):655, 2010.
- [161] Mattia Walschaers, Claude Fabre, Valentina Parigi, and Nicolas Treps. Entanglement and wigner function negativity of multimode non-gaussian states. *Physical Review Letters*, 119(18):183601, 2017.
- [162] Timothy C Ralph, Alexei Gilchrist, Gerard J Milburn, William J Munro, and Scott Glancy. Quantum computation with optical coherent states. *Physical Review A*, 68(4):042319, 2003.
- [163] Alexei Ourjoumtsev, Rosa Tualle-Brouri, Julien Laurat, and Philippe Grangier. Generating optical schrödinger kittens for quantum information processing. *Science*, 312(5770):83–86, 2006.
- [164] Jonas S Neergaard-Nielsen, B Melholt Nielsen, C Hettich, Klaus Mølmer, and Eugene S Polzik. Generation of a superposition of odd photon number states for quantum information networks. *Physical Review Letters*, 97(8):083604, 2006.
- [165] Warit Asavanant, Kota Nakashima, Yu Shiozawa, Jun-Ichi Yoshikawa, and Akira Furusawa. Generation of highly pure schrödinger’s cat states and real-time quadrature measurements via optical filtering. *Optics Express*, 25(26):32227–32242, 2017.
- [166] Daniel Gottesman, Alexei Kitaev, and John Preskill. Encoding a qubit in an oscillator. *Physical Review A*, 64:012310, Jun 2001.
- [167] Nicolas C Menicucci, Peter Van Loock, Mile Gu, Christian Weedbrook, Timothy C Ralph, and Michael A Nielsen. Universal quantum computation with continuous-variable cluster states. *Physical Review Letters*, 97(11):110501, 2006.

- [168] Nicolas C Menicucci. Fault-tolerant measurement-based quantum computing with continuous-variable cluster states. *Physical Review Letters*, 112(12):120504, 2014.
- [169] Warit Asavanant, Yu Shiozawa, Shota Yokoyama, Baramée Charoensombutamon, Hiroki Emura, Rafael N. Alexander, Shuntaro Takeda, Jun-ichi Yoshikawa, Nicolas C. Menicucci, Hidehiro Yonezawa, and Akira Furusawa. Generation of time-domain-multiplexed two-dimensional cluster state. *Science*, 366(6463):373–376, 2019.
- [170] Ben Q Baragiola, Giacomo Pantaleoni, Rafael N Alexander, Angela Karanjai, and Nicolas C Menicucci. All-gaussian universality and fault tolerance with the gottesman-kitaev-preskill code. *Physical Review Letters*, 123(20):200502, 2019.
- [171] Olivier Pfister. Continuous-variable quantum computing in the quantum optical frequency comb. *Journal of Physics B*, 53(1):012001, 2019.
- [172] Christos N. Gagatsos and Saikat Guha. Efficient representation of gaussian states for multimode non-gaussian quantum state engineering via subtraction of arbitrary number of photons. *Physical Review A*, 99:053816, May 2019.
- [173] Daiqin Su, Casey R. Myers, and Krishna Kumar Sabapathy. Conversion of gaussian states to non-gaussian states using photon-number-resolving detectors. *Physical Review A*, 100:052301, Nov 2019.
- [174] Gil Triginer Garces, Helen M. Chrzanowski, Shakib Daryanoosh, Valerian Thiel, Anna L. Marchant, Raj B. Patel, Peter C. Humphreys, Animesh Datta, and Ian A. Walmsley. Quantum-enhanced stimulated emission detection for label-free microscopy. *Applied Physics Letters*, 117(2):024002, 2020.
- [175] Richard E Slusher, Ph Grangier, A LaPorta, B Yurke, and MJ Potasek. Pulsed squeezed light. *Physical Review Letters*, 59(22):2566, 1987.
- [176] Chonghoon Kim and Prem Kumar. Quadrature-squeezed light detection using a self-generated matched local oscillator. *Physical Review Letters*, 73(12):1605, 1994.
- [177] Yujiro Eto, Takashi Tajima, Yun Zhang, and Takuya Hirano. Observation of squeezed light at  $1.535 \mu\text{m}$  using a pulsed homodyne detector. *Optics Letters*, 32(12):1698–1700, 2007.
- [178] Andreas Eckstein, Andreas Christ, Peter J Mosley, and Christine Silberhorn. Highly efficient single-pass source of pulsed single-mode twin beams of light. *Physical Review Letters*, 106(1):013603, 2011.

- [179] Ulrik L Andersen, Tobias Gehring, Christoph Marquardt, and Gerd Leuchs. 30 years of squeezed light generation. *Physica Scripta*, 91(5):053001, 2016.
- [180] Wojciech Wasilewski, AI Lvovsky, Konrad Banaszek, and Czesław Radzewicz. Pulsed squeezed light: Simultaneous squeezing of multiple modes. *Physical Review A*, 73(6):063819, 2006.
- [181] Giuseppe Patera, Nicolas Treps, Claude Fabre, and German J De Valcarcel. Quantum theory of synchronously pumped type i optical parametric oscillators: characterization of the squeezed supermodes. *European Physical Journal D*, 56(1):123, 2010.
- [182] Shifeng Jiang, Nicolas Treps, and Claude Fabre. A time/frequency quantum analysis of the light generated by synchronously pumped optical parametric oscillators. *New Journal of Physics*, 14(4):043006, 2012.
- [183] Yujiro Eto, Takashi Tajima, Yun Zhang, and Takuya Hirano. Observation of quadrature squeezing in a  $\chi^{(2)}$  nonlinear waveguide using a temporally shaped local oscillator pulse. *Optics Express*, 16(14):10650–10657, 2008.
- [184] Claude Bloch and Albert Messiah. The canonical form of an antisymmetric tensor and its application to the theory of superconductivity. *Nuclear Physics*, 39:95–106, 1962.
- [185] Samuel L Braunstein. Squeezing as an irreducible resource. *Physical Review A*, 71(5):055801, 2005.
- [186] Markus Aspelmeyer, Tobias J Kippenberg, and Florian Marquardt. Cavity optomechanics. *Reviews of Modern physics*, 86(4):1391, 2014.
- [187] Xiang Guo, Chang-ling Zou, Carsten Schuck, Hojoong Jung, Risheng Cheng, and Hong X Tang. Parametric down-conversion photon-pair source on a nanophotonic chip. *Light: Science & Applications*, 6(5):e16249–e16249, 2017.
- [188] Linran Fan, Chang-Ling Zou, Risheng Cheng, Xiang Guo, Xu Han, Zheng Gong, Sihao Wang, and Hong X Tang. Superconducting cavity electro-optics: a platform for coherent photon conversion between superconducting and photonic circuits. *Science Advances*, 4(8):eaar4994, 2018.
- [189] Biswarup Guha, Felix Marsault, Fabian Cadiz, Laurence Morgenroth, Vladimir Ulin, Vladimir Berkovitz, Aristide Lemaître, Carmen Gomez, Alberto Amo, Sylvain Combrié, et al. Surface-enhanced gallium arsenide photonic resonator with quality factor of  $6 \times 10^6$ . *Optica*, 4(2):218–221, 2017.

- [190] Rui Luo, Haowei Jiang, Steven Rogers, Hanxiao Liang, Yang He, and Qiang Lin. On-chip second-harmonic generation and broadband parametric down-conversion in a lithium niobate microresonator. *Optics Express*, 25(20):24531–24539, 2017.
- [191] Cheng Wang, Carsten Langrock, Alireza Marandi, Marc Jankowski, Mian Zhang, Boris Desiatov, Martin M Fejer, and Marko Lončar. Ultrahigh-efficiency wavelength conversion in nanophotonic periodically poled lithium niobate waveguides. *Optica*, 5(11):1438–1441, 2018.
- [192] Juanjuan Lu, Joshua B Surya, Xianwen Liu, Alexander W Bruch, Zheng Gong, Yuntao Xu, and Hong X Tang. Periodically poled thin-film lithium niobate microring resonators with a second-harmonic generation efficiency of 250,000%/w. *Optica*, 6(12):1455–1460, 2019.
- [193] Alexander W Bruch, Xianwen Liu, Joshua B Surya, Chang-Ling Zou, and Hong X Tang. On-chip  $\chi^{(2)}$  microring optical parametric oscillator. *Optica*, 6(10):1361–1366, 2019.
- [194] Michael Kues, Christian Reimer, Piotr Roztockı, Luis Romero Cortés, Stefania Sciarra, Benjamin Wetzler, Yanbing Zhang, Alfonso Cino, Sai T Chu, Brent E Little, et al. On-chip generation of high-dimensional entangled quantum states and their coherent control. *Nature*, 546(7660):622–626, 2017.
- [195] Yun Zhao, Yoshitomo Okawachi, Jae K Jang, Xingchen Ji, Michal Lipson, and Alexander L Gaeta. Near-degenerate quadrature-squeezed vacuum generation on a silicon-nitride chip. *Physical Review Letters*, 124(19):193601, 2020.
- [196] Varun D Vaidya, B Morrison, LG Helt, R Shahrokshahi, DH Mahler, MJ Collins, K Tan, J Lavoie, A Repington, M Menotti, et al. Broadband quadrature-squeezed vacuum and nonclassical photon number correlations from a nanophotonic device. *Science Advances*, 6(39):eaba9186, 2020.
- [197] Juan Yin, Yuan Cao, Yu-Huai Li, Sheng-Kai Liao, Liang Zhang, Ji-Gang Ren, Wen-Qi Cai, Wei-Yue Liu, Bo Li, Hui Dai, et al. Satellite-based entanglement distribution over 1200 kilometers. *Science*, 356(6343):1140–1144, 2017.
- [198] Chin-Wen Chou, Julien Laurat, Hui Deng, Kyung Soo Choi, Hugues De Riedmatten, Daniel Felinto, and H Jeff Kimble. Functional quantum nodes for entanglement distribution over scalable quantum networks. *Science*, 316(5829):1316–1320, 2007.
- [199] Sheng-Kai Liao, Wen-Qi Cai, Wei-Yue Liu, Liang Zhang, Yang Li, Ji-Gang Ren, Juan Yin, Qi Shen, Yuan Cao, Zheng-Ping Li, et al. Satellite-to-ground quantum key distribution. *Nature*, 549(7670):43, 2017.



- [200] Alberto Boaron, Gianluca Boso, Davide Rusca, Cédric Vulliez, Claire Autebert, Misael Caloz, Matthieu Perrenoud, Gaëtan Gras, Félix Bussièrès, Ming-Jun Li, et al. Secure quantum key distribution over 421 km of optical fiber. *Physical Review Letters*, 121(19):190502, 2018.
- [201] Vittorio Giovannetti, Seth Lloyd, and Lorenzo Maccone. Advances in quantum metrology. *Nature Photonics*, 5(4):222, 2011.
- [202] Zheshen Zhang, Sara Mouradian, Franco NC Wong, and Jeffrey H Shapiro. Entanglement-enhanced sensing in a lossy and noisy environment. *Physical Review Letters*, 114(11):110506, 2015.
- [203] Stefano Pirandola, B Roy Bardhan, Tobias Gehring, Christian Weedbrook, and Seth Lloyd. Advances in photonic quantum sensing. *Nature Photonics*, 12(12):724–733, 2018.
- [204] Malte C Tichy. Sampling of partially distinguishable bosons and the relation to the multidimensional permanent. *Physical Review A*, 91(2):022316, 2015.
- [205] Alex Neville, Chris Sparrow, Raphaël Clifford, Eric Johnston, Patrick M Birchall, Ashley Montanaro, and Anthony Laing. Classical boson sampling algorithms with superior performance to near-term experiments. *Nature Physics*, 13(12):1153, 2017.
- [206] JJ Renema, A Menssen, WR Clements, G Triginer, WS Kolthammer, and IA Walmsley. Efficient classical algorithm for boson sampling with partially distinguishable photons. *Physical Review Letters*, 120(22):220502, 2018.
- [207] Murphy Yuezhen Niu, Isaac L Chuang, and Jeffrey H Shapiro. Qudit-basis universal quantum computation using  $\chi^{(2)}$  interactions. *Physical Review Letters*, 120(16):160502, 2018.
- [208] Bryn A Bell and Benjamin J Eggleton. Multiphoton interference in the spectral domain by direct heralding of frequency superposition states. *Physical Review Letters*, 121(3):033601, 2018.
- [209] H Jeff Kimble. The quantum internet. *Nature*, 453(7198):1023, 2008.
- [210] Stephanie Wehner, David Elkouss, and Ronald Hanson. Quantum internet: A vision for the road ahead. *Science*, 362(6412):eaam9288, 2018.
- [211] L-M Duan, MD Lukin, J Ignacio Cirac, and Peter Zoller. Long-distance quantum communication with atomic ensembles and linear optics. *Nature*, 414(6862):413, 2001.

- [212] Yuan Liang Lim, Almut Beige, and Leong Chuan Kwek. Repeat-until-success linear optics distributed quantum computing. *Physical Review Letters*, 95(3):030505, 2005.
- [213] Alessio Serafini, Stefano Mancini, and Sougato Bose. Distributed quantum computation via optical fibers. *Physical Review Letters*, 96(1):010503, 2006.
- [214] Pieter Kok, William J Munro, Kae Nemoto, Timothy C Ralph, Jonathan P Dowling, and Gerard J Milburn. Linear optical quantum computing with photonic qubits. *Reviews of Modern Physics*, 79(1):135, 2007.
- [215] Timothy J Proctor, Paul A Knott, and Jacob A Dunningham. Multiparameter estimation in networked quantum sensors. *Physical Review Letters*, 120(8):080501, 2018.
- [216] Wenchao Ge, Kurt Jacobs, Zachary Eldredge, Alexey V Gorshkov, and Michael Foss-Feig. Distributed quantum metrology with linear networks and separable inputs. *Physical Review Letters*, 121(4):043604, 2018.
- [217] Quntao Zhuang, Zheshen Zhang, and Jeffrey H Shapiro. Distributed quantum sensing using continuous-variable multipartite entanglement. *Physical Review A*, 97(3):032329, 2018.
- [218] Yi Xia, Quntao Zhuang, William Clark, and Zheshen Zhang. Repeater-enhanced distributed quantum sensing based on continuous-variable multipartite entanglement. *Physical Review A*, 99(1):012328, 2019.
- [219] Changchen Chen, Cao Bo, Murphy Yuezhen Niu, Feihu Xu, Zheshen Zhang, Jeffrey H Shapiro, and Franco NC Wong. Efficient generation and characterization of spectrally factorable biphotons. *Optics Express*, 25(7):7300–7312, 2017.
- [220] Changchen Chen, Jane E Heyes, Kyung-Han Hong, Murphy Yuezhen Niu, Adriana E Lita, Thomas Gerrits, Sae Woo Nam, Jeffrey H Shapiro, and Franco NC Wong. Indistinguishable single-mode photons from spectrally engineered biphotons. *Optics Express*, 27(8):11626–11634, 2019.
- [221] K Fradkin, A Arie, A Skliar, and G Rosenman. Tunable midinfrared source by difference frequency generation in bulk periodically poled KTiOPO<sub>4</sub>. *Applied Physics Letters*, 74(7):914–916, 1999.
- [222] Warren P Grice, Alfred B U'Ren, and Ian A Walmsley. Eliminating frequency and space-time correlations in multiphoton states. *Physical Review A*, 64(6):063815, 2001.

- [223] Peter J Mosley, Jeff S Lundeen, Brian J Smith, Piotr Wasylczyk, Alfred B U'Ren, Christine Silberhorn, and Ian A Walmsley. Heralded generation of ultrafast single photons in pure quantum states. *Physical Review Letters*, 100(13):133601, 2008.
- [224] Agata M Brańczyk, Alessandro Fedrizzi, Thomas M Stace, Tim C Ralph, and Andrew G White. Engineered optical nonlinearity for quantum light sources. *Optics Express*, 19(1):55–65, 2011.
- [225] P Ben Dixon, Jeffrey H Shapiro, and Franco NC Wong. Spectral engineering by gaussian phase-matching for quantum photonics. *Optics Express*, 21(5):5879–5890, 2013.
- [226] Nicolás Quesada and Agata M Brańczyk. Gaussian functions are optimal for waveguided nonlinear-quantum-optical processes. *Physical Review A*, 98(4):043813, 2018.
- [227] Annamaria Dosseva, Łukasz Cincio, and Agata M Brańczyk. Shaping the joint spectrum of down-converted photons through optimized custom poling. *Physical Review A*, 93(1):013801, 2016.
- [228] JL Tambasco, A Boes, LG Helt, MJ Steel, and A Mitchell. Domain engineering algorithm for practical and effective photon sources. *Optics Express*, 24(17):19616–19626, 2016.
- [229] Francesco Graffitti, Dmytro Kundys, Derryck T Reid, Agata M Brańczyk, and Alessandro Fedrizzi. Pure down-conversion photons through sub-coherence-length domain engineering. *Quantum Science and Technology*, 2(3):035001, 2017.
- [230] Francesco Graffitti, Peter Barrow, Massimiliano Proietti, Dmytro Kundys, and Alessandro Fedrizzi. Independent high-purity photons created in domain-engineered crystals. *Optica*, 5(5):514–517, 2018.
- [231] Francesco Graffitti, Jérémy Kelly-Massicotte, Alessandro Fedrizzi, and Agata M Brańczyk. Design considerations for high-purity heralded single-photon sources. *Physical Review A*, 98(5):053811, 2018.
- [232] Rui-Bo Jin, Ryosuke Shimizu, Kentaro Wakui, Hugo Benichi, and Masahide Sasaki. Widely tunable single photon source with high purity at telecom wavelength. *Optics Express*, 21(9):10659–10666, 2013.
- [233] Rui-Bo Jin, Pei Zhao, Peigang Deng, and Qing-Lin Wu. Spectrally pure states at telecommunications wavelengths from periodically poled MTiOXO<sub>4</sub> (M= K, Rb, Cs; X= P, As) crystals. *Physical Review Applied*, 6(6):064017, 2016.

- [234] Fabian Laudenbach, Rui-Bo Jin, Chiara Greganti, Michael Hentschel, Philip Walther, and Hannes Hübel. Numerical investigation of photon-pair generation in periodically poled MTiOXO<sub>4</sub> (M= K, Rb, Cs; X= P, As). *Physical Review Applied*, 8(2):024035, 2017.
- [235] Rui-Bo Jin, Neng Cai, Ying Huang, Xiang-Ying Hao, Shun Wang, Fang Li, Hai-Zhi Song, Qiang Zhou, and Ryosuke Shimizu. Theoretical investigation of a spectrally pure-state generation from isomorphs of KDP crystal at near-infrared and telecom wavelengths. *Physical Review Applied*, 11(3):034067, 2019.
- [236] Qi-Chao Sun, Yang-Fan Jiang, Ya-Li Mao, Li-Xing You, Wei Zhang, Wei-Jun Zhang, Xiao Jiang, Teng-Yun Chen, Hao Li, Yi-Dong Huang, et al. Entanglement swapping over 100 km optical fiber with independent entangled photon-pair sources. *Optica*, 4(10):1214–1218, 2017.
- [237] Chong-Ki Hong, Zhe-Yu Ou, and Leonard Mandel. Measurement of subpicosecond time intervals between two photons by interference. *Physical Review Letters*, 59(18):2044, 1987.
- [238] H Fearn and R Loudon. Theory of two-photon interference. *Journal of the Optical Society of America B*, 6(5):917–927, 1989.
- [239] Charles Santori, David Fattal, Jelena Vučković, Glenn S Solomon, and Yoshihisa Yamamoto. Indistinguishable photons from a single-photon device. *Nature*, 419(6907):594, 2002.
- [240] Atature Kiraz, M Atatüre, and A Imamoğlu. Quantum-dot single-photon sources: Prospects for applications in linear optics quantum-information processing. *Physical Review A*, 69(3):032305, 2004.
- [241] CI Osorio, N Sangouard, and Robert Thomas Thew. On the purity and indistinguishability of down-converted photons. *Journal of Physics B*, 46(5):055501, 2013.
- [242] Agata M Brańczyk. Hong-Ou-Mandel interference. *arXiv preprint arXiv:1711.00080*, 2017.
- [243] Sebastian Ruder. An overview of gradient descent optimization algorithms. *arXiv preprint arXiv:1609.04747*, 2016.
- [244] Quoc V Le, Jiquan Ngiam, Adam Coates, Abhik Lahiri, Bobby Prochnow, and Andrew Y Ng. On optimization methods for deep learning. In *Proceedings of the 28th International Conference on International Conference on Machine Learning*, pages 265–272. Omnipress, 2011.

- [245] Diederik P Kingma and Jimmy Ba. Adam: A method for stochastic optimization. *arXiv preprint arXiv:1412.6980*, 2014.
- [246] Soham De, Anirbit Mukherjee, and Enayat Ullah. Convergence guarantees for RMSProp and ADAM in non-convex optimization and an empirical comparison to Nesterov acceleration, 2018.
- [247] Kiyoshi Kato and Eiko Takaoka. Sellmeier and thermo-optic dispersion formulas for KTP. *Applied Optics*, 41(24):5040–5044, 2002.
- [248] Ryan S Bennink. Optimal collinear gaussian beams for spontaneous parametric down-conversion. *Physical Review A*, 81(5):053805, 2010.
- [249] P Ben Dixon, Danna Rosenberg, Veronika Stelmakh, Matthew E Grein, Ryan S Bennink, Eric A Dauler, Andrew J Kerman, Richard J Molnar, and Franco NC Wong. Heralding efficiency and correlated-mode coupling of near-IR fiber-coupled photon pairs. *Physical Review A*, 90(4):043804, 2014.
- [250] Lutfi Arif Ngah, Olivier Alibart, Laurent Labonté, Virginia d’Auria, and Sébastien Tanzilli. Ultra-fast heralded single photon source based on telecom technology. *Laser & Photonics Reviews*, 9(2):L1–L5, 2015.
- [251] Nicola Montaut, Linda Sansoni, Evan Meyer-Scott, Raimund Ricken, Viktor Quiring, Harald Herrmann, and Christine Silberhorn. High-efficiency plug-and-play source of heralded single photons. *Physical Review Applied*, 8(2):024021, 2017.
- [252] Nicolas Sangouard, Christoph Simon, Hugues De Riedmatten, and Nicolas Gisin. Quantum repeaters based on atomic ensembles and linear optics. *Reviews of Modern Physics*, 83(1):33, 2011.
- [253] Matthäus Halder, Alexios Beveratos, Nicolas Gisin, Valerio Scarani, Christoph Simon, and Hugo Zbinden. Entangling independent photons by time measurement. *Nature Physics*, 3(10):692, 2007.
- [254] Xiyuan Lu, Qing Li, Daron A Westly, Gregory Moille, Anshuman Singh, Vikas Anant, and Kartik Srinivasan. Chip-integrated visible–telecom entangled photon pair source for quantum communication. *Nature Physics*, 15(4):373–381, 2019.
- [255] Kurt Hornik, Maxwell Stinchcombe, and Halbert White. Multilayer feedforward networks are universal approximators. *Neural Networks*, 2(5):359–366, 1989.